# On crystal growth kinetics in the BaCO$_3$-MgCO$_3$ system

Dissertation zur Erlangung des Doktorgrades
an der Fakultät für Geowissenschaften
der Ludwig-Maximilians-Universität München

Vorgelegt von

## Michael Lindner

München, 29.08.2018

# On crystal growth kinetics in the BaCO₃-MgCO₃ system

Michael Lindner

# Acknowledgments

# Abstract

The BaCO$_3$-MgCO$_3$ system can be seen as a close analogue to the CaCO$_3$-MgCO$_3$ system regarding the chemical and structural similarities of the phases occurring in these systems. The fast and easy growth of norsethite, BaMg(CO$_3$)$_2$, however, is in vast contrast to the problems associated with the precipitation of dolomite, CaMg(CO$_3$)$_2$. This contrasting behavior is of highest importance as Mg, which is equally part of both minerals, is supposed to be the reason for the growth problems of dolomite and other anhydrous Mg-bearing carbonates. In order to attain a comprehensive understanding on growth of anhydrous Mg-bearing carbonates, kinetic studies on mineral growth in the BaCO$_3$-MgCO$_3$ system were performed. Not only growth of norsethite as the intermediate phase in the system but also the growth of the two endmembers (magnesite, MgCO$_3$, and witherite, BaCO$_3$) in the presence of the respective other cation was investigated. This allowed for a direct and quantitative comparison with the growth behavior in other carbonate systems in general and with the CaCO$_3$-MgCO$_3$ system in particular.

The effect of Ba$^{2+}$ on magnesite growth at 100 °C was assessed in a complementary micro- and macroscopical study. Growth experiments have been conducted on magnesite seeds in hydrothermal mixed-flow reactors (T = 100 °C, pH $\sim$7.8, 0 – 100 µM Ba$^{2+}$, supersaturations $\Omega$ with respect to magnesite: $\sim$100 – 200) and by hydrothermal atomic force microscopy (T = 100 °C, pH $\sim$8.2, 0 – 50 µM Ba$^{2+}$, $\Omega_{magnesite}$ $\sim$60 – 90). The experiments showed that aqueous barium leaves magnesite growth rates unaffected but leads to norsethite precipitation. At the conditions of the experiments, norsethite growth rates were found to be controlled by the aqueous Ba$^{2+}$ concentration. Given enough Ba$^{2+}$, Mg$^{2+}$ withdrawal from solution by norsethite clearly exceeded the withdrawal by magnesite growth. At high Ba$^{2+}$ concentrations, however, norsethite nucleated and grew simultaneously to magnesite. Microscopic investigations of the growth on the (104) surface of magnesite did not reveal any signs of Ba$^{2+}$ incorporation yielding a partitioning coefficient of Ba$^{2+}$ between magnesite and solution in the range of 10$^{-2}$ or smaller.

Growth behavior in the BaCO$_3$-rich side of the BaCO$_3$-MgCO$_3$ system was explored in mixed-flow reactors at 50 °C and various Mg$^{2+}$-concentrations (0.25 – 2 mM Ba$^{2+}$, 0 – 20 mM Mg$^{2+}$, pH 7.8 – 8.5, ionic strength 0.1 M). At Mg$^{2+}$:Ba$^{2+}$ ratios in solution smaller than 6:1, Mg$^{2+}$ did not affect witherite growth kinetics. No significant amount of Mg$^{2+}$ was incorporated. The rate constant $k$ and reaction order $n$ for witherite growth were determined for the first time ($k$ = 0.65 ± 0.05 x 10$^{-7}$ mol m$^{-2}$ s$^{-1}$; $n$ = 1.3 ± 0.1; supersaturation $\Omega_{witherite}$ = 1 – 4). Mg$^{2+}$:Ba$^{2+}$ ratios in solution larger than 12:1 led to a replacement of witherite by norsethite.

Norsethite solubility was determined in 0.1 M NaCl aqueous solutions from 30 to 150 °C using a hydrogen-electrode concentration cell, which provided a continuous in-situ measurement of hydrogen ion molality. The solubility product of norsethite can be described by $\log_{10}K_{sp°\text{-nrs}} = a + b/T + cT$, where $a = 31.007$, $b = -7321.122$, and $c = -0.0811$. Gibbs free energy ($\Delta_f G^0_{298.15}$) and enthalpy ($\Delta_f H^0_{298.15}$) of norsethite formation were determined to be $-2167 \pm 2$ kJ/mol and $-2351 \pm 2$ kJ/mol, respectively. Growth experiments were conducted in mixed-flow reactors covering a significant span of solution compositions (pH: $7.0 - 8.5$, $3 \times 10^{-6} - 5 \times 10^{-3}$ M $Ba^{2+}$, $1 \times 10^{-4} - 9 \times 10^{-2}$ M $Mg^{2+}$, ionic strength: 0.1 M, $\Omega_{\text{norsethite}} = 1 - 95$) and temperatures (40, 65, and 100 °C). From the experimental data, the apparent activation energy of norsethite growth rate constant was determined to be $E_a = 54 \pm 4$ kJ/mol. An extrapolation to 25 °C resulted in a rate constant of $k^{25\,°C}_{nrs} = 0.11$ nmol m$^{-2}$ s$^{-1}$ with a reaction order of $1.2 \pm 0.1$. A direct comparison of experimentally acquired growth rates showed that the growth rate constant of norsethite is five orders of magnitude higher than that of dolomite and still three orders of magnitude higher than that of magnesite at 100 °C.

In summary, the reported studies clearly showed that the occurrence and growth of norsethite dominated the $BaCO_3$-$MgCO_3$ system over a wide range of conditions. No sign of solid solution formation could be discerned. The large difference in cationic radii presumably prevented the incorporation of considerable amounts of $Mg^{2+}$ into witherite and of $Ba^{2+}$ into magnesite, respectively. This behavior is in vast contrast to the $CaCO_3$-$MgCO_3$ system where solid solutions easily form and the occurrence of ordered dolomite is impaired.

The significantly faster growth of norsethite indicates that some rate promoting mechanism must exist which is active only during norsethite growth, but not during dolomite or magnesite growth. This mechanism can only be located at the norsethite surface where parameters like the hydration energy of $Mg^{2+}$ can differ significantly from the well-known values in bulk solution.

# Table of contents

# 1  Introduction

## 1.1  Water-mineral interactions

Interactions between water and minerals are decisive in many natural processes, scientific fields and technical activities. Examples include weathering, paleoclimate research, biomineralization, element cycling, water treatment, the storage safety of nuclear waste and $CO_2$, and mineral scale formation. Therefore, detailed scientific knowledge about water-mineral interaction is of great societal interest as it allows interpreting, modeling and predicting the short- and long-term behavior of many natural and anthropogenic systems. In this way, knowledge about water-mineral interaction provides technical criteria for policies and regulations inspired by environmental sustainability. The basis of such knowledge is a fundamental understanding about the thermodynamic equilibrium relations between minerals and their surroundings as well as the kinetics of these reactions i. e., the reaction mechanisms and the rates at which these equilibriums can be reached (Garrels, 1959).

   Given the physical and chemical complexity and heterogeneity of natural and engineered systems, it is often necessary to employ experimental approaches to decouple the impacts of concurrent processes and to gain insight into the fundamental controls on water-mineral interaction. Processes occurring in systems which are not accessible by experiments, however, may be investigated indirectly by the utilization of "analogue systems". Such analogues exhibit similar properties as the system of interest but are more easily explorable. Data collected in such systems then allows for identification of the principles and mechanisms controlling reactions and may be transferred to systems of broader interest.

   An important example for such an analogue is the mineral norsethite, $BaMg(CO_3)_2$, which has tremendous chemical and structural similarities to the geologically important mineral dolomite, $CaMg(CO_3)_2$. Due to the easiness of norsethite growth, studies on this mineral are expected to yield direct experimental information on the problems associated with the precipitation of dolomite and other anhydrous Mg-bearing carbonates (Lippmann, 1973). In the present thesis the occurrence and growth kinetics of minerals in the $BaCO_3$-$MgCO_3$ system were quantitatively investigated to replace the existing qualitative experience of fast and easy norsethite precipitation.

## 1.2   Carbonate minerals in natural and technical systems

Vast amounts of the minerals on Earth's surface are carbonates. Studies on carbonate nucleation, growth, and dissolution, therefore, are of tremendous importance to obtain a fundamental understanding of both sedimentological problems and chemical processes in engineered systems (e.g., Hasson et al., 1968; Morse and Mackenzie, 1990).

To date, research has mainly focused on calcium carbonate, $CaCO_3$, with its three polymorphs (calcite, aragonite, and vaterite), as it is by far the most abundant carbonate compound. In most natural and engineered carbonate-systems, however, the pure phase is of little interest because of the omnipresence of foreign ions and compounds in differring amounts. These foreign substances can have an impact on the growth and dissolution behavior by adsorption on the surface or incorporation into the growing crystal (e.g., Pina and Jordan, 2010; Rodríguez-Navarro and Benning, 2013). Particularly important in that respect is the study of complex carbonate solid solutions, which can precipitate from aqueous fluids of various chemical compositions. In solid solution systems, it is known that the incorporation of foreign ions, or trace elements, can have a dramatic impact on the rates of precipitation of simple carbonate phases and the conditions at which they form (Astilleros et al., 2003; 2010; Davis et al., 2000; Prieto, 2009). These effects, however, have been investigated by only few studies. A comprehensive kinetic description of these processes, which may help developing reactive transport models (e.g., Noguera et al., 2012; 2017; Prieto et al., 2016; Steefel et al., 2005), is missing.

The current treatment of precipitation reactions is generally accomplished by using extremely simplified models, which only involve the nucleation and growth of either pure phases or solid solutions with fixed stoichiometry. Formation of carbonate minerals in highly complex chemical systems, however, is key to ensure the safety of $CO_2$ capture and sequestration strategies and provides an efficient mechanism to control the levels of contaminants in drinking-water aquifers (Kampman et al., 2014; Little and Jackson, 2010). The development and success of $CO_2$ sequestration strategies, for instance, depends on the capability of predicting performance of storage sites over periods of hundreds to thousands of years (Audigane et al., 2007). In this context water-mineral reactions are of highest importance as even small amounts of dissolution and/or precipitation can significantly affect the porosity and permeability of reservoir rocks over time.

Understanding of water-mineral reactions can be obtained for instance from field observations like veins or alteration zones, which are indicative of former presence of fluids in rocks (e.g., Meunier, 1995). In addition, reaction fronts in minerals or porosity may give valuable information down to the nanometer scale (e.g., Putnis, 2009). Information may also be obtained from mineral assemblages

and isotopic compositions, which can serve as proxies for environmental conditions and fluid-rock interactions of the past (e.g., Holland and Turekian, 2014). Due to the physico-chemical complexity and heterogeneity of natural systems, however, it is often necessary to employ experimental approaches, which systematically decouple the effects of concurrent processes.

Based on experimentally acquired thermodynamic and kinetic data, the application of modern computer codes then allows for a far reaching definition of many geochemical systems by the rapid calculation of mineral solubilities and solution speciation (Oelkers et al., 2009). In this way, geochemical modeling has become a powerful tool for the interpretation and prediction of manifold relations between minerals and their surroundings, e.g., the numerical evaluation of the consequences of storage of toxic or radioactive waste and $CO_2$ in various host rocks (Oelkers and Cole, 2008; Steefel et al., 2005; van der Lee and Windt, 2001).

For such an numerical evaluation, however, the thermodynamic databases need to comprise high precision data for all chemical species and mineral phases involved. Even traces of phases might have extensive consequences on solution speciations and mineral solubilities. Often, however, the databases miss the relevant entries. Data for non-rock-forming minerals, for instance, are scarce in general. Therefore, the acquisition and improvement of thermodynamic and kinetic data of mineral dissolution and growth is a tremendously important task in science.

## 1.3   The dolomite and magnesite problem

On Earth's surface, dolomite [$CaMg(CO_3)_2$] is the second most common carbonate mineral after calcite [$CaCO_3$]. It occurs in sizes ranging from thin layers to massive geological bodies in many sedimentary environments and in most geologic eras and forms important petroleum reservoirs, rocks hosting base metal deposits, and fresh water aquifers (Braithwaite et al., 2004; Gregg et al., 2015; Lippmann, 1973; Rodriguez-Blanco et al., 2015; Warren, 2000). Most dolomites can be found in Precambrian marine sediments while younger dolomites are more rare, even though modern seawater is highly supersaturated with respect to dolomite (Holland and Zimmermann, 2000; Lippmann, 1973; McKenzie and Vasconcelos, 2009; Warren, 2000).

Until today it is not entirely clear why huge amounts of dolomite rocks were formed in the geological past but no formation of equivalent amounts of dolomite is observed in modern marine environments (e.g., Arvidson and Mackenzie, 1999). To add to this inconsistency, syntheses of dolomite in the laboratory at ambient conditions generally fail (Land, 1998; Lippmann, 1973). This issue has been termed "dolomite question" (Fairbridge, 1957) or "dolomite problem" (Arvidson and Mackenzie, 1999; Lippmann, 1973). As contemporary seawater is supersaturated

with respect to dolomite, from the thermodynamic point of view it should readily precipitate. However, due to an activation barrier inherent to the system, precipitation and growth of dolomite is kinetically inhibited near room temperature.

There are different explanations for the formation of the large amounts of ancient dolomite. It could have been precipitated from a seawater different in composition from today's seawater (Given and Wilkinson, 1987; Hardie, 1987). As another solution to this problem, the presence of microorganisms was discussed (McKenzie and Vasconcelos, 2009; Sánchez-Román et al., 2009; Vasconcelos, 1997; Zhang et al., 2012b; 2013), which, irrespective of the sulfate content of the medium, allowed the formation of dolomite in experiments. In an alternative approach, the older dolomite could be a secondary product from primary calcium-rich carbonate minerals and magnesium rich solutions (Land, 1985; Reinhold, 1998). The secondary dolomite formation, thus, ultimately corresponds to an Ostwald ripening of metastable precursor phases. In laboratory experiments, this secondary dolomitization was successfully confirmed (Kessels et al., 2000; Usdowski, 1967; 1989; 1994). However, significant amounts of dolomite could only be achieved at higher temperatures. Such temperature conditions may not necessarily be given in sedimentary environments with a thin sediment cover. Other findings such as limited fluid permeability or razor-sharp calcite-dolomite changes give rise to doubts if the secondary dolomitization is a model that describes dolomite formation satisfactorily well in all cases (even in consideration of geological time frames). The formation of ordered dolomite in uroliths of a Dalmatian dog within several months at ~38 °C (Mansfield, 1980) clearly shows that dolomite can form under the influence of biogenic molecules or bacterial activity even at lower temperatures. Nevertheless, most claims of ambient temperature dolomite synthesis are heavily debated (Gregg et al., 2015, and references therein)

Like dolomite, magnesite [$MgCO_3$] has a growth problem at low temperature. Although its occurrence in natural environments is rather scarce, magnesite growth has been keenly investigated, as it is a promising candidate for geological $CO_2$ storage (Bénézeth et al., 2011; Bracco et al., 2014; Felmy et al., 2015; Gautier et al., 2015; 2016; Hänchen et al., 2008; King et al., 2013; Saldi et al., 2009). However, magnesite precipitation experiments in the laboratory succeed only at temperatures above 80 °C (e.g., Saldi et al., 2009). When trying to synthesize magnesite from aqueous solutions at ambient conditions, the usual product phases are hydrated magnesium carbonates like nesquehonite, $MgCO_3 \cdot 3H_2O$, or hydromagnesite, $Mg_5(CO_3)_4(OH)_2 \cdot 4H_2O$, but not the anhydrous magnesite (Hopkinson et al., 2012).

Recent work concerning dolomite and magnesite growth has focused on the effects of the presence of organic or inorganic compounds as well as microorganisms (Berninger et al., 2016; Bontognali et al., 2014; Kenward et al., 2013; Gautier et al., 2015; 2016; Roberts et al., 2013; Vasconcelos et al., 1995; Wu et al., 2011; Zhang et al., 2012b; 2012a; 2013). Irrespective of ordering problems, anhydrous Mg-bearing

carbonates were reported to form in some of the experiments even at ambient conditions. The enhanced dehydration and incorporation of $Mg^{2+}$ emphasizes the importance of functional additives and surfaces. In this context a notable study reports on the formation of magnesite on the surface of poorly defined polystyrene microspheres with a high density of carboxyl groups at ambient conditions (Power et al., 2017).

The cause of all these problems associated with the growth of dolomite and magnesite at low temperatures is supposed to be the magnesium ion, which is part of both minerals (e.g., Lippmann, 1973). The common explanation is the relative high stability of the hydrated magnesium complex and the resulting low water exchange rate between the first hydration shell and the bulk solution or mineral surface (Bleuzen et al., 1997; Lippmann, 1973; Pokrovsky and Schott, 2002; Sayles and Fyfe, 1973; Schott et al., 2009). In comparison to $Ca^{2+}$ or $Ba^{2+}$, the ligand exchange rate and consequently the mineral growth rate are much slower for $Mg^{2+}$ (Pokrovsky and Schott, 2002).

Nevertheless there are signs that processes additional to the dehydration of the $Mg^{2+}$-complex may contribute to the growth problems of dolomite and magnesite: a growth study in non-aqueous solutions also failed to produce magnesite or dolomite (Xu et al., 2013). Another important indication is the occurrence of "dolomite analogue" phases like norsethite, $BaMg(CO_3)_2$, or $PbMg(CO_3)_2$, which can be precipitated at ambient conditions easily (e.g., Lippmann, 1973).

## 1.4 The "dolomite analogue" mineral norsethite

Norsethite has been recognized in the Green River Formation as "new unnamed mineral" with the composition $BaMg(CO_3)_2$ by Milton and Eugster in 1958. Shortly after this, the first structural analysis has been conducted and the mineral was named "norsethite", after Keith Norseth, an engineering geologist who assisted in the study of this mineral (Mrose et al., 1961). Since then, numerous findings of the mineral have been reported: as hydrothermal gangue-mineral in Namibia (Steyn and Watson, 1967), in carbonatites of Brazil (Secco and Lavina, 1999), and as supergene mineral in a Bulgarian ore deposit (Zidarov et al., 2009).

The recognition of the chemical and structural similarity to dolomite (see chapter 1.5) led to an increased interest in this mineral and made norsethite a prominent object for various research topics over several decades: synthesis (Chang, 1964; Hood et al., 1974; Lippmann, 1967b; 1968; 1973; Morrow and Ricketts, 1986; Longo and Voight, 1989; Pimentel and Pina, 2014; 2016), structure (Effenberger and Zemann, 1985; Effenberger et al., 2014; Ende et al., 2017; Lippmann, 1967a; 1967b; Pippinger et al., 2014), solubility (Königsberger et al., 1998), Raman- and IR-spectra

(Böttcher et al., 1997; Scheetz and White, 1977; Schmidt et al., 2013), and isotope fractionation (Böttcher, 2000; Zheng and Böttcher, 2014).

The main reason for this keen interest in norsethite is the fact that its synthesis from aqueous solution can be easily achieved at ambient conditions within very short timescales, while this is certainly not the case for dolomite (Lippmann, 1967c). In fact, several routes for the precipitation of norsethite from aqueous solution are known: i) the aging of an amorphous precursor precipitated from solutes:

$$Ba^{2+}_{(aq)} + Mg^{2+}_{(aq)} + 2\ CO_3^{2-}_{(aq)} \rightarrow BaMg(CO_3)_{2(s)} \qquad (1.4\text{-}1)$$

(Hood et al., 1974; Pimentel and Pina, 2014), ii) the "norsethitization" of witherite ($BaCO_3$) in contact with a magnesium rich solution:

$$BaCO_{3(s)} + Mg^{2+}_{(aq)} + CO_3^{2-}_{(aq)} \rightarrow BaMg(CO_3)_{2(s)} \qquad (1.4\text{-}2)$$

(Lippmann, 1967a; 1967c; 1968), and iii) dry grinding of the reaction educts:

$$BaCO_{3(s)} + MgCO_{3(s)} \rightarrow BaMg(CO_3)_{2(s)} \qquad (1.4\text{-}3)$$
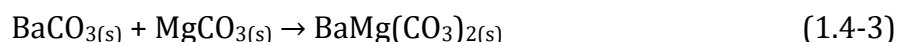
(Longo and Voight, 1989). Given this diversity of formation routes, it is surprising that it is so troublesome to form dolomite in analogous ways. Therefore, there is reasonable hope that the investigation of the easiness of norsethite growth can give valuable information on the problems associated with the growth of dolomite and anhydrous, Mg-bearing carbonates in general.

## 1.5    Structural relationships of carbonate phases

Anhydrous carbonate minerals crystallize with either a trigonal or an orthorhombic crystal structure, depending on the ionic radius of the cation. Small cations form trigonal minerals in which each cation is coordinated by six oxygens, while the large cations form orthorhombic minerals with a coordination number of nine (Speer, 1983; Reeder, 1983). The $Ca^{2+}$ ion defines the border between the two structure types and can form trigonal calcite or orthorhombic aragonite (Figure 1.5-1, all crystal structures drawn with VESTA 3, Momma and Izumi, 2011). Consequently, magnesite is exclusively rhombohedral, witherite only orthorhombic. In both structure types, the carbonate group is arranged in a nearly planar orientation perpendicular to the crystallographic $c$-axis. Detailed crystallographic data of selected carbonate minerals is given in Table 1.5-1.

In a simplified view, dolomite and norsethite structures can both be derived from the calcite structure (cf. Figure 1.6-1) where alternating Ca- and carbonate-layers lie perpendicular to the $c$-axis and every $Ca^{2+}$ is coordinated by six equidistant (2.360 Å) oxygen ions (Effenberger et al., 1981; Lippmann, 1973). In dolomite, every
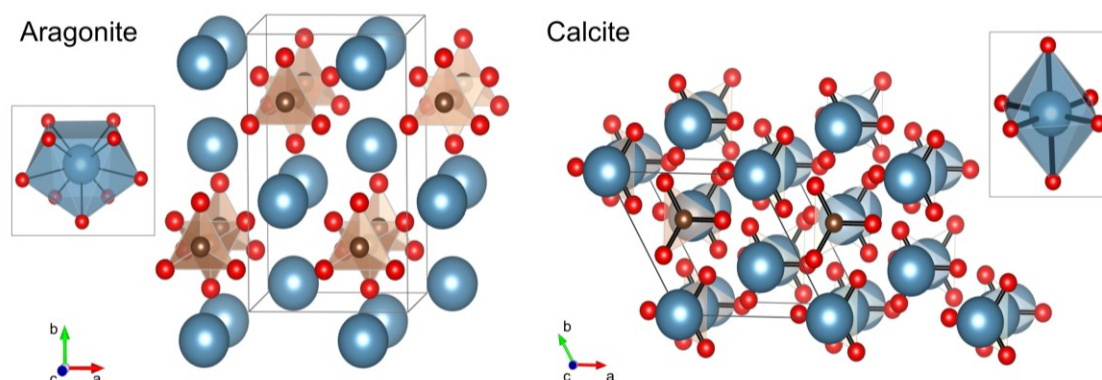
Figure 1.5-1: Crystal structures of aragonite and calcite. Blue: calcium, red: oxygen, black: carbon. Carbonate groups are indicated by triangles. Insets show Ca-coordination of the respective mineral.

other Ca-layer is replaced by a Mg-layer. This replacement is accompanied by a small rotation of the carbonate groups resulting in smaller Mg-O (2.082 Å) and larger Ca-O (2.382 Å) distances. The resulting symmetry is reduced from $R\bar{3}c$ to $R\bar{3}$. However, both Mg and Ca are still coordinated by six oxygen ions, respectively.

The first structure determination of norsethite was carried out by Friedrich Lippmann on synthetic crystals grown at room temperature in aqueous solution (Lippmann, 1967a; 1967b). He determined unit cell parameters of $a = 5.017$ Å and $c = 16.77$ Å in the space group $R32$ and recognized that $Ba^{2+}$ and $Mg^{2+}$ are arranged in alternating layers perpendicular to the $c$-axis, just like $Ca^{2+}$ and $Mg^{2+}$ in dolomite, which are in turn intermitted by $CO_3^{2-}$ layers. Technological advancement of X-ray diffractometers encouraged the reinvestigation of the norsethite structure in 1985 (Effenberger and Zemann) and 2014 (Effenberger et al.). Both studies used single crystals grown by Lippmann. In the 1985 study, lattice constants of $a = 5.022(1)$ Å and $c = 16.77(1)$ Å in the space group $R\bar{3}m$ have been determined. The most recent study gave reason to double the unit cell parameter $c$ due to a rotation of the carbonate groups, resulting in $a = 5.0212(9)$ Å and $c = 33.581(6)$ Å in space group $R\bar{3}c$. The carbonate groups in norsethite show some differences to the orientation in the dolomite structure, which results in an irregular and asymmetrical coordination of $Ba^{2+}$ by six strongly bonded oxygens (2.790 Å) and by six weakly bonded oxygens with a larger Ba-O distance (3.097 Å) (Ende et al. 2017). $Mg^{2+}$ is coordinated sixfold, like in dolomite, with a Mg-O distance of 2.060 Å. Therefore, the coordination polyhedra of the two cations in norsethite, $Ba^{2+}$ and $Mg^{2+}$, are highly diverse (cf. Figure 1.6-1). Although dolomite and norsethite are not isostructural, the similarity is large enough to give reason for a keen interest in norsethite.

It is worth to mention that the phase $PbMg(CO_3)_2$ is isostructural to norsethite and although its growth is slower than the growth of norsethite, it is much faster than dolomite and magnesite growth and also possible at ambient conditions (Lippmann, 1966; 1973; Pimentel and Pina, 2016). Pb is coordinated 12-

Table 1.5-1: Crystallographic data of aragonite, witherite, calcite, magnesite, norsethite, and dolomite. Note that Ba in norsethite is coordinated by six strongly and six weakly bonded oxygens.

| Mineral | Aragonite[a] | Witherite[a] | Calcite[b] | Magnesite[b] | Norsethite[c] | Dolomite[b] |
|---|---|---|---|---|---|---|
| composition | $CaCO_3$ | $BaCO_3$ | $CaCO_3$ | $MgCO_3$ | $BaMg(CO_3)_2$ | $CaMg(CO_3)_2$ |
| space group | $Pmcn$ | $Pmcn$ | $R\bar{3}c$ | $R\bar{3}c$ | $R\bar{3}c$ | $R\bar{3}$ |
| $a$ [Å] | 4.9614 | 5.3127 | 4.9896 | 4.6328 | 5.0212 | 4.812 |
| $b$ [Å] | 7.9671 | 8.8959 | 4.9896 | 4.6328 | 5.0212 | 4.812 |
| $c$ [Å] | 5.7404 | 6.4285 | 17.0610 | 15.0129 | 33.581 | 16.020 |
| $V_{cell}$ [Å$^3$] | 227 | 304 | 425 | 322 | 847 | 371 |
| coordination | Ca: [IX] | Ba: [IX] | Ca: [VI] | Mg: [VI] | Ba: [VI]$^s$+[VI]$^w$ Mg: [VI] | Ca: [VI] Mg: [VI] |

[a] De Villiers, 1971

[b] Effenberger et al., 1981

[c] Effenberger et al., 2014

fold with six shorter (~2.5 Å) and six longer (~3.2 Å) bonds, like Ba in norsethite, while the Mg-O distance of the Mg-octahedron is 2.095 Å (Lippmann, 1966).

## 1.6 Binary carbonate systems

In general, ions with similar radii (and charge) can substitute each other in a crystal structure. Therefore, the occurrence of solid solutions generally can be related to the cation size differences (Table 1.6-1). Differences of ionic radii ≤ 0.11 Å can lead to complete solid solutions (except Ni-Mg), while cations with a larger difference may lead to solid solutions with limited miscibility (Reeder, 1983). Ion pairs with limited miscibility often are able to form ordered double carbonates (e. g., Ca-Mg, Cd-Mg, Ca-Mn), although there are exceptions to this rule (e. g., Ca-Fe) (Reeder, 1983).

Table 1.6-1: Effective ionic radii of selected cations with different coordination numbers from Shannon (1976).

| Cation | Ionic radius [Å] [VI] | Ionic radius [Å] [IX] | Ionic radius [Å] [XII] |
|---|---|---|---|
| $Mn^{2+}$ | 0.67 | - | - |
| $Mg^{2+}$ | 0.57 | - | - |
| $Ca^{2+}$ | 1.00 | 1.18 | 1.34 |
| $Sr^{2+}$ | 1.18 | 1.31 | 1.44 |
| $Ba^{2+}$ | 1.35 | 1.47 | 1.61 |
| $Pb^{2+}$ | 1.19 | 1.35 | 1.49 |
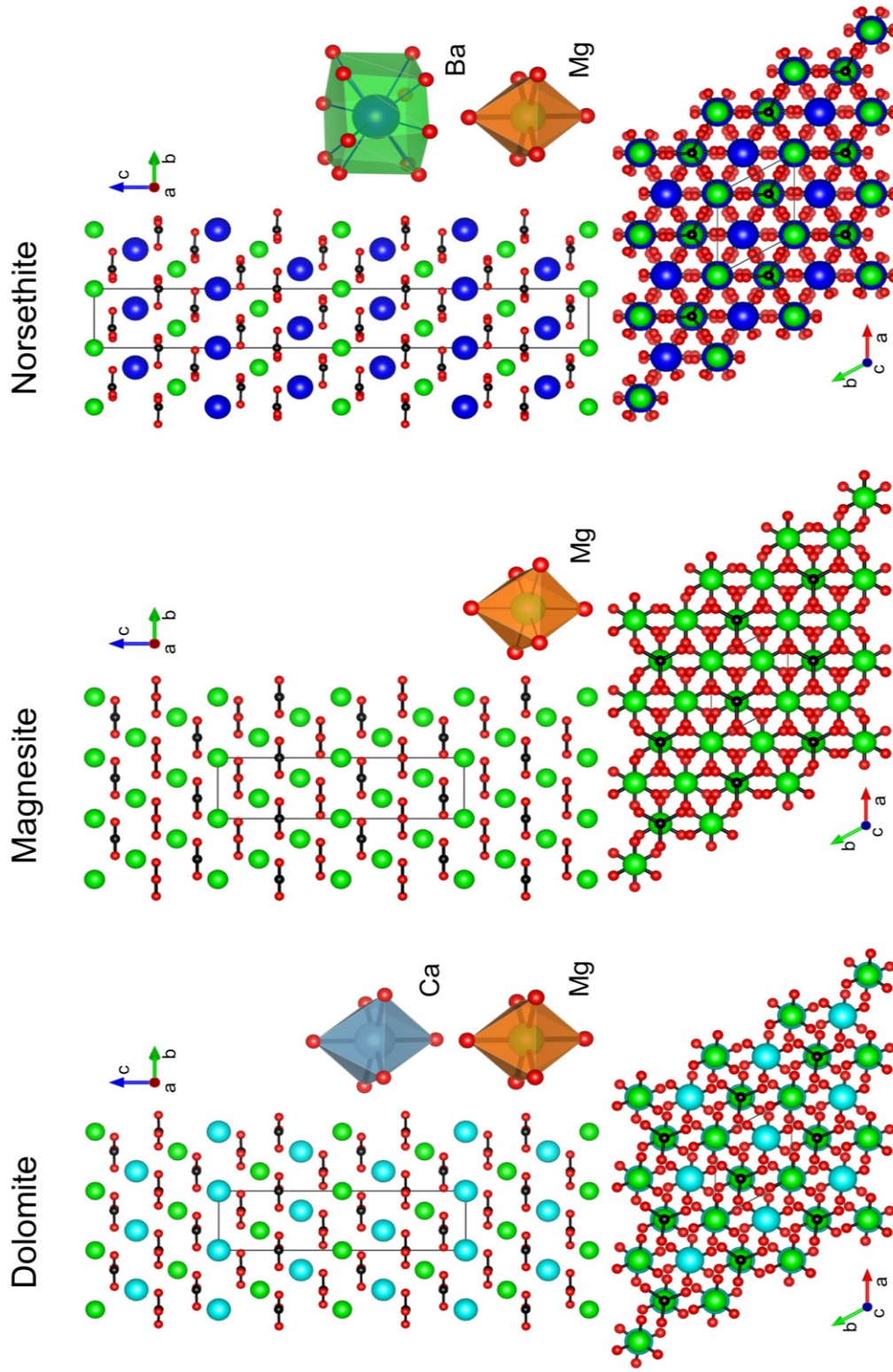
Figure 1.6-1: Crystal structures of dolomite, magnesite, and norsethite. Light blue: calcium, blue: barium, green: magnesium, red: oxygen, black: carbon, black lines: unit cell. Minerals are built up by an alternating cation-anion layer structure in $c$-direction. Due to slightly different carbonate group rotations, cation polyhedra in norsethite are different to dolomite and magnesite. The overall similarity of the structures, however, is easily recognizable.

### 1.6.1  CaCO$_3$-MgCO$_3$

The endmembers of the CaCO$_3$-MgCO$_3$ system can be structurally related or diverse. A lot of studies have focused on the effect of aqueous magnesium on the precipitation and growth of calcite (Astilleros et al., 2010; Berner, 1975; Bischoff, 1968; Choudens-Sánchez and Gonzalez, 2009; Davis et al., 2000; Gutjahr et al., 1996; Mucci and Morse, 1983; Reddy and Nancollas, 1976; Reddy and Wang, 1980; Wasylenki et al., 2005; Zhang and Dawe, 2000) and to smaller extents on aragonite (Berner, 1975; Gaetani and Cohen, 2006; Gutjahr et al., 1996; Karoui et al., 2008). It has been found, that magnesium can be incorporated up to several mol% into calcite, but only in minor amounts into aragonite. Consequently, Ca$_x$Mg$_{1-x}$CO$_3$ solid solutions with calcite structure occur commonly, while aragonite does not contain significant amounts of magnesium (Berner, 1975; Berninger et al., 2016; Mucci and Morse, 1983). While calcite growth is inhibited, aragonite growth is not influenced by the presence of magnesium (Berner, 1975; Gutjahr et al., 1996). Experimentally determined partitioning coefficients of magnesium between calcite and aqueous solution lie between $k_{d\,Mg\,cc} = \left(\frac{X_{Mg}}{X_{Ca}}\right)/\left(\frac{m_{Mg}}{m_{Ca}}\right) = 0.0123 - 0.0573$ (Katz, 1973; Mucci and Morse, 1983), indicating a preference of magnesium for the solution ($X_i$ is the mole fraction of Ca$^{2+}$ and Mg$^{2+}$ in the precipitated calcite, $m_i$ stands for the concentration of Ca$^{2+}$ and Mg$^{2+}$ in the aqueous solution).

Studies on magnesite are more scarce because of the fact that it is a much less common and hence less relevant mineral than calcite and due to the lack of growth below temperatures of approx. 80 °C, which makes experimental work more troublesome. Nevertheless, magnesite solubility and growth kinetics have been evaluated in several studies. Because of its high stability and the huge amounts of magnesium in basaltic rocks, magnesite is thought to be a promising candidate for geological CO$_2$ storage (Dufaud et al., 2009; Giammar et al., 2005; Oelkers and Cole, 2008; Prigiobbe et al., 2009). Therefore, studies concerning dissolution (Jordan et al., 2001; Higgins et al., 2002; Saldi et al., 2010) and growth behavior under the influence of various organic and inorganic compounds and ions have been conducted (Berninger et al., 2016; Freeman et al., 2009; Gautier et al., 2015; 2016; Saldi et al., 2009). An investigation on the growth of the Mg-rich side of the CaCO$_3$-MgCO$_3$ system (the effect of aqueous calcium on magnesite growth), showed that calcium is incorporated into magnesite with up to 8 mol% but has no detectable influence on the growth rate (Berninger et al., 2016). The determined partitioning coefficient for Ca between growing magnesite and aqueous solution at 100 °C was found to be $k_{d\,Ca\,mgs} = 6.9 \pm 0.9$, which implies a preferred incorporation of calcium into magnesite. The prediction of the partitioning coefficient at ambient conditions using a linear free energy correlation approach yields a value of $k_{d\,Ca\,mgs} = 53.7$

(Wang and Xu, 2001), which, although much higher than the experimental value, points in the same general direction.

Summing up there is a strong preference for calcium to be incorporated into magnesite, but reluctance of magnesium incorporation into calcite. This behavior has direct consequences for the intermediate phase of the system, dolomite: the stacking order of alternating cation- and carbonate layers in dolomite gives rise to the emergence of structural units which can be imaged as "calcite layers" and "magnesite layers". During dolomite growth the two cations $Ca^{2+}$ and $Mg^{2+}$ can be incorporated in a carbonate environment of the respective other cation. For dolomite growing from a stoichiometric solution this means that the calcite-layer will stay relatively magnesium free, while the magnesite layer can be expected to have a high amount of calcium incorporated on magnesite sites. This accumulation of Ca at the growth front of the mineral slows down growth rates up to a complete inhibition due to increasing lattice mismatch (Berninger et al., 2017; Fenter et al., 2007). Therefore an unordered Ca-rich phase can be expected, which should not be called "dolomite" as it lacks the order into distinct Ca- and Mg-layers. In literature the terms "protodolomite" or "high Mg-calcite" are often used, although there are no clear definitions of these expressions. This can be even more confusing as the cation ordering, which defines dolomite, is not limited into one layer, but also concerns the succession of the layers. After a sequence of dolomitic composition, several layers of magnesitic or calcitic composition might follow, which each individually are perfectly ordered Ca- or Mg-layers. However, as the growth of dolomite is not likely taking place in a layer-by-layer way (i. e. on the polar (001)-surfaces) but on the (104) surface, where $Ca^{2+}$, $Mg^{2+}$, and $CO_3^{2-}$ are attached in turn, such a layer disordering is unlikely.

## 1.6.2 $CaCO_3$-$MnCO_3$

The $CaCO_3$-$MnCO_3$ system can be seen as a direct structural analogue to the $CaCO_3$-$MgCO_3$ system. Rhodochrosite ($MnCO_3$) and magnesite (Effenberger et al., 1981) as well as the ordered double carbonates kutnahorite [$CaMn(CO_3)_2$] and dolomite are isostructural. Precipitation of kutnahorite, however, is kinetically inhibited in favor of an unordered $(Ca,Mn)CO_3$ solid solution (Katsikopoulos et al., 2009). Given its chemistry, however, none of the peculiarities of the $Mg^{2+}$ ion takes effect in this system. Therefore, it will not be discussed in further detail in this thesis.

### 1.6.3 SrCO$_3$-MgCO$_3$

The SrCO$_3$-MgCO$_3$ system is highly related to the BaCO$_3$-MgCO$_3$ system. Strontianite, SrCO$_3$, and witherite, BaCO$_3$, are both orthorhombic (Speer, 1983) and the structure of SrMg(CO$_3$)$_2$ is similar to dolomite and norsethite (Froese, 1967). Furthermore, no solid-solution was found to occur between SrCO$_3$ and MgCO$_3$. In contrast to norsethite, however, syntheses of SrMg(CO$_3$)$_2$ only succeeded at temperatures >500 °C (Froese, 1967; Pimentel and Pina, 2016; Zheng and Böttcher, 2014). Moreover, norsethite is known to occur naturally, which is not the case for SrMg(CO$_3$)$_2$.

### 1.6.4 BaCO$_3$-MgCO$_3$

Studies of growth of witherite and its solid solutions (e.g., with SrCO$_3$) were mostly aimed at isotopic fractionation during mineral growth (Mavromatis et al., 2016; Prieto et al., 1997; Sánchez-Pastor et al., 2011). Knowledge about barium incorporation during mineral growth is of additional relevance, because barium concentration and its isotopical signatures can be used as proxies for paleoenvironmental reconstruction (Hall and Chan, 2004; Lea et al., 1989; Montaggioni et al., 2006; Pingitore and Eastman, 1984; Pretet et al., 2015; Rubin et al., 2003; von Allmen et al., 2010). Furthermore, due to the chemical similarities of the homologues barium and radium, information about the behavior of barium can provide important insights into mobility and transport of radium. During calcite growth incorporation of small amounts of barium was reported (Astilleros et al., 2000; Pingitore and Eastman, 1984; Pingitore, 1986; Reeder, 1996; Tesoriero and Pankow, 1996). Moreover, barium has been found adsorbing to magnesite surfaces but its behavior during magnesite growth is unknown (Jones et al., 2011; Shahwan et al., 1998).

# 2    Objectives and outline

## 2.1    Aim of this work

This thesis aims at a detailed quantitative description of the growth kinetics and behavior in the $BaCO_3$-$MgCO_3$ system in order to get a better understanding on the growth of anhydrous, Mg-containing carbonate minerals in general. To understand the growth of norsethite $[BaMg(CO_3)_2]$, knowledge is required about the growth kinetics of the two endmembers witherite ($BaCO_3$) and magnesite ($MgCO_3$) and, more importantly, of the impact of aqueous $Mg^{2+}$ and $Ba^{2+}$ on the growth of witherite and magnesite, respectively. Therefore, three main subjects of interest emerge in the $BaCO_3$-$MgCO_3$ system:

1) On the $MgCO_3$-rich side:

   Growth of magnesite under the influence of aqueous Ba

   i)   Can $Ba^{2+}$ be incorporated into magnesite during growth?
   ii)  Is there any precipitation of additional phases?
   iii) What is the effect of $Ba^{2+}$ on magnesite growth kinetics?

2) On the $BaCO_3$-rich side:

   Growth of witherite under the influence of aqueous Mg

   i)   What is the rate constant of witherite growth?
   ii)  Does aqueous magnesium have an impact on witherite growth rates?
   iii) Is $Mg^{2+}$ incorporated into witherite during growth?
   iv)  Is norsethite precipitating from the Mg-bearing growth solutions?

3) At 1:1 stoichiometry:

   Growth of norsethite

   i)   What is the temperature dependence of norsethite solubility and growth rates?
   ii)  How does norsethite growth compare to magnesite and dolomite growth?
   iii) What causes the different abilities to incorporate dehydrated magnesium ions into their respective structures?

Answers to these questions may considerably help to improve the understanding of why some anhydrous Mg-bearing carbonate minerals have severe growth problems but others not.

Following this division into distinct main research objectives, three manuscripts were published in appropriate journals. This dissertation is based on these three publications, which are described in the following chapter in more detail.

## 2.2 Overview of publications and author contributions

The first manuscript is a complementary micro- and macroscopic study to assess the effect of $Ba^{2+}$ on magnesite growth at 100 °C. It was found that $Ba^{2+}$ does neither inhibit nor promote the growth rate of magnesite and is not incorporated into the mineral. At high $Ba^{2+}$ concentrations, however, norsethite forms and grows parallel to magnesite. The manuscript was published as:

> Michael Lindner, Giuseppe D. Saldi, Guntram Jordan, and Jacques Schott (2017) On the effect of aqueous barium on magnesite growth – A new route for the precipitation of the ordered anhydrous Mg-bearing double carbonate norsethite. *Chemical Geology,* **460**, 93–105.
>
> DOI: 10.1016/j.chemgeo.2017.04.019

ML and GJ designed the study. ML and GDS conducted the experiments and analyses. ML merged the data and drafted the manuscript. All authors contributed to discussions and the final manuscript.

In the second manuscript, the effect of $Mg^{2+}$ on witherite growth was examined at 50 °C. Analogously to the lack of an effect of $Ba^{2+}$ on magnesite growth, witherite growth is not affected by the presence of $Mg^{2+}$. Instead norsethite is formed at $Mg^{2+}:Ba^{2+}$ ratios larger than 12:1. Reaction order and reaction constant of witherite growth have been determined from the acquired dataset. The manuscript was published as:

> Michael Lindner and Guntram Jordan (2018) On the growth of witherite and its replacement by the Mg-bearing double carbonate norsethite – Implications for the dolomite problem. *American Mineralogist,* **103**, 252–259.
>
> DOI: 10.2138/am-2018-6232

ML and GJ designed the study and the mixed-flow reactors. ML performed the experiments and analyses, merged the data and wrote the manuscript. ML and GJ contributed to data interpretation, discussions, and manuscript editing.

Finally, the solubility and growth of norsethite was investigated at different temperatures in the third manuscript. It was shown that norsethite growth is approx. five orders of magnitude faster than dolomite and three orders of magnitude faster than magnesite growth at 100 °C. The manuscript was published as:

Michael Lindner, Giuseppe D. Saldi, Salvatore Carrocci, Pascale Bénézeth, Jacques Schott and Guntram Jordan (2018) On the growth of anhydrous Mg-bearing carbonates – Implications from norsethite growth experiments, *Geochimica et Cosmochimica Acta,* **238**, 424–437.

DOI: 10.1016/j.gca.2018.07.013

ML and GJ conceived of the study. PB designed the hydrogen electrode concentration cell and performed the solubility measurements. PB, GDS, and ML carried out analyses in the course of these measurements. GDS, SC, and ML performed the norsethite growth experiments and subsequent analyses. ML merged the data and drafted the manuscript. All authors contributed to data interpretation, discussion and the final manuscript.

Permission to reproduce the published articles as part of this dissertation has been granted by *Elsevier* and the *Mineralogical Society of America*, respectively.

# 3 Main Methods

## 3.1 Mixed-flow reactors

Mixed-flow reactors (MFR) were employed to follow precipitation reactions and allow for the calculation of mineral growth rates. The basic setup consists of a reactor which holds mineral seed powder of known mass and surface area. Supersaturated solutions are pumped into the reactor. Growth of the seed crystals causes a reduction the concentration of the fluid within the reactor and the effluent. Using this decrease in concentration, the mineral growth rate can be determined.

Reactive solutions were prepared from $BaCl_2 \cdot 2H_2O$, $MgCl_2 \cdot 6H_2O$, NaCl, $Na_2CO_3$ and $NaHCO_3$ (reagent grade or p. a.) and high purity deionized water (resistivity 18.2 MΩcm). Ionic strength of the solutions was adjusted to 0.1 M with NaCl.

### 3.1.1 Hydrothermal titanium mixed-flow reactor

A hydrothermal mixed flow reactor (HMFR) setup as described by Saldi et al. (2012) and Berninger et al. (2016) was used for experiments at 100 °C. The titanium reactors have a volume of 200 ml. Inlet solutions were kept in collapsible polyethylene containers at room temperature and injected into the reactor using a *Gilson* high pressure chromatography (HPLC) pump. After the crystals had been placed in the reactor, it was filled with growth solution and closed. Solutions inside the reactors were stirred at 200 – 700 rpm and kept at 100 °C by a *Parr* magnetic stirrer and a *Parr* furnace, respectively. Fluids passed a 10 μm Ti-frit before leaving the reactor, were cooled down and flowed through a back-pressure regulator allowing fluid sampling at atmospheric pressure. Three different sample volumes were collected at each time. One part was kept for the measurement of pH; a second part was acidified with concentrated $HNO_3$ and stored for Mg and Ba analyses; a third part was kept for alkalinity determination.

pH measurements were performed at room temperature immediately after sampling with a standard glass electrode (*Mettler Toledo*) calibrated with 4.01, 7.01 and 9.18 NIST pH buffers. The estimated uncertainty of the pH measurements is ± 0.05 pH units.

Total alkalinities were determined by standard HCl titration using a *Schott* TA 10plus automatic titrator with an uncertainty of ± 1 % and a detection limit of $2 \times 10^{-5}$ eq/L.

Aqueous Mg concentrations were measured by flame atomic absorption spectroscopy (AAS) using a *Perkin Elmer* AANalyst 400 Atomic absorption

spectrometer with an uncertainty of $\pm 2\%$ and a detection limit of $1 \times 10^{-7}$ molal. Ba concentrations were measured by inductively coupled optical emission spectroscopy (ICP-OES) using a *Horiba* Ultima 2 with an uncertainty of $\pm 2\%$ and detection limit of $5 \times 10^{-9}$ molal.

### 3.1.2   PTFE mixed-flow reactor

Growth experiments at temperatures between 40 and 65 °C were performed in self-constructed PTFE mixed-flow reactors with a volume of approx. 200 ml (Figure 3.1-1). Inlet and outlet of the reactor were equipped with nylon net filters with a pore size of 30 μm (*Merck*) to prevent loss of seed material. Furthermore, an externally driven magnetic stirring bar was placed inside the reactor in order to avoid sedimentation of the seed crystals and to ensure homogenous solution composition within the entire reactor. To maintain a constant temperature throughout the experiments ($\pm 1$ °C), the reactors were submerged in a thermostatic water bath.

Solution pH and temperature was constantly monitored inside the reactor using an in-situ pH electrode (*Meinsberger Elektroden* EGA142), which was calibrated at the experimental temperature with pH 4.01, 7.01 and 10.01 buffers (*Hanna Instruments*).

In order to avoid premature crystallization of carbonate phases in storage containers and tubing, both carbonate and Ba-Mg containing solutions were simultaneously pumped into the reactor from two separate collapsible PE containers using a two-channel peristaltic pump (*GILSON* Minipuls 3). The flowrates of the two feed-lines were adjusted to be the same before the start of the experiment. During the experiments, the pump rates in the individual feed-lines were checked periodically by measuring the weight loss of the storage containers. The ratio of the two feed rates did not vary significantly during an experiment and the total feed rate agreed well with the measured amount of effluent of the reactor.

The outflow was collected periodically and the pH of the sample solution was measured immediately after cooling down to room temperature using a *SI Instruments* Titroline 7000 pH electrode A192, previously calibrated with pH 4.01, 7.01 and 10.01 buffers (*Hanna Instruments*). Total alkalinity was determined by potentiometric end point titration with 0.01 M HCl with an uncertainty of $\pm 1\%$ and a detection limit of $2 \times 10^{-5}$ eq/l (*SI Instruments* Titroline 7000, pH electrode A192). $Ba^{2+}$ and $Mg^{2+}$ concentrations were determined by potentiometric titration with 0.01 or 0.001 M $Na_2$-EDTA solutions with an uncertainty of $\pm 1\%$ and a detection limit of $2 \times 10^{-5}$ molal (*SI Instruments* Titroline 7000, Ca ion selective electrode Ca1100, reference electrode B2920+).
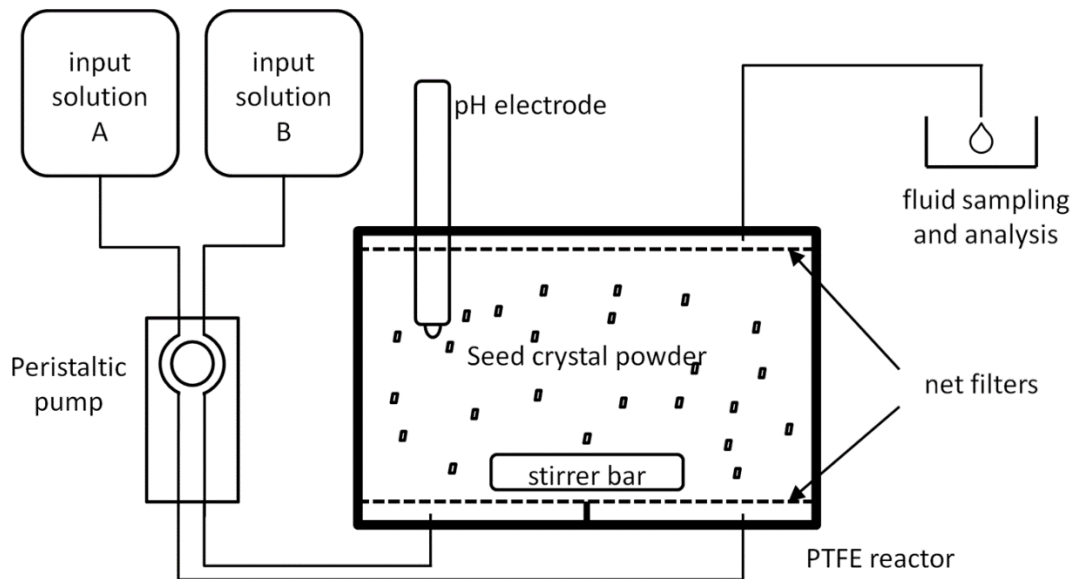
Figure 3.1-1: Experimental setup of mixed flow reactor with in-situ pH electrode. The two input solutions are mixed inside the reactor to avoid supersaturation and precipitation in the absence of seed crystals. The PTFE reactor is placed inside a water bath for constant temperature (from Lindner and Jordan, 2018).

### 3.1.3   Mixed-flow reactor experimental protocol

Each experimental mixed-flow reactor run consisted of a sequence of different flow rates using the same inlet fluid and seed crystal powder. Due to the substantial incorporation of solutes by the growing magnesite, each flow rate leads to a different solution composition within the reactor. Flow rate was not changed before steady-state had been reached, i.e., before outlet fluid composition remained constant within analytical uncertainty. At this point crystal growth kinetics was assumed to be in steady state. Subsequently, flowrate was changed leading to a new steady state with a different solution composition within the reactor. After three or more different steady states had been established, the experimental run was finished and the reactor was opened. The crystals were retrieved by vacuum filtration using filter paper, quickly rinsed with deionized water and ethanol, and dried for at least 12 hours at 60 °C.

Growth of crystals inside the reactor caused the solute concentration to decrease. This decrease $\Delta M$ could be measured by the difference between inlet and outlet solution concentration ($\Delta M = M^{in} - M^{out}$). Precipitation rates $R$ then were calculated using the equation (Saldi et al., 2012):

$$R = \frac{\Delta M \, R_f}{m \, S}, \tag{3.1-1}$$

where $\Delta M$ is the difference of divalent metal concentration between inlet and outlet fluid, $R_f$ is the flow rate, $m$ stands for the mass of crystals at a given moment, and $S$ is the specific surface area of the crystals at this moment.

## 3.2 Hydrothermal atomic force microscopy

Atomic force microscopy (AFM) allows scanning the topography of a sample on the nanoscale. As the method can also be applied in solution, it is possible to follow and measure mineral growth on the molecular level and identify growth mechanisms.

Hydrothermal atomic force microscope (HAFM) experiments were conducted using a custom-made system working in contact mode with uncoated silicon cantilevers from *Nanosensors* (Aldushin et al., 2004; Higgins et al., 1998; Jordan and Astilleros, 2006). This apparatus allowed to probe the surface microtopography of the reacting crystals at an applied nitrogen pressure $\leq 2$ bar and under a continuous gravity-flow (flow rates $\approx 10-25\,\mu l/s$). Samples were fixed inside the HAFM cell (volume $\approx 500\,\mu l$) with a titanium wire before pressurizing and heating the system. Although the HAFM cell represents a single pass flow reactor, the withdrawal of solutes by the growth of the sample crystal is insignificant with respect to the supply rate within the established range of flow rates. The compositional differences between inlet and outlet solutions, therefore, lie within the range of analytical error and the fluid composition within the reactor is largely independent of the flow rate.

## 3.3 Geochemical calculations with PHREEQC

The geochemistry program PHREEQC v. 3 (Parkhurst and Appelo, 2013) was used to model solution composition and speciation and compute supersaturations with respect to the phases of interest. Saturation states of aqueous solutions are expressed as $\Omega = \frac{IAP}{K_s}$, where $IAP$ stands for the ionic activity product of the solution and $K_s$ for the solubility product of the respective mineral phase. For the calculations the llnl database was modified by inserting the solubility constants of witherite ($\log_{10} K_{s\,wit}$ = $-8.562$, Busenberg and Plummer, 1986b), norsethite ($\log_{10} K_{s\,nrs}$ = $-16.72$, Königsberger et al., 1998 – only 25 °C data available) and northupite [$Na_3Mg(CO_3)_2Cl$] ($\log_{10} K_{s\,nrt}$ = $-4.8$, Vančina et al., 1986). $Mg^{2+}$ hydrolysis and carbonic acid dissociation equilibrium constants were modified after the values of Brown et al. (1996) and Millero et al. (2007), respectively. Furthermore, aqueous barium carbonate species ($BaHCO_3{}^+{}_{(aq)}$ and $BaCO_3{}_{(aq)}$) and their stability constants (Busenberg and Plummer, 1986b) were added to the database.

## 3.4 X-ray diffraction

Seed crystal powders were analyzed before and after the experiments by X-ray diffraction (*GE Seifert* 3003 TT, Cu $K_{\alpha 1}$ radiation, Bragg-Brentano geometry) to investigate the phases that precipitated during the experimental runs.

Small amounts of samples were crushed in a mortar, suspended in acetone, and dispersed on a zero-background quartz sample holder to create a thin and smooth film.

## 3.5 Scanning electron microscopy

In order to evaluate changes of crystal shape and identify newly grown grains, images of the crystals were taken with a scanning electron microscope (SEM; *Zeiss* DSM 960 A or *Hitachi* SU 5000 with an accelerating voltage of 20 kV and a working distance of 25 mm or 5 kV and 5 mm, respectively). Energy dispersive X-ray analysis (EDX) was performed on selected spots.

Powder samples were dispersed on carbon adhesive on an aluminium sample holder and subsequently coated with carbon for SEM imaging.

# 4 Results and Discussion

## 4.1 The effect of aqueous Ba on magnesite growth

Although magnesite growth under the influence of various compounds and elements has been thoroughly investigated before (cf. chapter 1.6.1), nothing is known about the influence of aqueous barium on magnesite growth. Such knowledge, however, would allow for the important comparison with magnesite growth under the influence of aqueous calcium. The comparison of these two analogue systems is expected to yield important information regarding the easiness of norsethite formation and the difficulties of dolomite formation, respectively. The aim of this part of the study, therefore, is to gain deeper insights into the fate and behavior of aqueous barium during magnesite growth.

### 4.1.1 Detailed materials and methods

*4.1.1.1 Hydrothermal mixed-flow reactor experiments*

Hydrothermal mixed-flow reactors as described in chapter 3.1.1 have been used for the experiments. Inlet fluid compositions are listed in Table 4.1-1. Mg, $NaHCO_3$ and NaCl concentrations were chosen close to the ones used by Berninger et al. (2016) in the investigation of the effect of aqueous Ca on magnesite growth in order to ensure maximum comparability of the studies. Ba concentrations varied between 5 x $10^{-8}$ and 1 x $10^{-4}$ molal yielding Ba:Mg ratios of inlet solutions of approximately $10^{-5}$:1 to $10^{-1}$:1. About 1.4 g of synthetic magnesite seed crystals were used in each experimental run. The crystals originated from the same batch synthesis as the crystals used by Berninger et al. (2016). The initial specific surface area $S$ of the magnesite seeds ($0.087 \pm 10$ % $m^2$/g) was determined by a geometric evaluation of the crystals in SEM images (average rhombohedral edge length: 25 µm). In all experiments, temperature was held constant at 100 °C. Flow rates ranged from 0.2 to 3 ml/min.

Based on the amount of precipitated magnesite, a final specific surface area for every experiment was calculated assuming an exclusive growth of seed crystals without homogeneous nucleation. Over an experimental run, the final specific surface area was found to be 8 – 12 % lower than the initial specific surface area (Table 4.1-2). For the calculation of the growth rates, a linear decrease over time of the specific surface area from its initial to final value was assumed whereas the mass of the magnesite crystals within the reactor was assumed to increase linearly.

Table 4.1-1: Inlet fluid compositions of hydrothermal mixed-flow reactor experiments.

| Experiment | crystals initial [g] | pH at 100 °C | Mg [mM] | Ba [μM] | alkalinity [meq/L] | NaCl [mM] | approx. Ba:Mg |
|---|---|---|---|---|---|---|---|
| mgsBa0 | 1.406 | 8.29 | 3.31 | 0 | 24.95 | 72.0 | 0 |
| mgsBa1 | 1.385 | 8.14 | 3.31 | 37 | 24.99 | 72.0 | $1 \times 10^{-2}$:1 |
| mgsBa2 | 1.409 | 8.11 | 3.36 | 75 | 23.44 | 72.0 | $2 \times 10^{-2}$:1 |
| mgsBa3 | 1.400 | 8.20 | 3.33 | 0.37 | 25.00 | 71.9 | $1 \times 10^{-4}$:1 |
| mgsBa3b | 1.288 | 8.27 | 2.91 | 0.36 | 24.73 | 71.9 | $1 \times 10^{-4}$:1 |
| mgsBa4 | 1.424 | 8.14 | 1.63 | 107 | 24.92 | 72.0 | $1 \times 10^{-1}$:1 |
| mgsBa5 | 1.402 | 8.24 | 3.32 | 3.64 | 25.10 | 72.0 | $1 \times 10^{-3}$:1 |
| mgsBa6 | 1.401 | 8.26 | 3.32 | 0.05 | 24.91 | 72.0 | $1 \times 10^{-5}$:1 |

Table 4.1-2: Masses of precipitated norsethite (nrs) and magnesite (mgs) calculated according to the difference of metal concentration between inlet and outlet fluid and according to Rietveld refinement. The table list also the calculated specific geometric surface area of magnesite crystals after the experiments [$S_{geo}$(mgs)].

| Experiment | recovered crystals – initial crystals [mg] | nrs mass-% by Rietveld | Total precipitate mass [mg] | nrs prec. [mg] | mgs prec. [mg] | Calc. $S_{geo}$(mgs) [m²/g] | nrs exp. mass-% |
|---|---|---|---|---|---|---|---|
| mgsBa0 | 405 | 0 | 496 | 0 | 496 | 0.078 | 0 |
| mgsBa1 | 139 | 1.5 | 654 | 78 | 576 | 0.077 | 3.83 |
| mgsBa2 | 448 | 1.7 | 645 | 165 | 480 | 0.079 | 8.03 |
| mgsBa3 | 395 | 0 | 678 | 0.16 | 678 | 0.076 | 0.01 |
| mgsBa3b | 129 | 0 | 357 | 0.11 | 357 | 0.080 | 0.01 |
| mgsBa4 | −284 | 0.7 | 165 | 98 | 67 | 0.085 | 6.17 |
| mgsBa5 | 150 | 0.03 | 448 | 3.2 | 445 | 0.079 | 0.17 |
| mgsBa6 | 180 | 0 | 464 | 0.02 | 464 | 0.079 | 0.00 |

In most experiments the mass of the recovered crystals was higher than the initial seed crystal mass confirming substantial growth of the seed crystals. However, in few cases, the product powder partly stuck to the reactor walls forming crusts and could not be recovered completely, leading to a negative mass balance between finally retrieved crystals and initial seeds, such as for the experiment mgsBa4 (see Table 4.1-2). In general, the mass of crystals increased by more than 30 % over an experimental run.

### 4.1.1.2 Hydrothermal atomic force microscopy

In the experimental HAFM runs (see chapter 3.2), magnesite growth was studied on the (104) cleavage plane of freshly cleaved magnesite single crystals (surface area ≈ 10 mm²) from Brumado (Brasil). Heights, velocities and appearances of monolayer steps generated by growth were compared for aqueous solutions with and without $Ba^{2+}$. For this comparison, Ba-free solutions were exchanged in-situ for Ba-containing solutions (and vice versa) while continuously monitoring the same surface area. In all experiments, temperature was held constant at 100 °C.

## 4.1.2 Results

### 4.1.2.1 SEM and XRD of reaction products from HMFR experiments

SEM images of the product powders (Figure 4.1-1) clearly show that the size of the magnesite crystals increased in all runs. In the product powder from experiments with Ba:Mg ratios $>2 \times 10^{-4}$, crystals and aggregates with a morphology different from the rhombohedral shape of magnesite were recognized. These needle-like prisms were either attached to magnesite seeds in random orientation or located separately. Back scattered electron (BSE) images showed that the concentration of heavy elements (i.e., Ba) in these crystals is significantly higher than in the magnesite seeds (Figure 4.1-2). EDX spectroscopy performed on several spots on the needle-like prisms revealed both barium and magnesium as well as oxygen and carbon. EDX analyses on the rhombohedral crystals confirmed their identification as magnesite with no barium detectable. In the product powder of experiments with Ba:Mg ratios $<2 \times 10^{-4}$, neither BSE imaging nor EDX analyses revealed the existence of any barium containing phase.

Representative parts of the retrieved products were examined by XRD. In the diffraction patterns of the crystals from experiments with Ba:Mg ratios $>2 \times 10^{-4}$, peaks relating to an additional phase besides magnesite could be discerned. This additional phase was identified as norsethite (PDF: 12-530, Effenberger and Zemann, 1985, Figure 4.1-3). In the barium free reference experiment and in experiments with Ba:Mg ratios $<2 \times 10^{-4}$, no phase other than magnesite could be found. Rietveld analysis of the diffraction patterns allowed the determination of the amount of norsethite in the retrieved powders (Table 4.1-2). As the phase composition of the retrieved powder is not necessarily identical to the composition of total reaction product, the Rietveld refinement has to be considered as yes-or-no test for the presence of norsethite rather than a quantitative analysis of the amount of norsethite precipitated. Furthermore, concentrations of less than approximately 0.1 weight-% norsethite cannot be detected by conventional lab-based XRD.

### 4.1.2.2 Chemical analysis of solutions in HMFR experiments

After the HMFR experiments had reached steady-state, the outlet solution of the reactor was sampled several times and analyzed (Table A 4.1–1). For a given steady-state, average values of Mg and Ba concentrations as well as alkalinities were then calculated from the individual sample data (Table 4.1-4). The comparison of these average values with the composition of corresponding inlet solutions showed decreasing concentrations for all steady-states. From the inlet solutions with Ba concentrations higher than 4 µM even more than 90 % of barium was withdrawn.
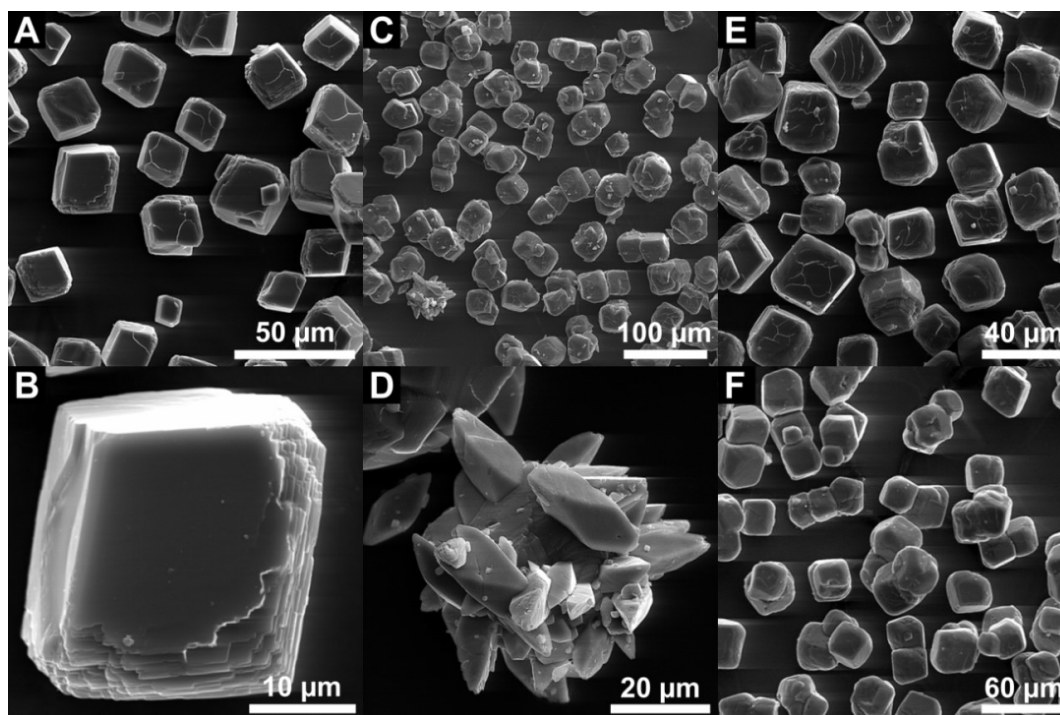
Figure 4.1-1: SEM images of magnesite crystals before (A & B) and after (C−F) experiments. C & D show crystals from experiment mgsBa1: magnesite seed crystals continued to grow (C); some magnesite crystals are covered with well crystallized norsethite needles (D), while others remained free. Experiments mgsBa6 (E) and mgsBa3b (F) yielded only magnesite
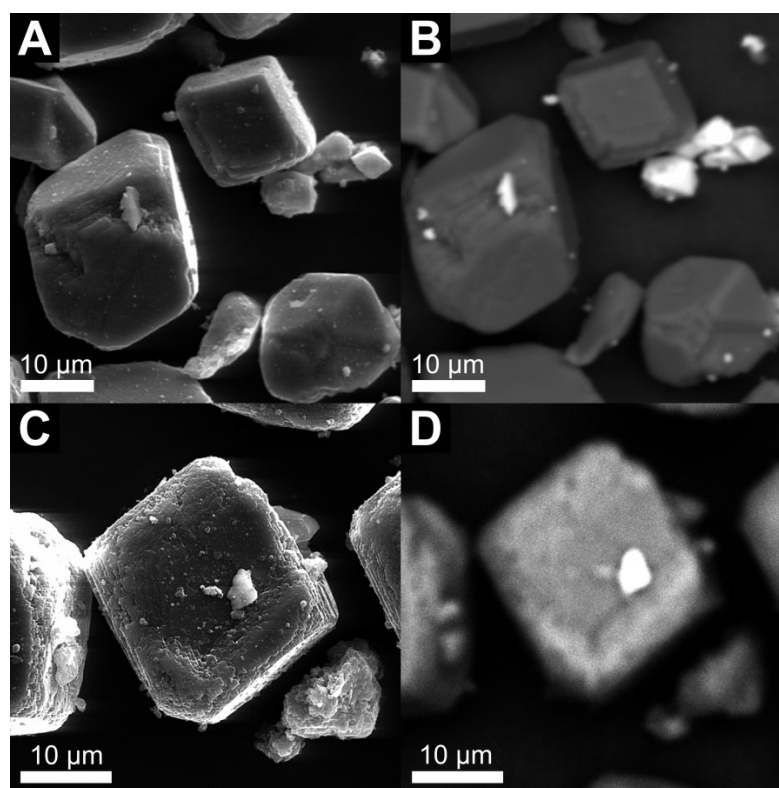


Figure 4.1-2 SEM images pairs of the same crystals after the experiments mgsBa4 (A: SE-contrast; B: BSE-contrast) and mgsBa5 (C: SE-contrast; D: BSE-contrast). Barium containing phases appear brighter in BSE contrast whereas magnesite remains dark.
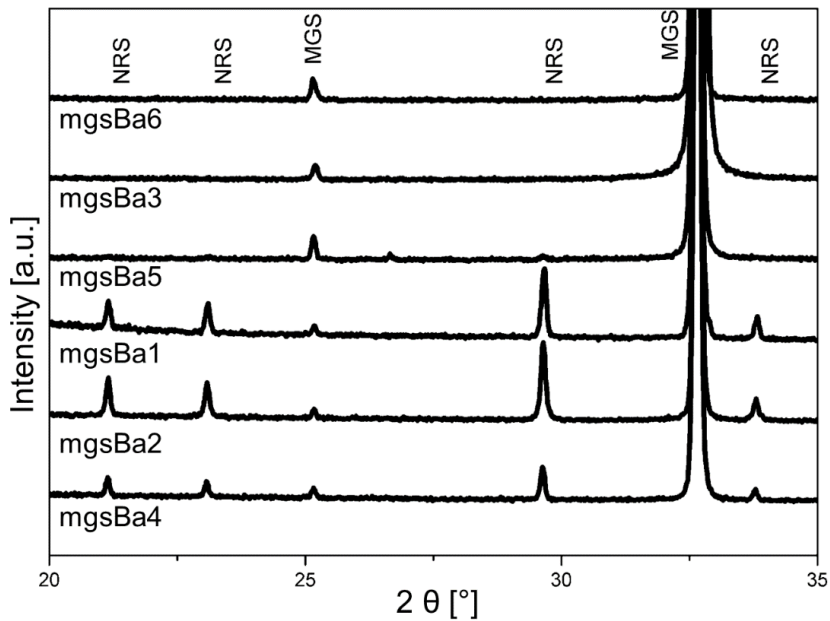
Figure 4.1-3: X-ray diffractograms of crystals retrieved from the reactors after experimental runs. Crystals of experiments mgsBa3 and mgsBa6 (Ba:Mg $< 2 \times 10^{-4}$) show only peaks resulting from magnesite (MGS). In experiments mgsBa5, mgsBa1, mgsBa2 and mgsBa2 (Ba:Mg $> 2 \times 10^{-4}$), norsethite reflections can be identified additionally (NRS). Unlabeled peaks stem from contamination by graphite from the stirrer inside the HMFR reactor.

Based on measured Ba and Mg withdrawals from the inlet fluid over the experimental time, the precipitated mass of crystals was calculated under the assumption that all Ba withdrawn precipitated as $BaMg(CO_3)_2$ and the remaining Mg as magnesite (see Table 4.1-2). This assumption was verified by XRD and EDX analyses and supported by SEM images of reaction products for the experiments with Ba:Mg ratios $> 2 \times 10^{-4}$, in which only mixtures of norsethite and nominally Ba-free magnesite were detected. In the experiments with Ba:Mg ratios $< 2 \times 10^{-4}$, in which no norsethite was detected, total Ba withdrawal was so low that the effect on the calculated magnesite mass could be neglected as it lied within the analytical error.

SEM images of the retrieved powders allowed the determination of the approximate specific surface area of the norsethite precipitated during the experimental runs. For this approximation, the average grain size of norsethite (Table 4.1-3) and a cubic shape model was used. As the mass of norsethite precipitated between subsequent sampling events was known by mass balance calculation of Ba withdrawal, the total norsethite surface area present inside the reactor could be calculated at each sampling time. Using these surface areas, the norsethite growth rates could be calculated according to Eqn. (3.1-1) with $\Delta M = \Delta[Ba]$ (see Table 4.1-3). These calculated rates are likely lower than the true rates because the specific surface area was kept constant throughout an experiment although norsethite nucleated and grw to its final size, which leads to a decrease of

specific surface area during an experimental run. As there is no temperature dependence of the solubility product $K_s$ of norsethite available from literature, the ionic activity product of norsethite ($IAP_{nrs} = a[Ba^{2+}]\, a[Mg^{2+}]\, a[CO_3^{2-}]^2$), which is proportional to the solution saturation state with respect to norsethite ($\Omega = IAP/K_s$)), was used for the plot of rate data (Figure 4.1-4). The plot of the norsethite growth rate vs. $IAP_{nrs}$ shows the typical increase of rate with increasing supersaturation.

Magnesite growth rates were calculated according to Eqn. (3.1-1) with the assumption that all Ba withdrawn from solution precipitated as $BaMg(CO_3)_2$ and only the remaining Mg was available for magnesite growth ($\Delta M = \Delta[Mg] - \Delta[Ba]$).

Table 4.1-3: Values used to calculate norsethite growth rates in HMFR experiments. The accumulated masses of norsethite inside the reactor were calculated from Ba mass balance at given sampling times during each experimental run. Surface areas were calculated according to the size distribution of norsethite particles in SEM images of retrieved seed crystals (see text for details). Norsethite growth rates were normalized by calculated norsethite surface areas.

| sample | calc. mass of accumulated norsethite [mg] | Avg. final norsethite size [μm] | calc. norsethite surface area [m²/g] | $IAP_{nrs}$ (x 10⁻¹⁸) | norsethite growth rate [nmol/m²/s] |
|---|---|---|---|---|---|
| mgsBa1 2–5 | 13.6 | 3.5 | 0.05 | $1.5 \pm 0.3$ | $807 \pm 100$ |
| mgsBa1 8–10 | 38.0 | 3.5 | 0.05 | $1.8 \pm 0.4$ | $609 \pm 100$ |
| mgsBa1 11–14 | 53.4 | 3.5 | 0.05 | $0.8 \pm 0.2$ | $52 \pm 40$ |
| mgsBa1 15–18 | 67.0 | 3.5 | 0.05 | $0.9 \pm 0.2$ | $87 \pm 75$ |
| mgsBa1 19–20 | 77.5 | 3.5 | 0.05 | $1.3 \pm 0.3$ | $151 \pm 100$ |
| mgsBa2 1–5 | 27.2 | 1.5 | 0.12 | $0.8 \pm 0.2$ | $381 \pm 100$ |
| mgsBa2 6–10 | 75.6 | 1.5 | 0.12 | $0.8 \pm 0.2$ | $67 \pm 50$ |
| mgsBa2 11–17 | 126.5 | 1.5 | 0.12 | $0.7 \pm 0.1$ | $163 \pm 100$ |
| mgsBa2 18–20 | 163.5 | 1.5 | 0.12 | $0.7 \pm 0.1$ | $62 \pm 50$ |
| mgsBa3 1–10 | 0.08 | – | – | $0.2 \pm 0.1$ | – |
| mgsBa3 11–14 | 0.12 | – | – | $0.3 \pm 0.1$ | – |
| mgsBa3 15–17 | 0.14 | – | – | $0.2 \pm 0.1$ | – |
| mgsBa3b 1–5 | 0.05 | – | – | $0.4 \pm 0.1$ | – |
| mgsBa3b 6–8 | 0.12 | – | – | $0.4 \pm 0.1$ | – |
| mgsBa4 1–7 | 49.7 | 1.9 | 0.09 | $0.7 \pm 0.1$ | $203 \pm 100$ |
| mgsBa4 8 | 97.8 | 1.9 | 0.09 | $0.6 \pm 0.1$ | $199 \pm 100$ |
| mgsBa5 1–4 | 0.52 | 3.0 | 0.06 | $2.3 \pm 0.5$ | $392 \pm 100$ |
| mgsBa5 5–8 | 1.34 | 3.0 | 0.06 | $2.0 \pm 0.4$ | $349 \pm 100$ |
| mgsBa5 9–12 | 2.69 | 3.0 | 0.06 | $2.1 \pm 0.4$ | $417 \pm 100$ |
| mgsBa5 13–14 | 3.23 | 3.0 | 0.06 | $1.6 \pm 0.3$ | $84 \pm 60$ |
| mgsBa6 1–4 | 0.01 | – | – | $(1.4 \pm 0.3) \times 10^{-2}$ | – |
| mgsBa6 5–8 | 0.02 | – | – | $(2.6 \pm 0.5) \times 10^{-2}$ | – |
| mgsBa6 9–12 | 0.05 | – | – | $(2.7 \pm 0.6) \times 10^{-3}$ | – |

Table 4.1-4: Mean outlet fluid compositions of HMFR experiments with calculated magnesite (mgs) growth rates and corresponding saturation state values with respect to magnesite [Ω(mgs)] and witherite [Ω(wth)]. The ion activity product for norsethite (IAP$_{nrs}$) is also provided.

| Sample | flowrate [ml/min] | alkalinity [meq/L] | Δ alkalinity [meq/L] | Ba [µM] | Mg [mM] | Δ Ba [µM] | Δ Mg [mM] | Magnesite growth rate [nmol/m²/s] | pH (100 °C) | Ω(mgs) | Ω(wth) | IAP$_{nrs}$ (x 10$^{-18}$) | a Mg$^{2+}$ / a CO$_3^{2-}$ | a Ba$^{2+}$ / a Mg$^{2+}$ (x 10$^{-4}$) |
|---|---|---|---|---|---|---|---|---|---|---|---|---|---|---|
| mgsBa0 1-10 | 0.5 | 22.91 | 1.99 | 0.00 | 2.32 | 0.00 | 0.98 | 76 ± 7 | 7.69 | 131 ± 5 | 0.00 | 0.00 | 11.5 | 0 |
| mgsBa0 11-14 | 1.0 | 23.49 | 1.42 | 0.00 | 2.63 | 0.00 | 0.68 | 122 ± 12 | 7.75 | 169 ± 5 | 0.00 | 0.00 | 11.0 | 0 |
| mgsBa0 15-17 | 0.2 | 22.53 | 2.37 | 0.00 | 2.15 | 0.00 | 1.16 | 69 ± 7 | 7.70 | 122 ± 6 | 0.00 | 0.00 | 10.6 | 0 |
| mgsBa0 18-21 | 2.0 | 24.02 | 0.88 | 0.00 | 2.90 | 0.00 | 0.41 | 217 ± 22 | 7.84 | 227 ± 2 | 0.00 | 0.00 | 9.5 | 0 |
| mgsBa1 2-5 | 1.0 | 22.07 | 1.26 | 2.31 | 2.57 | 34.73 | 0.74 | 96 ± 10 | 7.66 | 130 ± 5 | 0.04 | 1.46 | 14.6 | 9.1 |
| mgsBa1 8-10 | 2.0 | 22.13 | 1.21 | 2.09 | 2.76 | 34.95 | 0.55 | 140 ± 14 | 7.71 | 155 ± 3 | 0.04 | 1.77 | 13.9 | 7.7 |
| mgsBa1 11-14 | 0.2 | 20.94 | 2.40 | 1.62 | 2.06 | 35.41 | 1.25 | 39 ± 4 | 7.68 | 104 ± 3 | 0.03 | 0.83 | 12.0 | 8.0 |
| mgsBa1 15-18 | 0.5 | 21.30 | 2.03 | 1.45 | 2.31 | 35.58 | 0.99 | 64 ± 6 | 7.68 | 119 ± 3 | 0.03 | 0.86 | 13.1 | 6.4 |
| mgsBa1 19-20 | 1.0 | 21.79 | 1.55 | 1.56 | 2.56 | 35.48 | 0.74 | 95 ± 10 | 7.72 | 146 ± 1 | 0.03 | 1.26 | 12.7 | 6.2 |
| mgsBa2 1-5 | 1.0 | 21.84 | 1.60 | 1.26 | 2.59 | 73.95 | 0.77 | 90 ± 9 | 7.67 | 132 ± 2 | 0.02 | 0.81 | 14.8 | 4.9 |
| mgsBa2 6-10 | 0.5 | 21.54 | 1.90 | 1.10 | 2.39 | 74.11 | 0.97 | 52 ± 5 | 7.67 | 122 ± 6 | 0.02 | 0.67 | 13.5 | 4.7 |
| mgsBa2 11-17 | 2.0 | 22.00 | 1.44 | 0.85 | 2.68 | 74.36 | 0.68 | 136 ± 14 | 7.70 | 147 ± 10 | 0.02 | 0.67 | 13.9 | 3.2 |
| mgsBa2 18-20 | 1.0 | 21.47 | 1.97 | 0.98 | 2.42 | 74.23 | 0.94 | 93 ± 9 | 7.67 | 122 ± 1 | 0.02 | 0.58 | 14.1 | 4.1 |
| mgsBa3 1-10 | 0.5 | 23.19 | 1.81 | 0.23 | 2.35 | 0.15 | 0.98 | 64 ± 6 | 7.69 | 133 ± 7 | 0.00 | 0.17 | 11.4 | 1.0 |
| mgsBa3 11-14 | 1.0 | 23.14 | 1.86 | 0.33 | 2.46 | 0.04 | 0.87 | 109 ± 11 | 7.73 | 150 ± 7 | 0.01 | 0.29 | 11.0 | 1.4 |
| mgsBa3 15-17 | 0.2 | 22.16 | 2.84 | 0.30 | 1.93 | 0.08 | 1.40 | 41 ± 4 | 7.69 | 108 ± 3 | 0.01 | 0.18 | 9.8 | 1.6 |
| mgsBa3b 1-5 | 2.0 | 23.63 | 1.10 | 0.28 | 2.35 | 0.07 | 0.56 | 164 ± 16 | 7.82 | 176 ± 3 | 0.01 | 0.37 | 8.3 | 1.3 |
| mgsBa3b 6-8 | 1.4 | 23.49 | 1.24 | 0.32 | 2.29 | 0.04 | 0.63 | 132 ± 3 | 7.84 | 179 ± 2 | 0.01 | 0.44 | 7.6 | 1.4 |
| mgsBa4 1-7 | 0.5 | 22.46 | 0.91 | 1.01 | 1.25 | 105.50 | 0.38 | 19 ± 5 | 7.84 | 96 ± 3 | 0.03 | 0.74 | 4.4 | 8.4 |
| mgsBa4 8 | 1.0 | 22.64 | 0.74 | 0.84 | 1.33 | 105.67 | 0.30 | 27 ± 4 | 7.84 | 102 ± 2 | 0.02 | 0.65 | 4.7 | 6.6 |
| mgsBa5 1-4 | 0.5 | 23.20 | 1.90 | 2.52 | 2.39 | 1.12 | 0.93 | 61 ± 6 | 7.74 | 149 ± 5 | 0.05 | 2.31 | 10.5 | 10.9 |
| mgsBa5 5-8 | 1.0 | 23.55 | 1.55 | 1.95 | 2.55 | 1.69 | 0.77 | 98 ± 10 | 7.75 | 165 ± 5 | 0.04 | 2.04 | 10.7 | 7.9 |
| mgsBa5 9-12 | 2.0 | 24.12 | 0.98 | 1.60 | 2.77 | 2.04 | 0.55 | 137 ± 14 | 7.78 | 191 ± 4 | 0.04 | 2.08 | 10.6 | 6.0 |
| mgsBa5 13-14 | 0.5 | 22.89 | 2.21 | 1.69 | 2.30 | 1.95 | 1.02 | 63 ± 6 | 7.76 | 148 ± 2 | 0.04 | 1.57 | 9.8 | 7.5 |
| mgsBa6 1-4 | 0.5 | 22.73 | 2.28 | 0.02 | 2.29 | 0.03 | 1.04 | 67 ± 7 | 7.71 | 132 ± 16 | 0.00 | 0.01 | 11.1 | 0.1 |
| mgsBa6 5-8 | 1.0 | 23.30 | 1.70 | 0.03 | 2.49 | 0.02 | 0.83 | 115 ± 12 | 7.71 | 147 ± 3 | 0.00 | 0.03 | 11.6 | 0.1 |
| mgsBa6 9-12 | 2.0 | 23.67 | 1.34 | 0.00 | 2.75 | 0.04 | 0.57 | 159 ± 16 | 7.75 | 178 ± 5 | 0.00 | 0.00 | 11.4 | 0.0 |
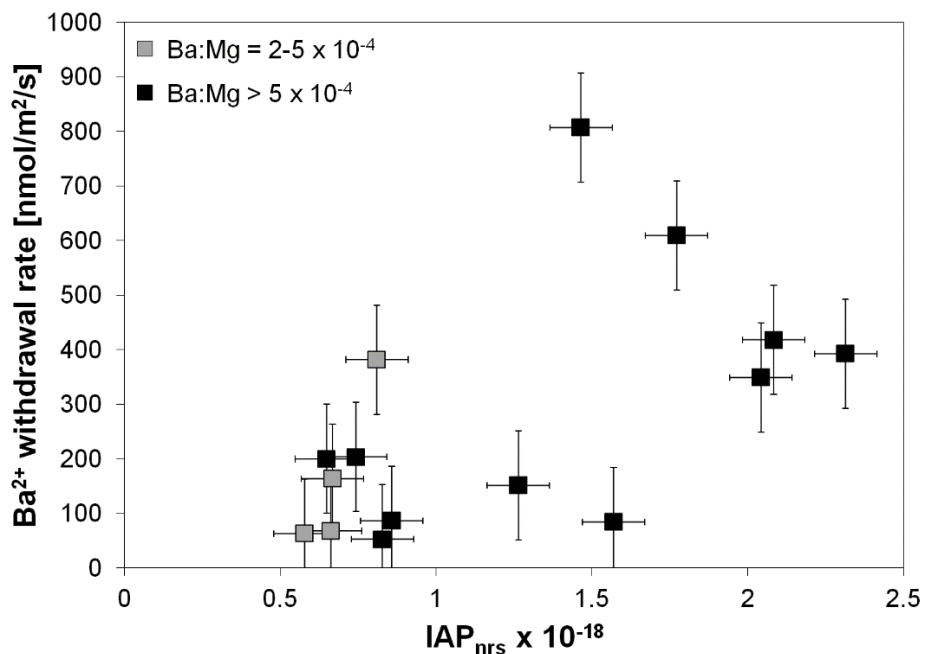
Figure 4.1-4: norsethite growth rate vs. ion activity product of norsethite. Barium withdrawal rate is equal to norsethite growth rate if norsethite precipitation is the only mechanism consuming barium. Only in experiments with Ba:Mg > $2 \times 10^{-4}$ norsethite was detected.
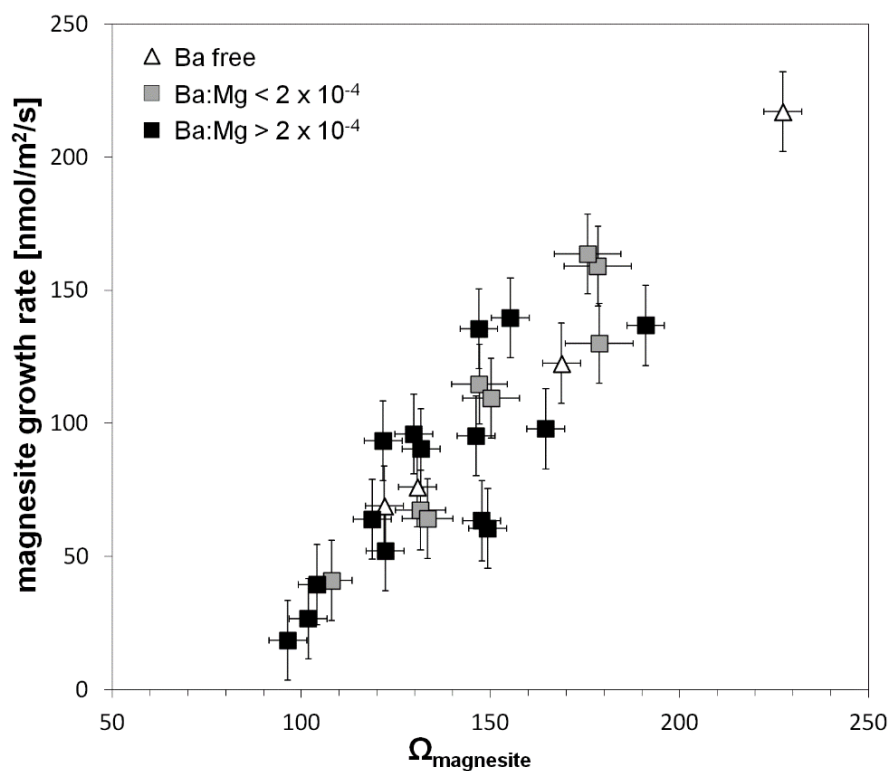


Figure 4.1-5: Growth rate of magnesite at 100 °C as a function of solution saturation state with respect to magnesite ($\Omega_{magnesite}$). Growth rates show no dependence on aqueous barium concentration within analytical error.

*4.1.2.3 Analysis of surface morphology of growing magnesite in HAFM experiments*

In order to confirm the findings of the macroscopic HMFR experiments and to investigate the whereabouts of barium further, HAFM experiments have been conducted with Ba:Mg ratios down to $3 \times 10^{-4}:1$ (Table 4.1-5). HAFM experiments with low barium concentrations ($1 - 3\ \mu M$) revealed no change in magnesite growth behavior when changing from Ba-free to Ba-containing solution. No change of the thickness of a molecular monolayer ($2.74\ \text{Å}$) or other alterations of growth morphology could be detected (Figure 4.1-6). The overgrowths at pre-existing etch pits showed no height contrast to the surrounding surface, indicating that the height of newly grown layers is the same as in pristine magnesite (Figure 4.1-7). Obtuse step velocities and growth rates showed no significant variation with different barium concentrations and agree with the Ba-free data by Berninger et al. (2016) and Saldi et al. (2009) within analytical uncertainty (Table 4.1-5, Figure 4.1-8).

Switching to Ba-free solution instantaneously restored high image quality. This behavior may indicate precipitation of a solid phase floating within the solution. These crystals can interfere with the laser beam and weaken the signal/noise ratio. The nature of the crystals is unknown. Likely, a Ba-carbonate phase precipitated when the solution entered the heated HAFM cell.

Table 4.1-5: Inlet fluid compositions, step advancement velocities and magnesite growth rates for the HAFM experiments at 100 °C. Experiments with the same number were performed in the same experimental run on the same crystal surface by changing the solution flowing over the crystal. $\Omega$(mgs) and $\Omega$(wth) define the fluid saturation state relative to magnesite and witherite. $IAP_{nrs}$ identifies the norsethite ion activity product.

| Exp. | Ba [$\mu M$] | Mg [mM] | NaHCO$_3$ [mM] | NaCl [M] | pH | approx. Ba:Mg | $\Omega$ (mgs) | $IAP_{nrs}$ $\times 10^{-18}$ | $\Omega$ (wth) | obtuse step advancement rate [nm/s] | Magnesite growth rate [nmol/m$^2$/s] |
|---|---|---|---|---|---|---|---|---|---|---|---|
| Mg 2 | 0 | 0.73 | 27 | 0.1 | 8.3 | 0 | 85 | 0 | – | $5.0 \pm 0.1$ | $120 \pm 40$ |
| BaMg 2 | 50 | 0.73 | 27 | 0.1 | 8.3 | $7 \times 10^{-2}:1$ | 85 | 30 | 1.6 | – | – |
| Mg 3 | 0 | 0.73 | 27 | 0.1 | 8.4 | 0 | 67 | 0 | – | $5.3 \pm 0.9$ | $170 \pm 50$ |
| BaMg 3 | 3 | 0.73 | 27 | 0.1 | 8.4 | $4 \times 10^{-3}:1$ | 67 | 1.9 | 0.09 | $5.4 \pm 0.6$ | $130 \pm 30$ |
| Mg 4 | 0 | 3.1 | 9 | 0.08 | 8.1 | 0 | 85 | 0 | – | $4.4 \pm 0.9$ | $150 \pm 50$ |
| BaMg 4 | 1 | 3.1 | 9 | 0.08 | 8.1 | $3 \times 10^{-4}:1$ | 85 | 0.2 | 0.01 | $4.7 \pm 0.9$ | $150 \pm 40$ |
| BaMg 5 | 2 | 0.8 | 27 | 0.1 | 8.2 | $3 \times 10^{-3}:1$ | 75 | 1.3 | 0.01 | $4.2 \pm 0.6$ | $160 \pm 50$ |
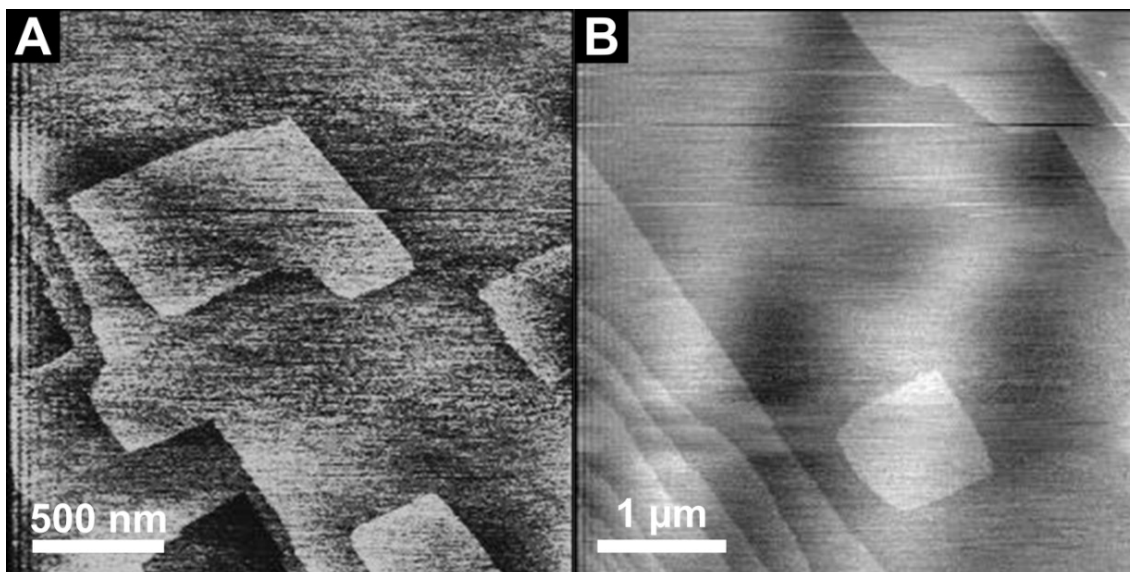
Figure 4.1-6: HAFM height images of the same (104) magnesite surface growing without (A) and with 3 µM of Ba (B) in the growth solution (BaMg 3). The solutions are undersaturated with respect to norsethite and witherite. No influence of barium on step morphology is detectable.
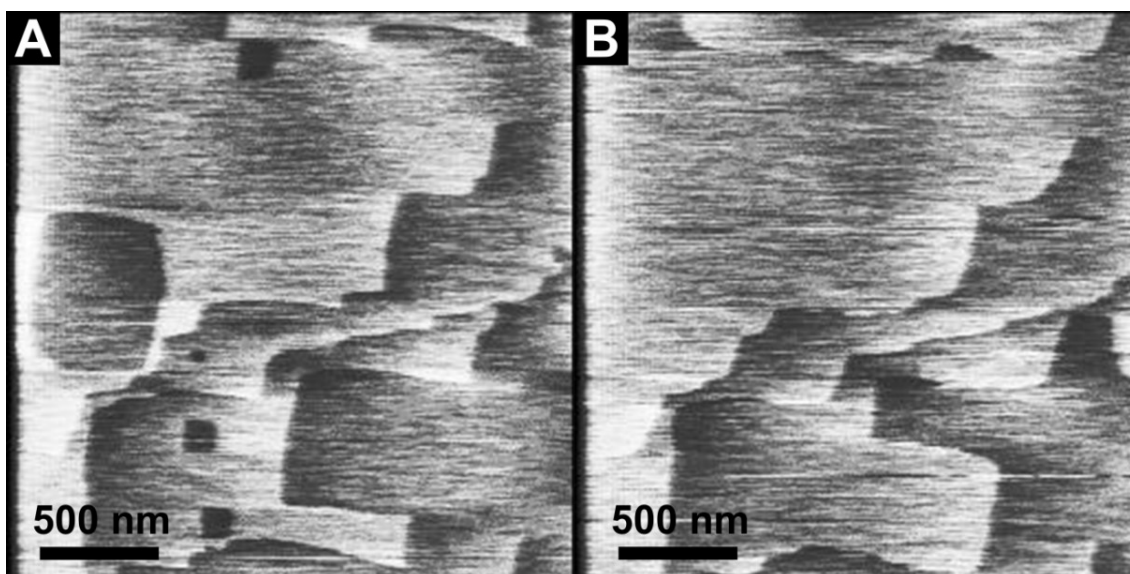


Figure 4.1-7: HAFM height images of experiment BaMg4 with 1 µM of Ba and Ba:Mg $\approx 4 \times 10^{-3}$:1 in the growth solution. Both images show the same area with a time difference of 168 s. Etch pits present in (A) have been overgrown in (B). There is no contrast to the surrounding surface indicating that the layer height of the newly grown material is the same as in the magnesite substrate. Therefore, no significant amount of $Ba^{2+}$ has been incorporated, as this would lead to evident height differences.
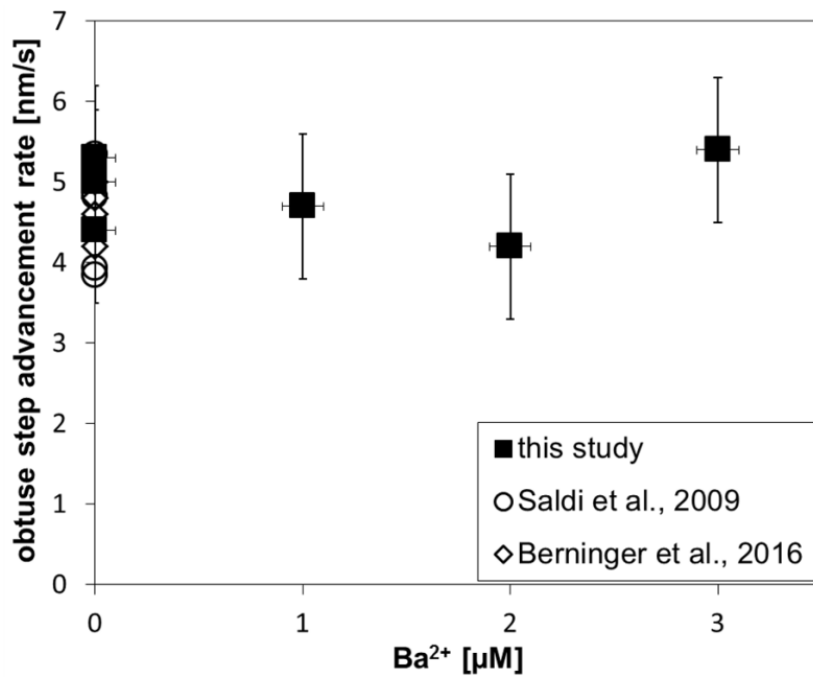
Figure 4.1-8: Obtuse step advancement rates on magnesite (104) surfaces show no dependence on aqueous Ba concentrations under the investigated experimental conditions. Velocities agree with Ba-free data by Saldi et al. (2009) and Berninger et al. (2016).
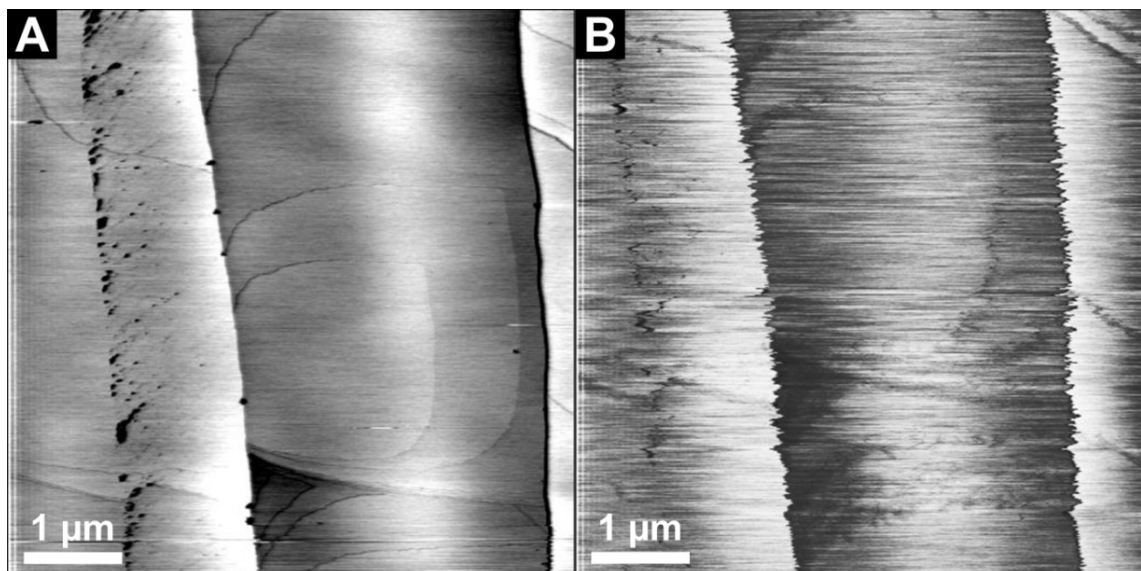


Figure 4.1-9: HAFM height images of the same surface area of experiment BaMg2 without Ba (A) and with 50 μM of Ba (Ba:Mg ≈ $7 \times 10^{-2}$:1) (B) in the growth solution. The presence of barium led to a significant decrease in image quality. This decrease is presumably caused by the precipitation of a Ba-carbonate phase floating within the growth solution.

33

### 4.1.3 Discussion

*4.1.3.1 Growth kinetics of norsethite as additionally precipitated phase*

From solutions with Ba:Mg ratios $> 2 \times 10^{-4}$ norsethite precipitated as shown by XRD and SEM analyses. In experiments with Ba:Mg ratios $< 2 \times 10^{-4}$, no norsethite was found although there is clear evidence for Ba withdrawal from the comparison of input and effluent solutions. This leaves room for three likely causes of the Ba withdrawal: 1) Norsethite precipitated in an amount too small to be detected by the methods used. 2) A combination of norsethite precipitation and incorporation of Ba by the growing magnesite crystals took place. 3) Exclusive Ba incorporation by the growing magnesite took place without any norsethite precipitation as the IAP$_{nrs}$ of the solutions could be below the precipitation threshold. The latter possibility gives way for the estimation of an upper limit of the solubility product of norsethite at 100 °C. Assuming that the lowest IAP$_{nrs}$, at which norsethite precipitation was verified in the experiments, corresponds to the maximum solubility product, a value of $\log_{10} K_{s\,nrs}^{100\,°C} < -18.2$ follows (for the calculation, IAP$_{nrs}$ of experiment mgsBa5 with little norsethite detectable was used). This maximum value roughly coincides with the solubility product of dolomite at 100 °C ($\log_{10} K_{s\,dol}^{100\,°C} = -18.3$) as suggested by Bénézeth et al. (2013). Further data on the solubility product of norsethite is presented in chapter 4.3.

The norsethite crystals present on the magnesite surfaces did not show any evidence of epitaxial growth such as a preferred crystal orientation (Figure 4.1-1D). Norsethite, therefore, likely grew directly from solution using aqueous barium and aqueous magnesium as source for crystallization via heterogeneous nucleation on reactor walls or magnesite seeds. Consequently, the growth mechanism of norsethite corresponds to equation 1.4-1. The growth rates calculated for norsethite (Figure 4.1-4) are about one order of magnitude higher than magnesite growth rates, but it should be noted that the supersaturations might differ significantly. Exchanging IAP$_{nrs}$ for $\Omega_{nrs}$ on the abscissa of the plot in Figure 4.1-4 would not alter the trend of the rate data but only laterally shift the values on the abscissa. Assuming a norsethite solubility product of $\log_{10} K_{s\,nrs}^{100\,°C} = -18.2$, the saturation states of the solutions with respect to norsethite were $\Omega \leq 6$. A lower solubility product results in higher supersaturations for the same solution.

*4.1.3.2 Incorporation of $Ba^{2+}$ into magnesite during growth*

As stated above, barium withdrawal from solution without detectable norsethite precipitation may be a consequence of barium incorporation by the growing magnesite. This assumption allows the calculation of a partitioning coefficient $k_d$ of barium between magnesite and solution at 100 °C according to $k_{d\,Ba\,mgs} = (\frac{X_{Ba}}{X_{Mg}})/(\frac{m_{Ba}}{m_{Mg}})$, ($X_i$: mole fraction of Ba$^{2+}$ and Mg$^{2+}$ in the precipitated magnesite, $m_i$:

concentration of $Ba^{2+}$ and $Mg^{2+}$ in aqueous solution, Rimstidt et al., 1998; Wang and Xu, 2001). The mole fractions were obtained by mass balance calculations of Ba and Mg withdrawal in experiments without any detected norsethite under the assumption that all withdrawn barium was incorporated into magnesite. Experiments with $Ba^{2+}$-concentrations > 0.3 μM were not used for the calculation as the norsethite precipitation observed in these experiments impedes deduction of $\left(\frac{x_{Ba}}{x_{Mg}}\right)$. The value obtained by this empirical approach is $k_{d\,Ba\,mgs} = 0.7 \pm 0.4$.

Using a linear free energy correlation mode, Wang and Xu (2001) calculated a partitioning coefficient of Ba between magnesite and solution. Their result ($k_{d\,Ba\,mgs} = 1.5$ at 25 °C) is larger than the experimental partitioning coefficient obtained here. This discrepancy may result from the fact that the value of Wang and Xu (2001) was calculated for chemical equilibrium at 25 °C, whereas the experimental value was measured during magnesite growth at 100 °C under the assumption that all withdrawn Ba is incorporated into magnesite.

### 4.1.3.3 General differences of Ba incorporation into calcite and magnesite

In order to assess the possibility of Ba incorporation into magnesite further, it is worth to consider the incorporation of this element into calcite. The effect of Ba on calcite growth has been studied by Astilleros et al. (2000, 2006), Gutjahr et al. (1996), Pingitore and Eastman (1984), Pingitore (1986), Reeder (1996), Reeder et al. (1999), Tesoriero and Pankow (1996), Tunusoglu et al. (2007), and Yoshida et al. (2008). For the partitioning coefficient of Ba between calcite and solution $k_{d\,Ba\,cc}$ a variety of experimental values were reported: 0.04 (Pingitore and Eastman, 1984), 0.06 (Pingitore, 1986), 0.012 (Tesoriero and Pankow, 1996), and 0.016 (Yoshida et al., 2008). Calculations with a linear free energy correlation model yielded $k_{d\,Ba\,cc} = 0.013$ (Wang and Xu, 2001). Although $k_{d\,Ba\,cc}$ certainly depends on the growth rate (e.g., Tesoriero and Pankow, 1996), all values are considerably smaller than the values of $k_{d\,Ba\,mgs}$ derived above. The small partitioning coefficients $k_{d\,Ba\,cc}$ still manifest a small amount of incorporation of Ba into calcite which can have significant effects on crystal growth. Such effects have been reported by Astilleros et al. (2000) who detected a decrease of the advancement rates of obtuse steps, changes in step morphology, and an increase of monolayer thickness. At least the latter finding is a clear sign of barium incorporation into the growing calcite. Barium can substitute calcium on its octahedral site and distort the calcite lattice as shown by Reeder et al. (1999). It is known that the attachment of various cations is affected by the anisotropy of calcite surface structure (Paquette and Reeder, 1995; Staudt et al., 1994). Cations smaller than $Ca^{2+}$ (e.g., $Mg^{2+}$, $Mn^{2+}$, $Cd^{2+}$) are more easily incorporated at acute steps while bigger ions (e.g., $Sr^{2+}$, $Ba^{2+}$) prefer obtuse steps. The same behavior should in principle apply to magnesite because it is isostructural to calcite. Thus, Ba incorporation on magnesite surfaces should be strongly favored

at obtuse steps and cause similar effects as observed on calcite by Astilleros et al. (2000). None of these effects were detected in HAFM experiments conducted here (Figures 4.1-6 & 4.1-7).

Assuming a partitioning coefficient of $Ba^{2+}$ between magnesite and solution close to unity (as obtained under the assumption that all withdrawn $Ba^{2+}$ is incorporated into magnesite if no norsethite was found in the experiments), the density of $Ba^{2+}$ incorporated into the growing (104) magnesite surface can be calculated. At an aqueous Ba:Mg ratio of $1 \times 10^{-4}$ and a partitioning coefficient $k_{d\,Ba\,mgs} = 1$, every ten thousandth cation is a barium ion ($\frac{X_{Ba}}{X_{Mg}} = k_{d\,Ba\,mgs}\frac{m_{Ba}}{m_{Mg}} = 1 \times 10^{-4}$). On the (104) surface, the distances between two next cation positions are $\sim 3.7\,\text{Å}$ and $\sim 4.6\,\text{Å}$ (Maslen et al., 1993). If one $Ba^{2+}$ in ten thousand cations is incorporated in a growing magnesite monolayer, an areal density of approximately $600\,Ba/\mu m^2$ follows. In AFM images, a single $Ba^{2+}$ within an otherwise flat magnesium carbonate terrace would appear as a single protrusion. An areal density of $600\,Ba^{2+}/\mu m^2$ would result in coalescing protrusions leading to an overall increased monolayer thickness (as observed on calcite by Astilleros et al., 2000). Note that incorporation at non-lattice sites as proposed for $Ba^{2+}$ incorporation into calcite (Pingitore and Eastman, 1984) would also have to take place within the growing terraces and would lead to the same morphologic effects. As none of such morphologic records were detected (Figures 4.1-6 & 4.1-7), it can be concluded that aqueous barium was not incorporated into magnesite in amounts indicated by any partitioning coefficient close to unity. A partitioning coefficient of $k_d = 0.01$ (corresponding to the partitioning coefficient of $Ba^{2+}$ between calcite and solution) would still lead to $6\,Ba/\mu m^2$ (i.e., one protrusion in approx. $400 \times 400\,nm^2$). Such a Ba protrusion density might be considered as lower limit which can be reliably detected by in-situ HAFM among other protrusions generated by mechanical noise for instance. The HAFM findings, therefore, more likely suggest a partitioning coefficient of approx. $10^{-2}$ rather than unity. Furthermore, the HAFM results imply that the Ba-withdrawal observed in HMFR-experiments with low Ba concentrations was caused by norsethite formation in amounts below the detection limit of the applied methods rather than by incorporation.

### 4.1.3.4 Magnesite growth kinetics

Magnesite growth rates were calculated from Mg mass balance between inlet and effluent solution compositions. The obtained rates of growth are plotted vs. the corresponding values of fluid supersaturation (as derived from the effluent speciation calculated by PHREEQC) and compared with other data from literature in Figure 4.1-10. It can be seen that a good agreement exists among the different sets of data, which provide an uniform trend of increasing rates with increasing supersaturation, although the reported rates were obtained using both MFR and
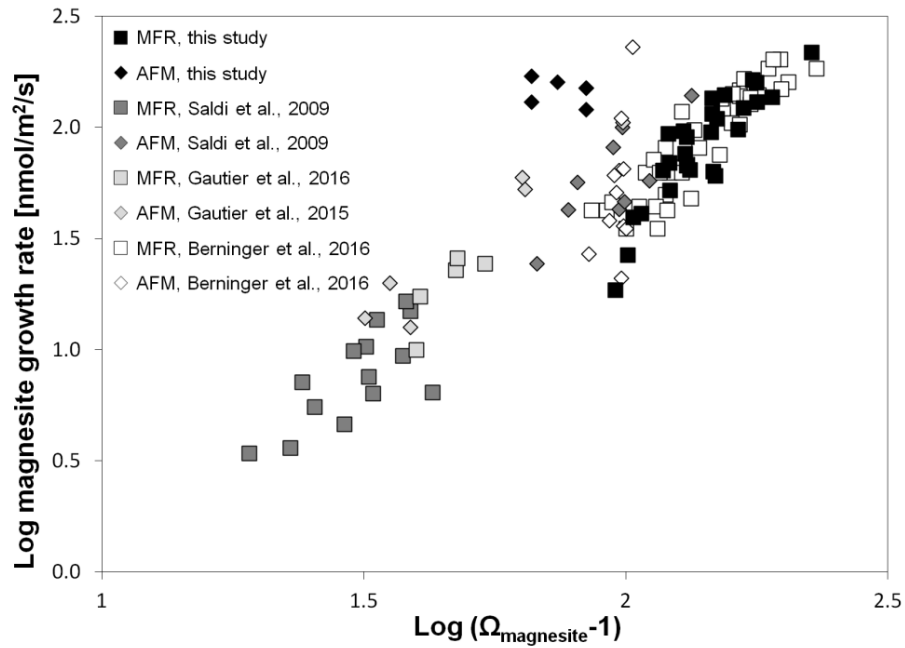
Figure 4.1-10: Compilation of magnesite growth rates at 100 °C derived from different studies. MFR: mixed flow reactor; AFM: atomic force microscopy. Note that for such comparison MFR data from Berninger et al. (2016) were recalculated using a geometrically derived seed surface area.
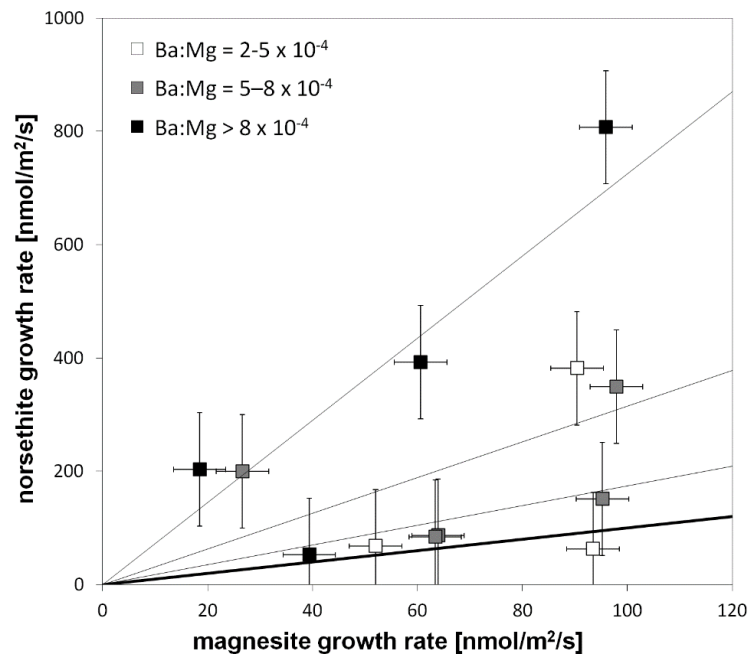


Figure 4.1-11: HMFR magnesite growth rate and norsethite growth rates are directly correlated as a function of the Ba:Mg ratios of aqueous solutions. At Ba:Mg $> 2 \times 10^{-4}$, norsethite growth rates exceed magnesite growth rates. Thin lines are linear fits to the three datasets; the bold line has a slope of one, indicating equality of magnesite and norsethite growth rate.

AFM and include experiments conducted with highly variable parameters (e.g., pH and $Mg^{2+}$:$CO_3^{2-}$ ratio). The comparison of rates with different Ba:Mg ratios and Ba concentrations (Figure 4.1-5) shows that none of these parameters has a significant effect on macroscopic magnesite growth rates. This insensitivity of magnesite growth rates might be a consequence of very low $Ba^{2+}$ incorporation into the growing crystal. The big $Ba^{2+}$ ion, however, is not the only cation without any significant effect on magnesite growth kinetics. As reported by Berninger et al. (2016) also the much smaller $Ca^{2+}$ ion does not affect magnesite growth rate, although $Ca^{2+}$ was incorporated into magnesite by up to 8 mol%.

Irrespectively of cationic effects, magnesite growth rate is independent of the concomitant norsethite growth (apart from the decrease of supersaturation with respect to magnesite caused by decreasing alkalinity and $Mg^{2+}$ activity induced by norsethite growth). Given enough barium, magnesite and norsethite can grow simultaneously with little mutual interference. Thus, the question arises whether norsethite can capture $Mg^{2+}$ more rapidly than magnesite – not only at ambient temperature but also at 100 °C. The comparison of norsethite and magnesite growth rates from individual experiments show a linear relationship depending on the aqueous Ba:Mg ratio (Figure 4.1-11). At Ba:Mg $> 2 \times 10^{-4}$ norsethite growth rates exceed magnesite growth rates. The limiting factor for norsethite growth at the given experimental conditions likely is $Ba^{2+}$ supply. Nevertheless, it is important to note that the solutions may have different supersaturations with respect to magnesite and norsethite. Whereas the supersaturation with respect to magnesite can be quantified, this is not yet possible for norsethite as the temperature dependence of the solubility constant of norsethite is still unknown. One of the most important tasks for future studies, therefore, is to quantify the solubility constant of norsethite at elevated temperatures.

Table A 4.1–1 Outlet fluid compositions of single samples of HMFR experiments with calculated magnesite growth rates and corresponding saturation state values with respect to magnesite [$\Omega$(mgs)] and witherite [$\Omega$(wth)]. The ion activity product for norsethite (IAP$_{nrs}$) is also provided.

| Sample | flowrate [ml/min] | alkalinity [meq/L] | Δ alkalinity [meq/L] | Ba [µM] | Mg [mM] | Δ Ba [µM] | Δ Mg [mM] | Magnesite growth rate [nmol/m²/s] | pH (100 °C) | $\Omega$(mgs) | $\Omega$(wth) | IAP$_{nrs}$ (x 10$^{-18}$) | a Mg$^{2+}$ / a CO$_3^{2-}$ | a Ba$^{2+}$ / a Mg$^{2+}$ (x 10$^{-4}$) |
|---|---|---|---|---|---|---|---|---|---|---|---|---|---|---|
| mgsBa0 1 | 0.5 | 22.94 | 1.96 | 0.00 | 2.35 | 0.00 | 0.95 | 67 | 7.68 | 130 | 0.00 | 0.00 | 11.8 | 0.0 |
| mgsBa0 2 | 0.5 | 22.91 | 1.99 | 0.00 | 2.37 | 0.00 | 0.94 | 67 | 7.68 | 131 | 0.00 | 0.00 | 12.0 | 0.0 |
| mgsBa0 3 | 0.5 | 22.90 | 2.00 | 0.00 | 2.34 | 0.00 | 0.96 | 69 | 7.69 | 133 | 0.00 | 0.00 | 11.4 | 0.0 |
| mgsBa0 4 | 0.5 | 22.90 | 2.00 | 0.00 | 2.33 | 0.00 | 0.97 | 73 | 7.67 | 125 | 0.00 | 0.00 | 12.1 | 0.0 |
| mgsBa0 5 | 0.5 | 22.89 | 2.01 | 0.00 | 2.34 | 0.00 | 0.97 | 74 | 7.65 | 122 | 0.00 | 0.00 | 12.6 | 0.0 |
| mgsBa0 6 | 0.5 | 22.89 | 2.01 | 0.00 | 2.34 | 0.00 | 0.96 | 74 | 7.71 | 138 | 0.00 | 0.00 | 11.0 | 0.0 |
| mgsBa0 7 | 0.5 | 22.92 | 1.98 | 0.00 | 2.11 | 0.00 | 1.20 | 98 | 7.73 | 130 | 0.00 | 0.00 | 9.4 | 0.0 |
| mgsBa0 8 | 0.5 | 22.92 | 1.98 | 0.00 | 2.36 | 0.00 | 0.95 | 78 | 7.69 | 132 | 0.00 | 0.00 | 11.7 | 0.0 |
| mgsBa0 9 | 0.5 | 22.94 | 1.96 | 0.00 | 2.36 | 0.00 | 0.95 | 78 | 7.67 | 127 | 0.00 | 0.00 | 12.3 | 0.0 |
| mgsBa0 10 | 0.5 | 22.93 | 1.97 | 0.00 | 2.34 | 0.00 | 0.97 | 82 | 7.71 | 138 | 0.00 | 0.00 | 10.9 | 0.0 |
| mgsBa0 11 | 1.0 | 23.47 | 1.43 | 0.00 | 2.62 | 0.00 | 0.68 | 122 | 7.73 | 163 | 0.00 | 0.00 | 11.4 | 0.0 |
| mgsBa0 12 | 1.0 | 23.50 | 1.40 | 0.00 | 2.63 | 0.00 | 0.68 | 122 | 7.73 | 164 | 0.00 | 0.00 | 11.4 | 0.0 |
| mgsBa0 13 | 1.0 | 23.49 | 1.41 | 0.00 | 2.63 | 0.00 | 0.67 | 122 | 7.76 | 174 | 0.00 | 0.00 | 10.6 | 0.0 |
| mgsBa0 14 | 1.0 | 23.48 | 1.42 | 0.00 | 2.63 | 0.00 | 0.68 | 124 | 7.76 | 174 | 0.00 | 0.00 | 10.7 | 0.0 |
| mgsBa0 15 | 0.2 | 22.54 | 2.36 | 0.00 | 2.14 | 0.00 | 1.16 | 68 | 7.67 | 115 | 0.00 | 0.00 | 11.2 | 0.0 |
| mgsBa0 16 | 0.2 | 22.51 | 2.39 | 0.00 | 2.16 | 0.00 | 1.15 | 69 | 7.73 | 131. | 0.00 | 0.00 | 9.9 | 0.0 |
| mgsBa0 17 | 0.2 | 22.53 | 2.37 | 0.00 | 2.15 | 0.00 | 1.16 | 70 | 7.69 | 120 | 0.00 | 0.00 | 10.8 | 0.0 |
| mgsBa0 18 | 2.0 | 24.01 | 0.89 | 0.00 | 2.90 | 0.00 | 0.41 | 216 | 7.84 | 229 | 0.00 | 0.00 | 9.4 | 0.0 |
| mgsBa0 19 | 2.0 | 24.04 | 0.86 | 0.00 | 2.91 | 0.00 | 0.40 | 212 | 7.83 | 225 | 0.00 | 0.00 | 9.7 | 0.0 |
| mgsBa0 20 | 2.0 | 24.01 | 0.89 | 0.00 | 2.92 | 0.00 | 0.39 | 208 | 7.84 | 230 | 0.00 | 0.00 | 9.5 | 0.0 |
| mgsBa0 21 | 2.0 | 24.02 | 0.88 | 0.00 | 2.88 | 0.00 | 0.43 | 232 | 7.84 | 225 | 0.00 | 0.00 | 9.5 | 0.0 |
| mgsBa0 22 | 0.5 | 23.40 | 1.50 | 0.00 | 2.47 | 0.00 | 0.83 | 126 | 7.76 | 178 | 0.00 | 0.00 | 10.2 | 0.0 |
| mgsBa1 2 | 1.0 | 1.38 | 1.38 | 2.32 | 2.56 | 34.72 | 0.75 | 98 | 7.64 | 124 | 0.04 | 1.34 | 15.4 | 9.2 |
| mgsBa1 3 | 1.0 | 21.88 | 1.46 | 2.31 | 2.57 | 34.73 | 0.74 | 96 | 7.66 | 129 | 0.04 | 1.45 | 14.8 | 9.1 |
| mgsBa1 4 | 1.0 | 22.25 | 1.09 | 2.30 | 2.57 | 34.74 | 0.74 | 96 | 7.69 | 138 | 0.04 | 1.67 | 13.5 | 9.1 |
| mgsBa1 5 | 1.0 | 22.21 | 1.13 | 2.30 | 2.58 | 34.73 | 0.73 | 95 | 7.65 | 127 | 0.04 | 1.40 | 15.0 | 9.1 |
| mgsBa1 8 | 2.0 | 21.94 | 1.40 | 2.10 | 2.75 | 34.94 | 0.56 | 143 | 7.73 | 159 | 0.04 | 1.88 | 13.4 | 7.8 |
| mgsBa1 9 | 2.0 | 22.21 | 1.13 | 2.09 | 2.74 | 34.95 | 0.56 | 145 | 7.70 | 152 | 0.04 | 1.71 | 14.0 | 7.8 |
| mgsBa1 10 | 2.0 | 22.23 | 1.10 | 2.08 | 2.79 | 34.96 | 0.51 | 131 | 7.70 | 154 | 0.04 | 1.73 | 14.2 | 7.6 |
| mgsBa1 11 | 0.2 | 20.86 | 2.48 | 1.63 | 2.09 | 35.41 | 1.22 | 39 | 7.66 | 101 | 0.03 | 0.77 | 12.8 | 7.9 |
| mgsBa1 12 | 0.2 | 20.93 | 2.41 | 1.62 | 2.06 | 35.42 | 1.24 | 39 | 7.67 | 103 | 0.03 | 0.80 | 12.2 | 8.0 |
| mgsBa1 13 | 0.2 | 20.99 | 2.35 | 1.63 | 2.03 | 35.41 | 1.28 | 40 | 7.70 | 109 | 0.03 | 0.93 | 11.0 | 8.2 |

| Sample | flowrate [ml/min] | alkalinity [meq/L] | Δ alkalinity [meq/L] | Ba [μM] | Mg [mM] | Δ Ba [μM] | Δ Mg [mM] | Magnesite growth rate [nmol/m²/s] | pH (100 °C) | $\Omega$(mgs) | $\Omega$(wth) | IAP$_{nrs}$ (x 10$^{-18}$) | a Mg$^{2+}$ / a CO$_3^{2-}$ | a Ba$^{2+}$ / a Mg$^{2+}$ (x 10$^{-4}$) |
|---|---|---|---|---|---|---|---|---|---|---|---|---|---|---|
| mgsBa1 14 | 0.2 | 20.97 | 2.37 | 1.63 | 2.06 | 35.41 | 1.24 | 39 | 7.67 | 103 | 0.03 | 0.81 | 12.1 | 8.0 |
| mgsBa1 15 | 0.5 | 21.20 | 2.14 | 1.46 | 2.31 | 35.58 | 0.99 | 64 | 7.67 | 115 | 0.02 | 0.81 | 13.6 | 6.4 |
| mgsBa1 16 | 0.5 | 21.29 | 2.05 | 1.43 | 2.30 | 35.61 | 1.00 | 64 | 7.69 | 122 | 0.03 | 0.89 | 12.6 | 6.3 |
| mgsBa1 17 | 0.5 | 21.36 | 1.98 | 1.48 | 2.32 | 35.56 | 0.99 | 64 | 7.67 | 118 | 0.03 | 0.85 | 13.3 | 6.5 |
| mgsBa1 18 | 0.5 | 21.37 | 1.97 | 1.45 | 2.31 | 35.59 | 0.99 | 64 | 7.69 | 121 | 0.03 | 0.88 | 12.8 | 6.4 |
| mgsBa1 19 | 1.0 | 21.78 | 1.56 | 1.57 | 2.54 | 35.47 | 0.76 | 98 | 7.72 | 146 | 0.03 | 1.28 | 12.5 | 6.3 |
| mgsBa1 20 | 1.0 | 21.79 | 1.54 | 1.55 | 2.58 | 35.49 | 0.73 | 93 | 7.72 | 146 | 0.03 | 1.25 | 12.9 | 6.1 |
| mgsBa2 1 | 1.0 | 21.72 | 1.72 | 1.28 | 2.60 | 73.93 | 0.76 | 90 | 7.66 | 130 | 0.02 | 0.80 | 15.1 | 5.0 |
| mgsBa2 2 | 1.0 | 21.75 | 1.69 | 1.25 | 2.62 | 73.96 | 0.74 | 88 | 7.68 | 136 | 0.02 | 0.86 | 14.5 | 4.8 |
| mgsBa2 3 | 1.0 | 21.80 | 1.64 | 1.27 | 2.61 | 73.93 | 0.75 | 88 | 7.66 | 130 | 0.02 | 0.80 | 15.1 | 4.9 |
| mgsBa2 4 | 1.0 | 21.99 | 1.45 | 1.24 | 2.56 | 73.96 | 0.80 | 95 | 7.67 | 131 | 0.02 | 0.81 | 14.4 | 4.9 |
| mgsBa2 5 | 1.0 | 21.94 | 1.50 | 1.24 | 2.59 | 73.97 | 0.77 | 91 | 7.66 | 130 | 0.02 | 0.79 | 14.8 | 4.9 |
| mgsBa2 6 | 0.5 | 21.67 | 1.77 | 0.97 | 2.46 | 74.23 | 0.90 | 48 | 7.70 | 132 | 0.02 | 0.67 | 13.1 | 4.0 |
| mgsBa2 7 | 0.5 | 21.59 | 1.85 | 1.03 | 2.42 | 74.18 | 0.94 | 50 | 7.67 | 123 | 0.02 | 0.62 | 13.8 | 4.3 |
| mgsBa2 8 | 0.5 | 21.47 | 1.97 | 1.12 | 2.38 | 74.08 | 0.98 | 53 | 7.66 | 119 | 0.02 | 0.65 | 13.9 | 4.8 |
| mgsBa2 9 | 0.5 | 21.52 | 1.92 | 1.19 | 2.32 | 74.02 | 1.04 | 56 | 7.66 | 115 | 0.02 | 0.66 | 13.6 | 5.2 |
| mgsBa2 10 | 0.5 | 21.45 | 1.99 | 1.19 | 2.35 | 74.01 | 1.01 | 54 | 7.68 | 121 | 0.02 | 0.72 | 13.2 | 5.1 |
| mgsBa2 11 | 2.0 | 22.16 | 1.28 | 0.85 | 2.69 | 74.36 | 0.67 | 135 | 7.68 | 143 | 0.02 | 0.63 | 14.4 | 3.2 |
| mgsBa2 12 | 2.0 | 22.16 | 1.28 | 0.86 | 2.69 | 74.35 | 0.67 | 134 | 7.69 | 145 | 0.02 | 0.66 | 14.1 | 3.3 |
| mgsBa2 13 | 2.0 | 22.07 | 1.37 | 0.86 | 2.72 | 74.35 | 0.64 | 128 | 7.68 | 144 | 0.02 | 0.64 | 14.6 | 3.2 |
| mgsBa2 14 | 2.0 | 21.94 | 1.50 | 0.86 | 2.69 | 74.35 | 0.67 | 134 | 7.75 | 162 | 0.02 | 0.82 | 12.5 | 3.3 |
| mgsBa2 15 | 2.0 | 22.00 | 1.44 | 0.85 | 2.59 | 74.36 | 0.77 | 155 | 7.65 | 129 | 0.01 | 0.53 | 15.0 | 3.3 |
| mgsBa2 16 | 2.0 | 21.90 | 1.53 | 0.85 | 2.71 | 74.36 | 0.65 | 129 | 7.71 | 151 | 0.02 | 0.69 | 13.8 | 3.2 |
| mgsBa2 17 | 2.0 | 21.78 | 1.66 | 0.84 | 2.68 | 74.37 | 0.68 | 134 | 7.72 | 153 | 0.02 | 0.71 | 13.3 | 3.2 |
| mgsBa2 18 | 1.0 | 21.53 | 1.91 | 0.99 | 2.43 | 74.22 | 0.93 | 92 | 7.66 | 122 | 0.02 | 0.58 | 14.1 | 4.1 |
| mgsBa2 19 | 1.0 | 21.45 | 1.99 | 0.98 | 2.43 | 74.23 | 0.93 | 93 | 7.66 | 121 | 0.02 | 0.57 | 14.2 | 4.1 |
| mgsBa2 20 | 1.0 | 21.42 | 2.02 | 0.98 | 2.41 | 74.23 | 0.95 | 95 | 7.67 | 122 | 0.02 | 0.58 | 13.9 | 4.1 |
| mgsBa3 1 | 0.5 | 24.69 | 0.31 | 0.11 | 2.44 | 0.27 | 0.89 | 60 | 7.69 | 146 | 0.00 | 0.10 | 10.9 | 0.5 |
| mgsBa3 2 | 0.5 | 23.50 | 1.50 | 0.13 | 2.42 | 0.24 | 0.91 | 60 | 7.70 | 141 | 0.00 | 0.11 | 11.3 | 0.6 |
| mgsBa3 3 | 0.5 | 23.25 | 1.75 | 0.14 | 2.42 | 0.23 | 0.91 | 61 | 7.69 | 136 | 0.00 | 0.11 | 11.8 | 0.6 |
| mgsBa3 4 | 0.5 | 23.09 | 1.91 | 0.23 | 2.37 | 0.15 | 0.96 | 63 | 7.70 | 137 | 0.00 | 0.18 | 11.3 | 1.0 |
| mgsBa3 5 | 0.5 | 22.99 | 2.01 | 0.25 | 2.32 | 0.12 | 1.01 | 66 | 7.67 | 126 | 0.00 | 0.17 | 12.0 | 1.1 |

| Sample | flowrate [ml/min] | alkalinity [meq/L] | Δ alkalinity [meq/L] | Ba [µM] | Mg [mM] | Δ Ba [µM] | Δ Mg [mM] | Magnesite growth rate [nmol/m²/s] | pH (100 °C) | Ω(mgs) | Ω(wth) | IAP$_{nrs}$ (x 10$^{-18}$) | a Mg$^{2+}$ / a CO$_3^{2-}$ | a Ba$^{2+}$ / a Mg$^{2+}$ (x 10$^{-4}$) |
|---|---|---|---|---|---|---|---|---|---|---|---|---|---|---|
| mgsBa3 6 | 0.5 | 22.93 | 2.07 | 0.25 | 2.34 | 0.12 | 0.99 | 65 | 7.71 | 138 | 0.01 | 0.20 | 10.9 | 1.1 |
| mgsBa3 7 | 0.5 | 22.87 | 2.13 | 0.28 | 2.30 | 0.09 | 1.03 | 66 | 7.69 | 129 | 0.01 | 0.20 | 11.4 | 1.3 |
| mgsBa3 8 | 0.5 | 22.89 | 2.11 | 0.28 | 2.30 | 0.09 | 1.03 | 67 | 7.68 | 127 | 0.01 | 0.19 | 11.6 | 1.3 |
| mgsBa3 9 | 0.5 | 22.87 | 2.13 | 0.29 | 2.29 | 0.08 | 1.04 | 67 | 7.67 | 123 | 0.01 | 0.19 | 11.9 | 1.3 |
| mgsBa3 10 | 0.5 | 22.85 | 2.15 | 0.29 | 2.28 | 0.08 | 1.05 | 67 | 7.70 | 130 | 0.01 | 0.21 | 11.1 | 1.3 |
| mgsBa3 11 | 1.0 | 23.09 | 1.91 | 0.33 | 2.46 | 0.04 | 0.87 | 110 | 7.70 | 141 | 0.01 | 0.26 | 11.8 | 1.4 |
| mgsBa3 12 | 1.0 | 23.17 | 1.83 | 0.33 | 2.47 | 0.04 | 0.86 | 108 | 7.73 | 152 | 0.01 | 0.30 | 11.0 | 1.4 |
| mgsBa3 13 | 1.0 | 23.17 | 1.83 | 0.32 | 2.45 | 0.05 | 0.88 | 111 | 7.76 | 160 | 0.01 | 0.33 | 10.1 | 1.3 |
| mgsBa3 14 | 1.0 | 23.14 | 1.86 | 0.32 | 2.46 | 0.05 | 0.87 | 109 | 7.72 | 147 | 0.01 | 0.28 | 11.3 | 1.3 |
| mgsBa3 15 | 0.2 | 22.25 | 2.75 | 0.30 | 1.94 | 0.07 | 1.39 | 41 | 7.68 | 106 | 0.01 | 0.17 | 10.1 | 1.6 |
| mgsBa3 16 | 0.2 | 22.11 | 2.89 | 0.29 | 1.93 | 0.08 | 1.40 | 41 | 7.71 | 112 | 0.01 | 0.19 | 9.3 | 1.5 |
| mgsBa3 17 | 0.2 | 22.11 | 2.89 | 0.30 | 1.92 | 0.07 | 1.41 | 41 | 7.69 | 106 | 0.01 | 0.17 | 9.9 | 1.6 |
| mgsBa3 18 | 2.0 | 23.11 | 1.89 | 0.35 | 2.43 | 0.02 | 0.90 | 209 | 7.74 | 151 | 0.01 | 0.32 | 10.7 | 1.5 |
| mgsBa3 19 | 2.0 | 23.09 | 1.91 | 0.35 | 2.42 | 0.02 | 0.90 | 211 | 7.73 | 148 | 0.01 | 0.31 | 10.8 | 1.5 |
| mgsBa3 20 | 2.0 | 23.07 | 1.93 | 0.35 | 2.41 | 0.02 | 0.92 | 213 | 7.72 | 144 | 0.01 | 0.30 | 11.0 | 1.5 |
| mgsBa3 21 | 2.0 | 23.06 | 1.94 | 0.35 | 2.39 | 0.03 | 0.94 | 218 | 7.71 | 140 | 0.01 | 0.28 | 11.3 | 1.5 |
| mgsBa3 22 | 0.5 | 22.10 | 2.90 | 0.35 | 1.88 | 0.02 | 1.45 | 83 | 7.65 | 95 | 0.01 | 0.17 | 10.6 | 1.9 |
| mgsBa3b 1 | 2.0 | 23.61 | 1.12 | 0.28 | 2.34 | 0.08 | 0.58 | 169 | 7.81 | 172 | 0.01 | 0.35 | 8.3 | 1.2 |
| mgsBa3b 2 | 2.0 | 23.60 | 1.13 | 0.27 | 2.35 | 0.08 | 0.57 | 165 | 7.83 | 179 | 0.01 | 0.37 | 8.0 | 1.2 |
| mgsBa3b 3 | 2.0 | 23.63 | 1.10 | 0.28 | 2.36 | 0.07 | 0.56 | 163 | 7.82 | 178 | 0.01 | 0.38 | 8.2 | 1.3 |
| mgsBa3b 4 | 2.0 | 23.72 | 1.01 | 0.29 | 2.37 | 0.07 | 0.54 | 159 | 7.81 | 175 | 0.01 | 0.37 | 8.4 | 1.3 |
| mgsBa3b 5 | 2.0 | 23.60 | 1.13 | 0.30 | 2.36 | 0.06 | 0.56 | 162 | 7.81 | 174 | 0.01 | 0.38 | 8.4 | 1.3 |
| mgsBa3b 6 | 1.4 | 23.51 | 1.22 | 0.32 | 2.28 | 0.04 | 0.63 | 129 | 7.84 | 178 | 0.01 | 0.44 | 7.6 | 1.4 |
| mgsBa3b 7 | 1.5 | 23.49 | 1.24 | 0.31 | 2.30 | 0.04 | 0.61 | 130 | 7.85 | 182 | 0.01 | 0.45 | 7.6 | 1.4 |
| mgsBa3b 8 | 1.4 | 23.47 | 1.26 | 0.32 | 2.28 | 0.04 | 0.64 | 131 | 7.83 | 176 | 0.01 | 0.43 | 7.7 | 1.4 |
| mgsBa4 1 | 0.5 | 22.43 | 0.95 | 1.02 | 1.27 | 105.50 | 0.36 | 17 | 7.85 | 99 | 0.03 | 0.79 | 4.3 | 8.4 |
| mgsBa4 2 | 0.5 | 22.53 | 0.84 | 1.01 | 1.25 | 105.50 | 0.38 | 19 | 7.81 | 91 | 0.03 | 0.66 | 4.7 | 8.4 |
| mgsBa4 3 | 0.5 | 22.55 | 0.82 | 0.97 | 1.26 | 105.54 | 0.37 | 18 | 7.82 | 93 | 0.02 | 0.66 | 4.6 | 8.0 |
| mgsBa4 4 | 0.5 | 22.49 | 0.89 | 1.01 | 1.26 | 105.51 | 0.38 | 18 | 7.83 | 95 | 0.03 | 0.72 | 4.5 | 8.3 |
| mgsBa4 5 | 0.5 | 22.41 | 0.97 | 1.01 | 1.25 | 105.50 | 0.39 | 19 | 7.86 | 99 | 0.03 | 0.79 | 4.2 | 8.4 |
| mgsBa4 6 | 0.5 | 22.41 | 0.97 | 1.01 | 1.23 | 105.50 | 0.41 | 20 | 7.86 | 98 | 0.03 | 0.78 | 4.1 | 8.6 |
| mgsBa4 7 | 0.5 | 22.41 | 0.96 | 1.04 | 1.26 | 105.48 | 0.37 | 18 | 7.85 | 99 | 0.03 | 0.80 | 4.3 | 8.6 |

| Sample | flowrate [ml/min] | alkalinity [meq/L] | Δ alkalinity [meq/L] | Ba [µM] | Mg [mM] | Δ Ba [µM] | Δ Mg [mM] | Magnesite growth rate [nmol/m²/s] | pH (100 °C) | Ω(mgs) | Ω(wth) | IAP$_{nrs}$ (x 10$^{-18}$) | a Mg$^{2+}$ / a CO$_3^{2-}$ | a Ba$^{2+}$ / a Mg$^{2+}$ (x 10$^{-4}$) |
|---|---|---|---|---|---|---|---|---|---|---|---|---|---|---|
| mgsBa4 8 | 1.0 | 22.64 | 0.74 | 0.84 | 1.33 | 105.67 | 0.30 | 27 | 7.84 | 102 | 0.02 | 0.65 | 4.7 | 6.6 |
| mgsBa5 1 | 0.5 | 23.30 | 1.80 | 2.38 | 2.41 | 1.26 | 0.92 | 62 | 7.71 | 142 | 0.05 | 1.95 | 11.3 | 10.2 |
| mgsBa5 2 | 0.5 | 23.10 | 2.00 | 2.63 | 2.39 | 1.01 | 0.94 | 60 | 7.76 | 155 | 0.06 | 2.61 | 10.0 | 11.3 |
| mgsBa5 3 | 0.5 | 23.20 | 1.90 | 2.58 | 2.38 | 1.06 | 0.94 | 61 | 7.74 | 149 | 0.06 | 2.38 | 10.3 | 11.2 |
| mgsBa5 4 | 0.5 | 23.20 | 1.90 | 2.51 | 2.40 | 1.13 | 0.93 | 60 | 7.74 | 150 | 0.05 | 2.33 | 10.4 | 10.8 |
| mgsBa5 5 | 1.0 | 23.50 | 1.60 | 1.94 | 2.55 | 1.70 | 0.77 | 98 | 7.76 | 168 | 0.04 | 2.13 | 10.4 | 7.9 |
| mgsBa5 6 | 1.0 | 23.50 | 1.60 | 1.98 | 2.55 | 1.66 | 0.77 | 98 | 7.76 | 168 | 0.05 | 2.17 | 10.4 | 8.0 |
| mgsBa5 7 | 1.0 | 23.70 | 1.40 | 1.95 | 2.56 | 1.69 | 0.77 | 97 | 7.75 | 166 | 0.04 | 2.06 | 10.6 | 7.9 |
| mgsBa5 8 | 1.0 | 23.50 | 1.60 | 1.94 | 2.54 | 1.70 | 0.78 | 99 | 7.73 | 155 | 0.04 | 1.81 | 11.3 | 7.9 |
| mgsBa5 9 | 2.0 | 24.34 | 0.76 | 1.62 | 2.77 | 2.02 | 0.55 | 137 | 7.77 | 188 | 0.04 | 2.04 | 10.7 | 6.1 |
| mgsBa5 10 | 2.0 | 24.28 | 0.82 | 1.59 | 2.79 | 2.05 | 0.54 | 133 | 7.79 | 198 | 0.04 | 2.22 | 10.2 | 5.9 |
| mgsBa5 11 | 2.0 | 24.01 | 1.09 | 1.62 | 2.78 | 2.02 | 0.55 | 135 | 7.77 | 189 | 0.04 | 2.05 | 10.8 | 6.0 |
| mgsBa5 12 | 2.0 | 23.86 | 1.24 | 1.58 | 2.75 | 2.06 | 0.57 | 142 | 7.78 | 189 | 0.04 | 2.02 | 10.6 | 5.9 |
| mgsBa5 13 | 0.5 | 22.91 | 2.19 | 1.67 | 2.31 | 1.97 | 1.02 | 62 | 7.75 | 146 | 0.04 | 1.51 | 10.0 | 7.4 |
| mgsBa5 14 | 0.5 | 22.87 | 2.23 | 1.71 | 2.30 | 1.93 | 1.03 | 64 | 7.76 | 149 | 0.04 | 1.63 | 9.7 | 7.7 |
| mgsBa6 1 | 0.5 | 22.80 | 2.20 | 0.01 | 2.32 | 0.04 | 1.00 | 64 | 7.65 | 117 | 0.00 | 0.01 | 13.1 | 0.0 |
| mgsBa6 2 | 0.5 | 22.80 | 2.20 | 0.02 | 2.24 | 0.03 | 1.08 | 71 | 7.71 | 130 | 0.00 | 0.02 | 10.7 | 0.1 |
| mgsBa6 3 | 0.5 | 22.80 | 2.20 | 0.02 | 2.28 | 0.03 | 1.05 | 68 | 7.67 | 120 | 0.00 | 0.01 | 12.2 | 0.1 |
| mgsBa6 4 | 0.5 | 22.50 | 2.50 | 0.02 | 2.31 | 0.03 | 1.02 | 67 | 7.79 | 158 | 0.00 | 0.02 | 9.2 | 0.1 |
| mgsBa6 5 | 1.0 | 23.30 | 1.70 | 0.03 | 2.51 | 0.02 | 0.81 | 112 | 7.72 | 149 | 0.00 | 0.03 | 11.6 | 0.1 |
| mgsBa6 6 | 1.0 | 23.30 | 1.70 | 0.03 | 2.49 | 0.02 | 0.83 | 115 | 7.73 | 152 | 0.00 | 0.03 | 11.2 | 0.1 |
| mgsBa6 7 | 1.0 | 23.30 | 1.70 | 0.03 | 2.49 | 0.02 | 0.84 | 116 | 7.70 | 144 | 0.00 | 0.03 | 11.9 | 0.1 |
| mgsBa6 8 | 1.0 | 23.30 | 1.70 | 0.03 | 2.49 | 0.02 | 0.84 | 116 | 7.70 | 144 | 0.00 | 0.03 | 11.9 | 0.1 |
| mgsBa6 9 | 2.0 | 23.68 | 1.32 | 0.00 | 2.77 | 0.04 | 0.55 | 155 | 7.75 | 179 | 0.00 | 0.00 | 11.5 | 0.0 |
| mgsBa6 10 | 2.0 | 23.66 | 1.34 | 0.00 | 2.75 | 0.04 | 0.57 | 159 | 7.76 | 180 | 0.00 | 0.00 | 11.2 | 0.0 |
| mgsBa6 11 | 2.0 | 23.66 | 1.34 | 0.00 | 2.73 | 0.04 | 0.59 | 165 | 7.74 | 170 | 0.00 | 0.00 | 11.8 | 0.0 |
| mgsBa6 12 | 2.0 | 23.66 | 1.34 | 0.00 | 2.76 | 0.04 | 0.56 | 157 | 7.76 | 183 | 0.00 | 0.00 | 11.1 | 0.0 |

## 4.2    The effect of aqueous Mg on witherite growth

Studies on witherite growth in the presence or absence of additives in the growth solution are scarce. However, as the first synthetic norsethite crystals were grown by reacting witherite in Mg-bearing solutions (Lippmann, 1966), knowledge about the kinetics of this reaction is essential for a detailed understanding on norsethite growth. Aim of this work, therefore, was to set a baseline for additive-free witherite growth and evaluate the influence of aqueous magnesium on subsequent witherite growth and norsethite formation.

### 4.2.1   Detailed materials and methods

Growth experiments were performed in PTFE mixed-flow reactors as described in chapter 3.1.2 at $50 \pm 1$ °C. The starting conditions of the experiments are listed in Table 4.2-1.

   Natural witherite crystals (Settlingstones Mine, England) were used as seeds for all experiments. The crystals were crushed in an agate mortar and passed through stainless steel sieves. The size fraction $63-200$ µm was used in all experiments. The crystals were washed several times with deionized water and ethanol in an ultrasonic bath to remove particles and dried for several hours at 60 °C in an oven. The resulting powder consisted of crystal fragments without any identifiable crystal faces (Figure 4.2-1A). As determined from SEM images, the average crystal diameter was 70 µm. Employing a cubic shape model, a specific surface area of 0.02 m²/g was calculated.

### 4.2.2   Results

*4.2.2.1 Analyses of retrieved crystals*

XRD patterns (Figure 4.2-2) of product crystals retrieved from experiments with solutions with Mg:Ba concentration ratios ≤6:1 showed no other phase than witherite. The diffraction pattern of the crystals of the experiment with a Mg:Ba solution concentration ratio >12:1, however, revealed a mixture of witherite and norsethite. Rietveld refinement of the diffractogram yielded 90 wt.% norsethite and 10 wt.% witherite. Within the reactor, crystallization of different phases may have taken place to a different extent at different locations. Because the product crystals could not be retrieved from the reactor completely, XRD samples may not be entirely representative for the mineral assemblage inside the reactor. The composition determined by XRD, therefore, should be considered as a rough estimate.
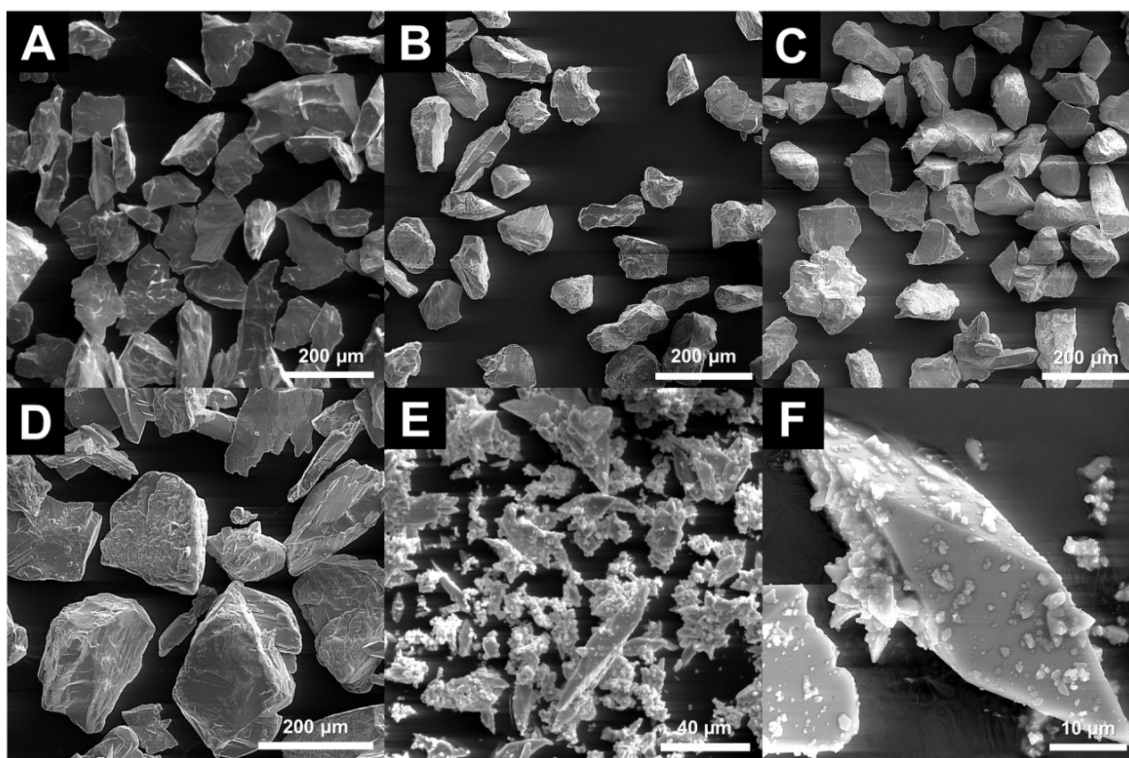
Figure 4.2-1: SEM images of crystals before (A) and after experiments without Mg (B), Mg:Ba ≤ 1:1 (C), and Mg:Ba ≤ 6:1 (D) show no difference to the used seed crystals. Mg:Ba > 12:1 (E & F) lead to dissolution of witherite and formation of many small norsethite needles.
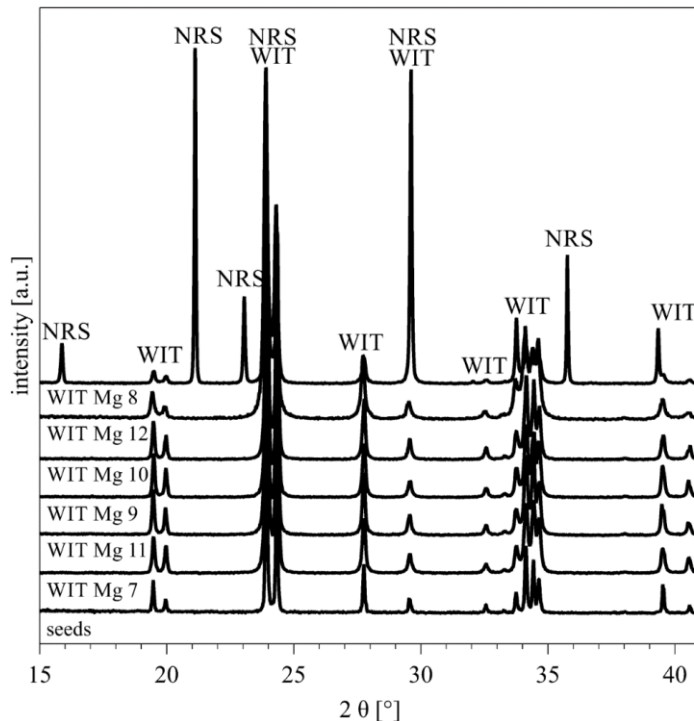


Figure 4.2-2: X-ray diffractograms of seeds and retrieved crystals. All experiments with Mg:Ba ≤ 6:1 yielded only witherite (WIT), except for experiment WITMg 8 (Mg:Ba > 12:1, top), which is mostly norsethite (NRS). Rietveld refinement yields a mixture of 90 wt.% norsethite and 10 wt.% witherite.

Table 4.2-1: Starting conditions of the mixed-flow reactor experiments as well as masses of recovered crystals. Inlet solutions from containers 1 and 2 were pumped into the reactor with a ratio of 1:1. Resulting reactor Mg:Ba ratios and supersaturations Ω for norsethite and witherite are also given.

| | Container 1 | | | | Container 2 | | | | | | | | |
| Experiment | Ba [mM] | Mg [mM] | NaCl [mM] | $pH_{RT}$ | $NaHCO_3$ [mM] | NaCl [mM] | $pH_{RT}$ | Mg:Ba | Ω witherite | Ω norsethite | crystals start [g] | crystals end [g] | Δ crystal mass [g] |
|---|---|---|---|---|---|---|---|---|---|---|---|---|---|
| WIT 6 | 3 | - | 97 | 5.64 | 10 | 90 | 8.35 | - | 4.0 | - | 1.225 | 2.218 | 0.993 |
| WIT 7 | 0.5 | - | 97 | 5.47 | 25 | 80 | 8.30 | - | 1.9 | - | 1.005 | 1.539 | 0.534 |
| WIT 8 | 2 | - | 95 | 5.55 | 20 | 90 | 8.46 | - | 5.8 | - | 1.505 | 4.13 | 2.625 |
| WIT 11 | 2 | - | 95 | 5.60 | 20 | 90 | 8.30 | - | 5.8 | - | 1.497 | 2.402 | 0.905 |
| WIT 12 | 2 | - | 90 | 5.69 | 10[a] | 90 | 8.61 | - | 6.2 | - | 1.007 | 1.382 | 0.372 |
| WITMg 7 | 0.5 | 0.05 | 97 | 5.52 | 25 | 80 | 8.28 | 0.1 | 1.9 | 0.9 | 1.005 | 1.532 | 0.527 |
| WITMg 8 | 4 | 40 | 10 | 5.88 | 20 | 60 | 8.40 | 10 | 5.0 | 631.0 | 1.293 | 0.765 | -0.528 |
| WITMg 9 | 2 | 2 | 95 | 5.61 | 20 | 90 | 8.31 | 1 | 5.2 | 67.6 | 1.500 | 3.659 | 2.159 |
| WITMg 10 | 4 | 4 | 78 | 5.55 | 11 | 90 | 8.21 | 1 | 5.1 | 67.6 | 1.501 | 2.105 | 0.604 |
| WITMg 11 | 2 | 0.2 | 95 | 5.59 | 20 | 90 | 8.28 | 0.1 | 5.6 | 7.9 | 1.498 | 2.081 | 0.583 |
| WITMg 12 | 2 | 6 | 90 | 5.63 | 10[a] | 90 | 8.60 | 3 | 4.3 | 138.0 | 1.015 | 1.285 | 0.270 |

[a] additionally 0.25 mM $Na_2CO_3$ was added to the solution.

Table 4.2-2: Mean values of steady state conditions of the mixed-flow reactor experiments.

| Sample | flowrate [ml/min] | pH [50°C] | total alkalinity [meq/l] | $Ba^{2+}$ [mM] | $Mg^{2+}$ [mM] | Mg:Ba | Δ total alkalinity [meq/l] | $\Delta Ba^{2+}$ [mM] | $\Delta Mg^{2+}$ [mM] | $Rate_{WIT}$ $[10^{-7}$ mol m$^{-2}$ s$^{-1}]$ | Ω witherite |
|---|---|---|---|---|---|---|---|---|---|---|---|
| WIT 6 6-8 | 0.2 | 7.79 | 4.16 | 1.07 | - | - | 0.79 | 0.42 | - | 0.48 ± 0.05 | 1.9 ± 0.2 |
| WIT 6 11-13 | 0.5 | 7.69 | 4.32 | 1.16 | - | - | 0.63 | 0.34 | - | 0.69 ± 0.07 | 1.7 ± 0.2 |
| WIT 6 18-20 | 0.1 | 7.79 | 3.79 | 0.90 | - | - | 1.19 | 0.59 | - | 0.27 ± 0.03 | 1.5 ± 0.1 |
| WIT 6 25-26 | 0.9 | 7.76 | 4.37 | 1.19 | - | - | 0.58 | 0.31 | - | 1.1 ± 0.1 | 2.1 ± 0.2 |
| WIT 7 8-16 | 0.2 | 8.53 | 11.92 | 0.06 | - | - | 0.28 | 0.24 | - | 0.18 ± 0.02 | 1.5 ± 0.1 |
| WIT 7 18-27 | 0.4 | 8.38 | 11.80 | 0.08 | - | - | 0.41 | 0.21 | - | 0.31 ± 0.03 | 1.6 ± 0.2 |
| WIT 7 31-40 | 0.8 | 8.27 | 11.94 | 0.13 | - | - | 0.12 | 0.13 | - | 0.36 ± 0.04 | 1.9 ± 0.2 |
| WIT 8 1-8 | 0.1 | 8.05 | 8.35 | 0.26 | - | - | 1.60 | 0.73 | - | 0.31 ± 0.03 | 1.6 ± 0.2 |
| WIT 8 9-15 | 0.5 | 8.02 | 8.79 | 0.38 | - | - | 1.16 | 0.60 | - | 1.0 ± 0.1 | 2.3 ± 0.2 |
| WIT 8 16-21 | 1.0 | 7.93 | 8.88 | 0.46 | - | - | 1.07 | 0.52 | - | 1.4 ± 0.1 | 2.4 ± 0.2 |
| WIT 8 22-24 | 1.3 | 8.02 | 8.89 | 0.49 | - | - | 1.07 | 0.49 | - | 1.7 ± 0.2 | 3.1 ± 0.3 |
| WIT 8 25-28 | 1.6 | 7.98 | 8.89 | 0.51 | - | - | 1.06 | 0.47 | - | 2 ± 0.2 | 2.9 ± 0.3 |
| WIT 8 29-36 | 1.9 | 8.07 | 8.84 | 0.52 | - | -- | 1.11 | 0.47 | - | 2.2 ± 0.2 | 3.6 ± 0.4 |
| WIT 8 37-40 | 1.7 | 8.04 | 8.50 | 0.54 | - | - | 1.45 | 0.44 | - | 1.7 ± 0.2 | 3.4 ± 0.3 |

| Sample | flowrate [ml/min] | pH [50°C] | total alkalinity [meq/l] | Ba²⁺ [mM] | Mg²⁺ [mM] | Mg:Ba | Δ total alkalinity [meq/l] | Δ Ba²⁺ [mM] | Δ Mg²⁺ [mM] | Rate$_{WIT}$ [10⁻⁷ mol m⁻² s⁻¹] | Ω witherite |
|---|---|---|---|---|---|---|---|---|---|---|---|
| WIT 11 2-5 | 0.1 | 8.01 | 8.26 | 0.27 | - | - | 1.66 | 0.78 | - | 0.5 ± 0.05 | 1.5 ± 0.2 |
| WIT 11 6-8 | 0.2 | 8.00 | 8.72 | 0.29 | - | - | 1.20 | 0.75 | - | 0.73 ± 0.07 | 1.7 ± 0.2 |
| WIT 11 9-12 | 0.5 | 8.05 | 8.67 | 0.42 | - | - | 1.25 | 0.62 | - | 1.4 ± 0.1 | 2.8 ± 0.3 |
| WIT 11 13-16 | 0.7 | 8.06 | 8.74 | 0.46 | - | - | 1.18 | 0.58 | - | 1.8 ± 0.2 | 3.1 ± 0.3 |
| WIT 11 17-21 | 1.0 | 8.08 | 8.81 | 0.47 | - | - | 1.11 | 0.58 | - | 2.5 ± 0.3 | 3.3 ± 0.3 |
| WIT 12 1-5 | 0.2 | 7.99 | 4.50 | 0.65 | - | - | 0.78 | 0.37 | - | 0.49 ± 0.05 | 2.0 ± 0.2 |
| WIT 12 6-10 | 0.5 | 8.04 | 4.75 | 0.72 | - | - | 0.54 | 0.30 | - | 1.1 ± 0.1 | 2.6 ± 0.3 |
| WIT 12 11-15 | 1.0 | 8.14 | 4.84 | 0.74 | - | - | 0.44 | 0.27 | - | 2 ± 0.2 | 3.4 ± 0.3 |
| WIT 12 16-19 | 0.6 | 8.10 | 4.74 | 0.72 | - | - | 0.54 | 0.30 | - | 1.4 ± 0.1 | 2.9 ± 0.3 |
| WITMg 7 1-10 | 0.2 | 8.59 | 11.64 | 0.04 | 0.03 | 0.8 | 0.64 | 0.25 | 0.00 | 0.21 ± 0.02 | 1.2 ± 0.1 |
| WITMg 7 11-16 | 0.1 | 8.62 | 11.78 | 0.05 | 0.03 | 0.7 | 0.50 | 0.25 | 0.00 | 0.2 ± 0.02 | 1.3 ± 0.1 |
| WITMg 7 18-29 | 0.4 | 8.49 | 11.72 | 0.07 | 0.03 | 0.5 | 0.54 | 0.21 | 0.00 | 0.37 ± 0.04 | 1.6 ± 0.2 |
| WITMg 7 31-40 | 0.7 | 8.46 | 11.76 | 0.10 | 0.03 | 0.2 | 0.27 | 0.14 | 0.00 | 0.5 ± 0.05 | 2.2 ± 0.2 |
| WITMg 8 10-19 | 0.4 | 7.03 | 7.17 | 1.39 | 17.20 | 12.3 | 2.78 | 0.64 | 2.95 | - | 0.7 ± 0.1 |
| WITMg 8 22-25 | 0.6 | 7.03 | 7.48 | 1.45 | 19.42 | 13.4 | 2.47 | 0.58 | 0.72 | - | 0.7 ± 0.1 |
| WITMg 8 29-32 | 1.1 | 7.06 | 7.70 | 1.57 | 19.46 | 12.4 | 2.24 | 0.47 | 0.69 | - | 0.8 ± 0.1 |
| WITMg 9 1-8 | 0.1 | 7.98 | 8.68 | 0.17 | 0.99 | 5.9 | 1.52 | 0.81 | 0.01 | 0.42 ± 0.04 | 1.3 ± 0.1 |
| WITMg 9 9-13 | 0.6 | 8.01 | 8.87 | 0.34 | 1.03 | 3.0 | 1.33 | 0.64 | -0.03 | 1.1 ± 0.1 | 3.0 ± 0.3 |
| WITMg 9 14-18 | 1.1 | 7.97 | 8.92 | 0.38 | 0.97 | 2.6 | 1.28 | 0.60 | 0.03 | 1.9 ± 0.2 | 3.0 ± 0.3 |
| WITMg 9 19-22 | 0.4 | 8.06 | 8.79 | 0.25 | 0.98 | 3.9 | 1.41 | 0.72 | 0.02 | 0.74 ± 0.07 | 2.4 ± 0.2 |
| WITMg 9 23-26 | 1.4 | 8.03 | 8.90 | 0.38 | 0.99 | 2.6 | 1.30 | 0.60 | 0.02 | 2.3 ± 0.2 | 3.5 ± 0.3 |
| WITMg 9 27-30 | 0.1 | 8.05 | 8.45 | 0.16 | 0.97 | 6.1 | 1.75 | 0.82 | 0.03 | 0.27 ± 0.03 | 1.5 ± 0.1 |
| WITMg 10 1-5 | 1.0 | 7.81 | 4.72 | 1.70 | 2.12 | 1.2 | 0.68 | 0.36 | 0.00 | 2 ± 0.2 | 3.4 ± 0.3 |
| WITMg 10 6-10 | 1.9 | 7.83 | 4.79 | 1.75 | 2.03 | 1.2 | 0.61 | 0.31 | 0.09 | 3.2 ± 0.3 | 3.8 ± 0.4 |
| WITMg 10 11-15 | 1.4 | 7.83 | 4.77 | 1.73 | 2.10 | 1.2 | 0.63 | 0.33 | 0.02 | 2.4 ± 0.2 | 3.7 ± 0.4 |
| WITMg 10 16-18 | 0.2 | 7.83 | 3.89 | 1.21 | 2.14 | 1.8 | 1.51 | 0.85 | -0.02 | 0.85 ± 0.09 | 2.1 ± 0.2 |
| WITMg 11 1-5 | 0.1 | 7.93 | 7.42 | 0.29 | 0.09 | 0.3 | 2.38 | 0.78 | 0.01 | 0.48 ± 0.05 | 1.8 ± 0.2 |
| WITMg 11 6-8 | 0.2 | 7.90 | 8.43 | 0.34 | 0.13 | 0.4 | 1.37 | 0.73 | -0.03 | 0.76 ± 0.08 | 2.3 ± 0.2 |
| WITMg 11 9-12 | 0.5 | 7.90 | 8.61 | 0.45 | 0.13 | 0.3 | 1.19 | 0.62 | -0.03 | 1.3 ± 0.1 | 3.0 ± 0.3 |
| WITMg 11 13-16 | 0.7 | 7.89 | 8.74 | 0.49 | 0.14 | 0.3 | 1.06 | 0.58 | -0.04 | 1.6 ± 0.2 | 3.3 ± 0.3 |
| WITMg 11 17-21 | 1.0 | 7.90 | 8.80 | 0.50 | 0.15 | 0.3 | 1.00 | 0.56 | -0.05 | 2.2 ± 0.2 | 3.5 ± 0.3 |
| WITMg 12 1-5 | 0.2 | 7.90 | 4.47 | 0.67 | 2.83 | 4.2 | 0.85 | 0.33 | 0.15 | 0.40 ± 0.05 | 1.5 ± 0.2 |
| WITMg 12 6-10 | 0.5 | 7.89 | 4.76 | 0.78 | 2.93 | 3.7 | 0.56 | 0.21 | 0.05 | 0.71 ± 0.08 | 1.9 ± 0.2 |
| WITMg 12 11-15 | 0.9 | 7.93 | 4.80 | 0.82 | 2.94 | 3.6 | 0.52 | 0.17 | 0.04 | 1.1 ± 0.1 | 2.2 ± 0.2 |
| WITMg 12 16-19 | 0.6 | 7.93 | 4.74 | 0.80 | 2.90 | 3.6 | 0.58 | 0.20 | 0.08 | 0.79 ± 0.08 | 2.1 ± 0.2 |

SEM images of the retrieved crystals of experimental runs with Mg:Ba ≤ 6:1 revealed no significant change of morphology in comparison to the seed crystals. The product consisted of grown witherite seeds (Figure 4.2-1 B-D). However, crystals from the experiment with Mg:Ba > 12:1 mainly consisted of columns with lengths up to 70 μm, showing the same morphology as synthetic norsethite (e.g., Lippmann, 1973). These crystals were partially covered by smaller crystallites with sizes of 0.2 to 2 μm, which can also be identified as norsethite (Figure 4.2-1 E & F). Only a small amount of the witherite seed material was recognizable, matching the large norsethite/witherite ratio determined by Rietveld analysis. Growth of the norsethite crystals on the witherite surfaces revealed no crystallographically preferred orientation. It should be noted that a decrease of seed crystal mass was detected only in the experiment where norsethite was found in the reactor (Table 4.2-1). In other experimental runs, the mass of witherite increased.

### 4.2.2.2 Analyses of solutions

Solute concentrations of the effluent were measured in frequent intervals (Table A 4.2-1). From the individual samples, mean concentrations were calculated for each steady state condition (Table 4.2-2). A significant decrease of input solution Mg besides total alkalinity and barium by the growth within the reactor was only detected in the experiment for which the X-ray diffractograms and SEM images revealed the formation of norsethite. The analyses of all other experiments revealed a decrease of total alkalinities and barium but not of Mg in solution. From the latter experiments, witherite growth rates were calculated according to equation 3.1-1 based on the analyzed Ba decrease ($\Delta M = \Delta Ba$).

Witherite growth rates vs. solution supersaturation with respect to witherite showed no dependence on aqueous magnesium concentrations at Mg:Ba ≤ 6:1 (Figure 4.2-3). However, even at low supersaturations ($1 < \Omega < 3$), heterogeneous nucleation of witherite at the reactor walls, on the membranes and in the effluent tubing was evident. The precipitates led to an increased reactive surface area. In the calculation of the growth rates, the increase of the surface area has been taken into account by linearly increasing the mass of the crystals within the reactor with time while the specific surface area was kept constant. The total increase of mass was calculated on basis of the accumulated decrease of solutes from the inflow. Irrespective of the correction applied to the rate calculations, SEM images of retrieved crystals showed clearly that growth of the seed crystals rather than the newly nucleated crystals was the main cause of mass increase.

In the experimental run with Mg:Ba ratio > 12:1, witherite seed crystals dissolved and norsethite precipitated. The reactor solution of this experiment was obviously undersaturated with respect to witherite and supersaturated versus norsethite, as confirmed by PHREEQC calculations from the analyzed effluent concentrations.
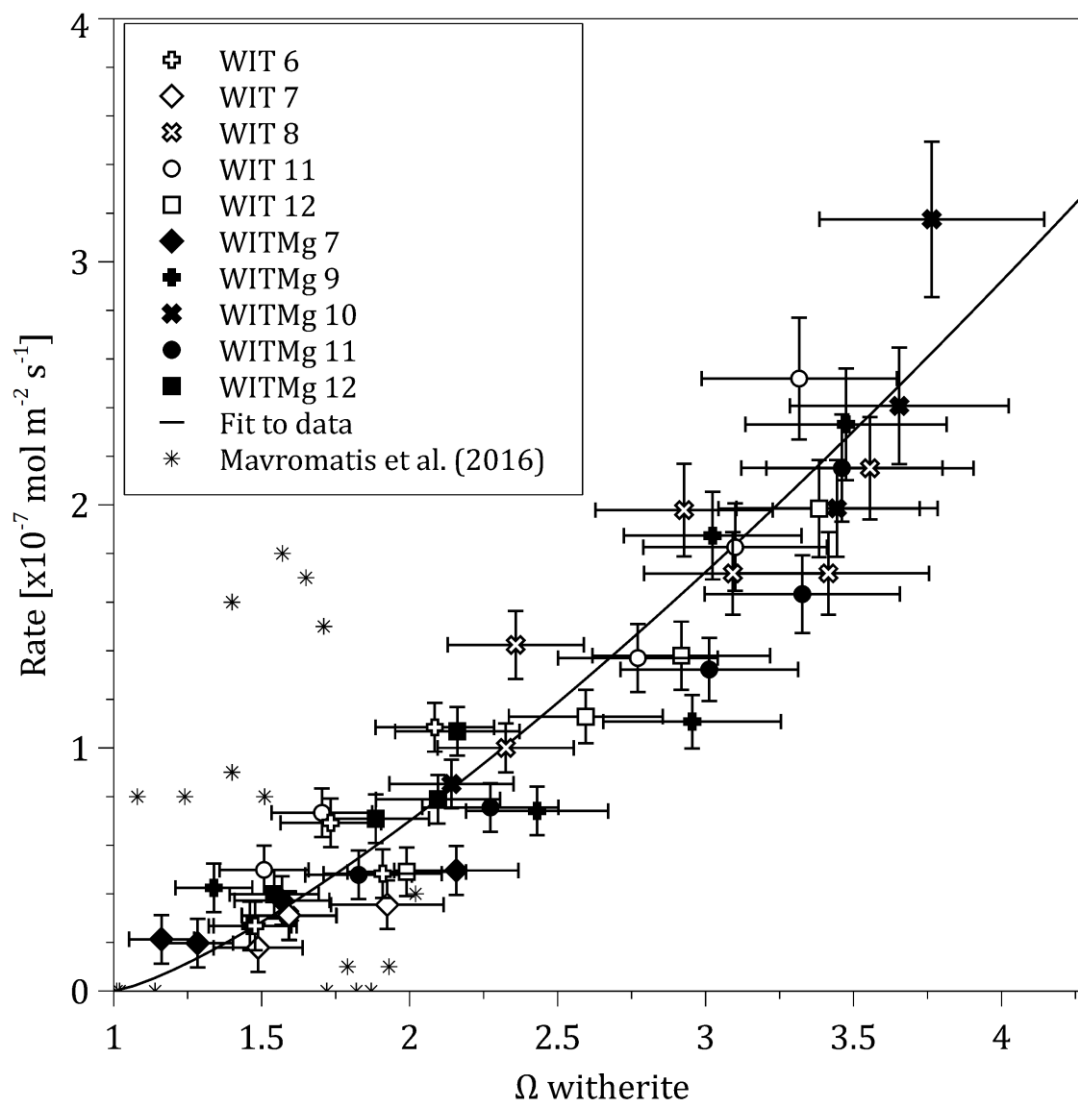
Figure 4.2-3: Witherite growth rate vs. supersaturation Ω with respect to witherite. Black symbols stand for Mg-containing samples with Mg:Ba ≤ 6:1, white symbols for Mg-free samples. There is no effect of Mg on the growth rates detectable. Data for norsethite precipitating experiment is not shown. Asterisks refer to values of Mavromatis et al. (2016). The line refers to a fit with the equation $R=k(\Omega-1)^n$ with $k = 0.65 \times 10^{-7}$ $mol\,m^{-2}\,s^{-1}$ and $n = 1.3$

## 4.2.3  Discussion

### 4.2.3.1 The growth rate of witherite

The conducted growth experiments represent the first systematic quantitative study of witherite growth kinetics covering a significant span of different solution supersaturations and additive concentrations. The results confirm the rough order of magnitude of growth rates of Mavromatis et al. (2016) obtained from Mg-free solutions (Figure 4.2-3). Due to the different temperature, though, one might expect that the data of Mavromatis et al. (2016) lie below the data obtained here

throughout the entire range of conditions. Differences in solution speciation (e.g., $Ba^{2+}/CO_3^{2-}$ ratio), experimental methodology (e.g., determination of specific surface area), and seed crystals may be accountable for these deviations. Measured growth rates $R$ were fitted by the empirical equation

$$R = k(\Omega - 1)^n, \qquad (4.2\text{-}1)$$

which is commonly used to calculate the rate constant $k$ and the order $n$ the growth reaction of experimental carbonate precipitation data (e.g., Arvidson and Mackenzie, 1999; Berninger et al., 2016; Busenberg and Plummer, 1986a; Gautier et al., 2015; Mucci and Morse, 1983; Nancollas and Reddy, 1971; Saldi et al., 2009). Our experiments yielded a rate constant $k$ of $0.65 \pm 0.05 \times 10^{-7}$ mol m$^{-2}$ s$^{-1}$ and a reaction order $n$ of $1.3 \pm 0.1$. A Mg:Ba ratio in solution of up to 6:1 had no discernible influence on measured witherite growth rates (Figure 4.2-3).

### 4.2.3.2 The insignificance of incorporation of Mg into witherite

Based on the balance of the inflowing and outflowing solutions there was no reduction of Mg detectable within analytical limits (mean $\Delta Mg = 0.02 \pm 0.05$ mM), which implies that there is no incorporation of Mg into the growing witherite. This finding is in accordance with analyses of natural witherites (Pi et al., 2014), which showed Mg-concentrations of up to $\approx 0.12$ wt.%. Moreover, these low magnesium values may not even originate from incorporation into the witherite lattice exclusively but from a different accessory phase as well. The large difference in ionic radii of Ba and Mg (as illustrated by the fact that $MgCO_3$ precipitates in calcite structure and $BaCO_3$ in aragonite structure) renders the incorporation of magnesium on Ba-sites unfavorable

It is worth to compare the incorporation of Mg into witherite with the incorporation into aragonite. Based on linear free energy correlation, Wang and Xu (2001) predicted a partitioning of Mg between aragonite and solution at ambient conditions $\log k_{d\,Mg\,Ara} = \left(\frac{X_{Mg}}{X_{Ca}}\right) / \left(\frac{m_{Mg}}{m_{Ca}}\right) = -2.06$ ($X_i$: mole fraction of $Ca^{2+}$ and $Mg^{2+}$ in the precipitated aragonite, $m_i$: concentration of $Ca^{2+}$ and $Mg^{2+}$ in aqueous solution). Dietzel et al. (2004) suggested that experimentally measured Mg incorporation during aragonite growth might likely be caused by complex adsorption and entrapment rather than by lattice site substitution. Ab-initio calculations suggested that Mg incorporation into aragonite is energetically reasonable, although the investigated range of substituent concentration (13–100 % Mg) is not observed in natural aragonites (Menadakis et al., 2009).

As the ionic radius of barium is much larger than that of calcium (1.35 Å vs. 1.00 Å) and the lattice mismatch, therefore, is much higher, the partition coefficient of Mg for witherite can be expected to be even lower than for aragonite. For trace elements with partition coefficients $k_d < 1$, the coefficients measured during crystal growth are likely higher than the equilibrium values (Rimstidt et al., 1998).

Therefore, the lack of measurable incorporation of Mg into the growing witherite points to an extremely small equilibrium partition coefficient $k_{d\,Mg\,Wit} \ll 10^{-2}$. This result is in accordance with the findings in the inverse system, i.e., the very low incorporation of Ba into magnesite during growth (Lindner et al., 2017). This agreement supports the idea of a general absence of solid solution formation in the entire $BaCO_3$-$MgCO_3$ system.

### 4.2.3.3 The formation of norsethite

A Mg:Ba ratio >12:1 in the growth solution led to witherite dissolution and norsethite precipitation (experiment WITMg 8). The ratio of barium and magnesium decreases in the solutions was in the range of $\Delta Ba$:$\Delta Mg \approx 1$:2 and did not correspond to the stoichiometry of $BaMg(CO_3)_2$. However, ($\Delta Ba$+$\Delta Mg$):$\Delta$alkalinity was about 1:2 in all samples, which implies a growth reaction according,

$$(Ba^{2+}, Mg^{2+})_2 + 4\,HCO_3^- \leftrightarrow (Ba, Mg)_2(CO_3)_2 + 2CO_2 + 2H_2O$$

This equation is in good agreement for stoichiometric norsethite growth, if dissolution of witherite in the reactor provided the deficient amounts of Ba and $CO_3^{2-}$. Mass balance calculations of Ba and Mg decreases show that 4.2 mmoles Ba and 7 mmoles Mg were precipitated from the solution over the total experimental runtime of 10 days. The missing 2.8 mmoles Ba to form stoichiometric $BaMg(CO_3)_2$, therefore, may be assigned to dissolution of 0.55 g witherite seeds, yielding a composition of 17 % witherite and 83 % norsethite in the final product of the reactor. This result is supported by XRD and SEM analysis of the retrieved crystals, which showed norsethite to be the major component ($\sim$90 mass %). The assumption is further backed by the geochemical calculations of the solution speciation, which showed that the solutions were undersaturated with respect to witherite and strongly supersaturated with respect to norsethite.

Assuming that no Mg-bearing phase other than norsethite has been crystallizing (as evident from XRD and SEM), the Mg precipitation rate is equal to the norsethite growth rate. Norsethite growth rates, therefore, were calculated according to Eqn. 3.1-1 with $\Delta M = \Delta Mg^{2+}$ (Table 4.2-3-3). The final surface area of norsethite was estimated from SEM images of the product powder employing a rectangular shape model with an average crystal size of 25 x 7 x 7 µm. The resulting specific surface area was $0.17 \pm 0.07$ m$^2$/g. Furthermore, it has been assumed that norsethite surface area and mass increased linearly over experimental time starting from zero. Solution saturation states were calculated using the solubility product of norsethite at 50 °C ($\log K_{s\,nrs}{}^{50\,°C} = -17.57$), which has been obtained by linear interpolation of the $\log K_s$ vs. 1/T line given by the room temperature value from Königsberger et al. (1998) and the 100 °C value estimated by Lindner et al. (2017).

The plot of growth rates against supersaturation reveals a positive correlation (Figure 4.2-4). The fit of the data with Eqn. (4.2-1) yields a rate constant

Table 4.2-3: Effluent results of experiment WITMg 8, which precipitated norsethite. Cumulative amounts of precipitated barium and magnesium over the run of the experiment based on mass balance calculations of the wet chemical analyses are given. Norsethite growth rates (Rate$_{NRS}$) have been calculated using the decrease in solution Mg and a surface area estimated from SEM images of retrieved crystals.

| Sample | Flowrate [ml/min] | pH [50 °C] | Mg:Ba | Δ Ba [mM] | Δ Mg [mM] | Δ alkalinity [meq/L] | Ω witherite | Ω norsethite | cum. Ba precip. [mmol] | cum. Mg precip. [mmol] | Rate$_{NRS}$ [10$^{-7}$ mol m$^{-2}$ s$^{-1}$] |
|---|---|---|---|---|---|---|---|---|---|---|---|
| WITMg 8-1 | 0.4 | 8.18 | 23.5 | 1.30 | 3.03 | 2.68 | 1.3 | 96.8 | 0.56 | 1.30 | 18 ± 5 |
| WITMg 8-2 | 0.5 | 8.18 | 22.0 | 1.21 | 2.03 | 2.48 | 1.1 | 69.5 | 0.63 | 1.42 | 12 ± 3 |
| WITMg 8-3 | 0.4 | 8.19 | 21.9 | 1.21 | 2.04 | 2.39 | 1.2 | 74.4 | 0.67 | 1.50 | 10 ± 3 |
| WITMg 8-5 | 0.4 | 8.06 | 24.8 | 1.24 | 0.54 | 2.44 | 0.6 | 24.8 | 0.78 | 1.54 | 1.2 ± 0.3 |
| WITMg 8-6 | 0.4 | 8.06 | 22.3 | 1.14 | 0.31 | 2.44 | 0.7 | 25.5 | 0.90 | 1.57 | 0.7 ± 0.2 |
| WITMg 8-7 | 0.4 | 8.02 | 17.5 | 0.91 | 0.50 | 2.62 | 0.7 | 24.4 | 1.28 | 1.79 | 0.8 ± 0.2 |
| WITMg 8-8 | 0.4 | 8.03 | 16.9 | 0.88 | 0.76 | 2.69 | 0.7 | 23.3 | 1.36 | 1.85 | 1.1 ± 0.3 |
| WITMg 8-9 | 0.4 | 8.05 | 14.9 | 0.75 | 1.01 | 2.78 | 0.8 | 24.2 | 1.42 | 1.93 | 1.4 ± 0.4 |
| WITMg 8-10 | 0.4 | 7.97 | 13.5 | 0.61 | 1.04 | 3.00 | 0.7 | 15.9 | 2.42 | 3.64 | 0.7 ± 0.2 |
| WITMg 8-11 | 0.4 | 8.00 | 13.2 | 0.59 | 1.07 | 2.96 | 0.7 | 16.3 | 2.46 | 3.70 | 0.7 ± 0.2 |
| WITMg 8-12 | 0.4 | 7.95 | 13.5 | 0.62 | 1.18 | 2.96 | 0.7 | 15.2 | 2.52 | 3.81 | 0.8 ± 0.2 |
| WITMg 8-13 | 0.4 | 8.00 | 13.8 | 0.63 | 0.77 | 2.97 | 0.7 | 16.0 | 2.79 | 4.14 | 0.5 ± 0.1 |
| WITMg 8-14 | 0.4 | 8.12 | 11.6 | 0.40 | 1.15 | 2.49 | 0.8 | 19.9 | 2.80 | 4.18 | 0.6 ± 0.2 |
| WITMg 8-15 | 0.4 | 8.09 | 12.3 | 0.46 | 0.77 | 2.48 | 0.8 | 17.7 | 2.82 | 4.21 | 0.4 ± 0.1 |
| WITMg 8-17 | 0.4 | 8.05 | 11.3 | 0.35 | 1.15 | 2.83 | 0.7 | 15.6 | 2.98 | 4.74 | 0.6 ± 0.2 |
| WITMg 8-18 | 0.4 | 8.06 | 11.5 | 0.36 | 1.01 | 2.69 | 0.7 | 16.1 | 2.99 | 4.78 | 0.5 ± 0.1 |
| WITMg 8-19 | 0.5 | 8.05 | 11.2 | 0.34 | 1.17 | 2.80 | 0.7 | 15.1 | 3.01 | 4.84 | 0.7 ± 0.2 |
| WITMg 8-20 | 0.7 | 7.90 | 11.2 | 0.34 | 1.14 | 2.55 | 0.8 | 17.7 | 3.05 | 4.99 | 0.9 ± 0.2 |
| WITMg 8-21 | 0.6 | 7.90 | 12.1 | 0.46 | 1.19 | 2.46 | 0.8 | 19.2 | 3.35 | 5.77 | 0.9 ± 0.2 |
| WITMg 8-22 | 0.6 | 7.90 | 17.0 | 0.86 | 0.29 | 2.54 | 0.6 | 13.8 | 3.39 | 5.78 | 0.2 ± 0.1 |
| WITMg 8-23 | 0.7 | 7.90 | 12.6 | 0.50 | 0.93 | 2.54 | 0.7 | 17.7 | 3.44 | 5.87 | 0.7 ± 0.2 |
| WITMg 8-24 | 0.7 | 7.90 | 12.2 | 0.46 | 0.89 | 2.48 | 0.8 | 18.5 | 3.47 | 5.93 | 0.6 ± 0.2 |
| WITMg 8-25 | 0.6 | 7.91 | 12.6 | 0.49 | 0.79 | 2.31 | 0.8 | 18.9 | 3.50 | 5.97 | 0.6 ± 0.1 |
| WITMg 8-26 | 1.1 | 7.80 | 12.0 | 0.43 | 0.88 | 2.32 | 0.8 | 21.5 | 3.53 | 6.04 | 1.1 ± 0.3 |
| WITMg 8-27 | 1.1 | 7.75 | 12.6 | 0.49 | 0.70 | 2.29 | 0.8 | 21.0 | 4.04 | 6.77 | 0.8 ± 0.2 |
| WITMg 8-28 | 1.1 | 7.75 | 12.8 | 0.50 | 0.60 | 2.29 | 0.8 | 19.9 | 4.08 | 6.83 | 0.7 ± 0.2 |
| WITMg 8-29 | 1.1 | 7.75 | 12.2 | 0.45 | 0.76 | 2.24 | 0.9 | 22.8 | 4.14 | 6.92 | 0.9 ± 0.2 |
| WITMg 8-30 | 1.1 | 7.74 | 12.3 | 0.46 | 0.76 | 2.22 | 0.9 | 22.7 | 4.17 | 6.97 | 0.8 ± 0.2 |
| WITMg 8-31 | 1.1 | 7.76 | 12.8 | 0.50 | 0.47 | 2.26 | 0.8 | 21.1 | 4.20 | 7.00 | 0.5 ± 0.1 |
| WITMg 8-32 | 1.1 | 7.74 | 12.3 | 0.46 | 0.75 | 2.26 | 0.8 | 21.4 | 4.23 | 7.04 | 0.8 ± 0.2 |
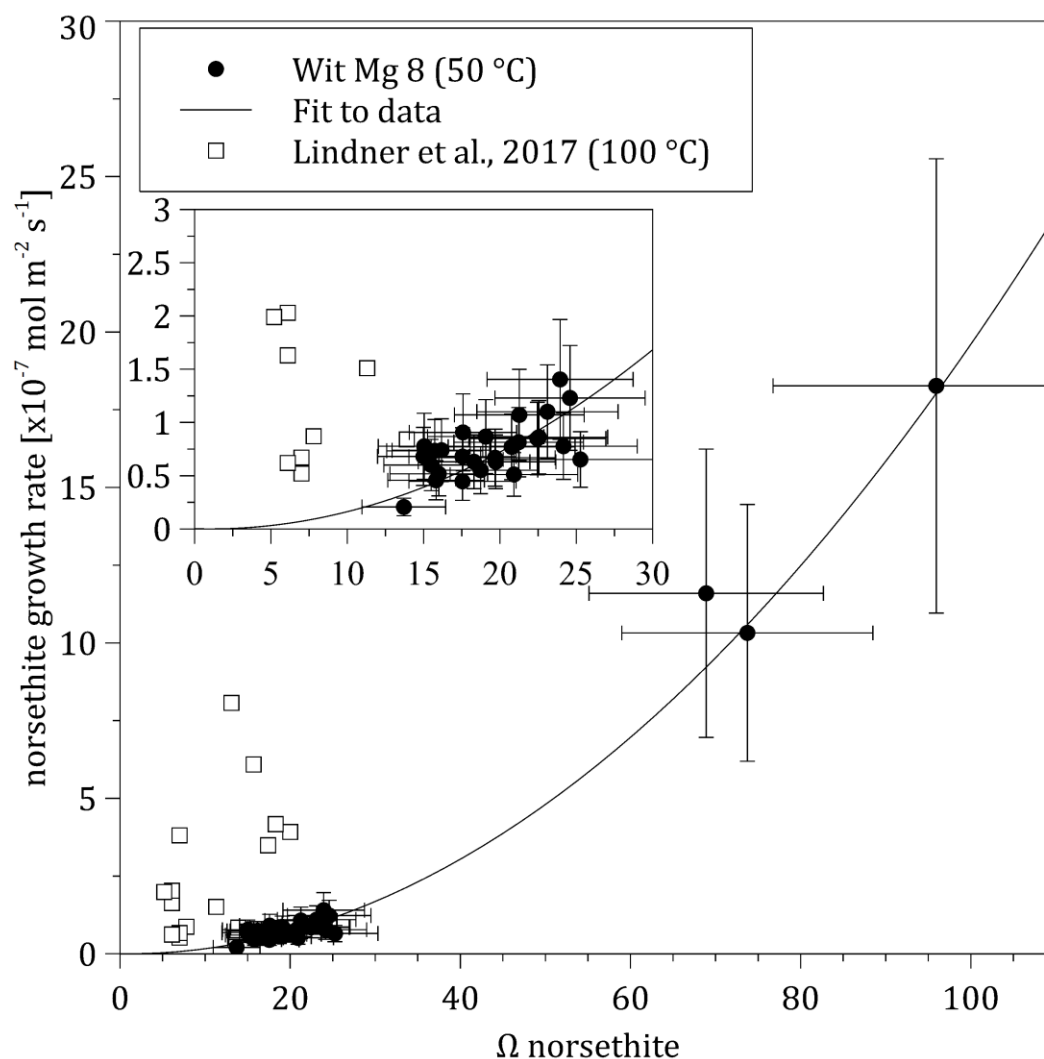
Figure 4.2-4: Norsethite growth rates vs. norsethite supersaturation. The first three samples give higher supersaturations and faster corresponding growth rates than the following samples. Rates are comparable to norsethite growth rates obtained at 100 °C (Lindner et al. 2017). The data has been fitted with an equation of the form $R=k(\Omega-1)^n$. For details on calculation method, see text

of $k=0.0020\pm0.0004\times10^{-7}$ mol m$^{-2}$ s$^{-1}$ and a reaction order of $n=2.0\pm0.1$. The comparison with norsethite growth rates at 100 °C (Lindner et al., 2017) confirms the expected positive correlation of the rate constant with temperature (Figure 4.2-4).

The dissolution of witherite and precipitation of norsethite is in accordance with the synthesis experiments of Lippmann (1968; 1973), who immersed witherite in solutions with high magnesium concentrations (20 mM Mg$^{2+}$) at ambient conditions. From the solution, norsethite crystallized within days to weeks. In these experiments, dissolving witherite was the only Ba source. The Mg:Ba ratios of the solutions, therefore, were likely well above 12:1. In the mixed-flow reactor experiment conducted here, witherite in the reactor was not the only Ba source but aqueous Ba was constantly supplied by the feed solution. However, decrease of Ba

by norsethite growth deprived the reactor in barium even below the solubility product of witherite. As long as solid $BaCO_3$ was present, dissolution of witherite tried to maintain the aqueous Ba concentration given by the solubility product of witherite. As no sign of epitaxial growth or passivation of the parental witherite crystals was detected in the SEM images, replacement of witherite by norsethite will continue until witherite is completely consumed. The witherite-norsethite replacement, therefore, can be classified as a dissolution-precipitation reaction (e.g., Putnis, 2009) without any pseudomorphism of the newly formed phase being evident.

### 4.2.3.4 Comparison with the effect of Mg on CaCO₃ growth

*4.2.3.4 Comparison with the effect of Mg on CaCO₃ growth*

Berner (1975) showed that magnesium slows calcite growth in artificial seawater but leaves aragonite growth rates unaffected. He concluded that Mg is not easily adsorbed on the aragonite surface or incorporated into the growing crystal and, thus, there is no effect on aragonite growth. This hypothesis was confirmed by Auger-spectroscopic measurements on the surface of aragonite following contact with seawater (Mucci and Morse, 1985). As described above, Mg incorporation into aragonite is limited by a very small partition coefficient; for witherite, we observed a similar or even smaller partition coefficient. Our results further show that the growth rates of witherite are as unaffected by the presence of magnesium as the growth rates of the isostructural mineral aragonite (Berner, 1975). Although the size difference between $Ba^{2+}$ and $Mg^{2+}$ is larger than between $Ca^{2+}$ and $Mg^{2+}$, the structural and chemical similarities between aragonite and witherite suffice to facilitate the same insensitivity of growth rates to the presence of $Mg^{2+}$ in amounts as studied here. Notable differences, however, occur in the presence of higher Mg concentrations common in lagoonal settings forming recent unordered Ca-Mg carbonates (e.g., Bathurst, 1971; Lippmann, 1973; Machel, 2004; Usdowski, 1967). At ambient conditions, witherite is rapidly replaced by the ordered double carbonate norsethite (e.g., Lippmann, 1968) while parental $CaCO_3$ is left unaffected and a replacement by the ordered double carbonate dolomite has never been observed (Berner, 1975; Choudens-Sánchez and Gonzalez, 2009; Jonas et al., 2017; Land, 1998; Usdowski, 1989; 1994). Only at a temperature of 60 °C, Usdowski (1989; 1994) accomplished a replacement of 1 g aragonite in 7 years, while at the temperature of this study (50 °C) he still found both aragonite and calcite unaffected by the Mg-containing solution. Witherite, in contrast, dissolves at 50 °C (dissolved witherite/runtime: $\sim 2.6 \times 10^{-5}$ mol/h) and norsethite grows (total precipitated norsethite/runtime: $\sim 3.0 \times 10^{-5}$ mol/h). This witherite-norsethite replacement at 50 °C is approx. 200 times faster than the replacement of aragonite by dolomite at 60 °C (Usdowski, 1989; 1994).

The rapidity of norsethite growth in comparison to the sluggishness of dolomite formation is evident throughout the temperature range from ambient to

100 °C (Lindner et al., 2017; Lippmann, 1968). This rate discrepancy clearly indicates that the slow ligand exchange of the Mg-aquo-complex cannot be the only factor inhibiting dolomite (and magnesite) precipitation at low temperatures. This finding is also supported by the failure to precipitate dolomite and magnesite from water-free solutions (Xu et al., 2013). Furthermore, the possibility to precipitate high-Mg calcite (Glover and Sippel, 1967; Kitano and Kanamori, 1966) and benstonite [$MgCa_6Ba_6(CO_3)_{13}$] (Hood and Steidl, 1973) at room temperature within relatively short timescales clearly shows that the formation of unordered anhydrous carbonate minerals with moderate magnesium contents can be achieved easily. Moreover, the direct precipitation of ordered anhydrous Mg-bearing double carbonates from aqueous solution has been demonstrated at ambient conditions for norsethite (Böttcher et al., 1997; Hood et al., 1974; Pimentel and Pina, 2014) and $PbMg(CO_3)_2$ (Lippmann, 1966; Morrow and Ricketts, 1986; Pimentel and Pina, 2016), but has not yet been achieved for dolomite at temperatures below 120 °C (e. g., Berninger et al., 2017; Land, 1998; Higgins and Hu, 2005).

Table A 4.2-1: Results of single mixed-flow reactor samples ($R_F$: flowrate, TA: total alkalinity, R: witherite growth rate).

| Sample | $R_F$ [ml/ min] | pH [50°C] | TA [meq/l] | $Ba^{2+}$ [mM] | $Mg^{2+}$ [mM] | Mg:Ba | Δ TA [meq/l] | $\Delta Ba^{2+}$ [mM] | $\Delta Mg^{2+}$ [mM] | R [$10^{-7}$ mol/m$^2$/s] | Ω Wit | Ω Nrs |
|---|---|---|---|---|---|---|---|---|---|---|---|---|
| WIT 6-01 | 0.3 | 7.79 | 2.98 | 0.85 | – | – | 1.96 | 0.65 | – | 0.9 | 1.1 | – |
| WIT 6-02 | 0.3 | 7.80 | 3.29 | 0.92 | – | – | 1.58 | 0.61 | – | 0.8 | 1.3 | – |
| WIT 6-03 | 0.2 | 7.73 | 4.19 | 1.13 | – | – | 0.80 | 0.36 | – | 0.4 | 1.8 | – |
| WIT 6-04 | 0.2 | 7.72 | 4.24 | 1.16 | – | – | 0.75 | 0.33 | – | 0.4 | 1.8 | – |
| WIT 6-05 | 0.2 | 7.74 | 4.16 | 1.12 | – | – | 0.83 | 0.37 | – | 0.4 | 1.8 | – |
| WIT 6-06 | 0.2 | 7.79 | 4.16 | 1.08 | – | – | 0.80 | 0.41 | – | 0.5 | 1.9 | – |
| WIT 6-07 | 0.2 | 7.80 | 4.20 | 1.07 | – | – | 0.75 | 0.42 | – | 0.5 | 2.0 | – |
| WIT 6-08 | 0.2 | 7.77 | 4.11 | 1.06 | – | – | 0.84 | 0.43 | – | 0.5 | 1.8 | – |
| WIT 6-09 | 0.5 | 7.72 | 4.32 | 1.16 | – | – | 0.62 | 0.34 | – | 0.7 | 1.8 | – |
| WIT 6-10 | 0.5 | 7.70 | 4.37 | 1.15 | – | – | 0.58 | 0.35 | – | 0.7 | 1.8 | – |
| WIT 6-11 | 0.5 | 7.68 | 4.32 | 1.17 | – | – | 0.62 | 0.33 | – | 0.7 | 1.7 | – |
| WIT 6-12 | 0.5 | 7.65 | 4.32 | 1.15 | – | – | 0.63 | 0.35 | – | 0.7 | 1.6 | – |
| WIT 6-13 | 0.5 | 7.75 | 4.31 | 1.15 | – | – | 0.63 | 0.35 | – | 0.7 | 2.0 | – |
| WIT 6-14 | 0.1 | 7.80 | 3.87 | 0.96 | – | – | 1.06 | 0.55 | – | 0.2 | 1.6 | – |
| WIT 6-15 | 0.1 | 7.78 | 3.90 | 0.93 | – | – | 1.02 | 0.57 | – | 0.3 | 1.5 | – |
| WIT 6-16 | 0.1 | 7.82 | 3.85 | 0.91 | – | – | 1.09 | 0.59 | – | 0.3 | 1.6 | – |
| WIT 6-17 | 0.1 | 7.81 | 3.85 | 0.94 | – | – | 1.00 | 0.58 | – | 0.3 | 1.6 | – |
| WIT 6-18 | 0.1 | 7.78 | 3.81 | 0.92 | – | – | 1.09 | 0.60 | – | 0.3 | 1.5 | – |
| WIT 6-19 | 0.1 | 7.81 | 3.77 | 0.88 | – | – | 1.17 | 0.62 | – | 0.3 | 1.5 | – |
| WIT 6-20 | 0.1 | 7.79 | 3.78 | 0.89 | – | – | 1.30 | 0.57 | – | 0.3 | 1.5 | – |
| WIT 6-21 | 0.9 | 7.75 | 4.26 | 1.13 | – | – | 0.65 | 0.38 | – | 1.3 | 1.9 | – |
| WIT 6-22 | 0.9 | 7.76 | 4.27 | 1.15 | – | – | 0.71 | 0.34 | – | 1.2 | 2.0 | – |
| WIT 6-23 | 0.9 | 7.76 | 4.32 | 1.14 | – | – | 0.58 | 0.37 | – | 1.3 | 2.0 | – |
| WIT 6-24 | 0.9 | 7.75 | 4.33 | 1.17 | – | – | 0.62 | 0.33 | – | 1.2 | 2.0 | – |
| WIT 6-25 | 0.9 | 7.75 | 4.37 | 1.19 | – | – | 0.59 | 0.30 | – | 1.1 | 2.0 | – |
| WIT 6-26 | 0.9 | 7.77 | 4.36 | 1.18 | – | – | 0.57 | 0.32 | – | 1.1 | 2.1 | – |
| WIT 7-1 | 0.2 | 8.50 | 11.38 | 0.07 | – | – | 0.82 | 0.23 | – | 0.2 | 1.5 | – |
| WIT 7-2 | 0.2 | 8.49 | 11.50 | 0.07 | – | – | 0.70 | 0.23 | – | 0.2 | 1.6 | – |
| WIT 7-3 | 0.2 | 8.42 | 11.74 | 0.05 | – | – | 0.47 | 0.24 | – | 0.2 | 1.1 | – |

| Sample | $R_F$ [ml/ min] | pH [50°C] | TA [meq/l] | $Ba^{2+}$ [mM] | $Mg^{2+}$ [mM] | Mg:Ba | Δ TA [meq/l] | $ΔBa^{2+}$ [mM] | $ΔMg^{2+}$ [mM] | R [$10^{-7}$ mol/m$^2$/s] | Ω Wit | Ω Nrs |
|---|---|---|---|---|---|---|---|---|---|---|---|---|
| WIT 7-4 | 0.2 | 8.41 | 11.67 | 0.05 | – | – | 0.54 | 0.24 | – | 0.2 | 1.1 | – |
| WIT 7-5 | 0.2 | 8.50 | 11.78 | 0.06 | – | – | 0.42 | 0.23 | – | 0.2 | 1.5 | – |
| WIT 7-6 | 0.2 | 8.48 | 11.91 | 0.06 | – | – | 0.29 | 0.24 | – | 0.2 | 1.4 | – |
| WIT 7-7 | 0.2 | 8.52 | 11.93 | 0.06 | – | – | 0.28 | 0.23 | – | 0.2 | 1.6 | – |
| WIT 7-8 | 0.2 | 8.52 | 11.98 | 0.06 | – | – | 0.22 | 0.24 | – | 0.2 | 1.5 | – |
| WIT 7-9 | 0.2 | 8.54 | 11.95 | 0.06 | – | – | 0.25 | 0.24 | – | 0.2 | 1.6 | – |
| WIT 7-10 | 0.2 | 8.52 | 11.79 | 0.06 | – | – | 0.41 | 0.24 | – | 0.2 | 1.4 | – |
| WIT 7-11 | 0.2 | 8.59 | 12.10 | 0.06 | – | – | 0.10 | 0.23 | – | 0.2 | 1.8 | – |
| WIT 7-12 | 0.2 | 8.52 | 11.95 | 0.06 | – | – | 0.26 | 0.24 | – | 0.2 | 1.5 | – |
| WIT 7-13 | 0.2 | 8.50 | 11.83 | 0.06 | – | – | 0.37 | 0.24 | – | 0.2 | 1.4 | – |
| WIT 7-14 | 0.2 | 8.52 | 11.92 | 0.06 | – | – | 0.28 | 0.24 | – | 0.2 | 1.5 | – |
| WIT 7-15 | 0.2 | 8.53 | 11.92 | 0.05 | – | – | 0.28 | 0.25 | – | 0.2 | 1.3 | – |
| WIT 7-16 | 0.2 | 8.53 | 11.83 | 0.06 | – | – | 0.37 | 0.24 | – | 0.2 | 1.4 | – |
| WIT 7-18 | 0.4 | 8.36 | 11.79 | 0.08 | – | – | 0.41 | 0.21 | – | 0.4 | 1.5 | – |
| WIT 7-19 | 0.4 | 8.36 | 11.77 | 0.09 | – | – | 0.43 | 0.21 | – | 0.3 | 1.5 | – |
| WIT 7-20 | 0.4 | 8.38 | 11.84 | 0.09 | – | – | 0.37 | 0.21 | – | 0.3 | 1.7 | – |
| WIT 7-21 | 0.4 | 8.41 | 11.81 | 0.09 | – | – | 0.39 | 0.21 | – | 0.3 | 1.8 | – |
| WIT 7-22 | 0.4 | 8.38 | 11.73 | 0.08 | – | – | 0.48 | 0.22 | – | 0.4 | 1.5 | – |
| WIT 7-23 | 0.4 | 8.42 | 11.74 | 0.08 | – | – | 0.46 | 0.22 | – | 0.4 | 1.6 | – |
| WIT 7-24 | 0.4 | 8.39 | 11.85 | 0.09 | – | – | 0.35 | 0.21 | – | 0.3 | 1.7 | – |
| WIT 7-25 | 0.4 | 8.37 | 11.81 | 0.09 | – | – | 0.40 | 0.21 | – | 0.0 | 1.7 | – |
| WIT 7-26 | 0.4 | 8.37 | 11.77 | 0.08 | – | – | 0.43 | 0.22 | – | 0.3 | 1.5 | – |
| WIT 7-27 | 0.4 | 8.42 | 11.85 | 0.08 | – | – | 0.35 | 0.22 | – | 0.3 | 1.6 | – |
| WIT 7-28 | 0.4 | 8.40 | 11.81 | 0.08 | – | – | 0.40 | 0.22 | – | 0.3 | 1.5 | – |
| WIT 7-29 | 0.4 | 8.39 | 11.89 | 0.10 | – | – | 0.17 | 0.16 | – | 0.2 | 1.9 | – |
| WIT 7-31 | 0.8 | 8.26 | 11.93 | 0.14 | – | – | 0.14 | 0.12 | – | 0.3 | 2.0 | – |
| WIT 7-32 | 0.8 | 8.26 | 11.93 | 0.12 | – | – | 0.13 | 0.13 | – | 0.4 | 1.8 | – |
| WIT 7-33 | 0.8 | 8.26 | 11.90 | 0.12 | – | – | 0.17 | 0.13 | – | 0.4 | 1.8 | – |
| WIT 7-34 | 0.8 | 8.26 | 11.91 | 0.13 | – | – | 0.15 | 0.12 | – | 0.4 | 1.9 | – |
| WIT 7-35 | 0.8 | 8.27 | 11.96 | 0.12 | – | – | 0.11 | 0.13 | – | 0.4 | 1.9 | – |
| WIT 7-36 | 0.8 | 8.27 | 12.00 | 0.13 | – | – | 0.07 | 0.12 | – | 0.3 | 2.0 | – |
| WIT 7-37 | 0.8 | 8.24 | 11.99 | 0.14 | – | – | 0.08 | 0.11 | – | 0.3 | 2.0 | – |
| WIT 7-38 | 0.8 | 8.26 | 11.98 | 0.12 | – | – | 0.09 | 0.13 | – | 0.4 | 1.8 | – |
| WIT 7-39 | 0.7 | 8.30 | 11.93 | 0.13 | – | – | 0.13 | 0.13 | – | 0.3 | 2.0 | – |
| WIT 7-40 | 0.8 | 8.30 | 11.91 | 0.13 | – | – | 0.16 | 0.12 | – | 0.3 | 2.1 | – |
| WIT 8-1 | 0.1 | 8.06 | 6.56 | 0.26 | – | – | 3.40 | 0.72 | – | 0.4 | 1.3 | – |
| WIT 8-2 | 0.1 | 8.07 | 8.56 | 0.26 | – | – | 1.40 | 0.72 | – | 0.3 | 1.7 | – |
| WIT 8-3 | 0.1 | 8.04 | 8.59 | 0.27 | – | – | 1.36 | 0.71 | – | 0.3 | 1.7 | – |
| WIT 8-4 | 0.1 | 8.00 | 8.57 | 0.26 | – | – | 1.38 | 0.72 | – | 0.3 | 1.5 | – |
| WIT 8-5 | 0.1 | 8.06 | 8.78 | 0.25 | – | – | 1.18 | 0.74 | – | 0.3 | 1.7 | – |
| WIT 8-6 | 0.1 | 8.08 | 8.57 | 0.25 | – | – | 1.38 | 0.73 | – | 0.3 | 1.7 | – |
| WIT 8-7 | 0.1 | 8.02 | 8.64 | 0.27 | – | – | 1.32 | 0.71 | – | 0.3 | 1.6 | – |
| WIT 8-8 | 0.1 | 8.04 | 8.54 | 0.24 | – | – | 1.41 | 0.75 | – | 0.3 | 1.5 | – |
| WIT 8-9 | 0.5 | 8.07 | 8.65 | 0.29 | – | – | 1.30 | 0.69 | – | 1.2 | 2.0 | – |
| WIT 8-10 | 0.5 | 8.08 | 8.76 | 0.33 | – | – | 1.19 | 0.65 | – | 1.1 | 2.3 | – |
| WIT 8-11 | 0.5 | 8.08 | 8.77 | 0.33 | – | – | 1.19 | 0.65 | – | 1.1 | 2.3 | – |
| WIT 8-12 | 0.5 | 7.98 | 8.89 | 0.44 | – | – | 1.06 | 0.54 | – | 0.9 | 2.5 | – |
| WIT 8-13 | 0.5 | 7.96 | 8.89 | 0.45 | – | – | 1.07 | 0.54 | – | 0.9 | 2.4 | – |
| WIT 8-14 | 0.5 | 7.93 | 8.80 | 0.43 | – | – | 1.15 | 0.55 | – | 0.9 | 2.2 | – |
| WIT 8-15 | 0.5 | 8.03 | 8.79 | 0.41 | – | – | 1.16 | 0.58 | – | 0.9 | 2.6 | – |
| WIT 8-16 | 0.9 | 8.00 | 8.85 | 0.44 | – | – | 1.10 | 0.54 | – | 1.4 | 2.6 | – |
| WIT 8-17 | 1.0 | 8.00 | 8.89 | 0.44 | – | – | 1.06 | 0.54 | – | 1.5 | 2.7 | – |
| WIT 8-18 | 1.0 | 8.00 | 8.89 | 0.45 | – | – | 1.06 | 0.53 | – | 1.5 | 2.7 | – |
| WIT 8-19 | 0.9 | 7.87 | 8.89 | 0.47 | – | – | 1.06 | 0.51 | – | 1.3 | 2.1 | – |
| WIT 8-20 | 1.0 | 7.86 | 8.88 | 0.48 | – | – | 1.07 | 0.51 | – | 1.4 | 2.1 | – |
| WIT 8-21 | 1.0 | 7.86 | 8.89 | 0.48 | – | – | 1.07 | 0.50 | – | 1.4 | 2.1 | – |

| Sample | $R_F$ [ml/min] | pH [50°C] | TA [meq/l] | $Ba^{2+}$ [mM] | $Mg^{2+}$ [mM] | Mg:Ba | Δ TA [meq/l] | $\Delta Ba^{2+}$ [mM] | $\Delta Mg^{2+}$ [mM] | R [$10^{-7}$ mol/m²/s] | Ω Wit | Ω Nrs |
|---|---|---|---|---|---|---|---|---|---|---|---|---|
| WIT 8-22 | 1.3 | 8.03 | 8.90 | 0.50 | – | – | 1.05 | 0.48 | – | 1.7 | 3.2 | – |
| WIT 8-23 | 1.4 | 8.02 | 8.88 | 0.49 | – | – | 1.07 | 0.49 | – | 1.7 | 3.1 | – |
| WIT 8-24 | 1.4 | 8.02 | 8.88 | 0.49 | – | – | 1.07 | 0.50 | – | 1.8 | 3.0 | – |
| WIT 8-25 | 1.7 | 8.01 | 8.88 | 0.51 | – | – | 1.07 | 0.47 | – | 2.0 | 3.1 | – |
| WIT 8-26 | 1.6 | 7.96 | 8.96 | 0.50 | – | – | 1.00 | 0.48 | – | 2.0 | 2.7 | – |
| WIT 8-27 | 1.6 | 8.01 | 8.88 | 0.51 | – | – | 1.07 | 0.47 | – | 2.0 | 3.1 | – |
| WIT 8-28 | 1.6 | 7.96 | 8.86 | 0.51 | – | – | 1.10 | 0.47 | – | 2.0 | 2.8 | – |
| WIT 8-29 | 1.9 | 8.07 | 8.92 | 0.51 | – | – | 1.04 | 0.47 | – | 2.3 | 3.6 | – |
| WIT 8-30 | 1.9 | 8.06 | 8.89 | 0.52 | – | – | 1.06 | 0.46 | – | 2.1 | 3.5 | – |
| WIT 8-31 | 1.9 | 8.06 | 8.90 | 0.52 | – | – | 1.06 | 0.46 | – | 2.1 | 3.6 | – |
| WIT 8-32 | 1.7 | 8.06 | 8.58 | 0.53 | – | – | 1.37 | 0.45 | – | 1.9 | 3.5 | – |
| WIT 8-33 | 1.8 | 8.07 | 8.85 | 0.51 | – | – | 1.10 | 0.47 | – | 2.2 | 3.5 | – |
| WIT 8-34 | 1.9 | 8.06 | 8.89 | 0.51 | – | – | 1.06 | 0.47 | – | 2.2 | 3.5 | – |
| WIT 8-35 | 1.9 | 8.11 | 8.87 | 0.51 | – | – | 1.09 | 0.47 | – | 2.2 | 3.8 | – |
| WIT 8-36 | 1.9 | 8.06 | 8.86 | 0.50 | – | – | 1.09 | 0.48 | – | 2.2 | 3.4 | – |
| WIT 8-37 | 1.1 | 7.98 | 8.30 | 0.55 | – | – | 1.66 | 0.43 | – | 1.2 | 2.9 | – |
| WIT 8-38 | 1.8 | 8.05 | 8.06 | 0.59 | – | – | 1.90 | 0.39 | – | 1.6 | 3.6 | – |
| WIT 8-39 | 1.9 | 8.11 | 8.83 | 0.52 | – | – | 1.12 | 0.47 | – | 2.1 | 3.9 | – |
| WIT 8-40 | 1.9 | 8.03 | 8.82 | 0.52 | – | – | 1.14 | 0.46 | – | 2.0 | 3.3 | – |
| WIT 11-1 | 0.1 | 8.05 | 3.94 | 0.26 | – | – | 5.98 | 0.78 | – | 0.6 | 0.8 | – |
| WIT 11-2 | 0.1 | 7.99 | 8.18 | 0.28 | – | – | 1.74 | 0.77 | – | 0.5 | 1.5 | – |
| WIT 11-3 | 0.1 | 7.96 | 8.21 | 0.28 | – | – | 1.71 | 0.77 | – | 0.5 | 1.4 | – |
| WIT 11-4 | 0.1 | 8.05 | 8.34 | 0.24 | – | – | 1.58 | 0.80 | – | 0.5 | 1.5 | – |
| WIT 11-5 | 0.1 | 8.02 | 8.32 | 0.27 | – | – | 1.60 | 0.78 | – | 0.5 | 1.6 | – |
| WIT 11-6 | 0.2 | 7.94 | 8.48 | 0.33 | – | – | 1.44 | 0.72 | – | 0.8 | 1.7 | – |
| WIT 11-7 | 0.1 | 8.04 | 8.59 | 0.28 | – | – | 1.32 | 0.77 | – | 0.5 | 1.8 | – |
| WIT 11-8 | 0.2 | 8.01 | 9.08 | 0.27 | – | – | 0.83 | 0.78 | – | 0.9 | 1.7 | – |
| WIT 11-9 | 0.5 | 8.07 | 8.68 | 0.42 | – | – | 1.24 | 0.62 | – | 1.4 | 2.9 | – |
| WIT 11-10 | 0.5 | 8.04 | 8.72 | 0.42 | – | – | 1.19 | 0.62 | – | 1.4 | 2.7 | – |
| WIT 11-11 | 0.5 | 8.04 | 8.69 | 0.43 | – | – | 1.23 | 0.62 | – | 1.4 | 2.8 | – |
| WIT 11-12 | 0.5 | 8.04 | 8.59 | 0.43 | – | – | 1.33 | 0.62 | – | 1.4 | 2.7 | – |
| WIT 11-13 | 0.7 | 8.07 | 8.70 | 0.46 | – | – | 1.22 | 0.58 | – | 1.9 | 3.2 | – |
| WIT 11-14 | 0.7 | 8.05 | 8.70 | 0.47 | – | – | 1.21 | 0.58 | – | 1.9 | 3.0 | – |
| WIT 11-15 | 0.6 | 8.06 | 8.77 | 0.46 | – | – | 1.14 | 0.58 | – | 1.6 | 3.1 | – |
| WIT 11-16 | 0.7 | 8.04 | 8.79 | 0.47 | – | – | 1.13 | 0.58 | – | 1.9 | 3.0 | – |
| WIT 11-17 | 1.0 | 8.10 | 8.82 | 0.48 | – | – | 1.09 | 0.56 | – | 2.4 | 3.6 | – |
| WIT 11-18 | 1.0 | 8.07 | 8.81 | 0.48 | – | – | 1.10 | 0.56 | – | 2.4 | 3.4 | – |
| WIT 11-19 | 0.9 | 8.05 | 8.82 | 0.48 | – | – | 1.10 | 0.57 | – | 2.3 | 3.2 | – |
| WIT 11-20 | 1.1 | 8.08 | 8.77 | 0.47 | – | – | 1.14 | 0.57 | – | 2.8 | 3.3 | – |
| WIT 11-21 | 1.0 | 8.11 | 8.81 | 0.41 | – | – | 1.10 | 0.63 | – | 2.6 | 3.1 | – |
| WIT 12-1 | 0.2 | 8.03 | 4.40 | 0.68 | – | – | 0.89 | 0.34 | – | 0.5 | 2.2 | – |
| WIT 12-2 | 0.2 | 8.02 | 4.44 | 0.63 | – | – | 0.84 | 0.38 | – | 0.5 | 2.1 | – |
| WIT 12-3 | 0.2 | 7.97 | 4.55 | 0.64 | – | – | 0.73 | 0.38 | – | 0.5 | 1.9 | – |
| WIT 12-4 | 0.2 | 7.97 | 4.55 | 0.64 | – | – | 0.73 | 0.38 | – | 0.5 | 1.9 | – |
| WIT 12-5 | 0.2 | 7.97 | 4.54 | 0.64 | – | – | 0.74 | 0.37 | – | 0.5 | 1.9 | – |
| WIT 12-6 | 0.5 | 8.05 | 4.75 | 0.72 | – | – | 0.53 | 0.30 | – | 1.1 | 2.6 | – |
| WIT 12-7 | 0.5 | 8.04 | 4.77 | 0.71 | – | – | 0.51 | 0.31 | – | 1.2 | 2.6 | – |
| WIT 12-8 | 0.5 | 8.05 | 4.74 | 0.73 | – | – | 0.54 | 0.29 | – | 1.1 | 2.6 | – |
| WIT 12-9 | 0.5 | 8.04 | 4.74 | 0.72 | – | – | 0.54 | 0.30 | – | 1.1 | 2.6 | – |
| WIT 12-10 | 0.5 | 8.04 | 4.73 | 0.72 | – | – | 0.55 | 0.30 | – | 1.1 | 2.6 | – |
| WIT 12-11 | 1.0 | 8.15 | 4.84 | 0.74 | – | – | 0.44 | 0.28 | – | 2.0 | 3.4 | – |
| WIT 12-12 | 0.9 | 8.14 | 4.83 | 0.74 | – | – | 0.45 | 0.28 | – | 2.0 | 3.4 | – |
| WIT 12-13 | 0.9 | 8.14 | 4.87 | 0.75 | – | – | 0.41 | 0.27 | – | 2.0 | 3.4 | – |
| WIT 12-14 | 1.0 | 8.14 | 4.84 | 0.74 | – | – | 0.44 | 0.27 | – | 2.0 | 3.4 | – |
| WIT 12-15 | 1.0 | 8.14 | 4.82 | 0.75 | – | – | 0.46 | 0.27 | – | 2.0 | 3.4 | – |
| WIT 12-16 | 0.6 | 8.09 | 4.74 | 0.72 | – | – | 0.54 | 0.29 | – | 1.4 | 2.9 | – |

| Sample | $R_F$ [ml/min] | pH [50°C] | TA [meq/l] | $Ba^{2+}$ [mM] | $Mg^{2+}$ [mM] | Mg:Ba | Δ TA [meq/l] | $\Delta Ba^{2+}$ [mM] | $\Delta Mg^{2+}$ [mM] | $R$ [$10^{-7}$ mol/m²/s] | Ω Wit | Ω Nrs |
|---|---|---|---|---|---|---|---|---|---|---|---|---|
| WIT 12-17 | 0.6 | 8.09 | 4.74 | 0.72 | – | – | 0.55 | 0.30 | – | 1.4 | 2.9 | – |
| WIT 12-18 | 0.6 | 8.10 | 4.75 | 0.72 | – | – | 0.54 | 0.30 | – | 1.4 | 2.9 | – |
| WIT 12-19 | 0.6 | 8.10 | 4.74 | 0.72 | – | – | 0.54 | 0.30 | – | 1.4 | 2.9 | – |
| WITMg 7-1 | 0.2 | 8.60 | 11.30 | 0.04 | 0.03 | 0.79 | 0.98 | 0.25 | 0.00 | 0.22 | 1.1 | 0.3 |
| WITMg 7-2 | 0.2 | 8.59 | 11.40 | 0.04 | 0.03 | 0.92 | 0.88 | 0.25 | 0.00 | 0.22 | 1.0 | 0.3 |
| WITMg 7-3 | 0.2 | 8.54 | 11.50 | 0.04 | 0.03 | 0.77 | 0.77 | 0.25 | 0.00 | 0.21 | 1.0 | 0.3 |
| WITMg 7-4 | 0.2 | 8.51 | 11.62 | 0.05 | 0.03 | 0.74 | 0.66 | 0.25 | 0.00 | 0.21 | 1.0 | 0.3 |
| WITMg 7-5 | 0.2 | 8.59 | 11.61 | 0.05 | 0.03 | 0.71 | 0.66 | 0.25 | 0.00 | 0.21 | 1.2 | 0.4 |
| WITMg 7-6 | 0.2 | 8.57 | 11.84 | 0.05 | 0.03 | 0.74 | 0.44 | 0.25 | 0.00 | 0.21 | 1.2 | 0.4 |
| WITMg 7-7 | 0.2 | 8.62 | 11.86 | 0.05 | 0.03 | 0.75 | 0.42 | 0.25 | 0.00 | 0.21 | 1.3 | 0.4 |
| WITMg 7-8 | 0.2 | 8.62 | 11.79 | 0.05 | 0.03 | 0.74 | 0.49 | 0.25 | 0.00 | 0.23 | 1.3 | 0.4 |
| WITMg 7-9 | 0.2 | 8.64 | 11.71 | 0.05 | 0.03 | 0.74 | 0.57 | 0.25 | 0.00 | 0.20 | 1.4 | 0.4 |
| WITMg 7-10 | 0.2 | 8.63 | 11.72 | 0.04 | 0.04 | 0.94 | 0.56 | 0.25 | 0.00 | 0.21 | 1.1 | 0.3 |
| WITMg 7-11 | 0.1 | 8.59 | 11.61 | 0.05 | 0.03 | 0.71 | 0.67 | 0.24 | 0.00 | 0.20 | 1.2 | 0.4 |
| WITMg 7-12 | 0.1 | 8.63 | 11.68 | 0.05 | 0.04 | 0.76 | 0.59 | 0.25 | 0.00 | 0.20 | 1.3 | 0.4 |
| WITMg 7-13 | 0.1 | 8.61 | 11.86 | 0.05 | 0.03 | 0.73 | 0.42 | 0.24 | 0.00 | 0.20 | 1.3 | 0.4 |
| WITMg 7-14 | 0.1 | 8.61 | 11.90 | 0.05 | 0.03 | 0.72 | 0.37 | 0.25 | 0.00 | 0.20 | 1.3 | 0.4 |
| WITMg 7-15 | 0.1 | 8.65 | 11.92 | 0.04 | 0.03 | 0.80 | 0.35 | 0.25 | 0.00 | 0.20 | 1.2 | 0.4 |
| WITMg 7-16 | 0.1 | 8.63 | 11.69 | 0.05 | 0.03 | 0.73 | 0.59 | 0.25 | 0.00 | 0.19 | 1.3 | 0.4 |
| WITMg 7-18 | 0.4 | 8.47 | 11.66 | 0.08 | 0.03 | 0.44 | 0.62 | 0.22 | 0.00 | 0.42 | 1.5 | 0.4 |
| WITMg 7-19 | 0.4 | 8.47 | 11.71 | 0.07 | 0.04 | 0.49 | 0.57 | 0.22 | 0.00 | 0.42 | 1.5 | 0.4 |
| WITMg 7-20 | 0.4 | 8.47 | 11.67 | 0.07 | 0.03 | 0.49 | 0.61 | 0.22 | 0.00 | 0.42 | 1.5 | 0.4 |
| WITMg 7-21 | 0.4 | 8.50 | 11.67 | 0.07 | 0.04 | 0.50 | 0.61 | 0.22 | 0.00 | 0.42 | 1.6 | 0.4 |
| WITMg 7-22 | 0.4 | 8.48 | 11.56 | 0.07 | 0.03 | 0.48 | 0.71 | 0.22 | 0.00 | 0.42 | 1.5 | 0.4 |
| WITMg 7-23 | 0.4 | 8.50 | 11.75 | 0.08 | 0.03 | 0.40 | 0.53 | 0.21 | 0.00 | 0.40 | 1.8 | 0.5 |
| WITMg 7-24 | 0.4 | 8.49 | 11.73 | 0.07 | 0.03 | 0.47 | 0.55 | 0.22 | 0.00 | 0.42 | 1.5 | 0.4 |
| WITMg 7-25 | 0.4 | 8.48 | 11.73 | 0.08 | 0.03 | 0.45 | 0.55 | 0.22 | 0.00 | 0.00 | 1.6 | 0.4 |
| WITMg 7-26 | 0.4 | 8.47 | 11.73 | 0.08 | 0.03 | 0.43 | 0.55 | 0.21 | 0.00 | 0.40 | 1.7 | 0.4 |
| WITMg 7-27 | 0.4 | 8.51 | 11.77 | 0.07 | 0.03 | 0.51 | 0.51 | 0.23 | 0.00 | 0.43 | 1.5 | 0.4 |
| WITMg 7-28 | 0.4 | 8.50 | 11.80 | 0.08 | 0.03 | 0.45 | 0.48 | 0.22 | −0.01 | 0.41 | 1.7 | 0.4 |
| WITMg 7-29 | 0.4 | 8.49 | 11.84 | 0.07 | 0.03 | 0.52 | 0.20 | 0.18 | −0.01 | 0.33 | 1.5 | 0.4 |
| WITMg 7-31 | 0.7 | 8.44 | 11.72 | 0.11 | 0.03 | 0.24 | 0.32 | 0.14 | 0.00 | 0.50 | 2.1 | 0.3 |
| WITMg 7-32 | 0.7 | 8.47 | 11.79 | 0.10 | 0.03 | 0.27 | 0.25 | 0.14 | 0.00 | 0.53 | 2.0 | 0.4 |
| WITMg 7-33 | 0.7 | 8.47 | 11.77 | 0.12 | 0.02 | 0.21 | 0.27 | 0.12 | 0.00 | 0.45 | 2.5 | 0.4 |
| WITMg 7-34 | 0.7 | 8.46 | 11.76 | 0.10 | 0.03 | 0.27 | 0.28 | 0.14 | 0.00 | 0.52 | 2.0 | 0.4 |
| WITMg 7-35 | 0.7 | 8.48 | 11.77 | 0.13 | 0.03 | 0.19 | 0.27 | 0.11 | 0.00 | 0.41 | 2.8 | 0.5 |
| WITMg 7-36 | 0.7 | 8.46 | 11.79 | 0.11 | 0.02 | 0.23 | 0.25 | 0.13 | 0.00 | 0.48 | 2.2 | 0.4 |
| WITMg 7-37 | 0.7 | 8.44 | 11.76 | 0.10 | 0.02 | 0.25 | 0.28 | 0.14 | 0.00 | 0.52 | 2.0 | 0.3 |
| WITMg 7-38 | 0.7 | 8.45 | 11.78 | 0.10 | 0.03 | 0.25 | 0.26 | 0.14 | 0.00 | 0.48 | 2.1 | 0.3 |
| WITMg 7-39 | 0.7 | 8.48 | 11.71 | 0.09 | 0.03 | 0.29 | 0.33 | 0.16 | 0.00 | 0.55 | 1.9 | 0.3 |
| WITMg 7-40 | 0.7 | 8.48 | 11.78 | 0.10 | 0.02 | 0.26 | 0.26 | 0.15 | 0.00 | 0.52 | 2.1 | 0.4 |
| WITMg 8-1 | 0.4 | 7.55 | 7.26 | 0.73 | 17.11 | 23.5 | 2.68 | 1.30 | 3.03 | – | 1.3 | 96.8 |
| WITMg 8-2 | 0.5 | 7.47 | 7.47 | 0.82 | 18.12 | 22.0 | 2.48 | 1.21 | 2.03 | – | 1.1 | 69.5 |
| WITMg 8-3 | 0.4 | 7.47 | 7.56 | 0.83 | 18.10 | 21.9 | 2.39 | 1.21 | 2.04 | – | 1.2 | 74.4 |
| WITMg 8-5 | 0.4 | 7.23 | 7.51 | 0.79 | 19.60 | 24.8 | 2.44 | 1.24 | 0.54 | – | 0.6 | 24.8 |
| WITMg 8-6 | 0.4 | 7.22 | 7.50 | 0.89 | 19.83 | 22.3 | 2.44 | 1.14 | 0.31 | – | 0.7 | 25.5 |
| WITMg 8-7 | 0.4 | 7.16 | 7.32 | 1.12 | 19.64 | 17.5 | 2.62 | 0.91 | 0.50 | – | 0.7 | 24.4 |
| WITMg 8-8 | 0.4 | 7.15 | 7.26 | 1.15 | 19.39 | 16.9 | 2.69 | 0.88 | 0.76 | – | 0.7 | 23.3 |
| WITMg 8-9 | 0.4 | 7.15 | 7.17 | 1.29 | 19.13 | 14.9 | 2.78 | 0.75 | 1.01 | – | 0.8 | 24.2 |
| WITMg 8-10 | 0.4 | 7.05 | 6.94 | 1.42 | 19.10 | 13.5 | 3.00 | 0.61 | 1.04 | – | 0.7 | 15.9 |
| WITMg 8-11 | 0.4 | 7.05 | 6.99 | 1.44 | 19.07 | 13.2 | 2.96 | 0.59 | 1.07 | – | 0.7 | 16.3 |
| WITMg 8-12 | 0.4 | 7.04 | 6.98 | 1.41 | 18.97 | 13.5 | 2.96 | 0.62 | 1.18 | – | 0.7 | 15.2 |
| WITMg 8-13 | 0.4 | 7.05 | 6.98 | 1.40 | 19.38 | 13.8 | 2.97 | 0.63 | 0.77 | – | 0.7 | 16.0 |
| WITMg 8-14 | 0.4 | 7.04 | 7.46 | 1.63 | 18.99 | 11.6 | 2.49 | 0.40 | 1.15 | – | 0.8 | 19.9 |
| WITMg 8-15 | 0.4 | 7.02 | 7.46 | 1.57 | 19.38 | 12.3 | 2.48 | 0.46 | 0.77 | – | 0.8 | 17.7 |
| WITMg 8-17 | 0.4 | 7.00 | 7.12 | 1.69 | 18.99 | 11.3 | 2.83 | 0.35 | 1.15 | – | 0.7 | 15.6 |

| Sample | $R_F$ [ml/min] | pH [50°C] | TA [meq/l] | $Ba^{2+}$ [mM] | $Mg^{2+}$ [mM] | Mg:Ba | Δ TA [meq/l] | $\Delta Ba^{2+}$ [mM] | $\Delta Mg^{2+}$ [mM] | R [$10^{-7}$ mol/m$^2$/s] | Ω Wit | Ω Nrs |
|---|---|---|---|---|---|---|---|---|---|---|---|---|
| WITMg 8-18 | 0.4 | 7.00 | 7.26 | 1.67 | 19.13 | 11.5 | 2.69 | 0.36 | 1.01 | – | 0.7 | 16.1 |
| WITMg 8-19 | 0.5 | 7.00 | 7.14 | 1.70 | 18.98 | 11.2 | 2.80 | 0.34 | 1.17 | – | 0.7 | 15.1 |
| WITMg 8-20 | 0.7 | 7.01 | 7.40 | 1.70 | 19.00 | 11.2 | 2.55 | 0.34 | 1.14 | – | 0.8 | 17.7 |
| WITMg 8-21 | 0.6 | 7.04 | 7.48 | 1.57 | 18.95 | 12.1 | 2.46 | 0.46 | 1.19 | – | 0.8 | 19.2 |
| WITMg 8-22 | 0.6 | 7.03 | 7.41 | 1.17 | 19.85 | 17.0 | 2.54 | 0.86 | 0.29 | – | 0.6 | 13.8 |
| WITMg 8-23 | 0.7 | 7.03 | 7.41 | 1.53 | 19.22 | 12.6 | 2.54 | 0.50 | 0.93 | – | 0.7 | 17.7 |
| WITMg 8-24 | 0.7 | 7.03 | 7.46 | 1.57 | 19.26 | 12.2 | 2.48 | 0.46 | 0.89 | – | 0.8 | 18.5 |
| WITMg 8-25 | 0.6 | 7.03 | 7.64 | 1.54 | 19.35 | 12.6 | 2.31 | 0.49 | 0.79 | – | 0.8 | 18.9 |
| WITMg 8-26 | 1.1 | 7.05 | 7.63 | 1.60 | 19.26 | 12.0 | 2.32 | 0.43 | 0.88 | – | 0.8 | 21.5 |
| WITMg 8-27 | 1.1 | 7.05 | 7.66 | 1.54 | 19.44 | 12.6 | 2.29 | 0.49 | 0.70 | – | 0.8 | 21.0 |
| WITMg 8-28 | 1.1 | 7.04 | 7.65 | 1.53 | 19.54 | 12.8 | 2.29 | 0.50 | 0.60 | – | 0.8 | 19.9 |
| WITMg 8-29 | 1.1 | 7.06 | 7.71 | 1.59 | 19.38 | 12.2 | 2.24 | 0.45 | 0.76 | – | 0.9 | 22.8 |
| WITMg 8-30 | 1.1 | 7.06 | 7.73 | 1.57 | 19.38 | 12.3 | 2.22 | 0.46 | 0.76 | – | 0.9 | 22.7 |
| WITMg 8-31 | 1.1 | 7.05 | 7.69 | 1.54 | 19.67 | 12.8 | 2.26 | 0.50 | 0.47 | – | 0.8 | 21.1 |
| WITMg 8-32 | 1.1 | 7.05 | 7.69 | 1.57 | 19.39 | 12.3 | 2.26 | 0.46 | 0.75 | – | 0.8 | 21.4 |
| WITMg 9-1 | 0.1 | 7.97 | 8.64 | 0.18 | 0.96 | 5.21 | 1.56 | 0.79 | 0.04 | 0.5 | 1.4 | 3.5 |
| WITMg 9-2 | 0.1 | 7.96 | 8.74 | 0.18 | 1.00 | 5.58 | 1.46 | 0.80 | 0.01 | 0.5 | 1.4 | 3.4 |
| WITMg 9-3 | 0.1 | 7.97 | 8.78 | 0.18 | 1.00 | 5.69 | 1.42 | 0.80 | 0.00 | 0.5 | 1.4 | 3.5 |
| WITMg 9-4 | 0.1 | 7.97 | 8.73 | 0.18 | 0.98 | 5.37 | 1.47 | 0.79 | 0.02 | 0.5 | 1.4 | 3.6 |
| WITMg 9-5 | 0.1 | 7.97 | 8.73 | 0.18 | 0.98 | 5.36 | 1.46 | 0.79 | 0.03 | 0.5 | 1.4 | 3.6 |
| WITMg 9-6 | 0.1 | 7.96 | 8.74 | 0.18 | 1.02 | 5.71 | 1.46 | 0.80 | −0.01 | 0.5 | 1.4 | 3.5 |
| WITMg 9-7 | 0.1 | 8.01 | 8.56 | 0.13 | 1.00 | 7.49 | 1.64 | 0.84 | 0.00 | 0.3 | 1.1 | 3.1 |
| WITMg 9-8 | 0.1 | 8.01 | 8.54 | 0.13 | 1.02 | 7.63 | 1.66 | 0.84 | −0.01 | 0.3 | 1.1 | 3.1 |
| WITMg 9-9 | 0.6 | 7.97 | 8.86 | 0.35 | 1.04 | 2.96 | 1.33 | 0.63 | −0.03 | 1.1 | 2.8 | 7.4 |
| WITMg 9-10 | 0.6 | 8.02 | 8.92 | 0.34 | 1.06 | 3.15 | 1.28 | 0.64 | −0.06 | 1.1 | 3.0 | 9.1 |
| WITMg 9-11 | 0.6 | 8.03 | 8.84 | 0.34 | 1.03 | 2.99 | 1.36 | 0.63 | −0.02 | 1.1 | 3.1 | 9.3 |
| WITMg 9-12 | 0.6 | 8.01 | 8.85 | 0.33 | 1.02 | 3.08 | 1.35 | 0.64 | −0.02 | 1.1 | 2.9 | 8.2 |
| WITMg 9-13 | 0.6 | 8.02 | 8.87 | 0.34 | 1.02 | 2.99 | 1.33 | 0.64 | −0.01 | 1.1 | 3.0 | 8.8 |
| WITMg 9-14 | 1.1 | 7.99 | 8.93 | 0.38 | 0.91 | 2.38 | 1.27 | 0.59 | 0.09 | 1.9 | 3.2 | 7.9 |
| WITMg 9-15 | 1.1 | 7.97 | 8.92 | 0.38 | 0.99 | 2.59 | 1.28 | 0.60 | 0.02 | 1.8 | 3.0 | 7.7 |
| WITMg 9-16 | 1.1 | 7.96 | 8.89 | 0.38 | 0.99 | 2.60 | 1.30 | 0.60 | 0.01 | 1.8 | 3.0 | 7.4 |
| WITMg 9-17 | 1.1 | 7.96 | 8.92 | 0.38 | 0.99 | 2.63 | 1.28 | 0.60 | 0.01 | 1.9 | 2.9 | 7.3 |
| WITMg 9-18 | 1.1 | 7.96 | 8.93 | 0.38 | 0.99 | 2.61 | 1.27 | 0.60 | 0.02 | 1.9 | 3.0 | 7.4 |
| WITMg 9-19 | 0.4 | 8.08 | 8.81 | 0.26 | 0.98 | 3.78 | 1.39 | 0.72 | 0.03 | 0.7 | 2.6 | 8.2 |
| WITMg 9-20 | 0.4 | 8.05 | 8.77 | 0.26 | 0.99 | 3.89 | 1.43 | 0.72 | 0.01 | 0.7 | 2.4 | 7.2 |
| WITMg 9-21 | 0.4 | 8.06 | 8.79 | 0.26 | 0.97 | 3.78 | 1.41 | 0.72 | 0.04 | 0.7 | 2.5 | 7.4 |
| WITMg 9-22 | 0.4 | 8.04 | 8.80 | 0.24 | 1.00 | 4.09 | 1.40 | 0.73 | 0.01 | 0.8 | 2.3 | 6.7 |
| WITMg 9-23 | 1.4 | 8.02 | 8.93 | 0.38 | 0.98 | 2.57 | 1.27 | 0.60 | 0.03 | 2.3 | 3.4 | 9.5 |
| WITMg 9-24 | 1.5 | 8.03 | 8.91 | 0.38 | 1.00 | 2.64 | 1.29 | 0.60 | 0.01 | 2.4 | 3.4 | 10.0 |
| WITMg 9-25 | 1.5 | 8.03 | 8.89 | 0.38 | 0.99 | 2.59 | 1.30 | 0.60 | 0.02 | 2.4 | 3.4 | 10.0 |
| WITMg 9-26 | 1.4 | 8.05 | 8.88 | 0.38 | 0.99 | 2.59 | 1.32 | 0.59 | 0.01 | 2.3 | 3.6 | 10.9 |
| WITMg 9-27 | 0.1 | 8.00 | 8.37 | 0.16 | 0.97 | 6.11 | 1.82 | 0.82 | 0.04 | 0.3 | 1.3 | 3.3 |
| WITMg 9-28 | 0.1 | 8.07 | 8.51 | 0.16 | 0.97 | 6.19 | 1.69 | 0.82 | 0.04 | 0.2 | 1.5 | 4.5 |
| WITMg 9-29 | 0.1 | 8.06 | 8.51 | 0.18 | 0.96 | 5.27 | 1.69 | 0.80 | 0.05 | 0.2 | 1.7 | 4.9 |
| WITMg 9-30 | 0.1 | 8.08 | 8.40 | 0.14 | 1.00 | 7.11 | 1.80 | 0.84 | 0.00 | 0.3 | 1.4 | 4.2 |
| WITMg 10-1 | 1.0 | 7.81 | 4.70 | 1.68 | 2.12 | 1.26 | 0.70 | 0.38 | 0.00 | 2.1 | 3.4 | 5.1 |
| WITMg 10-2 | 1.0 | 7.81 | 4.70 | 1.71 | 2.05 | 1.20 | 0.70 | 0.34 | 0.07 | 1.9 | 3.4 | 5.0 |
| WITMg 10-3 | 1.0 | 7.82 | 4.73 | 1.71 | 2.11 | 1.23 | 0.67 | 0.35 | 0.02 | 1.9 | 3.5 | 5.6 |
| WITMg 10-4 | 1.0 | 7.81 | 4.73 | 1.69 | 2.15 | 1.27 | 0.67 | 0.37 | −0.03 | 2.0 | 3.4 | 5.3 |
| WITMg 10-5 | 1.0 | 7.82 | 4.73 | 1.70 | 2.19 | 1.29 | 0.67 | 0.36 | −0.07 | 1.9 | 3.5 | 5.6 |
| WITMg 10-6 | 2.0 | 7.85 | 4.84 | 1.76 | 2.02 | 1.15 | 0.56 | 0.30 | 0.10 | 3.1 | 4.0 | 6.5 |
| WITMg 10-7 | 2.0 | 7.84 | 4.82 | 1.76 | 2.04 | 1.16 | 0.58 | 0.30 | 0.08 | 3.1 | 3.9 | 6.2 |
| WITMg 10-8 | 1.9 | 7.83 | 4.76 | 1.75 | 2.03 | 1.16 | 0.64 | 0.31 | 0.09 | 3.1 | 3.7 | 5.8 |
| WEITMg 10-9 | 2.0 | 7.82 | 4.77 | 1.75 | 2.00 | 1.14 | 0.63 | 0.31 | 0.13 | 3.1 | 3.7 | 5.5 |
| WITMg 10-10 | 1.9 | 7.82 | 4.76 | 1.71 | 2.04 | 1.19 | 0.64 | 0.35 | 0.08 | 3.5 | 3.6 | 5.5 |
| WITMg 10-11 | 0.5 | 7.78 | 4.39 | 1.52 | 2.08 | 1.37 | 1.01 | 0.54 | 0.04 | 1.4 | 2.7 | 3.6 |

| Sample | $R_F$ [ml/ min] | pH [50°C] | TA [meq/l] | $Ba^{2+}$ [mM] | $Mg^{2+}$ [mM] | Mg:Ba | Δ TA [meq/l] | $\Delta Ba^{2+}$ [mM] | $\Delta Mg^{2+}$ [mM] | R [$10^{-7}$ mol/m$^2$/s] | Ω Wit | Ω Nrs |
|---|---|---|---|---|---|---|---|---|---|---|---|---|
| WITMg 10-12 | 0.5 | 7.78 | 4.31 | 1.30 | 2.17 | 1.67 | 1.09 | 0.76 | −0.05 | 2.0 | 2.3 | 3.0 |
| WITMg 10-13 | 0.5 | 7.79 | 4.32 | 1.47 | 2.08 | 1.41 | 1.08 | 0.59 | 0.04 | 1.5 | 2.6 | 3.4 |
| WITMg 10-14 | 0.5 | 7.80 | 4.31 | 1.49 | 2.07 | 1.40 | 1.09 | 0.57 | 0.05 | 1.5 | 2.7 | 3.6 |
| WITMg 10-15 | 0.5 | 7.79 | 4.42 | 1.52 | 2.06 | 1.35 | 0.98 | 0.54 | 0.06 | 1.4 | 2.8 | 3.7 |
| WITMg 10-16 | 0.2 | 7.82 | 3.89 | 1.26 | 2.05 | 1.63 | 1.51 | 0.80 | 0.07 | 0.7 | 2.2 | 2.8 |
| WITMg 10-17 | 0.2 | 7.83 | 3.79 | 1.20 | 2.17 | 1.81 | 1.61 | 0.86 | −0.05 | 0.8 | 2.1 | 2.8 |
| WITMg 10-18 | 0.2 | 7.85 | 3.97 | 1.17 | 2.20 | 1.87 | 1.43 | 0.89 | −0.07 | 1.0 | 2.2 | 3.2 |
| WITMg 10-19 | 0.1 | 7.86 | 2.98 | 0.84 | 2.06 | 2.45 | 2.42 | 1.22 | 0.06 | 0.5 | 1.2 | 1.3 |
| WITMg 11-1 | 0.1 | 8.09 | 4.00 | 0.28 | 0.02 | 0.05 | 5.80 | 0.78 | 0.09 | 0.6 | 1.5 | 0.0 |
| WITMg 11-2 | 0.1 | 7.89 | 8.16 | 0.31 | 0.11 | 0.35 | 1.64 | 0.76 | 0.00 | 0.5 | 2.0 | 0.4 |
| WITMg 11-3 | 0.1 | 7.89 | 8.29 | 0.31 | 0.11 | 0.37 | 1.51 | 0.76 | −0.01 | 0.5 | 2.0 | 0.5 |
| WITMg 11-4 | 0.1 | 7.89 | 8.37 | 0.28 | 0.11 | 0.38 | 1.43 | 0.79 | 0.00 | 0.5 | 1.8 | 0.4 |
| WITMg 11-5 | 0.1 | 7.90 | 8.28 | 0.29 | 0.10 | 0.36 | 1.52 | 0.78 | 0.00 | 0.4 | 1.9 | 0.4 |
| WITMg 11-6 | 0.3 | 7.90 | 8.45 | 0.33 | 0.14 | 0.43 | 1.35 | 0.74 | −0.04 | 0.8 | 2.2 | 0.7 |
| WITMg 11-7 | 0.2 | 7.90 | 8.42 | 0.35 | 0.13 | 0.38 | 1.38 | 0.72 | −0.03 | 0.7 | 2.3 | 0.7 |
| WITMg 11-8 | 0.2 | 7.90 | 8.43 | 0.34 | 0.12 | 0.36 | 1.37 | 0.72 | −0.02 | 0.7 | 2.3 | 0.6 |
| WITMg 11-9 | 0.5 | 7.90 | 8.55 | 0.43 | 0.14 | 0.32 | 1.25 | 0.63 | −0.03 | 1.2 | 2.9 | 0.9 |
| WITMg 11-10 | 0.5 | 7.90 | 8.55 | 0.44 | 0.13 | 0.30 | 1.25 | 0.62 | −0.03 | 1.4 | 3.0 | 0.9 |
| WITMg 11-11 | 0.5 | 7.89 | 8.62 | 0.45 | 0.12 | 0.28 | 1.18 | 0.62 | −0.02 | 1.4 | 3.0 | 0.8 |
| WITMg 11-12 | 0.5 | 7.89 | 8.70 | 0.46 | 0.13 | 0.27 | 1.10 | 0.61 | −0.02 | 1.3 | 3.1 | 0.9 |
| WITMg 11-13 | 0.7 | 7.89 | 8.82 | 0.47 | 0.15 | 0.32 | 0.98 | 0.60 | −0.05 | 1.8 | 3.2 | 1.1 |
| WITMg 11-14 | 0.7 | 7.89 | 8.66 | 0.49 | 0.14 | 0.28 | 1.14 | 0.58 | −0.04 | 1.7 | 3.3 | 1.0 |
| WITMg 11-15 | 0.6 | 7.89 | 8.73 | 0.50 | 0.13 | 0.26 | 1.07 | 0.56 | −0.03 | 1.4 | 3.4 | 1.0 |
| WITMg 11-16 | 0.7 | 7.89 | 8.76 | 0.50 | 0.13 | 0.26 | 1.04 | 0.56 | −0.03 | 1.7 | 3.4 | 1.0 |
| WITMg 11-17 | 1.0 | 7.89 | 8.83 | 0.51 | 0.14 | 0.28 | 0.97 | 0.55 | −0.04 | 2.1 | 3.5 | 1.1 |
| WITMg 11-18 | 1.0 | 7.90 | 8.81 | 0.45 | 0.20 | 0.44 | 0.99 | 0.61 | −0.10 | 2.4 | 3.1 | 1.4 |
| WITMg 11-19 | 0.9 | 7.90 | 8.79 | 0.52 | 0.13 | 0.26 | 1.01 | 0.54 | −0.03 | 2.0 | 3.6 | 1.0 |
| WITMg 11-20 | 1.0 | 7.90 | 8.77 | 0.52 | 0.14 | 0.26 | 1.03 | 0.55 | −0.03 | 2.1 | 3.6 | 1.1 |
| WITMg 11-21 | 1.0 | 7.90 | 8.78 | 0.51 | 0.14 | 0.27 | 1.02 | 0.56 | −0.03 | 2.1 | 3.5 | 1.1 |
| WITMg 12-1 | 0.2 | 7.90 | 4.38 | 0.65 | 2.75 | 4.24 | 0.95 | 0.35 | 0.23 | 0.4 | 1.5 | 0.1 |
| WITMg 12-2 | 0.2 | 7.90 | 4.41 | 0.67 | 2.81 | 4.20 | 0.91 | 0.32 | 0.17 | 0.4 | 1.5 | 0.2 |
| WITMg 12-3 | 0.2 | 7.90 | 4.49 | 0.67 | 2.90 | 4.35 | 0.83 | 0.33 | 0.08 | 0.4 | 1.5 | 0.2 |
| WITMg 12-4 | 0.2 | 7.90 | 4.51 | 0.69 | 2.83 | 4.11 | 0.81 | 0.30 | 0.15 | 0.4 | 1.6 | 0.2 |
| WITMg 12-5 | 0.2 | 7.90 | 4.54 | 0.66 | 2.88 | 4.35 | 0.78 | 0.33 | 0.10 | 0.4 | 1.6 | 0.2 |
| WITMg 12-6 | 0.5 | 7.89 | 4.75 | 0.77 | 2.91 | 3.76 | 0.57 | 0.22 | 0.07 | 0.7 | 1.9 | 0.2 |
| WITMg 12-7 | 0.5 | 7.89 | 4.76 | 0.77 | 2.99 | 3.86 | 0.56 | 0.22 | −0.01 | 0.7 | 1.9 | 0.2 |
| WITMg 12-8 | 0.5 | 7.89 | 4.79 | 0.80 | 2.91 | 3.64 | 0.53 | 0.20 | 0.07 | 0.6 | 1.9 | 0.2 |
| WITMg 12-9 | 0.5 | 7.89 | 4.76 | 0.79 | 2.91 | 3.69 | 0.56 | 0.21 | 0.07 | 0.7 | 1.9 | 0.2 |
| WITMg 12-10 | 0.5 | 7.89 | 4.73 | 0.78 | 2.92 | 3.76 | 0.59 | 0.22 | 0.06 | 0.7 | 1.9 | 0.2 |
| WITMg 12-11 | 0.8 | 7.93 | 4.82 | 0.82 | 2.93 | 3.58 | 0.51 | 0.18 | 0.05 | 1.0 | 2.2 | 0.3 |
| WITMg 12-12 | 0.9 | 7.92 | 4.81 | 0.81 | 2.98 | 3.70 | 0.51 | 0.19 | 0.00 | 1.2 | 2.1 | 0.3 |
| WITMg 12-13 | 0.9 | 7.92 | 4.79 | 0.84 | 2.91 | 3.46 | 0.53 | 0.15 | 0.07 | 1.0 | 2.2 | 0.3 |
| WITMg 12-14 | 0.9 | 7.92 | 4.78 | 0.83 | 2.91 | 3.52 | 0.54 | 0.17 | 0.07 | 1.1 | 2.2 | 0.3 |
| WITMg 12-15 | 0.9 | 7.92 | 4.79 | 0.82 | 2.95 | 3.60 | 0.53 | 0.18 | 0.03 | 1.1 | 2.1 | 0.3 |
| WITMg 12-16 | 0.6 | 7.93 | 4.74 | 0.78 | 2.97 | 3.81 | 0.58 | 0.22 | 0.01 | 0.8 | 2.1 | 0.2 |
| WITMg 12-17 | 0.6 | 7.93 | 4.74 | 0.78 | 2.99 | 3.81 | 0.58 | 0.21 | −0.01 | 0.8 | 2.1 | 0.3 |
| WITMg 12-18 | 0.6 | 7.93 | 4.75 | 0.79 | 2.96 | 3.75 | 0.57 | 0.20 | 0.02 | 0.8 | 2.1 | 0.3 |
| WITMg 12-19 | 0.6 | 7.93 | 4.75 | 0.83 | 2.66 | 3.22 | 0.57 | 0.17 | 0.32 | 0.7 | 2.2 | 0.2 |

## 4.3    Growth kinetics of norsethite

Although much has been learned about norsethite (cf. chapter 1.4), no quantitative growth rates were measured yet. This deficiency has prevented the important comparison with growth rates of other anhydrous Mg-bearing carbonates in order to gain knowledge about the span of possible incorporation rates of anhydrous $Mg^{2+}$ ions. Aim of this work, therefore, was to determine the solubility product and growth rates of norsethite over a wide range of conditions.

### 4.3.1   Detailed materials and methods

#### *4.3.1.1 Seed crystal synthesis*

Norsethite seed crystals were synthesized using a slightly modified method as proposed by Königsberger et al. (1998): 0.25 M $NaHCO_3$ solution was added to an equal amount of stirred 0.015 M $BaCl_2$ and 0.025 M $MgCl_2$ solution at a rate of 10 – 40 ml/min. The precipitate, which formed immediately upon adding the $NaHCO_3$ solution, subsequently aged for 60 days at room temperature without stirring. The crystal powder, then, was retrieved and separated from solution by vacuum filtration, washed several times with deionized water and ethanol, and dried at 60 °C in an oven for at least 12 hours.

#### *4.3.1.2 Solubility determination*

The solubility of norsethite was determined from 30 to 150 °C in 0.1 M NaCl aqueous solution using a hydrogen-electrode concentration cell (HECC), which provided continuous in-situ measurement of hydrogen ion molality and, therefore, allows for the determination of the pH-value of the solution (Bénézeth et al., 2009; Palmer et al., 2001) at each temperature investigated in this study. A precise measurement of pH is critical for the correct determination of the solution speciation and the consequent computation of the solubility product. In the experiments, the solutions were initially equilibrated with the seed crystals at the highest temperature of the run (runs 1 – 3) indicated in Table A 4.3-1. Once the cell attained thermal equilibrium, solution samples were retrieved over time and analyzed for Ba, Mg, and total dissolved inorganic carbon (TDIC) concentrations (Table A 4.3-1). Attainment of equilibrium was assumed when the concentrations of two successive samples taken over a period of no less than three days remained constant within analytical uncertainty. Once equilibrium had been reached, the temperature was decreased to approach equilibrium from undersaturation.

*4.3.1.3 Mixed-flow reactor experiments*

Growth experiments at 100 °C were conducted in hydrothermal mixed-flow reactors as described in chapter 3.1.1. Experiments 100.1, 100.5 and 100.6 were fed from one reservoir, while for the other experiments two different input solutions and two pumps were used. Experiments at 40 and 65 °C were performed in the PTFE reactors described in chapter 3.1.2.

The use of two separate input solutions, which only converge inside the reactor, allows working at high supersaturation without the risk of precipitation in the solution reservoir or along the flow line. The starting conditions of the mixed-flow reactor experiments are given in Table 4.3-1. Ba and Mg concentrations were in the range of $3 \times 10^{-6} - 5 \times 10^{-3}$ M and $1 \times 10^{-4} - 9 \times 10^{-2}$ M, respectively. Ionic strength was adjusted to 0.1 M with NaCl. For low concentrations, stock solutions were prepared and diluted to the desired concentrations. An experiment typically ran for $10 - 18$ days in total.

*4.3.1.4 Further analyses*

EDX measurements on the seed crystals revealed a nearly ideal stoichiometric Ba:Mg ratio of 1.04. Crystal powders were analyzed in a *Perkin-Elmer* Spectrum Two FT-IR-spectrometer using a diamond ATR setup (*Pike Technologies* GladiATR). The specific surface area of the seed crystals was determined by krypton gas adsorption following standard BET procedures. The BET surface area of the norsethite seed crystals was determined to be $0.035 \pm 10$ % m$^2$/g.

## 4.3.2 Results

*4.3.2.1 Determination of norsethite solubility product*

The results of the solubility experiments are listed in Table A 4.3-1and Table A 4.3-2. The ionic strength (reported in Table A 4.3-2) and carbonate speciation were calculated iteratively from the measured pH, TDIC values as well as Ba and Mg concentrations (Table A 4.3-1). The apparent solubility product for reaction 1.4-1 is defined as $K_{\text{app-sp-nrs}} = [Ba^{2+}][Mg^{2+}][CO_3^{2-}]^2$, where [$i$] designates the molal concentration of the $i^{th}$ aqueous species. The solubility product at infinite dilution can then be expressed as:

$$K_{\text{sp°-nrs}} = K_{\text{app-sp-nrs}}(\gamma_{Ba^{2+}})(\gamma_{Mg^{2+}})(\gamma_{CO_3^{2-}})^2, \qquad (4.3\text{-}1)$$

where $\gamma_i$, the mean activity coefficient of the $i^{th}$ aqueous species, was derived from the Meissner equation (Bénézeth et al., 2009; 2011; 2013; Gautier et al., 2016; Lindsay, Jr, 1989) assuming for an ion of charge $z$:

$$\gamma_i |z| = \gamma_{\pm(NaCl)}^{z^2},$$
(4.3-2)

where $\gamma_{\pm(NaCl)}$ stands for the mean molal stoichiometric activity coefficient of NaCl. The mean activity coefficient values were calculated from Archer (1992), and are reported in Table A 4.3-2 together with the ionic strength and the calculated solubility products (see details in Bénézeth et al., 2018). The uncertainties assigned to the constants ($\pm 0.3$) are estimated from the combined experimental uncertainties ($3\sigma$). Note that few data from Table A 4.3-2 (indicated by italics) were excluded from further consideration as the experimental equilibrium likely was not fully achieved. This was usually the case for the first sample after a temperature switch or because the Ba/Mg ratio indicated a possible precipitation of witherite (e.g., S3.5 and S3.6) reached a ratio of 0.51). XRD analysis of the crystals retrieved from such experiments confirmed precipitation of witherite (up to ~2 wt.%). No witherite has been found in experiment S1 and only traces (<1 wt.%) were found in experiment S2 (Figure Suppl1). The logarithms of the solubility products calculated in the way described above were plotted as a function of the reciprocal temperature (Figure 4.3-1). The only value of the solubility product existing so far was experimentally determined by Königsberger et al. (1998) at 25 °C. This data point has been added to the plot.

Table 4.3-1: Starting conditions of the individual growth experiments as well as masses of crystals before and after the experiments. Inlet solutions from containers 1 and 2 were pumped into the reactor with a flow rate ratio of 1:1. For each experiment. a new inlet fluid and seed crystal powder was used. Nomenclature of experiments corresponds to experimental temperature followed by an incremental number. ($m_0$: starting mass of seed crystals, $m_1$: final mass of seed crystals, $\Delta$ m: crystal mass difference)

| | | ——Reservoir 1—— | | | −Reservoir 2− | | | | | | |
|---|---|---|---|---|---|---|---|---|---|---|---|
| Exp. | T [°C] | Ba [mM] | Mg [mM] | NaCl [mM] | NaHCO$_3$ [mM] | NaCl [mM] | Mg: Ba | $m_0$ [g] | $m_1$ [g] | $\Delta$ m [g] | $\Delta$ m [%] |
| G40.1 | 40 | 10.00 | 180.00 | 35 | 6.0 | 35 | 18 | 0.490 | 0.626 | 0.127 | 25.5 |
| G40.2 | 40 | 1.50 | 50.00 | 25 | 10.0+ | 25 | 33 | 0.501 | 0.913 | 0.412 | 82.2 |
| G40.3 | 40 | 1.00 | 10.00 | 81 | 10.0 | 81 | 10 | 0.192 | 0.233 | 0.041 | 21.4 |
| G65.1 | 65 | 5.00 | 80.00 | 70 | 6.0 | 70 | 16 | 0.442 | 0.594 | 0.152 | 34.4 |
| G65.2 | 65 | 1.00 | 20.00 | 70 | 10.0+ | 70 | 20 | 0.437 | 0.766 | 0.329 | 75.3 |
| G65.3 | 65 | 2.00 | 10.00 | 81 | 5.0+ | 81 | 5 | 0.397 | 0.481 | 0.084 | 21.2 |
| G65.4 | 65 | 4.00 | 20.00 | 70 | 10.0 | 70 | 5 | 0.399 | 0.704 | 0.305 | 76.4 |
| G100.1 | 100 | 0.052 | 0.360 | 70 | 50.0 | 70 | 7 | 0.4035 | 0.4212 | 0.0177 | 4.4 |
| G100.2* | 100 | 0.021 | 0.150 | 70 | 25.0 | - | 7 | 0.4033 | 0.4697 | 0.0664 | 16.5 |
| G100.3 | 100 | 0.075 | 0.46 | 70 | 50.0 | 70 | 6 | 0.4031 | 0.4269 | 0.0238 | 5.9 |
| G100.4 | 100 | 0.110 | 0.70 | 70 | 25.0 | 70 | 6 | 0.4045 | 0.4314 | 0.0269 | 6.7 |
| G100.5* | 100 | 0.016 | 0.120 | 70 | 25.0 | - | 8 | 0.4019 | 0.4249 | 0.023 | 5.7 |
| G100.6* | 100 | 0.026 | 0.120 | 70 | 25.0 | - | 5 | 0.4008 | 0.3989 | -0.0019 | -0.5 |

*only one reservoir used
+0.5 mM Na$_2$CO$_3$ added

*4.3.2.2 Analysis of crystals and solutions from growth experiments*

SEM images of the retrieved product crystals revealed no significant change in morphology in comparison to the norsethite seed crystals (Figure 4.3-2). The product powders consisted of prisms (up to 500 μm long) with clearly defined crystal faces and an appearance similar to previously synthesized norsethite seeds (Lindner et al., 2017; Lindner and Jordan, 2018; Lippmann, 1973). XRD patterns of the starting seeds and the products of the growth experiments showed no other phase than norsethite (Figures 4.3-3 & Suppl1). All peaks could be indexed using the crystallographic data given in literature (Effenberger et al., 2014; Ende et al., 2017). IR spectroscopy measurements revealed no differences between seed and product crystals (Figures 4.3-4 & Suppl2) and all vibration modes could be attributed to norsethite bands (Böttcher et al., 1997).

In the course of the growth experiments, the mass of crystals in the reactor increased significantly (cf. Table 4.3-1). The increase in weight was attributed to newly precipitated norsethite as no other phase could be detected. Only in experiment NRS.8 a weight loss of −0.5 wt.% was found. The weight loss can be attributed to an incomplete retrieval of the solid material after the experiment (up to ten percent of crystals can easily be lost during retrieval from the reactor). This assumption is supported by solution analysis, which clearly indicated precipitation of 18 ± 2 mg of norsethite rather than dissolution.

Alkalinity as well as Ba and Mg concentrations of the effluents were measured at frequent intervals (Table A 4.3-3). Mean concentrations at steady state conditions were calculated from the individual samples (Table 4.3-2). Compared to the inlet solutions, significant decreases of alkalinities as well as Ba and Mg concentrations were detected. The decrease of alkalinity (Δalkalinity) was approximately two times as high as the sum of Ba and Mg decrease (ΔBa + ΔMg), whereas Ba and Mg decreases were similar in all samples (Figure 4.3-5). This concurs with the stoichiometric growth of norsethite according to Eq. 1.4-1.

Table 4.3-2: Mean values of steady state conditions of the growth experiments, which were calculated from the indicated range of samples given in Table A 4.3-3 (FR: flowrate, TA: total alkalinity, Rate$_{nrs}$: norsethite growth rate).

| Sample | FR [ml/ min] | pH | TA [meq/ l] | Ba [mM] | Mg [mM] | Ba: Mg | ΔTA [meq/ l] | ΔBa [mM] | ΔMg [mM] | Rate$_{nrs}$ [nmol m$^{-2}$ s$^{-1}$] | Ω norsethite |
|---|---|---|---|---|---|---|---|---|---|---|---|
| G40.1 1–5 | 0.6 | 7.52 | 2.65 | 4.69 | 88.69 | 19 | 0.43 | 0.09 | 0.13 | 53±4 | 150±12 |
| G40.1 6–12 | 0.3 | 7.61 | 2.53 | 4.65 | 88.78 | 19 | 0.54 | 0.14 | 0.13 | 31±2 | 191±15 |
| G40.2 2–5 | 0.7 | 7.89 | 5.12 | 0.45 | 24.29 | 54 | 1.00 | 0.25 | 0.25 | 140±11 | 210±17 |
| G40.2 6–12 | 0.3 | 7.99 | 5.01 | 0.45 | 24.51 | 55 | 1.06 | 0.26 | 0.27 | 55±4 | 290±23 |
| G40.3 3–6 | 0.27 | 8.23 | 4.92 | 0.39 | 4.93 | 13 | 0.32 | 0.05 | 0.10 | 52±4 | 249±20 |
| G40.3 7–12 | 0.45 | 8.16 | 4.99 | 0.38 | 4.98 | 13 | 0.24 | 0.07 | 0.05 | 99±8 | 191±15 |
| G40.3 13–18 | 0.15 | 8.27 | 4.84 | 0.37 | 4.93 | 13 | 0.39 | 0.08 | 0.12 | 33±3 | 271±22 |
| G40.3 19–21 | 0.72 | 8.22 | 5.11 | 0.42 | 4.99 | 12 | 0.14 | 0.03 | 0.04 | 55±4 | 279±22 |
| G65.1 8–11 | 0.5 | 7.21 | 2.59 | 2.29 | 39.58 | 17 | 0.49 | 0.10 | 0.14 | 43±3 | 33±3 |
| G65.1 12–14 | 0.8 | 7.20 | 2.67 | 2.30 | 39.54 | 17 | 0.42 | 0.09 | 0.12 | 57±5 | 38±3 |
| G65.1 15–18 | 0.2 | 7.07 | 2.25 | 2.19 | 39.52 | 18 | 0.84 | 0.20 | 0.20 | 31±2 | 13±1 |
| G65.2 3–7 | 0.3 | 7.57 | 4.48 | 0.25 | 9.75 | 38 | 1.02 | 0.23 | 0.28 | 62±5 | 30±2 |
| G65.2 8–12 | 0.5 | 7.62 | 4.71 | 0.28 | 9.87 | 35 | 0.77 | 0.20 | 0.19 | 75±6 | 46±4 |
| G65.2 13–15 | 0.8 | 7.46 | 4.78 | 0.30 | 9.93 | 33 | 0.69 | 0.19 | 0.15 | 103±8 | 37±3 |
| G65.2 16–19 | 0.2 | 7.47 | 4.41 | 0.21 | 9.82 | 46 | 1.07 | 0.27 | 0.25 | 34±3 | 16±1 |
| G65.3 3–8 | 0.3 | 7.79 | 2.76 | 0.77 | 4.59 | 6 | 0.53 | 0.15 | 0.18 | 101±8 | 49±4 |
| G65.3 9–12 | 0.8 | 7.91 | 2.86 | 0.78 | 4.61 | 6 | 0.45 | 0.14 | 0.14 | 205±16 | 91±7 |
| G65.3 13–17 | 0.5 | 7.77 | 2.78 | 0.71 | 4.64 | 7 | 0.53 | 0.20 | 0.10 | 168±13 | 36±3 |
| G65.4 5–8 | 0.3 | 7.32 | 4.06 | 1.73 | 9.83 | 6 | 1.10 | 0.23 | 0.31 | 120±10 | 56±4 |
| G65.4 9–12 | 0.8 | 7.35 | 4.25 | 1.81 | 9.88 | 5 | 0.89 | 0.15 | 0.29 | 165±13 | 73±6 |
| G65.4 13–16 | 0.4 | 7.28 | 4.07 | 1.65 | 9.95 | 6 | 1.06 | 0.31 | 0.23 | 165±13 | 46±4 |
| G100.1 1–7 | 1.2 | 8.07 | 24.54 | 0.0058 | 0.1652 | 29 | 0.08 | 0.0215 | 0.0188 | 29±2 | 13.1±1 |
| G100.1 8–11 | 1.6 | 8.05 | 18.36 | 0.0070 | 0.2057 | 29 | 0.10 | 0.0268 | 0.0229 | 49±4 | 11.5±0.9 |
| G100.1 12–17 | 1.4 | 8.03 | 13.88 | 0.0067 | 0.2336 | 35 | 0.12 | 0.0320 | 0.0274 | 51±4 | 7.7±0.6 |
| G100.2 1–7 | 1.0 | 7.82 | 25.01 | 0.0035 | 0.1233 | 35 | 0.11 | 0.0150 | 0.0152 | 18±1 | 2.2±0.2 |
| G100.2 8–11 | 0.5 | 7.85 | 25.02 | 0.0023 | 0.1219 | 52 | 0.11 | 0.0162 | 0.0166 | 9±1 | 1.4±0.1 |
| G100.2 12–16 | 1.8 | 7.88 | 25.04 | 0.0036 | 0.1235 | 34 | 0.08 | 0.0149 | 0.0150 | 32±3 | 3.3±0.3 |
| G100.3 4–8 | 1.2 | 7.85 | 25.11 | 0.0053 | 0.1997 | 37 | 0.13 | 0.0309 | 0.0279 | 42±3 | 5.9±0.5 |
| G100.3 9–13 | 1.1 | 7.84 | 25.46 | 0.0042 | 0.1962 | 46 | 0.14 | 0.0320 | 0.0315 | 43±3 | 4.5±0.4 |
| G100.4 1–3 | 1.5 | 7.72 | 12.40 | 0.0164 | 0.3083 | 19 | 0.15 | 0.0393 | 0.0411 | 67±5 | 5.4±0.4 |
| G100.4 5–8 | 1.5 | 7.77 | 12.35 | 0.0127 | 0.3044 | 24 | 0.17 | 0.0430 | 0.0452 | 72±6 | 5.1±0.4 |
| G100.4 10–13 | 1.5 | 7.75 | 12.25 | 0.0103 | 0.3036 | 30 | 0.19 | 0.0456 | 0.0469 | 74±6 | 3.6±0.3 |
| G100.5 1–9 | 0.5 | 7.82 | 25.01 | 0.0026 | 0.1087 | 42 | 0.11 | 0.0133 | 0.0142 | 8±1 | 1.6±0.1 |
| G100.5 10–16 | 1.2 | 7.84 | 25.06 | 0.0044 | 0.1122 | 26 | 0.06 | 0.0115 | 0.0106 | 16±1 | 2.5±0.2 |
| G100.5 17–21 | 2.0 | 7.89 | 25.07 | 0.0053 | 0.1127 | 21 | 0.05 | 0.0106 | 0.0101 | 25±2 | 3.8±0.3 |
| G100.6 1–7 | 1.5 | 7.82 | 24.96 | 0.0032 | 0.2005 | 62 | 0.08 | 0.0215 | 0.0251 | 38±3 | 3.1±0.2 |
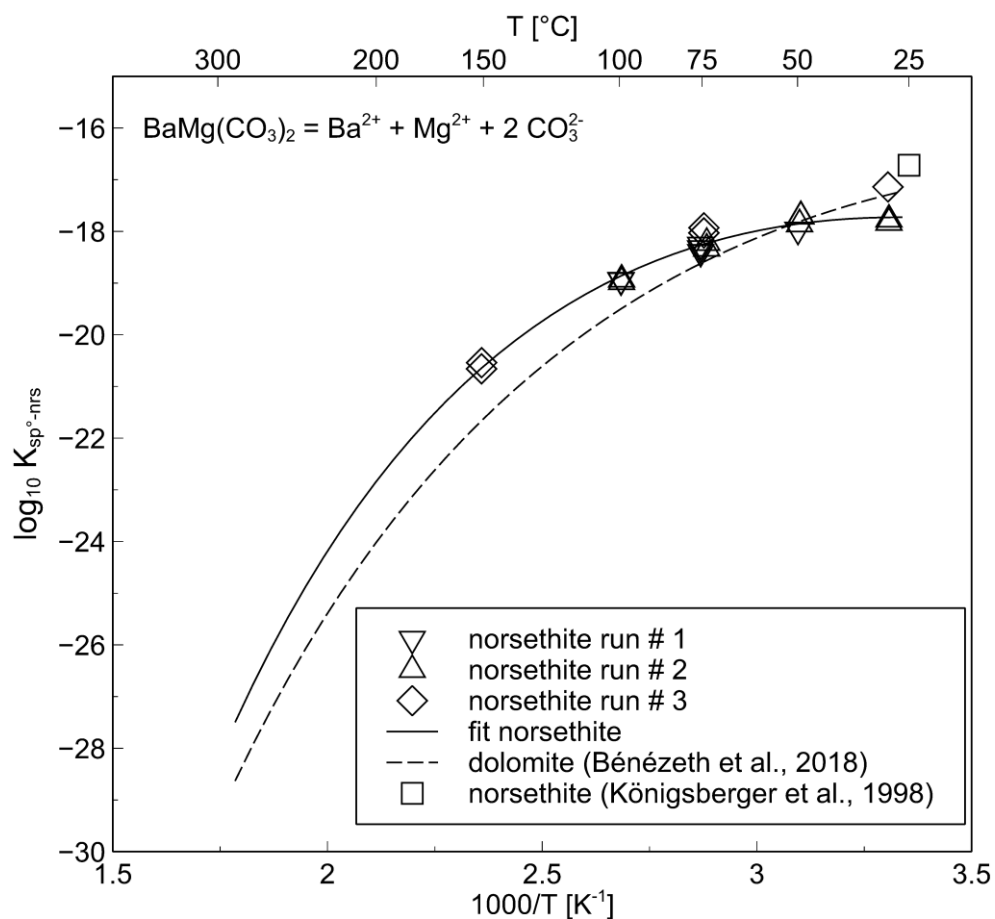
Figure 4.3-1: Logarithm of norsethite solubility product obtained in this study as a function of reciprocal temperature with the fit of the data (the uncertainties, ± 0.3, correspond to the size of the symbol). For comparison, the 25 °C value from Königsberger et al. (1998) as well as the fit of the dolomite solubility product determined by Bénézeth et al. (2018) is reported on the plot.
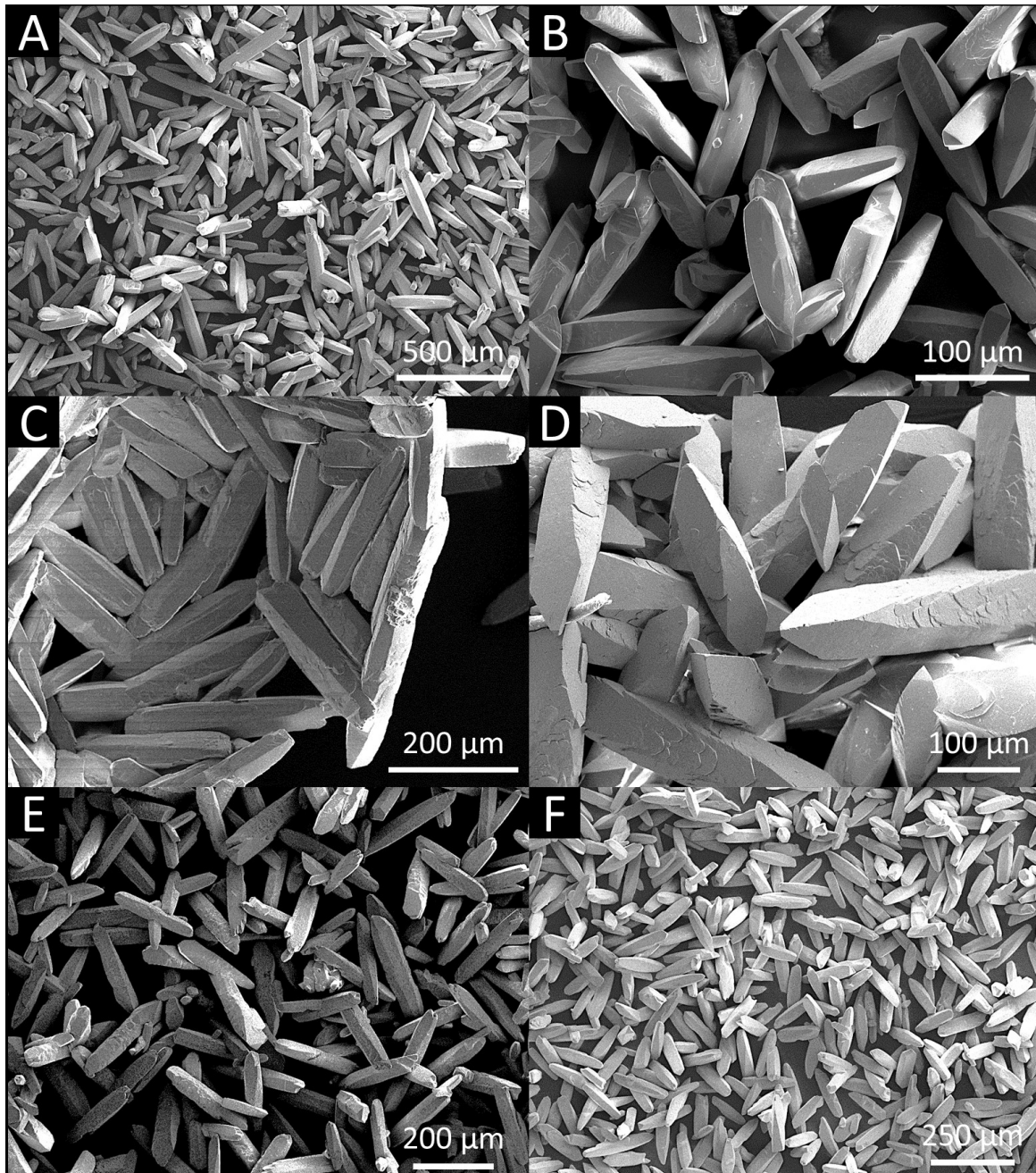
Figure 4.3-2: SEM images of norsethite seed crystals before experiments (A & B), after experiments at 40 °C (C: G40.1 & D: G40.2) and 100 °C (E: G100.1 & F: G100.6). No other phase than norsethite is discernible. Apart from an increase in size, no significant alteration of the crystals by the experiments is noticeable.
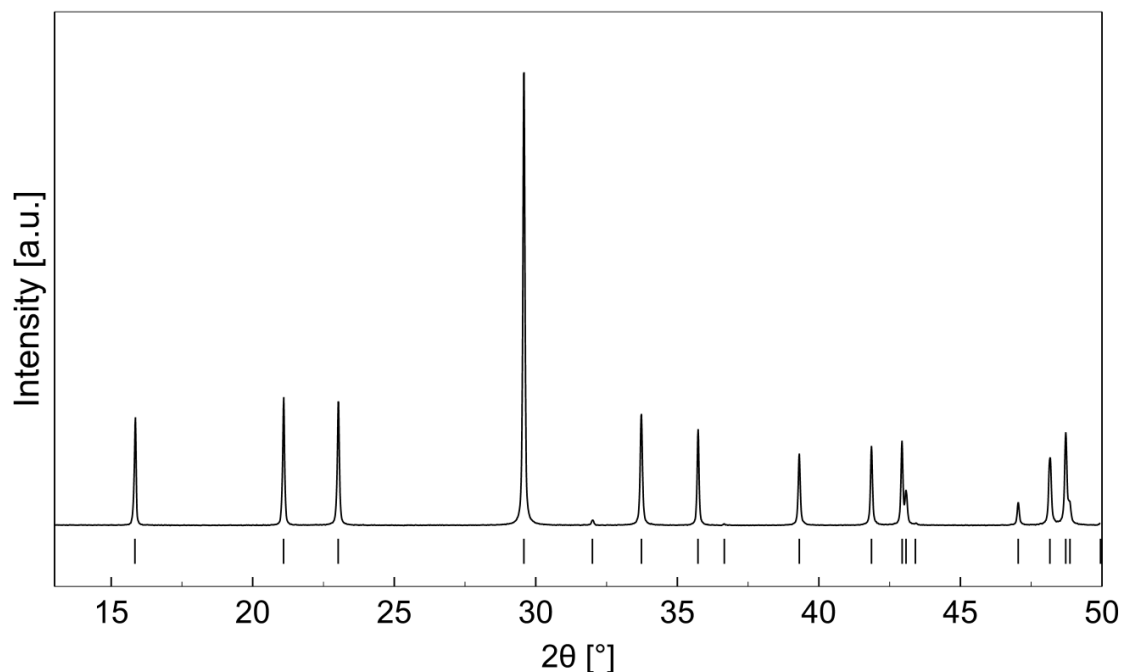
Figure 4.3-3: Exemplary X-ray diffractograms pattern of crystals retrieved from experiment G40.2 shows no signs of newly precipitated phases. All peaks can be attributed to norsethite (vertical lines, after Ende et al., 2017). The diffractograms of product powders of the other growth experiments (Figure Suppl1) do not differ significantly from the one shown.
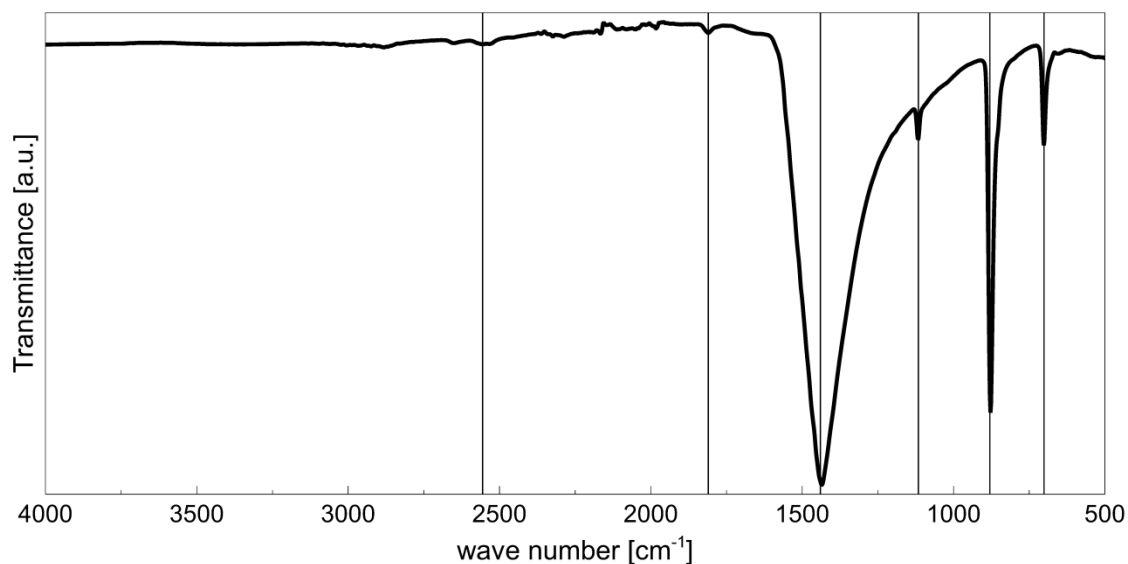


Figure 4.3-4: Exemplary infrared spectrum of norsethite seed crystals. The vertical lines indicate the positions of IR spectroscopic data of norsethite available in the literature (Böttcher et al., 1997), all of which can be detected in the measured spectra. No other phase is discernible apart from norsethite. No bands of OH-group vibrations are observable in the region around 3500 cm$^{-1}$, validating the water-free structure. Spectra of the product powders of the growth experiments (Figure Suppl2) do not differ significantly from the one shown
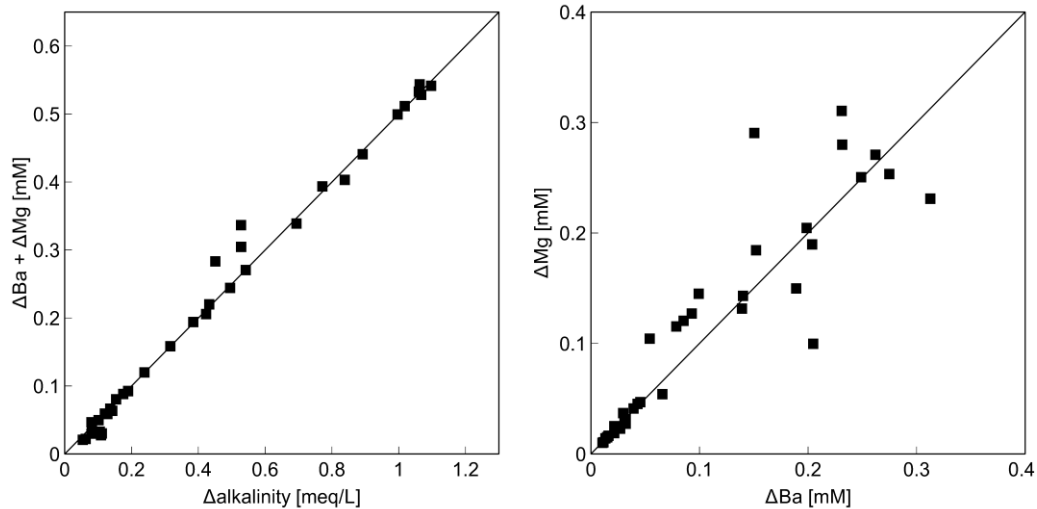
Figure 4.3-5: Mean measured concentration difference of cations (ΔBa + ΔMg) vs. total alkalinity (Δalkalinity) variation [left] and mean differences of Ba (ΔBa) and Mg (ΔMg) [right] between inlet and outlet fluid of the growth experiments show good charge balance and are consistent with stoichiometric norsethite growth (solid lines).

### 4.3.2.3 Determination of norsethite growth rates as a function of saturation state and temperature

By the application of SEM, IR spectroscopy, XRD and aqueous solution analysis, special emphasis was given to the detection of potential crystallization of witherite and various Mg-carbonate phases (e.g., magnesite, hydromagnesite, nesquehonite) accompanying norsethite precipitation, but none was found within the reaction products of the growth experiments. SEM images of retrieved crystals (Figure 4.3-2), for instance, showed clearly that growth of the seed crystals rather than nucleation of new secondary phases took place. Due to the analytical limitations of the applied techniques, however, the presence of foreign phases in the crystal powders cannot be excluded completely, but their abundance has to be less than 1 wt.%. The extensive precipitation observed during the experiments can thus be safely attributed to norsethite growth and the effects of secondary phases on the calculated growth rates can be neglected.

The precipitation reaction led to an increased surface area of norsethite crystals. In the calculation of the growth rates, the increase of the surface area has been taken into account by increasing the mass of the crystals linearly over the experimental time towards the final value measured after the experiment. The specific surface area has not been modified in the calculations. The uncertainty attached to this procedure is estimated to be less than 10 %. Irrespective of the correction applied to the rate calculations, SEM images of retrieved crystals (see Figure 4.3-2) showed clearly that growth of the seed crystals rather than newly nucleated crystals was the main cause of mass increase.
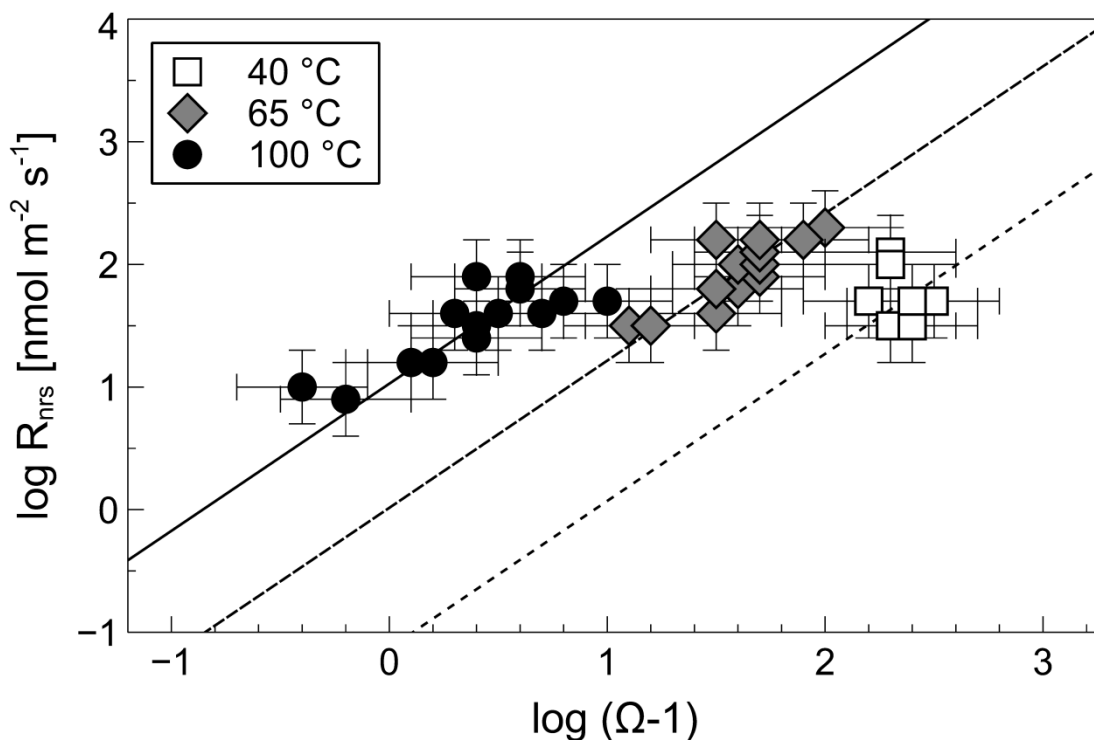
Figure 4.3-6: Logarithmic plots of measured norsethite growth rates $R_{nrs}$ vs. supersaturation $\Omega$ with respect to norsethite. Datasets at 40, 65 and 100 °C have been fitted to an equation of the form $R=k(\Omega-1)^n$ with an order of reaction n = 1.2 ± 0.1 (slope). The obtained values of the reaction constant $k$ (intercept with $y$-axis)are listed in Table 4.3-3.

Norsethite growth rates were calculated according to Eq. 3.1-1 using the measured decrease of Ba concentration ($\Delta M = \Delta Ba$). Growth rates calculated using $\Delta Mg$ values do not differ by more than 8 % from those calculated using $\Delta Ba$. However, speciation calculations showed that the solutions were supersaturated with respect to various Mg-carbonates while all Ba-containing phases except norsethite were undersaturated. Therefore, the use of $\Delta Ba$ further precludes potential effects of co-precipitating phases (although none was detected with the applied methods) on the calculation of norsethite growth rates.

Measured growth rates $R$ were fitted to the empirical equation:

$$R = k(\Omega - 1)^n, \tag{4.3-3}$$

which is commonly used to calculate the rate constant $k$ and the order $n$ of the growth reaction for carbonate minerals precipitation (e.g., Arvidson and Mackenzie, 1999; Berninger et al., 2016; Busenberg and Plummer, 1986a; Gautier et al., 2015; Mucci and Morse, 1983; Nancollas and Reddy, 1971; Saldi et al., 2009). For each of the investigated temperatures, an individual rate constant $k$ has been determined using a reaction order $n$ = 1.2 ± 0.1, as this value yielded the best fit of the data (Figure 4.3-6, Table 4.3-3).

Table 4.3-3: Values of rate constants $k$ obtained from the fit of growth rates plotted in Figure 4.3-6.

| Temperature [°C] | log $k$ [nmol m$^{-2}$ s$^{-1}$] | $\chi^2$ |
|---|---|---|
| 40 | −1.13 ± 0.03 | 8.2 |
| 65 | 0.02 ± 0.01 | 2.8 |
| 100 | 1.03 ± 0.02 | 6.6 |

The temperature variation of the rate constant $k$ is commonly described by the Arrhenius equation:

$$k = A \cdot e^{-E_a/RT}, \tag{4.3-4}$$

where $A$ refers to a pre-exponential factor, $E_a$ corresponds to the apparent activation energy of the reaction, $R$ stands for the gas constant and $T$ for the absolute temperature (Arvidson and Mackenzie, 1999; Berninger et al., 2014; Gautier et al., 2014; Saldi et al., 2012). An Arrhenius plot of the growth rate constants is shown in Figure 4.3-7. The determined rate constants are consistent with an Arrhenius behavior and the linear regression of the data points yields an apparent activation energy $E_a$ of 80 ± 7 kJ/mol with an intercept of 1921 ± 150 mol m$^{-2}$ s$^{-1}$. The extrapolation to 25 °C results in a rate constant of $k_{\text{nrs}}^{25\,°C}$ = 1.8 x 10$^{-2}$ nmol m$^{-2}$ s$^{-1}$. No effect of the displacive phase transition occurring at 90 °C (Effenberger et al., 2014; Ende et al., 2017) could be discerned in the kinetic and solubility data.

## 4.3.3 Discussion

### 4.3.3.1 Norsethite solubility

The experimentally determined solubility products of norsethite at different temperatures (Table A 4.3-2) were fitted with the function:

$$\log_{10} K_{\text{sp°-nrs}} = a + b/T + cT, \tag{4.3-5}$$

where $a$, $b$, and $c$ are regression coefficients, respectively equal to 31.007, −7321.122 and −0.0811, which yield the solid curve in Figure 4.3-1 from 25 to 300 °C and a log $K_{\text{sp°-nrs}}$ of −17.73 at 25 °C. This room temperature value is one log unit lower than the one determined by Königsberger et al.(1998) and 0.5 log unit lower than the value for dolomite determined by Bénézeth et al. (2018). In the temperature range of 25 to 50 °C, the norsethite fit exhibits a plateau. At temperatures up to 100 °C, the norsethite fit is 1.1 to 1.2 log units higher than the fit of the $T$-dependence of dolomite (dashed curve, Bénézeth et al., 2018).
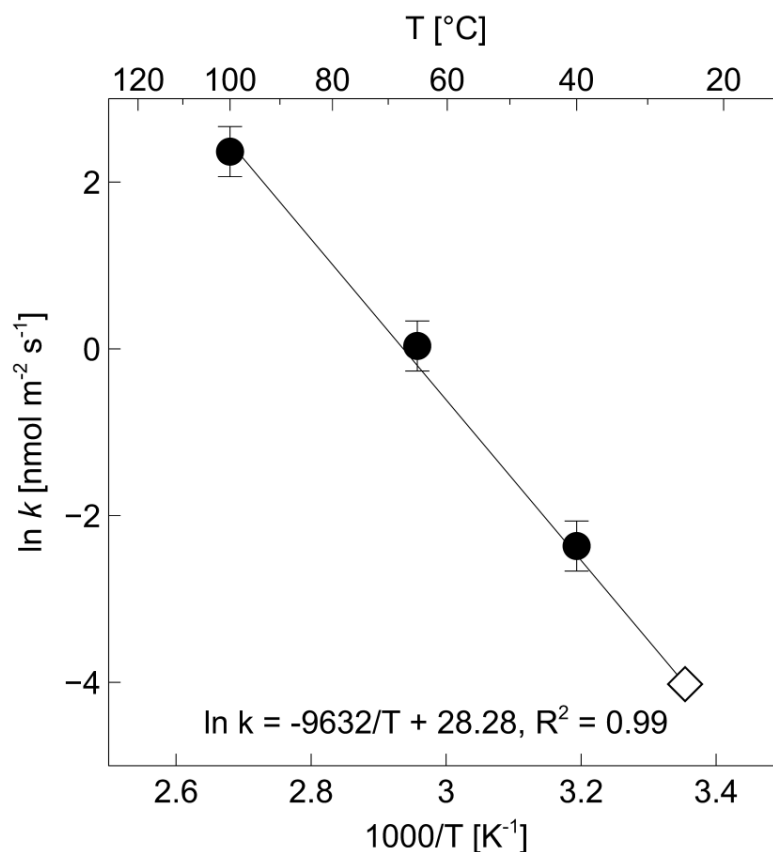
Figure 4.3-7: Arrhenius plot of growth rate constants $k$ as a function of reciprocal absolute temperature. Black circles represent rate constants listed in Table 4.3-3; the line corresponds to a linear least square fit of the rate constants. The slope of this line is consistent with $E_a = 80 \pm 7$ kJ/mol and $A = 1921 \pm 150$ mol m$^{-2}$ s$^{-1}$. The open diamond stands for the extrapolated value at 25 °C (ln $k^{25\,°C} = -4.02$ nmol m$^{-2}$ s$^{-1}$).

Based on Eq. 4.3-5 and its first and second derivatives with respect to $T$, the standard free energy and enthalpy for Eq. 1.4-1 (retrograde) can be calculated (see details in Bénézeth et al., 2013). Combining the values obtained with the thermodynamic properties of Ba$^{2+}$ given by Busenberg and Plummer (1986b) and of Mg$^{2+}$ and CO$_3^{2-}$ taken from Shock et al. (1997), the norsethite Gibbs energy of formation ($\Delta_f G^0_{298.15}$) yielded a value of $-2167 \pm 2$ kJ/mol and a norsethite enthalpy of formation ($\Delta_f H^0_{298.15}$) of $-2351 \pm 2$ kJ/mol. The Gibbs free energy of formation is in very good agreement with the one proposed by Böttcher et al., (1997) ($-2166.6$ kJ/mol), using a method described by La Iglesia and Félix (1994). However, the solubility product at 25 °C ($-16.81$) derived by Böttcher et al. (1997) is in closer agreement with Königsberger et al. (1998). The difference to our extrapolated value is mainly due to a difference in the thermodynamic properties of aqueous species (Ba$^{2+}$, Mg$^{2+}$ and CO$_3^{2-}$), taken from Wagman et al. (1982) by Böttcher et al. (1997). This disparity demonstrates that using various sources and not internally consistent thermodynamic properties can lead to large difference in the calculated solubility product when not directly measured or extrapolated by

using measurements performed in a wide range of temperature (e.g., Bénézeth et al., 2013).

The difference of the experimentally determined solubilities to the 25 °C value given by Königsberger et al. (1998) might be explained by the different solid material used. Crystallinity, crystal morphology, and size fraction of the material used by Königsberger et al. (1998) are unknown. These factors might have some impact on the determined solubility product.

Nevertheless, the new solubility data obtained here can serve as reliable input-parameters for the calculation of the solution speciation and supersaturation in norsethite growth experiments as all experiments were performed with the same type of norsethite seed material.

*4.3.3.2 Norsethite growth rates in comparison to other carbonate minerals*

The growth experiments conducted here represent the first systematic quantitative study of norsethite growth kinetics, covering a wide span of temperatures and solution compositions. The norsethite growth rate exhibits an almost linear dependence on solution saturation state ($n = 1.2$ in equation 4.3-3). Such a linear rate law was suggested to be related to a transport controlled or an adsorption controlled growth mechanism (Nielsen, 1983). Here, the transport controlled mechanism can be discarded given the high stirring speeds inside the reactors, the determined activation energy of norsethite growth (80 kJ/mol), as well as the general appearance of the crystals with clearly defined faces. Adsorption controlled growth was observed on a few occasions for calcite (Nancollas and Reddy, 1971; Reddy and Nancollas, 1971; Shiraki and Brantley, 1995) as well as a transient state in magnesite precipitation (Schott et al., 2012). However, without direct evidence (e.g., by atomic force microscopy), conclusions on the growth processes occurring at the mineral surface are to be made with caution (Teng et al., 2000)

Norsethite growth rates determined in this study can be directly compared to the growth rates of other anhydrous carbonate minerals. Experimentally determined magnesite growth rates in the temperature range of 80 – 200 °C have been reported by several authors using various micro- and macroscale techniques (Berninger et al., 2016; Bracco et al., 2014; Gautier et al., 2015; King et al., 2013; Saldi et al., 2009; 2012). At 100 °C, a rate constant equal to $6.5 \times 10^{-3}$ nmol m$^{-2}$ s$^{-1}$ was reported by Saldi et al. (2009). Quantitative rate data for dolomite growth are less numerous. One of the few quantitative studies was published by Arvidson and Mackenzie (1999), who provided growth rate constants, a reaction order, and an activation energy. Their macroscopic mixed-flow reactor study covered a temperature range of 120 – 200 °C. Extrapolating their rate constants to 100 °C yields a value of $2.3 \times 10^{-5}$ nmol m$^{-2}$ s$^{-1}$. Growth rates of calcite at 100 °C have been determined by Shiraki and Brantley (1995) with rate constants of $2.3 \times 10^4$ and $1 \times 10^4$ nmol m$^{-2}$ s$^{-1}$ for adsorption and spiral growth control, respectively. Witherite
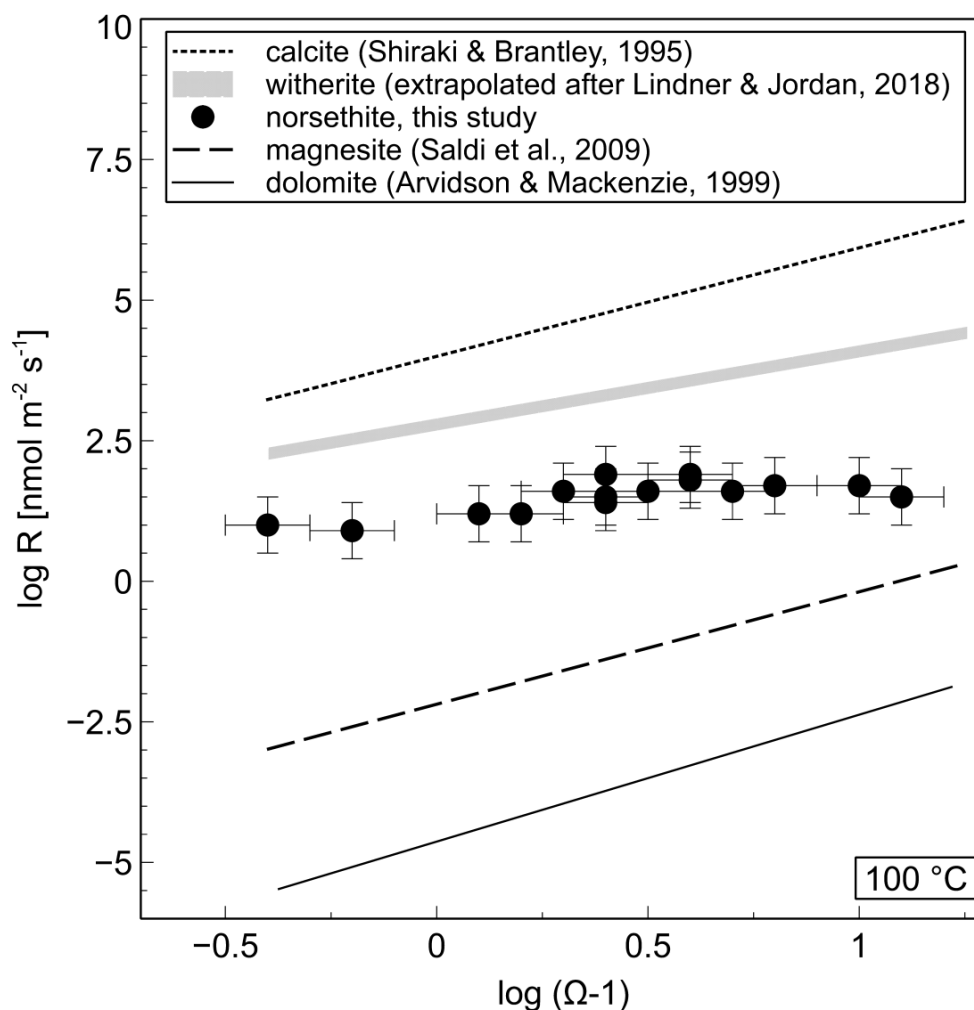
Figure 4.3-8: Logarithmic plot of experimentally determined growth rates of norsethite, growth rates of dolomite calculated after Arvidson and Mackenzie (1999), magnesite growth rates reported by Saldi et al. (2009), calcite growth rates (spiral growth mechanism, Shiraki and Brantley, 1995) and witherite growth rates (extrapolated with an apparent activation energy of 40–50 kJ/mol from the 50 °C value provided by Lindner and Jordan, 2018) at 100 °C vs. the solution saturation state with the respective phase. The growth rate constant of norsethite is about three and five orders of magnitude higher than that of magnesite and dolomite, respectively, and approximately two and three orders of magnitude lower than that of witherite and calcite, respectively.

growth has been measured at 50 °C (Lindner and Jordan, 2018). An estimated apparent activation energy in the range of 40–50 kJ/mol, comparable with calcite and norsethite values, was used to extrapolate the reported rate constant (65 nmol m$^{-2}$ s$^{-1}$ at 50 °C) to 100 °C. Comparison of all these data shows that the growth rate constant of norsethite at 100 °C is approximately three and five orders of magnitude higher than of magnesite and dolomite, respectively, while it is about two and three orders of magnitude lower than of witherite and calcite, respectively (Figure 4.3-8).

Although magnesite and dolomite do not precipitate at ambient conditions, it is possible to extrapolate the rate constants to a hypothetical growth at 25 °C using

the Arrhenius equation. The comparison of the hypothetical growth rate constants of magnesite ($k_{mgs}^{25\,°C} \approx 10^{-5}$ nmol m$^{-2}$ s$^{-1}$, Saldi et al., 2012) and dolomite ($k_{dol}^{25\,°C} \approx 10^{-10}$ nmol m$^{-2}$ s$^{-1}$, after after Arvidson and Mackenzie, 1999) with the norsethite value ($k_{nrs}^{25\,°C} \approx 10^{-2}$ nmol m$^{-2}$ s$^{-1}$) strikingly illustrates the extremely contrasting growth kinetics of anhydrous Mg-bearing carbonates at ambient conditions.

*4.3.3.3 Temperature dependence of growth of Mg-bearing carbonate minerals*

The data presented in this study yielded an apparent activation energy $E_a$ of 80 ± 7 kJ/mol for norsethite growth. The apparent activation energy derived from the measured macroscopic growth rates of magnesite between 100 – 200 °C is 80.2 kJ/mol (Saldi et al., 2012), while the activation energy for obtuse step advancement of magnesite determined by in-situ atomic force microscopy measurements at 80 – 120 °C is 159 kJ/mol (Saldi et al., 2009). Compared to magnesite, the hydrous Mg-carbonate hydromagnesite has a much lower apparent activation energy for growth (45.5 kJ/mol) and the mineral grows about 2.5 orders of magnitude faster at 90 °C (Gautier et al., 2014).

For the direct growth of dolomite from solution an activation energy of 133 kJ/mol has been reported by Arvidson and Mackenzie (1999). The activation energy for the dolomitization of CaCO$_3$ in Mg-rich solutions at 252 – 295 °C was determined to be ~200 kJ/mol (Katz and Matthews, 1977). Another study yielded an estimated activation energy for the reaction of calcite + magnesite to dolomite between 100 – 200 °C of 29 kJ/mol, which lies even below the value for magnesite growth, although it has to be noted that the experimental procedures are not necessarily comparable (Montes-Hernandez et al., 2014). Recently, the reaction of aragonite to dolomite at temperatures of 160 – 250 °C was studied in more detail, revealing a multi stage dissolution reprecipitation replacement reaction with several unordered intermediate phases (Kaczmarek and Sibley, 2014; Kaczmarek and Thornton, 2017). Their extrapolation of time to form dolomite down to lower temperatures fits well with the data of Usdowski (1989, 1994), who showed that it took about 7 years to produce dolomite in experiments at 60 °C.

The activation energies for the growth of magnesite (80.2 kJ/mol, Saldi et al., 2012) and dolomite (133 kJ/mol, Arvidson and Mackenzie, 1999) are comparable to norsethite (80 kJ/mol) and significantly higher than that for calcite (45 kJ/mol, Dromgoole and Walter, 1990; Nancollas and Reddy, 1971). However, neither cation-ordering nor Mg-dehydration inhibit norsethite growth to an extent anywhere close to the extent assumed for dolomite or magnesite. This is particularly pronounced at lower temperatures: below 60 °C neither magnesite nor dolomite have ever been synthesized from simple aqueous solutions – not even over a timespan of several years (Land, 1998; Usdowski, 1989; 1994), while norsethite can easily be grown at ambient conditions within days (e. g., Hood et al., 1974; Lippmann, 1973).

*4.3.3.4 Implication for anhydrous Mg-carbonate growth*

Recent work concerning dolomite and magnesite growth has focused on the effects of organic or inorganic compounds or microorganisms (e.g., Berninger et al., 2016, Bontognali et al., 2014, Gautier et al., 2015, 2016, Kenward et al., 2013, Krause et al., 2012, Petrash et al., 2017, Power et al., 2017, Roberts et al., 2013, Sanz-Montero and Rodríguez-Aranda, 2012,Wright and Wacey, 2005, Vasconcelos et al., 1995, Wu et al., 2011, Zhang et al., 2012b, 2012a, 2013). Although the emergence of "ordered" dolomite in many of these experiments is under debate (e.g., Gregg et al., 2015), the possibility to enhance dehydration and incorporation of $Mg^{2+}$ during the formation of magnesite and unordered "proto-dolomite" shows the important influence of functional groups of molecules and surfaces to accelerate mineral nucleation and growth.

During the growth of the anhydrous Mg-carbonate norsethite, therefore, some effective means must obviously exist which promotes the dehydration of the Mg ion and allows for the rapid incorporation of dehydrated $Mg^{2+}$ into the growing crystal. In the absence of functional additives (as in our experiments), this promoting process can only be located at the norsethite surface. There, the hydration energy of $Mg^{2+}$ can significantly differ from the value in the bulk solution enabling ready incorporation even at room temperature. In fact, two cases are known which show that norsethite surfaces are not the only surfaces where dehydration and incorporation of the Mg ions takes place at high rates:

i) $PbMg(CO_3)_2$ has been precipitated at ambient conditions following the same procedure as for norsethite (Lippmann, 1966; 1973; Morrow and Ricketts, 1986; Pimentel and Pina, 2016). As $PbMg(CO_3)_2$ and norsethite are isostructural, with similar lattice parameters and carbonate group orientations, the important role of the norsethite surface structure for the ability to promote $Mg^{2+}$-dehydration becomes even more evident and certainly urges further investigation.

ii) Large differences were measured in the advance velocities of obtuse and acute monolayer-steps during growth on the (104) surface of magnesite (Saldi et al. 2009). Based on atomic force microscopy (AFM) observations, Saldi et al. (2009) found that obtuse steps propagate ~12 times faster than acute steps. In the case of spiral growth, the overall crystal growth rate is controlled by the advancement of the slowest step (Pina et al., 1998). On magnesite surfaces, growth rate therefore is controlled by the propagation of the slow acute steps only. The different dehydration and incorporation rates of Mg ions at the different steps, however, imply that acute steps miss the maximum possible rates. Consequently, magnesite growth could be ~12 times faster in principle, if the dehydration and incorporation kinetics of Mg ions at acute steps were adapted to those at obtuse steps.

The detailed mechanisms of fast $Mg^{2+}$ dehydration and incorporation on norsethite and $PbMg(CO_3)_2$ surfaces as well as at specific sites on magnesite surfaces are still unknown. A plausible explanation, however, is that certain structural

surface configurations are able to distort adsorbed hydrous Mg-complexes to a point where Mg-OH$_2$ bonds are critically weakened, dehydration is facilitated, and bonding of Mg$^{2+}$ to surface carbonate is established. Given the large difference of ionic radii of Ba$^{2+}$ and Mg$^{2+}$, the structural settings of cations at norsethite surface sites are clearly different to the structural configurations of magnesite and dolomite surfaces. These different structural surface settings can likely cause different degrees of strain on adsorbed hydrous Mg-complexes, which result in tremendously different dehydration and incorporation kinetics.

Although the differences in reactivity of the various typed of magnesite (104) surface sites are not as large as the differences between norsethite and magnesite, the same reasoning is applicable to explain the dissimilarity among the magnesite surface sites. On magnesite, even subtle structural modifications can cause a difference of one order of magnitude in ion attachment rates. Taking into account these considerations, the suggestion that a given surface can have an important catalytic role in the dehydration of metal complexes is inevitable.

Table A 4.3-1: Results of norsethite solubility experiments S1–S3 performed in 0.1 M NaCl solutions using the HECC. From each experiment up to eleven samples were taken, as indicated by the last figure of the sample name

| Sample | Temp. [°C] | −log(H$^+$)[a] measured *in situ* | log(Mg$^{2+}$)[a] | log(Ba$^{2+}$)[a] | TDIC[a] x 10$^3$ | CO$_3^{2-}$[a] x 10$^6$ | Equilibrium time [h] |
|---|---|---|---|---|---|---|---|
| S1.1 | 99.5 | 7.112 | −2.992 | −3.027 | 1.329 | 4.360 | 72 |
| S1.2 | 99.5 | 7.081 | −2.995 | −3.030 | 1.223 | 3.719 | 168 |
| S1.3 | 99.5 | 7.068 | −2.997 | −3.024 | 1.245 | 3.655 | 240 |
| S1.4 | 75.4 | 7.234 | −2.956 | −2.974 | 1.684 | 7.034 | 72 |
| S1.5 | 75.4 | 7.224 | −2.961 | −2.974 | 1.577 | 6.415 | 168 |
| S1.6 | 75.4 | 7.212 | −2.958 | −2.986 | 1.516 | 5.989 | 288 |
| S1.7 | 75.4 | 7.120 | −2.965 | −2.987 | 1.769 | 5.578 | 600 |
| S1.8 | 49.9 | 7.293 | −2.912 | −2.938 | 1.867 | 7.247 | 168 |
| S2.1 | 99.3 | 7.126 | −3.157 | −3.008 | 1.219 | 4.127 | 168 |
| S2.2 | 99.3 | 7.082 | −3.096 | −2.933 | 1.227 | 3.728 | 408 |
| S2.3 | 73.7 | 7.251 | −3.046 | −2.899 | 1.569 | 6.758 | 168 |
| S2.4 | 73.3 | 7.222 | −3.050 | −2.899 | 1.484 | 5.956 | 432 |
| S2.5 | 49.2 | 7.465 | −2.994 | −2.889 | 2.067 | 11.97 | 216 |
| S2.6 | 49.2 | 7.435 | −2.995 | −2.882 | 1.885 | 10.17 | 408 |
| S2.7 | 49.2 | 7.435 | −2.997 | −2.889 | 1.879 | 10.13 | 552 |
| S2.8 | 49.2 | 7.470 | −3.025 | −2.882 | 1.496 | 8.804 | 696 |
| S2.9 | 29.2 | 7.582 | −2.988 | −2.889 | 1.937 | 10.71 | 504 |
| S2.10 | 29.2 | 7.441 | −2.938 | −2.889 | 2.117 | 8.373 | 864 |
| S2.11 | 29.2 | 7.403 | −2.915 | −2.889 | 2.108 | 7.614 | 1008 |
| S3.1 | 150.8 | 6.853 | −3.135 | −2.992 | 0.735 | 0.968 | 72 |
| S3.2 | 150.0 | 6.824 | −3.158 | −2.998 | 0.704 | 0.859 | 192 |
| S3.3 | 74.5 | 7.296 | −3.032 | −2.873 | 1.876 | 9.067 | 96 |
| S3.4 | 74.5 | 7.273 | −3.047 | −2.865 | 1.767 | 8.080 | 288 |
| S3.5 | 29.4 | 7.739 | −2.973 | −2.827 | 2.096 | 16.84 | 216 |
| S3.6 | 29.4 | 7.785 | −2.772 | −3.061 | 2.157 | 19.29 | 384 |

[a]Measured molal concentrations in the experimental solutions.

Table A 4.3-2: Norsethite apparent solubility products, $K_{app\text{-sp-nrs}}$, at $I \approx 0.1$ molal NaCl, ionic strengths, $I$, activity coefficients, $\gamma_{\pm(NaCl)}$, and norsethite solubility products, $K_{sp°\text{-nrs}}$, calculated for all experiments performed in this study.

| Sample | Temp. [°C] | $\log_{10}K_{app\text{-sp-nrs}}$ | $I$ [mol/kg] | $\gamma_{\pm(NaCl)}$ | $\log_{10}K_{sp°\text{-nrs}}$ $\pm 0.3$§ |
|--------|-----------|------------------------------------|--------------|----------------------|--------------------------------------------|
| *S1.1* | *99.5* | *−16.74* | *0.1033* | *0.7441* | *−18.79* |
| S1.2 | 99.5 | −16.88 | 0.1031 | 0.7442 | −18.94 |
| S1.3 | 99.5 | −16.89 | 0.1033 | 0.7441 | −18.95 |
| *S1.4* | *75.4* | *−16.24* | *0.1039* | *0.7564* | *−18.18* |
| S1.5 | 75.4 | −16.32 | 0.1039 | 0.7564 | −18.26 |
| S1.6 | 75.4 | −16.39 | 0.1038 | 0.7564 | −18.33 |
| S1.7 | 75.4 | −16.46 | 0.1038 | 0.7670 | −18.40 |
| S1.8 | 49.9 | −16.13 | 0.1045 | 0.7670 | −17.97 |
| S2.1 | 99.3 | −16.93 | 0.1025 | 0.7454 | −18.98 |
| S2.2 | 99.3 | −16.89 | 0.1032 | 0.7449 | −18.93 |
| S2.3 | 73.7 | −16.29 | 0.1037 | 0.7573 | −18.22 |
| S2.4 | 73.7 | −16.40 | 0.1036 | 0.7573 | −18.33 |
| *S2.5* | *49.2* | *−15.73* | *0.1044* | *0.7672* | *−17.57* |
| S2.6 | 49.2 | −15.86 | 0.1043 | 0.7674 | −17.70 |
| S2.7 | 49.2 | −15.87 | 0.1043 | 0.7673 | −17.71 |
| S2.8 | 49.5 | −16.02 | 0.1042 | 0.7674 | −17.86 |
| *S2.9* | *29.2* | *−15.82* | *0.1043* | *0.7736* | *−17.60* |
| S2.10 | 29.2 | −15.98 | 0.1047 | 0.7733 | −17.77 |
| S2.11 | 29.2 | −16.04 | 0.1049 | 0.7729 | −17.83 |
| S3.1 | 150.8 | −18.16 | 0.1027 | 0.7100 | −20.54 |
| S3.2 | 150.0 | −18.29 | 0.1026 | 0.7106 | −20.66 |
| S3.3 | 74.5 | −15.99 | 0.1041 | 0.7567 | −17.93 |
| S3.4 | 74.5 | −16.10 | 0.1041 | 0.7568 | −18.03 |
| *S3.5* | *29.4* | *−15.35* | *0.1049* | *−0.7731* | *−17.14* |
| *S3.6* | *29.4* | *−15.26* | *0.1049* | *−0.7730* | *−17.05* |

§Uncertainties estimated from the combined experimental uncertainties. The data in italic were not used for the fit (see the text).

Table A 4.3-3: Results of single growth experiment samples (FR: flowrate, TA: total alkalinity). The first digits stand for the experimental temperature, the second figure refers to the experiment number according to Table 4.3-1 and the last figure corresponds to the sample number of each experiment.

| Sample | run-time [h] | FR [ml/min] | pH | TA [meq/l] | Ba [mM] | Mg [mM] | Ba/Mg | ΔTA [meq/l] | ΔBa [mM] | ΔMg [mM] | Rate [nmol m$^{-2}$s$^{-1}$] | $\Omega_{nrs}$ |
|---|---|---|---|---|---|---|---|---|---|---|---|---|
| G40.1 1 | 23 | 0.6 | 7.53 | 2.59 | 4.75 | 89.82 | 19 | 0.45 | 0.10 | 0.14 | 57.5 | 151.2 |
| G40.1 2 | 28 | 0.6 | 7.51 | 2.65 | 4.70 | 88.80 | 19 | 0.43 | 0.09 | 0.13 | 54.0 | 141.2 |
| G40.1 3 | 40 | 0.6 | 7.52 | 2.68 | 4.69 | 88.68 | 19 | 0.40 | 0.10 | 0.11 | 54.3 | 147.2 |
| G40.1 4 | 45 | 0.6 | 7.53 | 2.66 | 4.67 | 88.18 | 19 | 0.44 | 0.09 | 0.12 | 50.6 | 152.3 |
| G40.1 5 | 47 | 0.6 | 7.53 | 2.66 | 4.66 | 87.94 | 19 | 0.45 | 0.09 | 0.13 | 46.8 | 156.1 |
| G40.1 6 | 114 | 0.3 | 7.61 | 2.50 | 4.60 | 88.04 | 19 | 0.60 | 0.15 | 0.12 | 38.0 | 187.2 |
| G40.1 7 | 119 | 0.3 | 7.63 | 2.52 | 4.63 | 88.81 | 19 | 0.55 | 0.16 | 0.13 | 41.1 | 206.1 |
| G40.1 8 | 166 | 0.3 | 7.61 | 2.58 | 4.61 | 87.89 | 19 | 0.53 | 0.13 | 0.11 | 31.4 | 199.0 |
| G40.1 9 | 196 | 0.3 | 7.61 | 2.54 | 4.72 | 89.67 | 19 | 0.50 | 0.12 | 0.12 | 27.2 | 193.5 |
| G40.1 10 | 331 | 0.3 | 7.58 | 2.52 | 4.65 | 88.94 | 19 | 0.55 | 0.15 | 0.17 | 29.7 | 173.4 |
| G40.1 11 | 334 | 0.3 | 7.59 | 2.53 | 4.58 | 87.59 | 19 | 0.58 | 0.15 | 0.13 | 28.7 | 184.3 |
| G40.1 12 | 354 | 0.3 | 7.60 | 2.54 | 4.78 | 90.49 | 19 | 0.48 | 0.11 | 0.14 | 19.9 | 196.7 |
| G40.2 1 | 23 | 0.7 | 7.90 | 4.94 | 0.46 | 25.07 | 54 | 1.00 | 0.26 | 0.25 | 156.2 | 208.2 |
| G40.2 2 | 28 | 0.7 | 7.88 | 5.07 | 0.47 | 24.53 | 52 | 1.00 | 0.24 | 0.26 | 139.1 | 202.7 |
| G40.2 3 | 41 | 0.7 | 7.89 | 5.18 | 0.45 | 24.17 | 54 | 0.97 | 0.25 | 0.23 | 140.3 | 204.4 |
| G40.2 4 | 45 | 0.7 | 7.91 | 5.14 | 0.45 | 24.21 | 54 | 1.00 | 0.25 | 0.25 | 137.7 | 225.7 |
| G40.2 5 | 47 | 0.7 | 7.90 | 5.11 | 0.45 | 24.27 | 54 | 1.01 | 0.26 | 0.26 | 141.3 | 209.2 |
| G40.2 6 | 114 | 0.3 | 7.99 | 4.93 | 0.43 | 24.55 | 57 | 1.13 | 0.28 | 0.26 | 85.6 | 272.7 |
| G40.2 7 | 119 | 0.3 | 7.99 | 4.92 | 0.43 | 24.51 | 57 | 1.13 | 0.28 | 0.30 | 67.0 | 282.2 |
| G40.2 8 | 166 | 0.3 | 7.98 | 5.06 | 0.44 | 24.63 | 56 | 0.98 | 0.27 | 0.26 | 58.9 | 287.1 |
| G40.2 9 | 196 | 0.3 | 8.00 | 5.03 | 0.43 | 24.45 | 56 | 1.05 | 0.27 | 0.27 | 55.8 | 299.8 |
| G40.2 10 | 331 | 0.3 | 7.97 | 5.01 | 0.46 | 24.45 | 53 | 1.07 | 0.25 | 0.28 | 41.6 | 280.9 |
| G40.2 11 | 334 | 0.3 | 7.98 | 5.03 | 0.46 | 24.42 | 54 | 1.06 | 0.25 | 0.27 | 41.9 | 295.4 |
| G40.2 12 | 354 | 0.3 | 7.98 | 5.05 | 0.48 | 24.58 | 51 | 1.00 | 0.23 | 0.25 | 37.0 | 315.5 |
| G40.3 1 | 45 | 0.3 | 8.21 | 4.67 | 0.25 | 4.83 | 19 | 0.65 | 0.19 | 0.13 | 207.5 | 128.5 |
| G40.3 2 | 48 | 0.3 | 8.20 | 4.70 | 0.38 | 4.74 | 13 | 0.60 | 0.06 | 0.23 | 68.1 | 190.2 |
| G40.3 3 | 117 | 0.3 | 8.23 | 4.87 | 0.35 | 4.97 | 14 | 0.35 | 0.10 | 0.07 | 95.9 | 215.8 |
| G40.3 4 | 120 | 0.3 | 8.19 | 4.95 | 0.39 | 4.93 | 13 | 0.30 | 0.06 | 0.10 | 55.6 | 214.3 |
| G40.3 5 | 122 | 0.3 | 8.22 | 4.93 | 0.42 | 4.91 | 12 | 0.30 | 0.03 | 0.13 | 27.5 | 255.0 |
| G40.3 6 | 141 | 0.3 | 8.27 | 4.92 | 0.42 | 4.92 | 12 | 0.31 | 0.03 | 0.12 | 29.7 | 311.0 |
| G40.3 7 | 170 | 0.4 | 8.16 | 5.00 | 0.36 | 4.99 | 14 | 0.24 | 0.09 | 0.04 | 132.5 | 173.8 |
| G40.3 8 | 189 | 0.4 | 8.12 | 4.99 | 0.37 | 4.99 | 13 | 0.25 | 0.07 | 0.05 | 110.0 | 153.4 |
| G40.3 9 | 194 | 0.5 | 8.13 | 4.99 | 0.39 | 4.98 | 13 | 0.24 | 0.06 | 0.06 | 93.9 | 165.7 |
| G40.3 10 | 212 | 0.4 | 8.21 | 4.99 | 0.43 | 4.95 | 12 | 0.24 | 0.02 | 0.10 | 28.6 | 254.5 |
| G40.3 11 | 214 | 0.4 | 8.16 | 5.00 | 0.37 | 5.00 | 14 | 0.23 | 0.08 | 0.04 | 117.1 | 183.9 |
| G40.3 12 | 219 | 0.4 | 8.20 | 5.00 | 0.37 | 4.99 | 13 | 0.24 | 0.08 | 0.04 | 109.0 | 213.3 |
| G40.3 13 | 287 | 0.2 | 8.29 | 4.85 | 0.39 | 4.90 | 12 | 0.38 | 0.05 | 0.14 | 24.4 | 304.7 |
| G40.3 14 | 313 | 0.2 | 8.27 | 4.84 | 0.35 | 4.95 | 14 | 0.39 | 0.10 | 0.09 | 43.9 | 258.3 |
| G40.3 15 | 336 | 0.1 | 8.22 | 4.85 | 0.38 | 4.91 | 13 | 0.38 | 0.06 | 0.13 | 27.6 | 221.3 |
| G40.3 16 | 360 | 0.1 | 8.28 | 4.87 | 0.38 | 4.92 | 13 | 0.36 | 0.07 | 0.12 | 27.9 | 297.0 |
| G40.3 17 | 384 | 0.1 | 8.28 | 4.84 | 0.34 | 4.96 | 15 | 0.39 | 0.11 | 0.09 | 44.5 | 257.7 |
| G40.3 18 | 455 | 0.1 | 8.29 | 4.82 | 0.36 | 4.92 | 14 | 0.41 | 0.08 | 0.12 | 32.3 | 285.8 |
| G40.3 19 | 476 | 0.7 | 8.24 | 5.10 | 0.42 | 4.99 | 12 | 0.14 | 0.03 | 0.04 | 53.4 | 302.6 |
| G40.3 20 | 477 | 0.7 | 8.22 | 5.11 | 0.40 | 5.01 | 12 | 0.14 | 0.04 | 0.02 | 82.3 | 265.7 |
| G40.3 21 | 479 | 0.7 | 8.21 | 5.12 | 0.43 | 4.97 | 12 | 0.13 | 0.02 | 0.05 | 28.2 | 268.0 |
| G65.1 8 | 169 | 0.5 | 7.20 | 2.59 | 2.30 | 39.75 | 17 | 0.48 | 0.10 | 0.14 | 44.3 | 32.2 |
| G65.1 9 | 186 | 0.5 | 7.20 | 2.59 | 2.31 | 39.73 | 17 | 0.49 | 0.09 | 0.14 | 38.3 | 33.1 |
| G65.1 10 | 192 | 0.5 | 7.21 | 2.61 | 2.28 | 39.58 | 17 | 0.48 | 0.11 | 0.15 | 47.2 | 33.9 |
| G65.1 11 | 210 | 0.5 | 7.22 | 2.58 | 2.27 | 39.25 | 17 | 0.53 | 0.10 | 0.15 | 40.3 | 34.0 |
| G65.1 12 | 260 | 0.8 | 7.28 | 2.66 | 2.31 | 39.67 | 17 | 0.42 | 0.09 | 0.10 | 57.4 | 49.5 |

| Sample | run-time [h] | FR [ml/min] | pH | TA [meq/l] | Ba [mM] | Mg [mM] | Ba/ Mg | ΔTA [meq/l] | ΔBa [mM] | ΔMg [mM] | Rate [nmol m$^{-2}$ s$^{-1}$] | $\Omega_{nrs}$ |
|---|---|---|---|---|---|---|---|---|---|---|---|---|
| G65.1 13 | 261 | 0.8 | 7.03 | 2.68 | 2.29 | 39.55 | 17 | 0.41 | 0.09 | 0.12 | 61.3 | 16.0 |
| G65.1 14 | 261 | 0.8 | 7.28 | 2.66 | 2.30 | 39.39 | 17 | 0.44 | 0.08 | 0.14 | 52.9 | 48.3 |
| G65.1 15 | 331 | 0.2 | 7.13 | 2.22 | 2.22 | 39.52 | 18 | 0.87 | 0.17 | 0.16 | 29.2 | 16.5 |
| G65.1 16 | 355 | 0.2 | 7.09 | 2.26 | 2.20 | 39.79 | 18 | 0.80 | 0.20 | 0.22 | 31.3 | 14.2 |
| G65.1 17 | 379 | 0.2 | 7.04 | 2.25 | 2.19 | 39.47 | 18 | 0.84 | 0.20 | 0.26 | 30.4 | 11.6 |
| G65.1 18 | 404 | 0.2 | 7.01 | 2.26 | 2.15 | 39.30 | 18 | 0.84 | 0.23 | 0.18 | 33.9 | 10.0 |
| G65.2 1 | 19 | 0.3 | 7.60 | 3.32 | 0.26 | 7.44 | 28 | 2.18 | 0.22 | 2.59 | 66.8 | 15.9 |
| G65.2 2 | 24 | 0.3 | 7.56 | 3.74 | 0.23 | 8.00 | 35 | 1.76 | 0.26 | 2.03 | 74.9 | 16.0 |
| G65.2 3 | 42 | 0.3 | 7.53 | 4.31 | 0.25 | 9.37 | 37 | 1.32 | 0.22 | 0.42 | 62.6 | 22.2 |
| G65.2 4 | 48 | 0.3 | 7.54 | 4.37 | 0.25 | 9.66 | 39 | 1.14 | 0.23 | 0.35 | 64.9 | 24.1 |
| G65.2 5 | 67 | 0.3 | 7.56 | 4.55 | 0.25 | 9.73 | 39 | 0.97 | 0.23 | 0.26 | 61.4 | 29.2 |
| G65.2 6 | 70 | 0.3 | 7.56 | 4.58 | 0.26 | 9.95 | 39 | 0.87 | 0.23 | 0.18 | 61.3 | 31.0 |
| G65.2 7 | 116 | 0.3 | 7.63 | 4.6 | 0.26 | 10.05 | 39 | 0.79 | 0.24 | 0.18 | 58.3 | 42.5 |
| G65.2 8 | 162 | 0.5 | 7.63 | 4.71 | 0.29 | 9.85 | 34 | 0.78 | 0.20 | 0.20 | 74.6 | 48.4 |
| G65.2 9 | 169 | 0.5 | 7.63 | 4.71 | 0.29 | 9.85 | 34 | 0.77 | 0.20 | 0.20 | 75.8 | 47.7 |
| G65.2 10 | 186 | 0.4 | 7.62 | 4.69 | 0.27 | 9.87 | 36 | 0.79 | 0.21 | 0.20 | 75.4 | 44.4 |
| G65.2 11 | 192 | 0.5 | 7.62 | 4.73 | 0.28 | 9.90 | 35 | 0.76 | 0.20 | 0.15 | 75.4 | 45.9 |
| G65.2 12 | 210 | 0.5 | 7.61 | 4.71 | 0.28 | 9.89 | 35 | 0.75 | 0.21 | 0.20 | 73.2 | 42.8 |
| G65.2 13 | 260 | 0.8 | 7.63 | 4.68 | 0.28 | 10.03 | 36 | 0.74 | 0.22 | 0.14 | 118.1 | 47.4 |
| G65.2 14 | 261 | 0.8 | 7.10 | 4.81 | 0.31 | 9.89 | 32 | 0.68 | 0.18 | 0.16 | 98.6 | 5.0 |
| G65.2 15 | 261 | 0.8 | 7.64 | 4.84 | 0.31 | 9.88 | 31 | 0.66 | 0.17 | 0.15 | 93.2 | 58.5 |
| G65.2 16 | 331 | 0.2 | 7.51 | 4.38 | 0.21 | 9.80 | 46 | 1.08 | 0.27 | 0.29 | 36.5 | 18.2 |
| G65.2 17 | 355 | 0.2 | 7.48 | 4.44 | 0.22 | 9.87 | 46 | 1.01 | 0.27 | 0.24 | 33.4 | 17.2 |
| G65.2 18 | 379 | 0.2 | 7.46 | 4.41 | 0.20 | 9.81 | 48 | 1.08 | 0.28 | 0.24 | 33.8 | 14.4 |
| G65.2 19 | 404 | 0.2 | 7.45 | 4.41 | 0.22 | 9.78 | 45 | 1.09 | 0.27 | 0.25 | 31.3 | 14.1 |
| G65.3 1 | 18 | 0.3 | 7.86 | 2.15 | 0.60 | 3.64 | 6 | 1.12 | 0.33 | 1.18 | 227.0 | 26.5 |
| G65.3 2 | 23 | 0.3 | 7.80 | 2.40 | 0.58 | 4.05 | 7 | 0.87 | 0.34 | 0.75 | 198.3 | 26.8 |
| G65.3 3 | 43 | 0.3 | 7.78 | 2.71 | 0.77 | 4.53 | 6 | 0.57 | 0.16 | 0.26 | 105.6 | 44.9 |
| G65.3 4 | 47 | 0.3 | 7.77 | 2.75 | 0.72 | 4.62 | 6 | 0.53 | 0.20 | 0.18 | 138.5 | 43.0 |
| G65.3 5 | 114 | 0.4 | 7.82 | 2.77 | 0.76 | 4.65 | 6 | 0.53 | 0.16 | 0.12 | 118.4 | 48.7 |
| G65.3 6 | 119 | 0.3 | 7.80 | 2.80 | 0.78 | 4.61 | 6 | 0.49 | 0.14 | 0.16 | 88.3 | 52.9 |
| G65.3 7 | 138 | 0.3 | 7.79 | 2.77 | 0.79 | 4.59 | 6 | 0.52 | 0.14 | 0.18 | 84.9 | 51.9 |
| G65.3 8 | 143 | 0.3 | 7.79 | 2.77 | 0.81 | 4.57 | 6 | 0.52 | 0.11 | 0.20 | 71.4 | 52.0 |
| G65.3 9 | 166 | 0.8 | 7.91 | 2.88 | 0.78 | 4.62 | 6 | 0.42 | 0.13 | 0.14 | 198.7 | 94.3 |
| G65.3 10 | 185 | 0.8 | 7.92 | 2.85 | 0.76 | 4.60 | 6 | 0.46 | 0.15 | 0.15 | 226.0 | 90.6 |
| G65.3 11 | 189 | 0.8 | 7.91 | 2.85 | 0.77 | 4.63 | 6 | 0.45 | 0.15 | 0.12 | 219.0 | 87.9 |
| G65.3 12 | 191 | 0.8 | 7.91 | 2.84 | 0.80 | 4.59 | 6 | 0.47 | 0.12 | 0.16 | 176.4 | 89.4 |
| G65.3 13 | 281 | 0.5 | 7.78 | 2.78 | 0.73 | 4.62 | 6 | 0.53 | 0.19 | 0.12 | 153.0 | 46.5 |
| G65.3 14 | 283 | 0.5 | 7.78 | 2.78 | 0.71 | 4.65 | 7 | 0.53 | 0.21 | 0.09 | 172.0 | 35.3 |
| G65.3 15 | 286 | 0.5 | 7.76 | 2.78 | 0.71 | 4.65 | 7 | 0.53 | 0.20 | 0.09 | 168.7 | 25.7 |
| G65.3 16 | 288 | 0.5 | 7.76 | 2.80 | 0.70 | 4.65 | 7 | 0.51 | 0.22 | 0.09 | 179.3 | 36.8 |
| G65.3 17 | 306 | 0.5 | 7.76 | 2.79 | 0.71 | 4.64 | 7 | 0.52 | 0.21 | 0.10 | 170.7 | 41.2 |
| G65.4 1 | 18 | 0.3 | 7.23 | 3.05 | 1.24 | 7.45 | 6 | 2.16 | 0.70 | 2.58 | 471.0 | 12.6 |
| G65.4 2 | 23 | 0.3 | 7.20 | 3.30 | 1.43 | 8.12 | 6 | 1.95 | 0.50 | 1.85 | 274.6 | 15.6 |
| G65.4 3 | 43 | 0.3 | 7.16 | 3.69 | 1.62 | 9.45 | 6 | 1.57 | 0.30 | 0.49 | 184.3 | 20.5 |
| G65.4 4 | 47 | 0.3 | 7.16 | 3.75 | 1.61 | 9.58 | 6 | 1.49 | 0.31 | 0.40 | 193.8 | 21.2 |
| G65.4 5 | 114 | 0.4 | 7.32 | 4.02 | 1.73 | 9.84 | 6 | 1.12 | 0.24 | 0.32 | 138.8 | 54.4 |
| G65.4 6 | 119 | 0.3 | 7.32 | 4.08 | 1.72 | 9.83 | 6 | 1.08 | 0.23 | 0.29 | 119.6 | 55.8 |
| G65.4 7 | 138 | 0.3 | 7.33 | 4.06 | 1.75 | 9.80 | 6 | 1.09 | 0.21 | 0.34 | 103.8 | 58.3 |
| G65.4 8 | 143 | 0.3 | 7.32 | 4.06 | 1.72 | 9.83 | 6 | 1.09 | 0.24 | 0.31 | 116.6 | 55.2 |
| G65.4 9 | 166 | 0.8 | 7.36 | 4.26 | 1.79 | 9.91 | 6 | 0.87 | 0.18 | 0.27 | 201.6 | 75.7 |
| G65.4 10 | 185 | 0.8 | 7.35 | 4.25 | 1.81 | 9.89 | 5 | 0.90 | 0.15 | 0.27 | 166.2 | 72.5 |
| G65.4 11 | 189 | 0.8 | 7.35 | 4.23 | 1.81 | 9.89 | 5 | 0.90 | 0.16 | 0.29 | 167.4 | 72.1 |
| G65.4 12 | 191 | 0.8 | 7.35 | 4.24 | 1.85 | 9.82 | 5 | 0.90 | 0.11 | 0.34 | 123.0 | 73.5 |
| G65.4 13 | 281 | 0.4 | 7.29 | 4.08 | 1.61 | 10.01 | 6 | 1.05 | 0.36 | 0.19 | 199.8 | 46.1 |
| G65.4 14 | 283 | 0.5 | 7.28 | 4.07 | 1.66 | 9.92 | 6 | 1.07 | 0.30 | 0.26 | 170.5 | 45.0 |

| Sample | run-time [h] | FR [ml/min] | pH | TA [meq/l] | Ba [mM] | Mg [mM] | Ba/Mg | ΔTA [meq/l] | ΔBa [mM] | ΔMg [mM] | Rate [nmol m$^{-2}$s$^{-1}$] | $\Omega_{nrs}$ |
|---|---|---|---|---|---|---|---|---|---|---|---|---|
| G65.4 15 | 286 | 0.5 | 7.28 | 4.08 | 1.68 | 9.93 | 6 | 1.05 | 0.29 | 0.25 | 158.5 | 45.7 |
| G65.4 16 | 288 | 0.4 | 7.29 | 4.08 | 1.64 | 9.97 | 6 | 1.06 | 0.32 | 0.19 | 175.6 | 47.0 |
| G65.4 17 | 306 | 0.4 | 7.28 | 4.05 | 1.68 | 9.91 | 6 | 1.09 | 0.29 | 0.27 | 156.2 | 44.9 |
| G100.1 1 | 20 | 1.1 | 8.07 | 24.59 | 0.0058 | 0.1637 | 28 | 0.08 | 0.0214 | 0.0199 | 28.3 | 13.1 |
| G100.1 2 | 24 | 1.2 | 8.06 | 24.45 | 0.0059 | 0.1653 | 28 | 0.08 | 0.0215 | 0.0194 | 29.2 | 12.7 |
| G100.1 3 | 28 | 1.2 | 8.06 | 24.52 | 0.0058 | 0.1661 | 29 | 0.07 | 0.0215 | 0.0182 | 29.5 | 12.8 |
| G100.1 4 | 45 | 1.2 | 8.07 | 24.54 | 0.0060 | 0.1656 | 28 | 0.08 | 0.0213 | 0.0185 | 29.1 | 13.5 |
| G100.1 5 | 50 | 1.2 | 8.07 | 24.55 | 0.0057 | 0.1654 | 29 | 0.09 | 0.0215 | 0.0185 | 29.3 | 13.1 |
| G100.1 6 | 53 | 1.2 | 8.07 | 24.55 | 0.0057 | 0.1648 | 29 | 0.08 | 0.0216 | 0.0192 | 29.3 | 13.1 |
| G100.1 7 | 69 | 1.2 | 8.07 | 24.60 | 0.0056 | 0.1654 | 30 | 0.08 | 0.0216 | 0.0182 | 29.7 | 13.5 |
| G100.1 8 | 94 | 1.6 | 8.04 | 18.28 | 0.0075 | 0.2064 | 27 | 0.10 | 0.0264 | 0.0228 | 48.8 | 12.6 |
| G100.1 9 | 101 | 1.6 | 8.04 | 18.33 | 0.0073 | 0.2062 | 28 | 0.09 | 0.0266 | 0.0228 | 49.5 | 11.1 |
| G100.1 10 | 117 | 1.6 | 8.06 | 18.35 | 0.0070 | 0.2055 | 30 | 0.10 | 0.0269 | 0.0233 | 48.9 | 11.9 |
| G100.1 11 | 144 | 1.6 | 8.06 | 18.47 | 0.0063 | 0.2049 | 32 | 0.11 | 0.0274 | 0.0229 | 49.7 | 10.3 |
| G100.1 12 | 150 | 1.4 | 8.04 | 14.26 | 0.0070 | 0.2302 | 33 | 0.12 | 0.0313 | 0.0280 | 49.8 | 8.2 |
| G100.1 13 | 164 | 1.4 | 8.04 | 13.80 | 0.0067 | 0.2344 | 35 | 0.13 | 0.0320 | 0.0271 | 50.8 | 8.0 |
| G100.1 14 | 166 | 1.4 | 8.02 | 13.80 | 0.0066 | 0.2335 | 35 | 0.13 | 0.0321 | 0.0280 | 51.6 | 7.4 |
| G100.1 15 | 168 | 1.4 | 8.02 | 13.81 | 0.0065 | 0.2339 | 36 | 0.12 | 0.0322 | 0.0276 | 50.9 | 7.4 |
| G100.1 16 | 170 | 1.4 | 8.03 | 13.77 | 0.0069 | 0.2347 | 34 | 0.12 | 0.0319 | 0.0271 | 51.0 | 7.6 |
| G100.1 17 | 187 | 1.4 | 8.06 | 13.82 | 0.0064 | 0.2350 | 37 | 0.11 | 0.0323 | 0.0265 | 51.6 | 7.5 |
| G100.2 1 | 23 | 1.0 | 7.83 | 24.98 | 0.0035 | 0.1240 | 36 | 0.14 | 0.0150 | 0.0145 | 17.7 | 1.9 |
| G100.2 2 | 27 | 1.0 | 7.82 | 25.02 | 0.0035 | 0.1219 | 35 | 0.10 | 0.0151 | 0.0166 | 17.7 | 1.9 |
| G100.2 3 | 31 | 1.0 | 7.82 | 25.01 | 0.0036 | 0.1239 | 35 | 0.11 | 0.0149 | 0.0146 | 17.6 | 2.5 |
| G100.2 4 | 47 | 1.0 | 7.82 | 25.02 | 0.0035 | 0.1259 | 36 | 0.10 | 0.0150 | 0.0126 | 17.6 | 2.6 |
| G100.2 5 | 53 | 1.0 | 7.84 | 25.02 | 0.0035 | 0.1239 | 35 | 0.10 | 0.0150 | 0.0146 | 17.7 | 2.7 |
| G100.2 6 | 55 | 1.0 | 7.83 | 25.01 | 0.0035 | 0.1227 | 35 | 0.11 | 0.0151 | 0.0158 | 17.7 | 1.9 |
| G100.2 7 | 72 | 1.0 | 7.81 | 25.00 | 0.0033 | 0.1210 | 36 | 0.12 | 0.0152 | 0.0174 | 17.9 | 1.8 |
| G100.2 8 | 97 | 0.5 | 7.85 | 25.01 | 0.0024 | 0.1219 | 51 | 0.11 | 0.0161 | 0.0166 | 9.4 | 1.4 |
| G100.2 9 | 105 | 0.5 | 7.83 | 25.01 | 0.0024 | 0.1210 | 50 | 0.11 | 0.0161 | 0.0174 | 9.5 | 1.3 |
| G100.2 10 | 120 | 0.5 | 7.85 | 25.01 | 0.0023 | 0.1227 | 52 | 0.11 | 0.0162 | 0.0158 | 9.2 | 1.4 |
| G100.2 11 | 147 | 0.5 | 7.87 | 25.03 | 0.0022 | 0.1222 | 55 | 0.09 | 0.0163 | 0.0163 | 9.4 | 1.5 |
| G100.2 12 | 153 | 1.8 | 7.87 | 25.06 | 0.0039 | 0.1234 | 32 | 0.06 | 0.0147 | 0.0151 | 30.9 | 3.1 |
| G100.2 13 | 167 | 1.8 | 7.89 | 25.04 | 0.0036 | 0.1233 | 34 | 0.08 | 0.0149 | 0.0152 | 31.8 | 3.3 |
| G100.2 14 | 169 | 1.8 | 7.89 | 25.02 | 0.0036 | 0.1226 | 34 | 0.10 | 0.0149 | 0.0158 | 31.9 | 3.3 |
| G100.2 15 | 170 | 1.8 | 7.89 | 25.05 | 0.0036 | 0.1235 | 34 | 0.07 | 0.0149 | 0.0150 | 31.5 | 3.3 |
| G100.2 16 | 172 | 1.8 | 7.88 | 25.03 | 0.0036 | 0.1246 | 35 | 0.09 | 0.0149 | 0.0139 | 31.4 | 3.3 |
| G100.3 1 | 14 | 1.2 | 7.84 | 24.63 | 0.0084 | 0.2046 | 24 | 0.10 | 0.0291 | 0.0311 | 39.8 | 8.9 |
| G100.3 2 | 17 | 1.2 | 7.84 | 24.75 | 0.0078 | 0.2035 | 26 | 0.10 | 0.0285 | 0.0242 | 39.2 | 8.9 |
| G100.3 3 | 24 | 1.2 | 7.84 | 24.93 | 0.0068 | 0.2017 | 30 | 0.11 | 0.0295 | 0.0260 | 40.4 | 7.6 |
| G100.3 4 | 39 | 1.1 | 7.84 | 25.10 | 0.0055 | 0.1994 | 36 | 0.12 | 0.0307 | 0.0282 | 41.5 | 6.7 |
| G100.3 5 | 41 | 1.2 | 7.84 | 25.09 | 0.0054 | 0.1992 | 37 | 0.13 | 0.0309 | 0.0285 | 42.4 | 5.6 |
| G100.3 6 | 44 | 1.2 | 7.85 | 25.13 | 0.0054 | 0.2002 | 37 | 0.13 | 0.0309 | 0.0274 | 42.1 | 5.8 |
| G100.3 7 | 46 | 1.2 | 7.84 | 25.11 | 0.0053 | 0.1995 | 38 | 0.12 | 0.0310 | 0.0282 | 42.4 | 5.6 |
| G100.3 8 | 49 | 1.2 | 7.85 | 25.11 | 0.0052 | 0.2003 | 39 | 0.13 | 0.0311 | 0.0273 | 42.5 | 5.8 |
| G100.3 9 | 64 | 1.1 | 7.85 | 25.74 | 0.0044 | 0.1956 | 45 | 0.13 | 0.0319 | 0.0321 | 42.1 | 4.7 |
| G100.3 10 | 68 | 1.1 | 7.84 | 25.56 | 0.0044 | 0.1958 | 44 | 0.16 | 0.0318 | 0.0318 | 42.8 | 4.4 |
| G100.3 11 | 71 | 1.2 | 7.84 | 25.49 | 0.0043 | 0.1968 | 45 | 0.15 | 0.0319 | 0.0309 | 43.4 | 4.4 |
| G100.3 12 | 86 | 1.1 | 7.85 | 25.38 | 0.0041 | 0.1971 | 48 | 0.14 | 0.0322 | 0.0305 | 43.5 | 4.6 |
| G100.3 13 | 89 | 1.1 | 7.84 | 25.42 | 0.0041 | 0.1950 | 47 | 0.11 | 0.0321 | 0.0326 | 43.4 | 4.5 |
| G100.4 1 | 16 | 1.5 | 7.73 | 12.36 | 0.0166 | 0.3107 | 19 | 0.15 | 0.0391 | 0.0391 | 67.4 | 5.7 |
| G100.4 2 | 18 | 1.5 | 7.73 | 12.39 | 0.0165 | 0.3082 | 19 | 0.16 | 0.0392 | 0.0412 | 67.1 | 5.5 |
| G100.4 3 | 19 | 1.5 | 7.70 | 12.44 | 0.0160 | 0.3059 | 19 | 0.16 | 0.0396 | 0.0430 | 67.6 | 4.9 |
| G100.4 4 | 22 | 1.5 | 7.82 | 12.57 | 0.0152 | 0.3039 | 20 | 0.18 | 0.0401 | 0.0436 | 68.4 | 7.6 |
| G100.4 5 | 23 | 1.5 | 7.82 | 12.45 | 0.0145 | 0.3041 | 21 | 0.20 | 0.0410 | 0.0444 | 69.7 | 7.4 |
| G100.4 6 | 38 | 1.5 | 7.76 | 12.33 | 0.0122 | 0.3047 | 25 | 0.17 | 0.0435 | 0.0452 | 72.8 | 4.6 |
| G100.4 7 | 40 | 1.5 | 7.73 | 12.32 | 0.0123 | 0.3058 | 25 | 0.18 | 0.0434 | 0.0441 | 72.5 | 4.2 |

| Sample | run-time [h] | FR [ml/min] | pH | TA [meq/l] | Ba [mM] | Mg [mM] | Ba/Mg | ΔTA [meq/l] | ΔBa [mM] | ΔMg [mM] | Rate [nmol m$^{-2}$s$^{-1}$] | $\Omega_{nrs}$ |
|---|---|---|---|---|---|---|---|---|---|---|---|---|
| G100.4 8 | 44 | 1.5 | 7.75 | 12.29 | 0.0118 | 0.3031 | 26 | 0.16 | 0.0440 | 0.0473 | 72.7 | 4.3 |
| G100.4 9 | 47 | 1.5 | 7.75 | 13.06 | 0.0107 | 0.2984 | 28 | 0.19 | 0.0440 | 0.0445 | 72.9 | 4.3 |
| G100.4 10 | 63 | 1.5 | 7.73 | 12.30 | 0.0102 | 0.2950 | 29 | 0.20 | 0.0455 | 0.0549 | 74.0 | 3.3 |
| G100.4 11 | 64 | 1.5 | 7.75 | 12.26 | 0.0105 | 0.3066 | 29 | 0.19 | 0.0453 | 0.0437 | 73.5 | 3.9 |
| G100.4 12 | 68 | 1.5 | 7.75 | 12.22 | 0.0102 | 0.3052 | 30 | 0.18 | 0.0457 | 0.0456 | 73.5 | 3.6 |
| G100.4 13 | 70 | 1.5 | 7.75 | 12.20 | 0.0101 | 0.3074 | 30 | 0.20 | 0.0458 | 0.0434 | 73.7 | 3.7 |
| G100.5 1 | 14 | 0.5 | 7.79 | 24.86 | 0.0019 | 0.1034 | 55 | 0.26 | 0.0140 | 0.0194 | 7.7 | 0.9 |
| G100.5 2 | 21 | 0.5 | 7.78 | 24.95 | 0.0022 | 0.1063 | 49 | 0.17 | 0.0137 | 0.0165 | 7.6 | 0.9 |
| G100.5 3 | 44 | 0.5 | 7.82 | 25.12 | 0.0025 | 0.1090 | 44 | 0.00 | 0.0134 | 0.0138 | 7.5 | 1.7 |
| G100.5 4 | 61 | 0.5 | 7.83 | 25.04 | 0.0027 | 0.1101 | 41 | 0.08 | 0.0132 | 0.0128 | 7.6 | 1.7 |
| G100.5 5 | 65 | 0.5 | 7.83 | 25.05 | 0.0027 | 0.1096 | 41 | 0.07 | 0.0132 | 0.0132 | 7.6 | 1.8 |
| G100.5 6 | 71 | 0.5 | 7.83 | 25.03 | 0.0027 | 0.1099 | 40 | 0.09 | 0.0132 | 0.0129 | 7.6 | 1.8 |
| G100.5 7 | 85 | 0.5 | 7.82 | 25.02 | 0.0028 | 0.1098 | 39 | 0.10 | 0.0131 | 0.0130 | 7.6 | 1.7 |
| G100.5 8 | 90 | 0.5 | 7.84 | 25.03 | 0.0029 | 0.1099 | 38 | 0.09 | 0.0131 | 0.0130 | 7.5 | 1.8 |
| G100.5 9 | 96 | 0.5 | 7.85 | 25.00 | 0.0028 | 0.1100 | 39 | 0.12 | 0.0131 | 0.0128 | 7.5 | 1.9 |
| G100.5 10 | 110 | 1.2 | 7.83 | 25.05 | 0.0044 | 0.1124 | 26 | 0.07 | 0.0115 | 0.0104 | 16.1 | 2.4 |
| G100.5 11 | 114 | 1.2 | 7.83 | 25.05 | 0.0043 | 0.1119 | 26 | 0.07 | 0.0116 | 0.0109 | 16.3 | 2.4 |
| G100.5 12 | 117 | 1.2 | 7.83 | 25.03 | 0.0044 | 0.1124 | 26 | 0.09 | 0.0115 | 0.0105 | 16.3 | 2.3 |
| G100.5 13 | 132 | 1.2 | 7.85 | 25.07 | 0.0044 | 0.1125 | 26 | 0.05 | 0.0115 | 0.0103 | 16.3 | 2.6 |
| G100.5 14 | 135 | 1.2 | 7.84 | 25.05 | 0.0043 | 0.1122 | 26 | 0.07 | 0.0116 | 0.0106 | 16.2 | 2.5 |
| G100.5 15 | 142 | 1.2 | 7.81 | 25.05 | 0.0044 | 0.1120 | 26 | 0.07 | 0.0115 | 0.0109 | 16.2 | 2.2 |
| G100.5 16 | 157 | 1.2 | 7.88 | 25.10 | 0.0044 | 0.1121 | 26 | 0.02 | 0.0116 | 0.0107 | 16.4 | 2.9 |
| G100.5 17 | 161 | 2.0 | 7.89 | 25.07 | 0.0054 | 0.1133 | 21 | 0.05 | 0.0105 | 0.0095 | 25.1 | 3.8 |
| G100.5 18 | 163 | 2.0 | 7.89 | 25.07 | 0.0053 | 0.1116 | 21 | 0.05 | 0.0106 | 0.0112 | 25.2 | 3.8 |
| G100.5 19 | 164 | 2.0 | 7.89 | 25.06 | 0.0054 | 0.1130 | 21 | 0.06 | 0.0106 | 0.0098 | 25.1 | 3.8 |
| G100.5 20 | 167 | 2.0 | 7.89 | 25.06 | 0.0053 | 0.1131 | 22 | 0.06 | 0.0107 | 0.0098 | 25.2 | 3.9 |
| G100.5 21 | 169 | 2.0 | 7.89 | 25.07 | 0.0054 | 0.1124 | 21 | 0.05 | 0.0106 | 0.0104 | 25.1 | 3.9 |
| G100.6 1 | 5 | 1.5 | 7.82 | 24.82 | 0.0031 | 0.1946 | 62 | 0.22 | 0.0215 | 0.0311 | 38.1 | 2.9 |
| G100.6 2 | 20 | 1.5 | 7.83 | 25.00 | 0.0033 | 0.2014 | 62 | 0.04 | 0.0214 | 0.0243 | 37.9 | 3.2 |
| G100.6 3 | 22 | 1.5 | 7.82 | 24.98 | 0.0031 | 0.2017 | 64 | 0.06 | 0.0216 | 0.0240 | 37.8 | 3.0 |
| G100.6 4 | 25 | 1.5 | 7.83 | 24.99 | 0.0031 | 0.2009 | 64 | 0.05 | 0.0215 | 0.0248 | 37.8 | 3.2 |
| G100.6 5 | 27 | 1.5 | 7.82 | 24.98 | 0.0033 | 0.2015 | 61 | 0.06 | 0.0214 | 0.0242 | 37.8 | 3.0 |
| G100.6 6 | 28 | 1.5 | 7.84 | 24.95 | 0.0033 | 0.2030 | 62 | 0.09 | 0.0214 | 0.0227 | 37.7 | 3.3 |
| G100.6 7 | 30 | 1.5 | 7.83 | 25.00 | 0.0033 | 0.2008 | 61 | 0.04 | 0.0214 | 0.0249 | 37.6 | 3.2 |
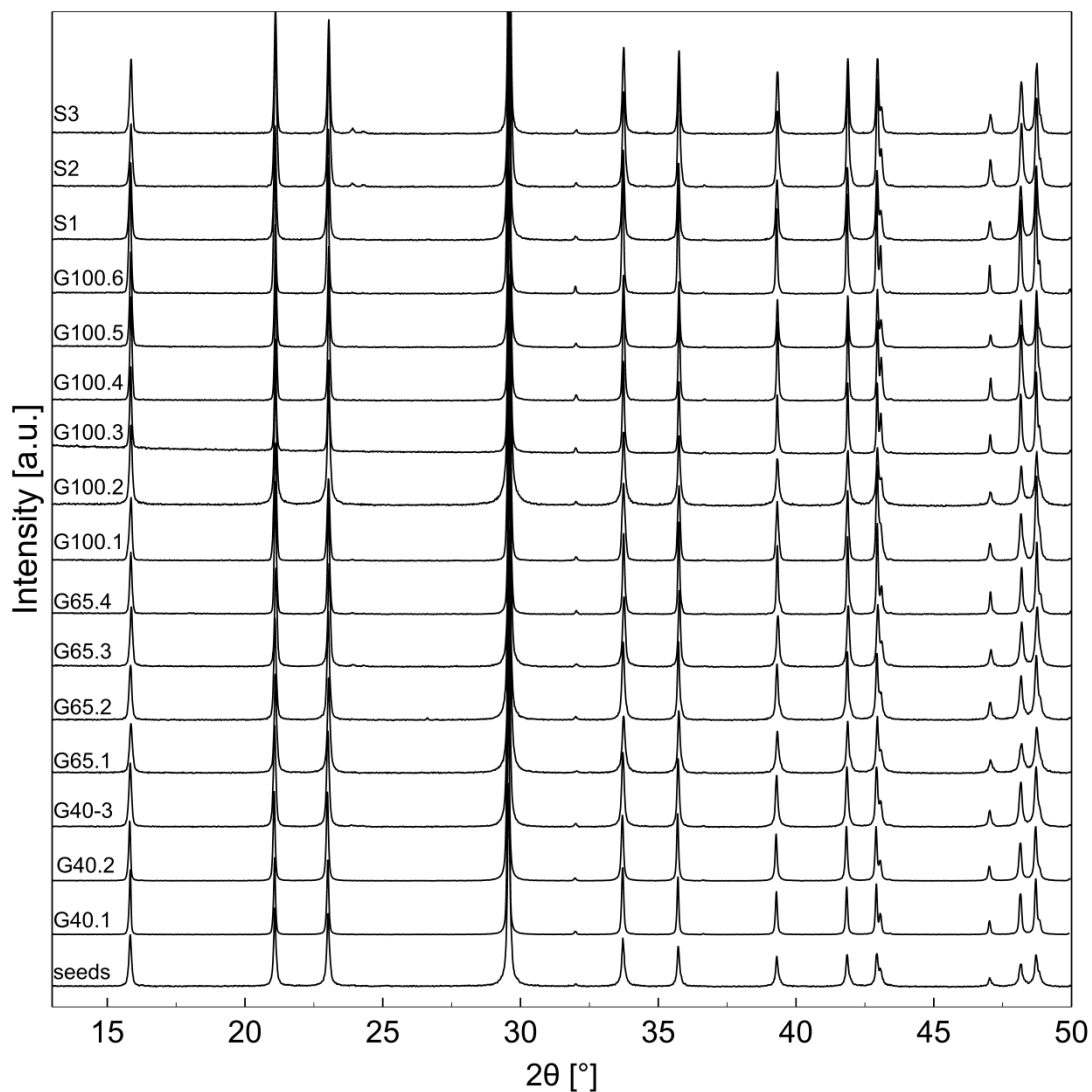
Figure Suppl1: X-ray diffractogram patterns of seed crystals and powders retrieved from the reactors after growth experiments (numbers of experiments are given) show no signs of newly precipitated phases. All major peaks can be attributed to norsethite (Ende et al., 2017). Minor amounts (~1 wt. %) of witherite can be detected in the powder retrieved after solubility measurements of experiments S2 and S3, while powder from experiment S1 is free of witherite.
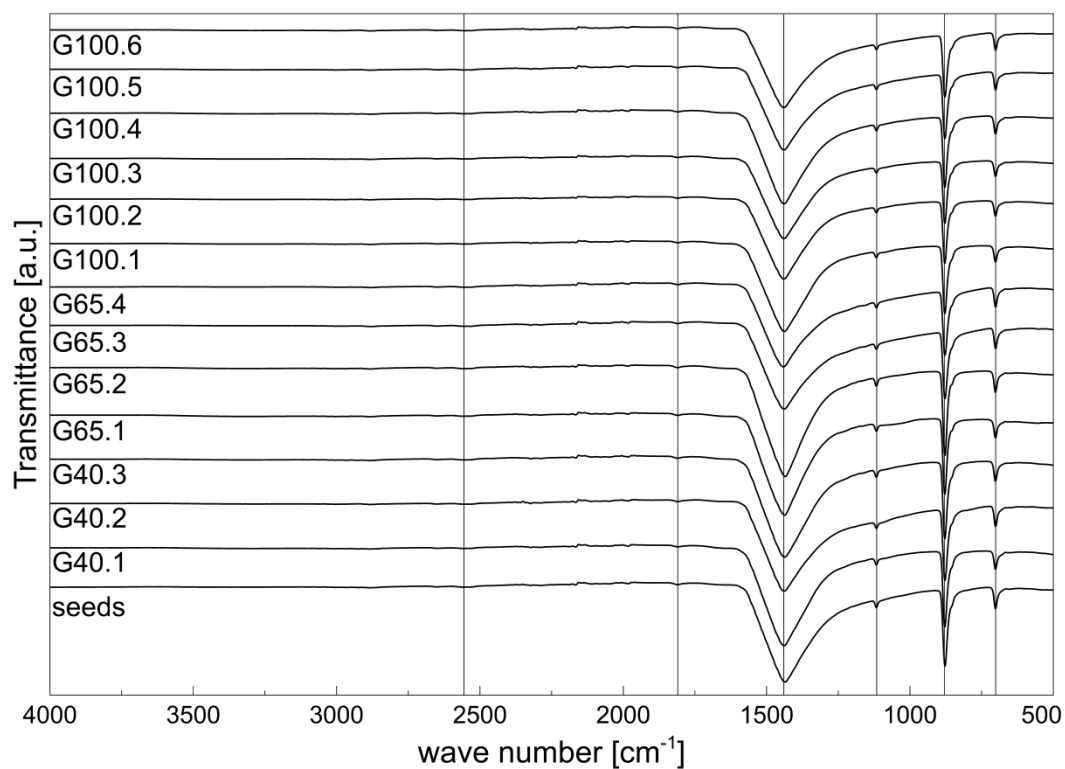
Figure Suppl2: Infrared spectra of seed crystals and powders recovered from the reactors after growth experiments (numbers of experiments are given) show no major changes during the experiments. The vertical lines indicate the positions of IR spectroscopic data of norsethite available in the literature (Böttcher et al., 1997), all of which can be detected in the measured spectra. No other phase is discernible apart from norsethite. No bands of OH-group vibrations are observable in the region around 3500 cm$^{-1}$, validating the water-free structure.

# 5    Conclusions and outlook

The research presented in this thesis comprised systematic investigations of mineral growth kinetics in the $BaCO_3$-$MgCO_3$ system with special focus on the mineral norsethite, $BaMg(CO_3)_2$. Experiments were performed in the facilities of the *Department für Geo- und Umweltwissenschaften* of the *Ludwig-Maximilans-Universität München (LMU)* and the laboratories of the *Géoscience Environnement Toulouse (GET)*. The different capabilities of these two laboratories allowed for complementary experiments elucidating the $BaCO_3$-$MgCO_3$ system at different length scales and temperatures. Over a wide range of conditions (including temperature, solution composition and the presence of given mineral surfaces) the occurrence and growth of norsethite dominated the $BaCO_3$-$MgCO_3$ system. Neither on the $BaCO_3$- nor on the $MgCO_3$-rich side of the system could any sign of solid solution formation be discerned. The large difference in ionic radii of $Mg^{2+}$ and $Ba^{2+}$ ($\Delta r_{cation}$ = 0.63 Å) presumably prevented the incorporation of detectable amounts of $Ba^{2+}$ into magnesite and $Mg^{2+}$ into witherite, respectively. The ordered phase norsethite was preferably formed instead of a solid solution or the two distinct endmembers magnesite and witherite. Ordering into distinct $Ba^{2+}$- and $Mg^{2+}$-layers with substantially different cation coordination spheres was the only way to combine both cations within one phase.

This behavior is considerably different to the $CaCO_3$-$MgCO_3$ system ($\Delta r_{cation}$ = 0.28 Å), where the occurrence of ordered dolomite is impaired but solid solutions form easily. At temperatures below 60 °C, none of the different routes to form norsethite has been shown to exist for dolomite. All Mg:Ca ratios in solution fail to directly precipitate (ordered) dolomite. An unordered Ca-Mg-carbonate is strongly favored instead: Adding $Mg^{2+}$ to calcite seeds leads to an unordered incorporation of Mg into the growing calcite and retards the growth rate (Mucci and Morse, 1983). At the opposite boundary of the system, $Ca^{2+}$ is incorporated into growing magnesite seeds without a noticeable effect on the growth rate (Berninger et al., 2016). The incorporation of the added ions into the growing seeds keeps the concentration of these ions in the growth solution low and counteracts nucleation of a new phase. In other words, the formation of the Ca-Mg-carbonate solid solution is effectively inhibiting the precipitation of dolomite in experiments seeded with calcite or magnesite. Therefore, the occurrence of a solid solution actively inhibits the formation of an ordered phase with distinct stoichiometry.

As pointed out by Pimentel and Pina (2016), the structural units related to the different cation coordination polyhedra of $Ca^{2+}$ in dolomite and $Ba^{2+}$ in norsethite (and also of $Pb^{2+}$ in $PbMg(CO_3)_2$) may have some influence on the ability

to form an ordered double carbonate. $Ca^{2+}$ can occur coordinated by six (calcite) and nine (aragonite) oxygen ions. $Mg^{2+}$ occupies sites with six-fold coordination exclusively. In dolomite, both $Ca^{2+}$ and $Mg^{2+}$ are coordinated by six oxygen ions. The similarity of coordination polyhedra of $Ca^{2+}$ and $Mg^{2+}$ is large enough to facilitate the mutual substitution of the two cations resulting in the precipitation of an unordered solid solution rather than of dolomite. $Ba^{2+}$ ions occur in nine-fold (witherite) and an irregular and asymmetric twelve-fold (norsethite) coordination (Ende et al., 2017; Effenberger et al., 2014; Lippmann, 1973). In norsethite, therefore the coordination polyhedra of $Ba^{2+}$ and $Mg^{2+}$ are more different than the coordination polyhedra of $Ca^{2+}$ and $Mg^{2+}$ in dolomite. The difference in norsethite is large enough to preclude the substitution of cations by the high free energy of formation associated with $BaO_6$ and $MgO_{12}$ polyhedra. Consequently, the formation of a $Ba_xMg_{1-x}CO_3$ solid solution is energetically unfavorable. In accordance with the experiments presented here, the only way to combine both cations within one phase is ordering into distinct cation layers. The failure to form a solid solution, therefore, is one important prerequisite for the preferred and rapid occurrence of ordered norsethite.

Neither cation ordering, as discussed above, nor $Mg^{2+}$ dehydration slow down norsethite growth rates at ambient conditions, as it is the case for dolomite and magnesite. This indicates that some rate promoting mechanism must exist which is active during norsethite growth, but not during dolomite or magnesite growth. This mechanism can only be located at the norsethite surface where parameters like the hydration energy of $Mg^{2+}$ can differ significantly from the well-known values in bulk solution. Although the detailed nature of this mechanism is unknown, a possible explanation might again be found in highly different coordination polyhedra of $Mg^{2+}$ and $Ba^{2+}$ in norsethite. Due to different compositions, lattice parameters, and carbonate group orientations, the surface sites on norsethite, magnesite and dolomite differ significantly. Therefore it is reasonable to assume that the aqueous Mg-complex, which is adsorbed on the norsethite surface, becomes distorted by the kink surroundings in such a way that dehydration and incorporation rates are enhanced. Even subtle structural modifications of kink sites, as it is the case for obtuse and acute steps on the magnesite (104) surface, can easily cause differences in reactivity of more than one order of magnitude (Saldi et al., 2009). This example strongly emphasizes the importance of the ability of a given mineral surface to destabilize the hydrous metal complex. A further sign pointing in this direction is the existence of $PbMg(CO_3)_2$, which is isostructural to norsethite, contains the same amount of magnesium, and also grows at ambient conditions within comparatively short timescales (Lippmann, 1966).

The direct comparison of the norsethite growth data measured here with corresponding data for magnesite and dolomite shows that the growth rate constants of anhydrous magnesium-bearing carbonate minerals span a range of more than five orders of magnitude. This fact undoubtedly proves that not only the

stability of the aqueous $Mg^{2+}$-complex per se is an important factor controlling the growth rate but also the means of a given surface to weaken the stability of the metal-complex. This finding implies that, in principle, it should be possible to accelerate the growth rates of anhydrous Mg-bearing carbonates, if the stability of the aqueous $Mg^{2+}$-complex can be weakened at the crystal surface. In the case of magnesite surfaces, the vast anisotropy of step propagation (as detected by AFM, e.g., Saldi et al., 2009) clearly shows that the prerequisite to enhance growth rates already exists at few specific surface sites. For the implementation of a fast overall growth rate, however, fast dehydration of the aqueous $Mg^{2+}$-complex has to take place at all sites controlling growth rate.

The work presented here provides first insights into norsethite growth kinetics. Nevertheless, the $BaCO_3$-$MgCO_3$ system offers more opportunities to study the growth of Mg-bearing carbonates. Norsethite growth experiments imaged with atomic force microscopy could yield valuable information on the processes happening directly at the mineral surface. Due to small crystal sizes and therefore difficult sample preparation, however, studies in this direction are highly challenging.

Likewise, the dissolution-reprecipitation reaction of witherite to norsethite has only been explored macroscopically. If the difficulties of sample preparation of an aragonite-type mineral for AFM experiments can be handled, this type of experiments certainly gives valuable insights into norsethite nucleation and growth mechanisms as well as $Mg^{2+}$ dehydration and incorporation at ambient conditions. Additionally, in-situ spectroscopic methods (e.g., μ-Raman or IR-spectroscopy) seem suitable to gain information on changes of carbonate speciation during norsethite precipitation.

Investigations in the $BaCO_3$-$MgCO_3$ system could be extended to studies of norsethite nucleation behavior. Growth of norsethite on given seeds has been characterized in the present work. The nucleation of norsethite, however, is largely unexplored territory. In this context, the determination of Mg-isotope fractionation during nucleation and growth of norsethite might give valuable insights into processes that happen at the mineral surface during the dehydration of Mg.

One important step towards a better understanding of Mg-carbonate growth is the deciphering of the detailed growth mechanism of norsethite. This involves the identification of the crystallographic structures of the mineral surfaces in contact to the growth solutions, which would allow for the determination of distinct kink sites that are able to incorporate and dehydrate $Mg^{2+}$ rapidly. Investigations in this direction can be tackled experimentally, e.g., with X-ray reflectivity methods, or by employing ab-initio molecular dynamics calculations of the surface and interactions with the aqueous $Mg^{2+}$ complex.

But not only the $BaCO_3$-$MgCO_3$ system offers more opportunities to obtain a better understanding of growth of anhydrous Mg-bearing carbonates. Systems with

other "dolomite analogues", like $SrMg(CO_3)_2$ and $PbMg(CO_3)_2$, can be expected to yield important information, too. Detailed knowledge about crystal structures and growth kinetics in these systems would allow for a direct comparison of structure-property relations of different Mg-bearing carbonates. This may result in a comprehensive understanding of the difficulties associated with the growth of some Mg-bearing carbonate minerals.

# References

Aldushin K., Jordan G., Rammensee W., Schmahl W. W. and Becker H.-W. (2004) Apophyllite (001) surface alteration in aqueous solutions studied by HAFM. *Geochimica et Cosmochimica Acta* **68**, 217–226.

Archer D. G. (1992) Thermodynamic Properties of the NaCl+$H_2O$ System: II. Thermodynamic Properties of $NaCl_{(aq)}$, $NaCl \cdot 2H_2O(cr)$, and Phase Equilibria. *Journal of Physical and Chemical Reference Data* **21**, 793–829.

Arvidson R. S. and Mackenzie F. T. (1999) The Dolomite Problem: Control of precipitation kinetics by temperature and saturation state. *American Journal of Science* **299**, 257–288.

Astilleros J. M., Fernández-Díaz L. and Putnis A. (2010) The role of magnesium in the growth of calcite: An AFM study. *Chemical Geology* **271**, 52–58.

Astilleros J. M., Pina C. M., Fernández-Díaz L., Prieto M. and Putnis A. (2006) Nanoscale phenomena during the growth of solid solutions on calcite $\{10\bar{1}4\}$ surfaces. *Chemical Geology* **225**, 322–335.

Astilleros J. M., Pina C. M., Fernández-Díaz L. and Putnis A. (2000) The effect of barium on calcite $\{10\bar{1}4\}$ surfaces during growth. *Geochimica et Cosmochimica Acta* **64**, 2965–2972.

Astilleros J. M., Pina C. M., Fernández-Díaz L. and Putnis A. (2003) Metastable phenomena on calcite $\{10\bar{1}4\}$ surfaces growing from $Sr^{2+}$–$Ca^{2+}$–$CO_3^{2-}$ aqueous solutions. *Chemical Geology* **193**, 93–107.

Audigane P., Gaus I., Czernichowski-Lauriol I., Pruess K. and Xu T. (2007) Two-dimensional reactive transport modeling of $CO_2$ injection in a saline aquifer at the Sleipner site, North Sea. *American Journal of Science* **307**, 974–1008.

Bathurst R. G. C. (1971) Carbonate sediments and their diagenesis. Elsevier, Amsterdam.

Bénézeth P., Berninger U.-N., Bovet N., Schott J. and Oelkers E. H. (2018) Experimental determination of the solubility product of dolomite at 50 to 253 °C. *Geochimica et Cosmochimica Acta* **224**, 262–275.

Bénézeth P., Dandurand J. L. and Harrichoury J. C. (2009) Solubility product of siderite ($FeCO_3$) as a function of temperature (25–250 °C). *Chemical Geology* **265**, 3–12.

Bénézeth P., Saldi G. D., Dandurand J.-L. and Schott J. (2011) Experimental determination of the solubility product of magnesite at 50 to 200 °C. *Chemical Geology* **286**, 21–31.

Bénézeth P., Stefánsson A., Gautier Q. and Schott J. (2013) Mineral Solubility and Aqueous Speciation Under Hydrothermal Conditions to 300 °C - The Carbonate System as an Example. *Reviews in Mineralogy and Geochemistry* **76**, 81–133.

Berner R. A. (1975) The role of magnesium in the crystal growth of calcite and aragonite from sea water. *Geochimica et Cosmochimica Acta* **39**, 489–504.

Berninger U.-N., Jordan G., Lindner M., Reul A., Schott J. and Oelkers E. H. (2016) On the effect of aqueous Ca on magnesite growth – Insight into trace element inhibition of carbonate mineral precipitation. *Geochimica et Cosmochimica Acta* **178**, 195–209.

Berninger U.-N., Jordan G., Schott J. and Oelkers E. H. (2014) The experimental determination of hydromagnesite precipitation rates at 22.5–75 °C. *Mineralogical Magazine* **78**, 1405–1416.

Berninger U.-N., Saldi G. D., Jordan G., Schott J. and Oelkers E. H. (2017) Assessing dolomite surface reactivity at temperatures from 40 to 120 °C by hydrothermal atomic force microscopy. *Geochimica et Cosmochimica Acta* **199**, 130–142.

Bischoff J. L. (1968) Kinetics of calcite nucleation Magnesium ion inhibition and ionic strength catalysis. *Journal of Geophysical Research* **73**, 3315–3322.

Bleuzen A., Pittet P.-A., Helm L. and Merbach A. E. (1997) Water exchange on magnesium(II) in aqueous solution: A variable temperature and pressure $^{17}$O NMR study. *Magnetic Resonance in Chemistry* **35**, 765–773.

Bontognali T. R. R., McKenzie J. A., Warthmann R. J. and Vasconcelos C. (2014) Microbially influenced formation of Mg-calcite and Ca-dolomite in the presence of exopolymeric substances produced by sulphate-reducing bacteria. *Terra Nova* **26**, 72–77.

Böttcher M. E. (2000) Stable Isotope Fractionation during Experimental Formation of Norsethite (BaMg[$CO_3$]$_2$): A Mineral Analogue of Dolomite. *Aquatic Geochemistry* **6**, 201–212.

Böttcher M. E., Gehlken P.-L., Skogby H. and Reutel C. (1997) The vibrational spectra of BaMg($CO_3$)$_2$ (norsethite). *Mineralogical Magazine* **61**, 249–256.

Bracco J. N., Stack A. G. and Higgins S. R. (2014) Magnesite Step Growth Rates as a Function of the Aqueous Magnesium:Carbonate Ratio. *Crystal Growth & Design* **14**, 6033–6040.

Braithwaite C. J. R., Rizzi G. and Darke G. (2004) The geometry and petrogenesis of dolomite hydrocarbon reservoirs. Geological Society of London.

Brown P. L., Drummond S. E. and Palmer D. A. (1996) Hydrolysis of magnesium(II) at elevated temperatures. *Journal of the Chemical Society, Dalton Transactions* **14**, 3071.

Busenberg E. and Plummer L. N. (1986a) A Comparative Study of the Dissolution and Crystal Growth Kinetics of Calcite and Aragonite. In *Studies in diagenesis* (ed. F. A. Mumpton), 139–168.

Busenberg E. and Plummer L. N. (1986b) The solubility of $BaCO_3$(cr) (witherite) in $CO_2$-$H_2O$ solutions between 0 and 90 °C, evaluation of the association constants of $BaHCO_3^+$(aq) and $BaCO_3^0$(aq) between 5 and 80 °C, and a preliminary evaluation of the thermodynamic properties of $Ba^{2+}$(aq). *Geochimica et Cosmochimica Acta* **50**, 2225–2233.

Chang L. L. Y. (1964) Synthesis of MBa($CO_3$)$_2$ compounds. *American Mineralogist* **49**, 1142–1143.

Choudens-Sánchez V. D. and Gonzalez L. A. (2009) Calcite and Aragonite Precipitation Under Controlled Instantaneous Supersaturation: Elucidating the Role of $CaCO_3$ Saturation State and Mg/Ca Ratio on Calcium Carbonate Polymorphism. *Journal of Sedimentary Research* **79**, 363–376.

Davis K. J., Dove P. M. and De Yoreo J. J. (2000) The Role of $Mg^{2+}$ as an Impurity in Calcite Growth. *Science* **290**, 1134–1137.

De Villiers J. P. (1971) Cystal Structures of aragonite, strontianite and witherite. *American Mineralogist* **56**, 758–767.

Dietzel M., Gussone N. and Eisenhauer A. (2004) Co-precipitation of $Sr^{2+}$ and $Ba^{2+}$ with aragonite by membrane diffusion of $CO_2$ between 10 and 50 °C. *Chemical Geology* **203**, 139–151.

Dromgoole E. L. and Walter L. M. (1990) Inhibition of calcite growth rates by $Mn^{2+}$ in $CaCl_2$ solutions at 10, 25, and 50°C. *Geochimica et Cosmochimica Acta* **54**, 2991–3000.

Dufaud F., Martinez I. and Shilobreeva S. (2009) Experimental study of Mg-rich silicates carbonation at 400 and 500 °C and 1 kbar. *Chemical Geology* **265**, 79–87.

Effenberger H., Mereiter K. and Zemann J. (1981) Crystal structure refinements of magnesite, calcite, rhodochrosite, siderite, smithonite, and dolomite, with discussion of some aspects of the stereochemistry of calcite type carbonates. *Zeitschrift für Kristallographie - Crystalline Materials* **156**, 783.

Effenberger H., Pippinger T., Libowitzky E., Lengauer C. L. and Miletich R. (2014) Synthetic norsethite, $BaMg(CO_3)_2$: revised crystal structure, thermal behaviour and displacive phase transition. *Mineralogical Magazine* **78**, 1589–1611.

Effenberger H. and Zemann J. (1985) Single crystal X-ray investigation of Norsethite, $BaMg(CO_3)_2$: one more mineral with an aplanar carbonate group. *Zeitschrift für Kristallographie* **171**, 275–280.

Ende M., Effenberger H. and Miletich R. (2017) Evolution of the $\alpha$-$BaMg(CO_3)_2$ low-temperature superstructure and the tricritical nature of its $\alpha$–$\beta$ phase transition. *Acta Crystallographica Section B, Structural Science, Crystal Engineering and Materials* **73**, 827–835.

Fairbridge R. W. (1957) The dolomite question. In *Regional Aspects of Carbonate Deposition: A Symposium* (eds. R. J. LeBlanc and J. G. Breeding). Tulsa, Oklahoma, pp. 125–178.

Felmy A. R., Qafoku O., Arey B. W., Kovarik L., Liu J., Perea D. and Ilton E. S. (2015) Enhancing magnesite formation at low temperature and high $CO_2$ pressure: The impact of seed crystals and minor components. *Chemical Geology* **395**, 119–125.

Fenter P., Zhang Z., Park C., Sturchio N. C., Hu X. M. and Higgins S. R. (2007) Structure and reactivity of the dolomite (104)–water interface: New insights into the dolomite problem. *Geochimica et Cosmochimica Acta* **71**, 566–579.

Freeman C. L., Asteriadis I., Yang M. and Harding J. H. (2009) Interactions of Organic Molecules with Calcite and Magnesite Surfaces. *The Journal of Physical Chemistry C* **113**, 3666–3673.

Froese E. (1967) A note on strontium magnesium carbonate. *The Canadian Mineralogist* **9**, 65–70.

Gaetani G. A. and Cohen A. L. (2006) Element partitioning during precipitation of aragonite from seawater A framework for understanding paleoproxies. *Geochimica et Cosmochimica Acta* **70**, 4617–4634.

Garrels R. M. (1959) Rates of geochemical reactions at low temperatures and pressures. In *Researches in Geochemistry* (ed. P. H. Abelson). John Wiley & Sons, Inc. New York, 25–37.

Gautier Q., Bénézeth P., Mavromatis V. and Schott J. (2014) Hydromagnesite solubility product and growth kinetics in aqueous solution from 25 to 75 °C. *Geochimica et Cosmochimica Acta* **138**, 1–20.

Gautier Q., Bénézeth P. and Schott J. (2016) Magnesite growth inhibition by organic ligands An experimental study at 100, 120 and 146 °C. *Geochimica et Cosmochimica Acta* **181**, 101–125.

Gautier Q., Berninger U.-N., Schott J. and Jordan G. (2015) Influence of organic ligands on magnesite growth: A hydrothermal atomic force microscopy study. *Geochimica et Cosmochimica Acta* **155**, 68–85.

Giammar D. E., Bruant R. G. and Peters C. A. (2005) Forsterite dissolution and magnesite precipitation at conditions relevant for deep saline aquifer storage and sequestration of carbon dioxide. *Chemical Geology* **217**, 257–276.

Given R. K. and Wilkinson B. H. (1987) Dolomite abundance and stratigraphic age; constraints on rates and mechanisms of Phanerozoic dolostone formation. *Journal of Sedimentary Research* **57**, 1068–1078.

Glover E. D. and Sippel R. F. (1967) Synthesis of magnesium calcites. *Geochimica et Cosmochimica Acta* **31**, 603–613.

Gregg J. M., Bish D. L., Kaczmarek S. E., Machel H. G. and Hollis C. (2015) Mineralogy, nucleation and growth of dolomite in the laboratory and sedimentary environment – A review. *Sedimentology* **62**, 1749–1769.

Gutjahr A., Dabringhaus H. and Lacmann R. (1996) Studies of the growth and dissolution kinetics of the $CaCO_3$ polymorphs calcite and aragonite: II. The influence of divalent cation additives on the growth and dissolution rates. *Journal of Crystal Growth* **158**, 310–315.

Hall J. M. and Chan L.-H. (2004) Ba/Ca in benthic foraminifera: Thermocline and middepth circulation in the North Atlantic during the last glaciation. *Paleoceanography* **19**, 1–13.

Hänchen M., Prigiobbe V., Baciocchi R. and Mazzotti M. (2008) Precipitation in the Mg-carbonate system – effects of temperature and $CO_2$ pressure. *Chemical Engineering Science* **63**, 1012–1028.

Hardie L. A. (1987) Dolomitization: A Critical View of some Current Views. *Journal of Sedimentary Petrology* **57**, 166–183.

Hasson D., Avriel M., Resnick W., Rozenman T. and Windreich S. (1968) Mechanism of Calcium Carbonate Scale Deposition on Heat-Transfer Surfaces. *Industrial & Engineering Chemistry Fundamentals* **7**, 59–65.

Higgins S. R., Eggleston C. M., Knauss K. G. and Boro C. O. (1998) A hydrothermal atomic force microscope for imaging in aqueous solution up to 150 °C. *Review of Scientific Instruments* **69**, 2994–2998.

Higgins S. R. and Hu X. (2005) Self-limiting growth on dolomite: Experimental observations with in situ atomic force microscopy. *Geochimica et Cosmochimica Acta* **69**, 2085–2094.

Higgins S. R., Jordan G. and Eggleston C. M. (2002) Dissolution kinetics of magnesite in acidic aqueous solution: A hydrothermal atomic force microscopy study assessing step kinetics and dissolution flux. *Geochimica et Cosmochimica Acta* **66**, 3201–3210.

Holland H. D. and Turekian K. K. (2014) Treatise on geochemistry. Elsevier Pergamon, Oxford, UK.

Holland H. D. and Zimmermann H. (2000) The Dolomite Problem Revisited[1]. *International Geology Review* **42**, 481–490.

Hood W. C. and Steidl P. F. (1973) Synthesis of Benstonite at Room Temperatur. *American Mineralogist* **58**, 347.

Hood W. C., Steidl P. F. and Tschopp D. G. (1974) Precipitation of Norsethite at Room Temperature. *American Mineralogist* **59**, 471–474.

Hopkinson L., Kristova P., Rutt K. and Cressey G. (2012) Phase transitions in the system $MgO$-$CO_2$-$H_2O$ during $CO_2$ degassing of Mg-bearing solutions. *Geochimica et Cosmochimica Acta* **76**, 1–13.

Jonas L., Müller T., Dohmen R., Immenhauser A. and Putlitz B. (2017) Hydrothermal replacement of biogenic and abiogenic aragonite by Mg-carbonates – Relation between textural control on effective element fluxes and resulting carbonate phase. *Geochimica et Cosmochimica Acta* **196**, 289–306.

Jones M. J., Butchins L. J., Charnock J. M., Pattrick R. A., Small J. S., Vaughan D. J., Wincott P. L. and Livens F. R. (2011) Reactions of radium and barium with the surfaces of carbonate minerals. *Applied Geochemistry* **26**, 1231–1238.

Jordan G. and Astilleros J. M. (2006) In situ HAFM study of the thermal dehydration on gypsum (010) surfaces. *American Mineralogist* **91**, 619–627.

Jordan G., Higgins S. R., Eggleston C. M., Knauss K. G. and Schmahl W. W. (2001) Dissolution kinetics of magnesite in acidic aqueous solution, a hydrothermal atomic force microscopy (HAFM) study: step orientation and kink dynamics. *Geochimica et Cosmochimica Acta* **65**, 4257–4266.

Kaczmarek S. E. and Sibley D. F. (2014) Direct physical evidence of dolomite recrystallization. *Sedimentology* **61**, 1862–1882.

Kaczmarek S. E. and Thornton B. P. (2017) The effect of temperature on stoichiometry, cation ordering, and reaction rate in high-temperature dolomitization experiments. *Chemical Geology* **468**, 32–41.

Kampman N., Bickle M., Wigley M. and Dubacq B. (2014) Fluid flow and $CO_2$-fluid-mineral interactions during $CO_2$-storage in sedimentary basins. *Chemical Geology* **369**, 22–50.

Karoui H., Korchef A., Tlili M. M., Mosrati H., Gil O., Mosrati R. and Ben Amor M. (2008) Effects of $Mg^{2+}$, $Ca^{2+}$ and $SO_4^{2-}$ ions on the precipitation kinetics and microstructure of aragonite. *Annales de chimie Science des Matériaux* **33**, 123–134.

Katsikopoulos D., Fernández-González Á. and Prieto M. (2009) Precipitation and mixing properties of the "Disordered" $(Mn,Ca)CO_3$ solid solution. *Geochimica et Cosmochimica Acta* **73**, 6147–6161.

Katz A. (1973) The interaction of magnesium with calcite during crystal growth at 25–90°C and one atmosphere. *Geochimica et Cosmochimica Acta* **37**, 1563–1586.

Katz A. and Matthews A. (1977) The dolomitization of $CaCO_3$: An experimental study at 252–295 °C. *Geochimica et Cosmochimica Acta* **41**, 297–308.

Kenward P. A., Fowle D. A., Goldstein R. H., Ueshima M., González L. A. and Roberts J. A. (2013) Ordered low-temperature dolomite mediated by carboxyl-group density of microbial cell walls. *AAPG Bulletin* **97**, 2113–2125.

Kessels L. S., Sibley, Duncan, F. and Nordeng S. H. (2000) Nanotopography of synthetic and natural dolomite crystals. *Sedimentology* **47**, 173–186.

King H. E., Satoh H., Tsukamoto K. and Putnis A. (2013) Nanoscale observations of magnesite growth in chloride- and sulfate-rich solutions. *Environmental Science & Technology* **47**, 8684–8691.

Kitano Y. and Kanamori N. (1966) Synthesis of magnesian calcite at low temperatures and pressures. *Geochemical Journal* **1**, 1–10.

Königsberger E., Tran-Ho L.-C. and Gamsjäger H. (1998) Solid-Solute Phase Equilibria in aqueous Solutions X. Solubility Constant and Stability of Norsethite. *Monatshefte für Chemie* **129**, 1061–1066.

Krause S., Liebetrau V., Gorb S., Sánchez-Román M., McKenzie J. A. and Treude T. (2012) Microbial nucleation of Mg-rich dolomite in exopolymeric substances under anoxic modern seawater salinity New insight into an old enigma. *Geology* **40**, 587–590.

La Iglesia A. and Félix J. (1994) Estimation of thermodynamic properties of mineral carbonates at high and low temperatures from the sum of polyhedral contributions. *Geochimica et Cosmochimica Acta* **58**, 3983–3991.

Land L. S. (1985) The Origin of Massive Dolomite. *Journal of Geological Education* **33**, 112–125.

Land L. S. (1998) Failure to Precipitate Dolomite at 25 °C from Dilute Solution Despite 1000-Fold Oversaturation after 32 Years. *Aquatic Geochemistry* **4**, 361–368.

Lea D. W., Shen G. T. and Boyle E. A. (1989) Coralline barium records temporal variability in equatorial Pacific upwelling. *Nature* **340**, 373–376.

Lindner M. and Jordan G. (2018) On the growth of witherite and its replacement by the Mg-bearing double carbonate norsethite – Implications for the dolomite problem. *American Mineralogist* **103**, 252–259.

Lindner M., Saldi G. D., Carrocci S., Bénézeth P., Schott J. and Jordan G. (2018) On the growth of anhydrous Mg-bearing carbonates – Implications from norsethite growth kinetics. *Geochimica et Cosmochimica Acta* **238**, 424–437.

Lindner M., Saldi G. D., Jordan G. and Schott J. (2017) On the effect of aqueous barium on magnesite growth – A new route for the precipitation of the ordered anhydrous Mg-bearing double carbonate norsethite. *Chemical Geology* **460**, 93–105.

Lindsay W. T., Jr (1989) Chemistry of steam cycle solutions: principles. In *The ASME handbook on water technology for thermal power systems* (ed. P. Cohen). American Society of Mechanical Engineers. New York, 341–544.

Lippmann F. (1966) $PbMg(CO_3)_2$, ein neues rhomboedrisches Doppelcarbonat. *Die Naturwissenschaften* **53**, 701.

Lippmann F. (1967a) Die Kristallstruktur des Norsethit, $BaMg(CO_3)_2$ Mit einem Strukturvorschlag für $PbMg(CO_3)_2$. *Tschermaks mineralogische und petrographische Mitteilungen* **12**, 299–318.

Lippmann F. (1967b) Die Kristallstruktur des Norsethit, $BaMg(CO_3)_2$ im Vergleich zum Dolomit, $CaMg(CO_3)_2$. *Die Naturwissenschaften* **54**, 514.

Lippmann F. (1967c) Die Synthese des Norsethit bei 20° und 1 at. – Ein Modell zu Dolomitisierung. *Neues Jahrbuch für Mineralogie, Monatshefte*, 23–29.

Lippmann F. (1968) Syntheses of $BaMg(CO_3)_2$ (Norsethite) at 20 °C and the Formation of Dolomite in Sediments. In *Recent Developments in Carbonate Sedimentology in Central Europe* (eds. G. Müller and G. M. Friedman). Springer. Berlin, 33–37.

Lippmann F. (1973) Sedimentary carbonate minerals. Springer, Berlin.

Little M. G. and Jackson R. B. (2010) Potential impacts of leakage from deep $CO_2$ geosequestration on overlying freshwater aquifers. *Environmental Science & Technology* **44**, 9225–9232.

Longo J. and Voight K. (1989) Synthesis of mixed-metal carbonates by grinding. *Solid State Ionics* **32/33**, 409–412.

Machel H. G. (2004) Concepts and models of dolomitization. In *The geometry and petrogenesis of dolomite hydrocarbon reservoirs* (eds. C. J. R. Braithwaite, G. Rizzi and G. Darke). Geological Society of London, 7–63.

Mansfield C. F. (1980) A urolith of biogenic dolomite—another clue in the dolomite mystery. *Geochimica et Cosmochimica Acta* **44**, 829–839.

Maslen E. N., Streltsov V. A. and Streltsova N. R. (1993) X-ray study of the electron density in magnesite $MgCO_3$. *Acta Crystallographica Section B Structural Science, Crystal Engineering and Materials* **49**, 980–984.

Mavromatis V., van Zuilen K., Purgstaller B., Baldermann A., Nägler T. F. and Dietzel M. (2016) Barium isotope fractionation during witherite ($BaCO_3$) dissolution, precipitation and at equilibrium. *Geochimica et Cosmochimica Acta* **190**, 72–84.

McKenzie J. A. and Vasconcelos C. (2009) Dolomite Mountains and the origin of the dolomite rock of which they mainly consist: historical developments and new perspectives. *Sedimentology* **56**, 205–219.

Menadakis M., Maroulis G. and Koutsoukos P. G. (2009) Incorporation of $Mg^{2+}$, $Sr^{2+}$, $Ba^{2+}$ and $Zn^{2+}$ into aragonite and comparison with calcite. *Journal of Mathematical Chemistry* **46**, 484–491.

Meunier A. (1995) Hydrothermal Alteration by Veins. In *Origin and Mineralogy of Clays* (ed. B. Velde). Springer Berlin, 247–267.

Millero F. J., Huang F., Graham T. and Pierrot D. (2007) The dissociation of carbonic acid in NaCl solutions as a function of concentration and temperature. *Geochimica et Cosmochimica Acta* **71**, 46–55.

Milton C. and Eugster H. P. (1959) Mineral Assamblages of the Green River Formation. In *Researches in Geochemistry* (ed. P. H. Abelson). John Wiley & Sons, Inc. New York, 118–150.

Momma K. and Izumi F. (2011) VESTA 3 for three-dimensional visualization of crystal, volumetric and morphology data. *Journal of Applied Crystallography* **44**, 1272–1276.

Montaggioni L. F., Le Cornec F., Corrège T. and Cabioch G. (2006) Coral barium/calcium record of mid-Holocene upwelling activity in New Caledonia, South-West Pacific. *Palaeogeography, Palaeoclimatology, Palaeoecology* **237**, 436–455.

Montes-Hernandez G., Findling N., Renard F. and Auzende A.-L. (2014) Precipitation of Ordered Dolomite via Simultaneous Dissolution of Calcite and Magnesite – New Experimental Insights into an Old Precipitation Enigma. *Crystal Growth & Design* **14**, 671–677.

Morrow D. W. and Ricketts B. D. (1986) Chemical controls on the precipitation of mineral analogues of dolomite: The sulfate enigma. *Geology* **14**, 408–410.

Morse J. W. and Mackenzie F. T. (1990) Geochemistry of Sedimentary Carbonates. Elsevier, Amsterdam.

Mrose M. E., Chao E., Fahey J. J. and Milton C. (1961) Norsethite, $BaMg(CO_3)_2$, a new Mineral from the Green River Formation, Wyoming. *American Mineralogist*, 420–429.

Mucci A. and Morse J. W. (1983) The incorporation of $Mg^{2+}$ and $Sr^{2+}$ into calcite overgrowths: influences of growth rate and solution composition. *Geochimica et Cosmochimica Acta* **47**, 217–233.

Mucci A. and Morse J. W. (1985) Auger spectroscopy determination of the surface-most adsorbed layer composition on aragonite, calcite, dolomite, and magnesite in synthetic seawater. *American Journal of Science* **285**, 306–317.

Nancollas G. H. and Reddy M. M. (1971) The crystallization of calcium carbonate: II. Calcite growth mechanism. *Journal of colloid and interface science* **37**, 824–830.

Nielsen A. E. (1983) Precipitates: Formation, coprecipitation, and aging. In *Treatise on analytical chemistry* (eds. I. M. Kolthoff and P. J. Elving). Wiley, New York, 269–347.

Noguera C., Fritz B. and Clément A. (2012) A Theoretical Treatment of the Precipitation of Doubly Substituted Solid Solutions in Aqueous Solutions. *Crystal Growth & Design* **12**, 3444–3457.

Noguera C., Fritz B. and Clément A. (2017) Kinetics of Precipitation of Non-ideal Binary Solid-solutions in an Aqueous Medium. *Procedia Earth and Planetary Science* **17**, 169–172.

Oelkers E. H., Bénézeth P. and Pokrovski G. S. (2009) Thermodynamic Databases for Water-Rock Interaction. *Reviews in Mineralogy and Geochemistry* **70**, 1–46.

Oelkers E. H. and Cole D. R. (2008) Carbon Dioxide Sequestration: A Solution to a Global Problem. *Elements* **4**, 305–310.

Palmer D. A., Bénézeth P. and Wesolowski D. J. (2001) Aqueous high-temperature solubility studies: I. The solubility of boehmite as functions of ionic strength (to 5 molal, NaCl), temperature (100–290 °C), and pH as determined by in situ measurements. *Geochimica et Cosmochimica Acta* **65**, 2081–2095.

Paquette J. and Reeder R. J. (1995) Relationship between surface structure, growth mechanism, and trace element incorporation in calcite. *Geochimica et Cosmochimica Acta* **59**, 735–749.

Parkhurst D. L. and Appelo C. A. J. (2013) Description of input and examples for PHREEQC version 3 – A computer program for speciation, batch-reaction, one-dimensional transport, and inverse geochemical calculations. In *U. S. Geological Survey Techniques and Methods* **6,** A43.

Petrash D. A., Bialik O. M., Bontognali T. R., Vasconcelos C., Roberts J. A., McKenzie J. A. and Konhauser K. O. (2017) Microbially catalyzed dolomite formation: From near-surface to burial. *Earth-Science Reviews* **171**, 558–582.

Pi D.-H., Jiang S.-Y., Luo L., Yang J.-H. and Ling H.-F. (2014) Depositional environments for stratiform witherite deposits in the Lower Cambrian black shale sequence of the Yangtze Platform, southern Qinling region, SW China Evidence from redox-sensitive trace element geochemistry. *Palaeogeography, Palaeoclimatology, Palaeoecology* **398**, 125–131.

Pimentel C. and Pina C. M. (2014) The formation of the dolomite-analogue norsethite: Reaction pathway and cation ordering. *Geochimica et Cosmochimica Acta* **142**, 217–223.

Pimentel C. and Pina C. M. (2016) Reaction pathways towards the formation of dolomite-analogues at ambient conditions. *Geochimica et Cosmochimica Acta* **178**, 259–267.

Pina C. M., Becker U., Risthaus P., Bosbach D. and Putnis A. (1998) Molecular-scale mechanisms of crystal growth in barite. *Nature* **395**, 483.

Pina C. M. and Jordan G. (2010) Reactivity of mineral surfaces at nano-scale. In *Nanoscopic Approaches in Earth and Planetary Sciences* (eds. G. Ferraris, F. E. Brenker and G. Jordan). Mineralogical Society of Great Britain and Ireland. London, 239–323.

Pingitore N. E. (1986) Modes of Coprecipitation of $Ba^{2+}$ and $Sr^{2+}$ with Calcite. In *Geochemical Processes at Mineral Surfaces* (eds. J. A. Davis and K. F. Hayes). American Chemical Society. Washington D.C., 574–586.

Pingitore N. E. and Eastman M. P. (1984) The experimental partitioning of $Ba^{2+}$ into calcite. *Chemical Geology* **45**, 113–120.

Pippinger T., Miletich R., Effenberger H., Hofer G., Lotti P. and Merlini M. (2014) High-pressure polymorphism and structural transitions of norsethite, $BaMg(CO_3)_2$. *Physics and Chemistry of Minerals* **41**, 737–755.

Pokrovsky O. S. and Schott J. (2002) Surface Chemistry and Dissolution Kinetics of Divalent Metal Carbonates. *Environmental Science & Technology* **36**, 426–432.

Power I. M., Kenward P. A., Dipple G. M. and Raudsepp M. (2017) Room Temperature Magnesite Precipitation. *Crystal Growth & Design* **17**, 5652–5659.

Pretet C., van Zuilen K., Nägler T. F., Reynaud S., Böttcher M. E. and Samankassou E. (2015) Constraints on barium isotope fractionation during aragonite precipitation by corals. *The Depositional Record* **1**, 118–129.

Prieto M. (2009) Thermodynamics of Solid Solution-Aqueous Solution Systems. *Reviews in Mineralogy and Geochemistry* **70**, 47–85.

Prieto M., Fernández-González A., Putnis A. and Fernández-Díaz L. (1997) Nucleation, growth, and zoning phenomena in crystallizing $(Ba,Sr)CO_3$, $Ba(SO_4,CrO_4)$, $(Ba,Sr)SO_4$, and $(Cd,Ca)CO_3$ solid solutions from aqueous solutions. *Geochimica et Cosmochimica Acta* **61**, 3383–3397.

Prieto M., Heberling F., Rodríguez-Galán R. M. and Brandt F. (2016) Crystallization behavior of solid solutions from aqueous solutions – An environmental perspective. *Progress in Crystal Growth and Characterization of Materials* **62**, 29–68.

Prigiobbe V., Hänchen M., Werner M., Baciocchi R. and Mazzotti M. (2009) Mineral carbonation process for $CO_2$ sequestration. *Energy Procedia* **1**, 4885–4890.

Putnis A. (2009) Mineral Replacement Reactions. *Reviews in Mineralogy and Geochemistry* **70**, 87–124.

Reddy M. M. and Nancollas G. H. (1971) The crystallization of calcium carbonate: I. Isotopic Exchange and Kinetics. *Journal of colloid and interface science* **36**, 166–172.

Reddy M. M. and Nancollas G. H. (1976) The crystallization of calcium carbonate: IV. The effect of magnesium, strontium and sulfate ions. *Journal of Crystal Growth* **35**, 33–38.

Reddy M. M. and Wang K. (1980) Crystallization of calcium carbonate in the presence of metal ions. *Journal of Crystal Growth* **50**, 470–480.

Reeder R. J. (1983) Crystal chemistry of the rhombohedral carbonates. In *Carbonates* (ed. R. J. Reeder). Mineralogical Society of America. Washington, D.C., 1–47.

Reeder R. J. (1996) Interaction of divalent cobalt, zinc, cadmium, and barium with the calcite surface during layer growth. *Geochimica et Cosmochimica Acta* **60**, 1543–1552.

Reeder R. J., Lamble G. M. and Northrup P. A. (1999) XAFS study of the coordination and local relaxation around $Co^{2+}$, $Zn^{2+}$, $Pb^{2+}$, and $Ba^{2+}$ trace elements in calcite. *American Mineralogist* **84**, 1049–1060.

Reinhold C. (1998) Multiple episodes of dolomitization and dolomite recrystallization during shallow burial in Upper Jurassic shelf carbonates Eastern Swabian Alb, southern Germany. *Sedimentary Geology* **121**, 71–95.

Rimstidt J. D., Balog A. and Webb J. (1998) Distribution of trace elements between carbonate minerals and aqueous solutions. *Geochimica et Cosmochimica Acta* **62**, 1851–1863.

Roberts J. A., Kenward P. A., Fowle D. A., Goldstein R. H., González L. A. and Moore D. S. (2013) Surface chemistry allows for abiotic precipitation of dolomite at low temperature. *Proceedings of the National Academy of Sciences* **110**, 14540–14545.

Rodriguez-Blanco J. D., Shaw S. and Benning L. G. (2015) A route for the direct crystallization of dolomite. *American Mineralogist* **100**, 1172–1181.

Rodríguez-Navarro C. and Benning L. G. (2013) Control of Crystal Nucleation and Growth by Additives. *Elements* **9**, 203–209.

Rubin S. I., King S. L., Jahnke R. A. and Froelich P. N. (2003) Benthic barium and alkalinity fluxes: Is Ba an oceanic paleo-alkalinity proxy for glacial atmospheric $CO_2$? *Geophysical Research Letters* **30**, 1885.

Saldi G. D., Jordan G., Schott J. and Oelkers E. H. (2009) Magnesite growth rates as a function of temperature and saturation state. *Geochimica et Cosmochimica Acta* **73**, 5646–5657.

Saldi G. D., Schott J., Pokrovsky O. S., Gautier Q. and Oelkers E. H. (2012) An experimental study of magnesite precipitation rates at neutral to alkaline conditions and 100–200 °C as a function of pH, aqueous solution composition and chemical affinity. *Geochimica et Cosmochimica Acta* **83**, 93–109.

Saldi G. D., Schott J., Pokrovsky O. S. and Oelkers E. H. (2010) An experimental study of magnesite dissolution rates at neutral to alkaline conditions and 150 and 200 °C as a function of pH, total dissolved carbonate concentration, and chemical affinity. *Geochimica et Cosmochimica Acta* **74**, 6344–6356.

Sánchez-Pastor N., Gigler A. M., Jordan G., Schmahl W. W. and Fernández-Díaz L. (2011) Raman Study of Synthetic Witherite-Strontianite Solid Solutions. *Spectroscopy Letters* **44**, 500–504.

Sánchez-Román M., McKenzie J. A., de Luca Rebello Wagener, A., Rivadeneyra M. A. and Vasconcelos C. (2009) Presence of sulfate does not inhibit low-temperature dolomite precipitation. *Earth and Planetary Science Letters* **285**, 131–139.

Sanz-Montero M. E. and Rodríguez-Aranda J. P. (2012) Magnesite formation by microbial activity Evidence from a Miocene hypersaline lake. *Sedimentary Geology* **263–264**, 6–15.

Sayles F. L. and Fyfe W. S. (1973) The crystallization of magnesite from aqueous solution. *Geochimica et Cosmochimica Acta* **37**, 87–99.

Scheetz B. E. and White W. B. (1977) Vibrational spectra of the alkaline earth double carbonates. *American Mineralogist* **62**, 16–50.

Schmidt B. C., Gehlken P.-L. and Böttcher M. E. (2013) Vibrational spectra of $BaMn(CO_3)_2$ and a re-analysis of the Raman spectrum of $BaMg(CO_3)_2$. *European Journal of Mineralogy* **25**, 137–144.

Schott J., Oelkers E. H., Bénézeth P., Goddéris Y. and François L. (2012) Can accurate kinetic laws be created to describe chemical weathering? *Comptes Rendus Geoscience* **344**, 568–585.

Schott J., Pokrovsky O. S. and Oelkers E. H. (2009) The Link Between Mineral Dissolution/Precipitation Kinetics and Solution Chemistry. *Reviews in Mineralogy and Geochemistry* **70**, 207–258.

Secco L. and Lavina B. (1999) Crystal chemistry of two natural magmatic norsethites, $BaMg(CO_3)_2$, from an Mg-carbonatite of the alkaline carbonatitic complex of Tapira (SE Brazil). *Neues Jahrbuch für Mineralogie, Monatshefte*, 87–96.

Shahwan T., Suzer S. and Erten H. N. (1998) Sorption studies of $Cs^+$ and $Ba^{2+}$ cations on magnesite. *Applied Radiation and Isotopes* **49**, 915–921.

Shannon R. D. (1976) Revised effective ionic radii and systematic studies of interatomic distances in halides and chalcogenides. *Acta Crystallographica Section A* **32**, 751–767.

Shiraki R. and Brantley S. L. (1995) Kinetics of near-equilibrium calcite precipitation at 100 °C: An evaluation of elementary reaction-based and affinity-based rate laws. *Geochimica et Cosmochimica Acta* **59**, 1457–1471.

Shock E. L., Sassani D. C., Willis M. and Sverjensky D. A. (1997) Inorganic species in geologic fluids: correlations among standard molal thermodynamic properties of aqueous ions and hydroxide complexes. *Geochimica et Cosmochimica Acta* **61**, 907–950.

Speer J. A. (1983) Crystal chemistry and phase relations of orthorhombic carbonates. In *Carbonates* (ed. R. J. Reeder). Mineralogical Society of America. Washington, D.C., 145–190.

Staudt W. J., Reeder R. J. and Schoonen M. A. (1994) Surface structural controls on compositional zoning of $SO_4^{2-}$ and $SeO_4^{2-}$ in synthetic calcite single crystals. *Geochimica et Cosmochimica Acta* **58**, 2087–2098.

Steefel C. I., DePaolo D. J. and Lichtner P. C. (2005) Reactive Transport Modeling: An Essential Tool and a New Research Approach for the Earth Sciences. *Earth & Planetary Science Letters* **240**, 539–558.

Steyn J. G. D. and Watson M. D. (1967) Notes on a new occurrence of norsethite. *American Mineralogist* **52**, 1770–1775.

Teng H. H., Dove P. M. and De Yoreo J. J. (2000) Kinetics of calcite growth: surface processes and relationships to macroscopic rate laws. *Geochimica et Cosmochimica Acta* **64**, 2255–2266.

Tesoriero A. J. and Pankow J. F. (1996) Solid solution partitioning of $Sr^{2+}$, $Ba^{2+}$, and $Cd^{2+}$ to calcite. *Geochimica et Cosmochimica Acta* **60**, 1053–1063.

Tunusoglu Ö., Shahwan T. and Eroglu A. E. (2007) Retention of aqueous $Ba^{2+}$ ions by calcite and aragonite over a wide range of concentrations: Characterization of the uptake capacity, and kinetics of sorption and precipitate formation. *Geochemical Journal* **41**, 379–389.

Usdowski H.-E. (1967) Die Genese von Dolomit in Sedimenten. Springer-Verlag, Berlin.

Usdowski H.-E. (1989) Synthesis of dolomite and magnesite at 60 °C in the system $Ca^{2+}$-$Mg^{2+}$-$CO_3^{2-}$-$Cl_2^{2-}$-$H_2O$. *Die Naturwissenschaften* **76**, 374–375.

Usdowski H.-E. (1994) Synthesis of Dolomite and Geochemical Implications. In *Dolomites: A Volume in Honour of Dolomieu* (eds. B. Purser, M. Tucker and D. H. Zenger). Blackwell Publishing Ltd. Oxford, UK, 345–360.

van der Lee J. and de Windt L. (2001) Present state and future directions of modeling of geochemistry in hydrogeological systems. *Journal of contaminant hydrology* **47**, 265–282.

Vančina V., Plavšić M., Bilinski H., Branica M. and Millero F. J. (1986) Preparation and solubility of northupite from brine and its adsorption properties for Cu(II) and Cd(II) in seawater. *Geochimica et Cosmochimica Acta* **50**, 1329–1336.

Vasconcelos C. (1997) Microbial Mediation of Modern Dolomite Precipitation and Diagenesis Under Anoxic Conditions (Lagoa Vermelha, Rio de Janeiro, Brazil). *SEPM Journal of Sedimentary Research* **67**, 378-390.

Vasconcelos C., McKenzie J. A., Bernasconi S., Grujic D. and Tiens A. J. (1995) Microbial mediation as a possible mechanism for natural dolomite formation at low temperatures. *Nature* **377**, 220–222.

von Allmen K., Böttcher M. E., Samankassou E. and Nägler T. F. (2010) Barium isotope fractionation in the global barium cycle: First evidence from barium minerals and precipitation experiments. *Chemical Geology* **277**, 70–77.

Wagman D. D., Evans W. H., Parker V. B., Schumm R. H., Halow I., Bailey S. M., Churney K. L. and Nuttall T. L. (1982) The NBS tables of chemical thermodynamic properties: Selected values for inorganic and $C_1$ and $C_2$ organic substances in SI units. *Journal of Physical and Chemical Reference Data* **11**, 2.

Wang Y. and Xu H. (2001) Prediction of trace metal partitioning between minerals and aqueous solutions: A linear free energy correlation approach. *Geochimica et Cosmochimica Acta* **65**, 1529–1543.

Warren J. (2000) Dolomite: occurrence, evolution and economically important associations. *Earth-Science Reviews* **52**, 1–81.

Wasylenki L. E., Dove P. M. and De Yoreo J. J. (2005) Effects of temperature and transport conditions on calcite growth in the presence of $Mg^{2+}$: Implications for paleothermometry. *Geochimica et Cosmochimica Acta* **69**, 4227–4236.

Wright D. T. and Wacey D. (2005) Precipitation of dolomite using sulphate-reducing bacteria from the Coorong Region, South Australia: Significance and implications. *Sedimentology* **52**, 987–1008.

Wu C., Wang X., Zhao K., Cao M., Xu H., Xia D. and Lu J. R. (2011) Molecular Modulation of Calcite Dissolution by Organic Acids. *Crystal Growth & Design* **11**, 3153–3162.

Xu J., Yan C., Zhang F., Konishi H., Xu H. and Teng H. H. (2013) Testing the cation-hydration effect on the crystallization of Ca-Mg-$CO_3$ systems. *Proceedings of the National Academy of Sciences* **110**, 17750–17755.

Yoshida Y., Yoshikawa H. and Nakanishi T. (2008) Partition coefficients of Ra and Ba in calcite. *Geochemical Journal* **42**, 295–304.

Zhang F., Xu H., Konishi H., Kemp J. M., Roden E. E. and Shen Z. (2012a) Dissolved sulfide-catalyzed precipitation of disordered dolomite – Implications for the formation mechanism of sedimentary dolomite. *Geochimica et Cosmochimica Acta* **97**, 148–165.

Zhang F., Xu H., Konishi H., Shelobolina E. S. and Roden E. E. (2012b) Polysaccharide-catalyzed nucleation and growth of disordered dolomite: A potential precursor of sedimentary dolomite. *American Mineralogist* **97**, 556–567.

Zhang F., Yan C., Teng H. H., Roden E. E. and Xu H. (2013) In situ AFM observations of Ca-Mg carbonate crystallization catalyzed by dissolved sulfide: Implications for sedimentary dolomite formation. *Geochimica et Cosmochimica Acta* **105**, 44–55.

Zhang Y. and Dawe R. A. (2000) Influence of $Mg^{2+}$ on the kinetics of calcite precipitation and calcite crystal morphology. *Chemical Geology* **163**, 129–138.

Zheng Y.-F. and Böttcher M. E. (2014) Oxygen isotope fractionation in double carbonates. *Isotopes in environmental and health studies* **52**, 29–46.

Zidarov N., Petrov O., Tarassov M., Damyanov Z., Tarassova E., Petkova V., Kalvachev Y. and Zlatev Z. (2009) Mn-rich norsethite from the Kremikovtsi ore deposit, Bulgaria. *Neues Jahrbuch für Mineralogie, Abhandlungen* **186**, 321–331.